

Transfer of Mass and Heat in Polymer Electrolyte Membrane Fuel Cell Cathode

by
Nada Zamel

A thesis presented to the
University of Waterloo
in fulfillment of the
thesis requirement
for the degree of
Master of Applied Science
in
Mechanical Engineering

Waterloo, Ontario, Canada, 2007
©Nada Zamel 2007

I hereby declare that I am the sole author of this thesis. This is a true copy of the thesis, including any required revisions, as accepted by my examiners.

I understand that my thesis may be made electronically available to the public.

Nada Zamel

Abstract

The need for alternative sources of energy with low to zero emissions has led to the development of polymer electrolyte membrane fuel cells. PEM fuel cells are electro-chemical devices that convert chemical energy to electricity by using hydrogen as the fuel and oxygen as the oxidant with water as the byproduct of this reaction. One of the major barriers to the commercialization of these cells is the losses that occur at the cathode due to the slow oxygen diffusion and sluggish electrochemical reaction, which are further amplified by the presence of liquid water. Numerous numerical and mathematical models are found in the literature, which investigate the transport phenomena in the cathode and their effects on the cell performance.

In this thesis, the discussion of a two-dimensional, steady state, half cell model is put forward. The conservation equations for mass, momentum, species charge and energy are solved using the commercial software COMSOL Multiphysics. The conservation equations are applied to the cathode bipolar plate, gas diffusion layer and catalyst layer. The flow of gaseous species are assumed to be uniform in the channel. The catalyst layer is assumed to be composed of a uniform distribution of catalyst, liquid water, electrolyte, and void space. The Stefan-Maxwell equation is used to model the multi-species diffusion in the gas diffusion and catalyst layers. Due to the low relative species' velocity, the Darcy law is used to describe the transport of gas and liquid phases in the gas diffusion and catalyst layers. A serpentine flow field is used to distribute the oxidant over the active cathode electrode surface, with pressure loss in the flow direction along the channel. A sensitivity analysis is carried out to investigate the effects of pressure drop in the channel, permeability, inlet relative humidity and shoulder/channel ratio on the performance of the cell.

Electron transport is shown to play an important role in determining the overall performance of the cathode. With a serpentine flow field, the oxygen consumption occurs more aggressively at the areas under the land since electrons are readily available at these areas. In addition, the reaction increases along the catalyst layer thickness and occurs more rapidly at the catalyst layer/membrane interface. The losses due to electron transport are much higher than those due to the proton transport.

The sensitivity analysis put forward illustrated that with the increase of pressure drop along the channel flow field, the performance of the cell and liquid water removal are enhanced. Similarly, an increase in permeability of the porous material results in an increase in liquid water removal and cell performance. Further, the investigation of the inlet relative humidity effects revealed that the electrolyte conductivity has a significant effect on the performance up to a point. On a similar fashion, a decrease in shoulder/channel width ratio leads to an increase in performance and an increase in the leakage between neighboring channels. Finally, the addition of heat is shown to have a negative effect on the cell performance.

Some recommendations can be drawn from the results of this thesis. It is recommended to develop a model to study the flow in the channel flow field in order to investigate the effects of the channel flow on the transport of species in the cell. Further, the geometry of the channel should be studied. Finally, the production of water should be analyzed. The analysis should be extended to investigate its production in vapor form only and its production as a mixture of vapor and liquid.

Acknowledgements

This work was supported by the Natural Sciences and Engineering Research Council of Canada. I would also like to thank Dr. Xianguo Li, for his guidance in the production of this thesis. Further, I want to extend my thanks to Jeff Baschuk and Hao Wu for explaining many concepts pertaining PEM fuel cells and numerical modeling. Lastly, but most importantly, I would like to thank my parents and my siblings for their support throughout all my endeavors.

Contents

1	Introduction	1
1.1	Background	3
1.2	Thesis Objectives	9
1.3	Outline of the Thesis	10
2	Literature Review	12
2.1	Single Phase Models	12
2.2	Multi-phase Models	15
2.3	Multi-phase Mixture Model	19
2.4	Volume of Fluid Model	19
2.5	Eulerian Model	19
2.6	Summary	20
3	Model Formulation	21
3.1	Physical Problem	21
3.2	Oxygen Concentration Drop in the Gas Channel	23
3.3	Gas Pressure Drop in the Channel	25
3.4	Single Phase Model	27
3.4.1	Assumptions	27
3.4.2	Conservation of Momentum	28
3.4.3	Conservation of Species	29
3.4.4	Conservation of Charge	32
3.4.5	Conservation of Energy	34
3.5	Multi-Phase Model	37
3.5.1	Assumptions	37
3.5.2	Conservation of Momentum	38
3.5.3	Conservation of Mass	43
3.5.4	Conservation of Species	46
3.5.5	Conservation of Charge	47
3.5.6	Conservation of Energy	48
3.6	Boundary Conditions	50
3.7	Parameters	53

4	Numerical Method	57
4.1	Integrating the Math Model into COMSOL Multiphysics	58
4.2	Inputs	59
4.3	Validation of the Model	60
4.4	Meshing and Grid Independency	61
5	Isothermal Model Results	63
5.1	Single Phase Model Results	64
5.2	Multi-Phase Model Results	83
5.3	Comparison of Single Phase and Multi-Phase Models	98
5.4	Sensitivity Analysis for Multi-Phase Model	101
5.4.1	Effect of Inlet Relative Humidity	101
5.4.2	Effect of Pressure Drop	113
5.4.3	Effect of Permeability	117
5.4.4	Effect of Shoulder(Land)/Channel (S/C) Width Ratio	120
6	Non-Isothermal Model Results	127
6.1	Single Phase Model Results	128
6.2	Multi-Phase Model Results	137
6.3	Sensitivity Analysis for Multi-Phase Model	142
6.3.1	Effect of Inlet Relative Humidity	142
6.3.2	Effect of Permeability	149
6.3.3	Effect of Shoulder(Land)/Channel Width Ratio	158
7	Concluding Remarks	165
7.1	Summary	169
7.2	Recommendations	171
	References	173

List of Tables

3.1	Summary of source term in energy equation in the different domains for the single phase model	37
3.2	Summary of source term in energy equation in the different domains for the multi-phase model	49
3.3	Operating and physical conditions	56
3.4	Thermal and physical properties of some materials @ 353 <i>K</i> [87][88]	56
5.1	Effect of shoulder/channel width ratio on the performance of the cathode using the Leverette function	121
5.2	Effect of shoulder/channel width ratio on the performance of the cathode - Brooks and Corey relation	122

List of Figures

1.1	The construction of polymer electrolyte membrane (PEM) fuel cell: bipolar plate with gas channels; porous electrodes; reactive layers; polymer membrane [13] . .	3
1.2	The nature of the flow in and the structure of the layers of a PEM fuel cell [13] . .	7
1.3	Polarization curve for a PEM fuel cell showing the regions of losses - Region A is of activation polarization, Region B is of ohmic polarization and Region C is of concentration polarization	8
3.1	Diagram of a serpentine flow field configuration [60]	22
3.2	Modeling Domain - x and y axes have been normalized - flow is in the y-direction (($0 \leq x \leq 6$) denotes a distance of 6 <i>mm</i> , ($0 \leq y \leq 2$) denotes a distance of 2 <i>mm</i> , ($2 \leq y \leq 3$) denotes a distance of 150 μm and ($3 \leq y \leq 4$) denotes a distance of 5 μm)	23
3.3	Effect of inlet relative humidity and cell current density on the pressure drop along a serpentine flow channel	27
3.4	Control volume describing the conservation of momentum in the gas diffusion and catalyst layers	29
3.5	Control volume describing species transport in the gas diffusion and catalyst layers	30
3.6	Control volume applied to the conservation of charge	33
3.7	Control volume of conservation of energy in the bipolar plate and gas diffusion and catalyst layers	35
3.8	Pore with (a) hydrophilic; (b) hydrophobic characteristics	39
3.9	The time dependent contact angle of a catalyst layer with wetting process (a) (0 s) The first attachment of the water droplet at the catalyst layer surface. The contact angle is 148.7°; (b)(60 s), the measured contact angle is 147.8°; (c) (100 s), the measured contact angle is 146.2° [68]	40
3.10	Capillary pressure versus effective saturation for different permeability values evaluated with the Leverette function and Brooks & Corey relation with permeability as the parameter given in the legend	42
3.11	Control volume representing the conservation of liquid water mass in the gas diffusion and catalyst layers	44

3.12	Modeling Domain - x and y axes have been normalized - flow is in the y-direction (($0 \leq x \leq 6$) denotes a distance of 6 mm, ($0 \leq y \leq 2$) denotes a distance of 2 mm, ($2 \leq y \leq 3$) denotes a distance of 150 μm and ($3 \leq y \leq 4$) denotes a distance of 5 μm)	50
3.13	Geometry of the cathode	55
4.1	Error in the average current density vs. the number of meshing elements	62
5.1	Modeling Domain - x and y axes have been normalized - flow is in the y-direction (($0 \leq x \leq 6$) denotes a distance of 6 mm, ($0 \leq y \leq 2$) denotes a distance of 2 mm, ($2 \leq y \leq 3$) denotes a distance of 150 μm and ($3 \leq y \leq 4$) denotes a distance of 5 μm)	64
5.2	(a) 3-D surface plot of oxygen mass fraction in the gas diffusion and catalyst layers. Note that $y = 4$ is the catalyst layer/membrane interface; (b) Distribution of oxygen mass fraction in the gas diffusion and catalyst layers for the single phase model. x and y coordinates have been normalized for better presentation of results (see Figure 5.1)	66
5.3	Velocity distribution in the gas diffusion layer at different points along the gas diffusion layer thickness (m/s) (a) x-component; (b) y-component	68
5.4	Velocity distribution in the catalyst layer at different points along the catalyst layer thickness (m/s) (a) x-component; (b) y-component	69
5.5	(a) 3-D surface plot of oxygen consumption rate in the catalyst layer. Note that $y = 4$ is the catalyst layer/membrane interface; (b) Rate of oxygen consumption in the catalyst layer (kg/m^3) for the single phase model. x and y coordinates have been normalized for better presentation of results. (see Figure 5.1)	71
5.6	(a) 3-D surface plot of overpotential in the catalyst layer. Note that $y = 4$ is the catalyst layer/membrane interface; (b) Overpotential in the catalyst layer (V) for the single phase model. x and y coordinates have been normalized for better presentation of results. (see Figure 5.1)	73
5.7	Streamline plot of the path taken by the electrons in the bipolar plate, gas diffusion and catalyst layers. x and y coordinates have been normalized for better presentation of results. (see Figure 5.1)	74
5.8	Solid potential (V) distribution in the (a) cathode; (b) bipolar plate; (c) gas diffusion layer; (d) catalyst layer for the single phase model. x and y coordinates have been normalized for better presentation of results. (see Figure 5.1)	75
5.9	3-D surface plot of the solid potential in the (a) bipolar plate; (b) gas diffusion layer; (c) catalyst layer.	76
5.10	3-D surface plot of the solid potential current density in the bipolar plate and gas diffusion and catalyst layers in the (a) x-direction; (b) y-direction. Solid potential current density (A/cm^2) in the (c) x-direction; (d) y-direction for the single phase model. x and y coordinates have been normalized for better presentation of results. (see Figure 5.1)	78

5.11	(a) 3-D surface plot of electrolyte potential in the catalyst layer. Note that $y = 4$ is the catalyst layer/membrane interface; (b) Electrolyte potential (V) distribution in the catalyst layer for the single phase model. x and y coordinates have been normalized for better presentation of results. (see Figure 5.1)	79
5.12	3-D surface plot of the electrolyte potential current density in the catalyst layer in the (a) x -direction; (b) y -direction. Electrolyte potential current density (A/cm^2) in the (c) x -direction; (d) y -direction for the single phase model. x and y coordinates have been normalized for better presentation of results. (see Figure 5.1)	81
5.13	(a) 3-D surface plot of relative humidity in the gas diffusion and catalyst layers. Note that $y = 4$ is the catalyst layer/membrane interface; (b) Relative humidity (or water vapor) in the gas diffusion and catalyst layers for the single phase model. x and y coordinates have been normalized for better presentation of results. (see Figure 5.1)	83
5.14	(a) 3-D surface plot of oxygen mass fraction for the multi-phase model. Note $y = 4$ is the catalyst layer/membrane interface; (b) Contour plot of oxygen mass fraction profile in the gas diffusion and catalyst layers for the multi-phase model. x and y coordinates have been normalized for better presentation of results. (see Figure 5.1)	85
5.15	(a) 3-D surface plot of oxygen consumption rate. Note $y = 4$ is the catalyst layer/membrane interface; (b) Contour plot of rate of oxygen consumption in the catalyst layer (kg/m^3) for the multi-phase model. x and y coordinates have been normalized for better presentation of results. (see Figure 5.1)	87
5.16	(a) 3-D surface plot of overpotential in the catalyst layer. Note $y = 4$ is the catalyst layer/membrane interface; (b) Contour plot of overpotential (V) in the catalyst layer for the multi-phase model. x and y coordinates have been normalized for better presentation of results. (see Figure 5.1)	89
5.17	Solid potential (V) distribution in the (a) cathode; (b) bipolar plate; (c) gas diffusion layer; (d) catalyst layer for the multi-phase model. x and y coordinates have been normalized for better presentation of results. (see Figure 5.1)	90
5.18	3-D surface plot of solid potential in (a) bipolar plate; (b) gas diffusion layer; (c) catalyst layer for the multi-phase model.	91
5.19	3-D surface plot of the solid potential current density in the bipolar plate and gas diffusion and catalyst layers in the (a) x -direction; (b) y -direction. Solid potential current density (A/cm^2) in the (c) x -direction; (d) y -direction for the multi-phase model. x and y coordinates have been normalized for better presentation of results. (see Figure 5.1)	92
5.20	(a) 3-D surface plot of electrolyte potential in the catalyst layer. Note $y = 4$ is the catalyst layer/membrane interface; (b) Contour plot of electrolyte potential (V) in the catalyst layer for the multi-phase model. x and y coordinates have been normalized for better presentation of results. (see Figure 5.1)	94

5.21	3-D profile of the electrolyte potential current density in catalyst layer in the (a) x-direction; (b) y-direction. Electrolyte potential current density (A/cm^2) in the (c) x-direction; (d) y-direction for the multi-phase model. x and y coordinates have been normalized for better presentation of results. (see Figure 5.1)	95
5.22	(a) 3-D surface plot of liquid water saturation in the gas diffusion and catalyst layers. Note $y = 4$ is the catalyst layer/membrane interface; (b) Contour plot of liquid water saturation profile in the gas diffusion and catalyst layers for the multi-phase model. x and y coordinates have been normalized for better presentation of results. (see Figure 5.1)	97
5.23	Streamline plot of the liquid water velocity with pressure drop along the flow channel field. x and y coordinates have been normalized. (see Figure 5.1)	98
5.24	Comparison of the oxygen mass fraction in the catalyst layer of the single phase and multi-phase models at different y positions along the catalyst layer. 1-P \equiv single phase, M-P \equiv multi-phase.	99
5.25	Comparison of the rate of oxygen consumption (kg/m^3) in the catalyst layer of the single phase and multi-phase models at different y positions along the catalyst layer. 1-P \equiv single phase, M-P \equiv multi-phase.	100
5.26	Comparison of the overpotential (V) in the catalyst layer of the single phase and multi-phase models at different y positions along the catalyst layer. 1-P \equiv single phase, M-P \equiv multi-phase.	101
5.27	Effect of inlet relative humidity on the performance of the cathode and the electrolyte conductivity using the Leverette function	103
5.28	Relative humidity in the backing and catalyst layers for inlet relative humidity of (a) 50%; (b) 60%; (c) 70%; (d) 80%; (e) 90% - using the Leverette function. x and y coordinates have been normalized for better presentation of results. (see Figure 5.1)	104
5.29	Liquid water saturation in the backing and catalyst layers for inlet relative humidity of (a) 50%; (b) 60%; (c) 70%; (d) 80%; (e) 90% - using the Leverette function. . .	105
5.30	Liquid water saturation in the backing and catalyst layers for inlet relative humidity of (a) 50%; (b) 60%; (c) 70%; (d) 80%; (e) 90% - using the Leverette function. x and y coordinates have been normalized for better presentation of results. (see Figure 5.1)	106
5.31	Liquid water saturation in the backing and catalyst layers for inlet relative humidity of (a) 50%; (b) 60%; (c) 70%; (d) 80%; (e) 90% - using the Leverette function . .	107
5.32	Effect of inlet relative humidity on the performance of the cathode and the electrolyte conductivity using the Brooks and Corey relation	108
5.33	Relative humidity in the backing and catalyst layers for inlet relative humidity of (a) 50%; (b) 60%; (c) 70%; (d) 80%; (e) 90% - using Brooks and Corey relation. x and y coordinates have been normalized for better presentation of results. (see Figure 5.1)	109
5.34	Relative humidity in the backing and catalyst layers for inlet relative humidity of (a) 50%; (b) 60%; (c) 70%; (d) 80%; (e) 90% - using Brooks and Corey relation .	110

5.35	Liquid water saturation in the backing and catalyst layers for inlet relative humidity of (a) 50%; (b) 60%; (c) 70%; (d) 80%; (e) 90%; (f) 100% - using the Brooks and Corey relation. x and y coordinates have been normalized for better presentation of results. (see Figure 5.1)	111
5.36	Liquid water saturation in the backing and catalyst layers for inlet relative humidity of (a) 50%; (b) 60%; (c) 70%; (d) 80%; (e) 90%; (f) 100% - using the Brooks and Corey relation	112
5.37	3-D surface plot of liquid water saturation in the gas diffusion and catalyst layers with the capillary pressure represented using (a) Leverette function; (b) Brooks & Corey relation. Liquid water saturation in the backing and catalyst layers with $\Delta P = 0$ - (c) Leverette Function; (d) Brooks and Corey Relation.	115
5.38	Plot of liquid water velocity streamlines with $\Delta P = 0$ along the channel flow field. x and y coordinates have been normalized for better presentation of results. (see Figure 5.1)	116
5.39	3-D surface plot of liquid water saturation with $\kappa = 5.5 \times 10^{-13} m^2$ - (a) Leverette function; (b) Brooks & Corey relation. Liquid water saturation in the backing and catalyst layers for $\kappa = 5.5 \times 10^{-13} m^2$ - (c) Leverette Function; (d) Brooks and Corey Relation. x and y coordinates have been normalized for better presentation of results. (see Figure 5.1)	118
5.40	3-D surface plot of liquid water saturation for $\kappa = 5.5 \times 10^{-10} m^2$ - (a) Leverette function; (b) Brooks & Corey relation. Liquid water saturation in the backing and catalyst layers for $\kappa = 5.5 \times 10^{-10} m^2$ - (c) Leverette Function; (d) Brooks and Corey Relation. x and y coordinates have been normalized for better presentation of results. (see Figure 5.1)	119
5.41	x -component of the velocity in m/s against the normalized x direction for different permeability values plotted at a normalized y value of 2.5.	120
5.42	Illustration of shoulder to channel width ratio	121
5.43	Total current density in the catalyst layer (A/m^2) along the normalized x -direction at different y positions (a) 3; (b) 3.5; (c) 4; with an S/C ratio of 1:2 and 2:1 and the capillary pressure is represented by the Leverette function	123
5.44	3-D surface plot of liquid water saturation in the gas diffusion and catalyst layers using the Leverette function and an S/C width ratio of (a) 2 : 1; (b) 1 : 2. Profile of liquid water saturation in the backing and catalyst layers with a S/C width ratio of (c) 2 : 1; (d) 1 : 2 using the Leverette function. x and y coordinates have been normalized for better presentation of results. (see Figure 5.1)	125
5.45	x -component of the velocity in m/s against the normalized x direction for an S/C width ratios of 1:2 and 2:1 plotted at a normalized y value of 2.5.	126
6.1	Modeling Domain - x and y axes have been normalized - flow is in the y -direction (($0 \leq x \leq 6$) denotes a distance of 6 mm , ($0 \leq y \leq 2$) denotes a distance of 2 mm , ($2 \leq y \leq 3$) denotes a distance of 150 μm and ($3 \leq y \leq 4$) denotes a distance of 5 μm)	128

6.2	(a) 3-D surface plot of temperature in the bipolar plate and gas diffusion and catalyst layers. Note that $y = 4$ is the catalyst layer/membrane interface; (b) Temperature (K) profile in the cathode bipolar plate and backing and catalyst layers for the single phase, non-isothermal model. x and y coordinates have been normalized for better presentation of results. (see Figure 6.1)	130
6.3	(a) 3-D surface plot of saturation pressure in the gas diffusion and catalyst layers. Note that $y = 4$ is the catalyst layer/membrane interface; (b) Saturation pressure (Pa) profile in the cathode backing and catalyst layers for the single phase, non-isothermal model. x and y coordinates have been normalized for better presentation of results. (see Figure 6.1)	131
6.4	(a) 3-D surface plot of relative humidity in the gas diffusion and catalyst layers. Note that $y = 4$ is the catalyst layer/membrane interface; (b) Relative humidity profile in the cathode backing and catalyst layers for single phase, non-isothermal model. x and y coordinates have been normalized for better presentation of results. (see Figure 6.1)	132
6.5	Relative humidity for the single phase isothermal and non-isothermal cases along the normalized x -direction for different normalized y values (a) 2.5; (b) 3; (c) 4	133
6.6	Rate of water production in (kg/m^3) for the single phase isothermal and non-isothermal cases along the normalized x -direction for different normalized y values (a) 3; (b) 3.5; (c) 4	135
6.7	Total current density (A/m^2) for the single phase isothermal and non-isothermal cases along the normalized x -direction for different normalized y values (a) 3; (b) 3.5; (c) 4	136
6.8	(a) 3-D surface plot of the temperature in the bipolar plate and backing and catalyst layers. Note $y = 4$ is the catalyst layer/membrane interface; (b) Contour plot of temperature (K) in the bipolar plate and gas diffusion and catalyst layers for the multi-phase model. The Leverette function is used to describe the capillary pressure relation against the liquid water saturation. x and y coordinates have been normalized for better presentation of results. (see Figure 6.1)	138
6.9	Temperature variation along the x -direction for different y values for a permeability value of $5.5 \times 10^{-11} m^2$	139
6.10	(a) 3-D surface plot of the liquid water saturation in the backing and catalyst layers. Note $y = 4$ is the catalyst layer/membrane interface; (b) Contour plot of liquid water saturation in the gas diffusion and catalyst layers for the multi-phase model. The Leverette function is used to describe the capillary pressure relation against the liquid water saturation. x and y coordinates have been normalized for better presentation of results. (see Figure 6.1)	140
6.11	Comparison of the saturation levels of the isothermal and non-isothermal models along the normalized x -direction for different normalized y values with a permeability value of $5.5 \times 10^{-11} (m^2)$ (a) 2.5; (b) 3; (c) 4	141

6.12	(a) 3-D surface plot of the temperature in the bipolar plate and the backing and catalyst layers with an inlet relative humidity of 50%. Note $y = 4$ is the catalyst layer/membrane interface; (b) Contour plot of the temperature in the bipolar plate and the gas diffusion and catalyst layers for the multi-phase model with an inlet relative humidity of 50%. The Leverette function is used to describe the capillary pressure relation against the liquid water saturation. x and y coordinates have been normalized for better presentation of results. (see Figure 6.1)	144
6.13	Effect of inlet relative humidity on the temperature variation along the normalized x -direction for different normalized y values (a) 2; (b) 2.5; (c) 3; (d) 4	145
6.14	Rate of water evaporation for the isothermal and non-isothermal cases with an inlet relative humidity of 50% along the normalized x -direction for different normalized y values (a) 3; (b) 3.5; (c) 4	147
6.15	(a) 3-D surface plot of the liquid water saturation in the backing and catalyst layers with an inlet relative humidity of 50%. Note $y = 4$ is the catalyst layer/membrane interface; (b) Contour plot of liquid water saturation in the gas diffusion and catalyst layers for the multi-phase model with an inlet relative humidity of 50%. The Leverette function is used to describe the capillary pressure relation against the liquid water saturation. x and y coordinates have been normalized for better presentation of results. (see Figure 6.1)	148
6.16	(a) 3-D surface plot of the temperature in the bipolar plate and backing and catalyst layers for $\kappa = 5.5 \times 10^{-13} (m^2)$. Note $y = 4$ is the catalyst layer/membrane interface; (b) Contour plot of temperature (K) in the bipolar plate and gas diffusion and catalyst layers for the multi-phase model for $\kappa = 5.5 \times 10^{-13} (m^2)$ and the Leverette function used to describe $P_c(S)$. x and y coordinates have been normalized for better presentation of results. (see Figure 6.1)	150
6.17	(a) 3-D surface plot of the temperature in the bipolar plate and backing and catalyst layers for $\kappa = 5.5 \times 10^{-10} (m^2)$. Note $y = 4$ is the catalyst layer/membrane interface; (b) Contour plot of temperature (K) in the bipolar plate and gas diffusion and catalyst layers for the multi-phase model for $\kappa = 5.5 \times 10^{-10} (m^2)$ and the Leverette function used to describe $P_c(S)$. x and y coordinates have been normalized for better presentation of results. (see Figure 6.1)	151
6.18	Effect of permeability on the temperature variation along the normalized x -direction for different normalized y values (a) 2; (b) 2.5; (c) 3; (d) 4	153
6.19	(a) 3-D surface plot of the liquid water saturation in the backing and catalyst layers for $\kappa = 5.5 \times 10^{-13} (m^2)$. Note $y = 4$ is the catalyst layer/membrane interface; (b) Contour plot of liquid water saturation in the bipolar plate and gas diffusion and catalyst layers for the multi-phase model for $\kappa = 5.5 \times 10^{-13} (m^2)$. The Leverette function used to describe $P_c(S)$. x and y coordinates have been normalized for better presentation of results. (see Figure 6.1)	155

6.20	(a) 3-D surface plot of the liquid water saturation in the backing and catalyst layers for $\kappa = 5.5 \times 10^{-10} \text{ (m}^2\text{)}$. Note $y = 4$ is the catalyst layer/membrane interface; (b) Contour plot of liquid water saturation in the bipolar plate and gas diffusion and catalyst layers for the multi-phase model for $\kappa = 5.5 \times 10^{-10} \text{ (m}^2\text{)}$. The Leverette function used to describe $P_c(S)$. x and y coordinates have been normalized for better presentation of results. (see Figure 6.1)	156
6.21	Comparison of the cross flow amount between the isothermal and non-isothermal multi-phase cases at a normalized y value of 3.5 for different permeability values of (a) $5.5 \times 10^{-13} \text{ (m}^2\text{)}$; (b) $5.5 \times 10^{-11} \text{ (m}^2\text{)}$; (c) $5.5 \times 10^{-10} \text{ (m}^2\text{)}$	157
6.22	Illustration of shoulder to channel width ratio	158
6.23	(a) 3-D surface plot of temperature (K) in the bipolar plate and the gas diffusion and catalyst layers for an S/C width ratio of 1 : 2; (b) Profile of temperature (K) in the bipolar plate and the backing and catalyst layers with an S/C width ratio of 1 : 2. x and y coordinates have been normalized for better presentation of results. (see Figure 6.1)	159
6.24	(a) 3-D surface plot of temperature (K) in the bipolar plate and the gas diffusion and catalyst layers for an S/C width ratio of 2 : 1; (b) Profile of temperature (K) in the bipolar plate and the backing and catalyst layers with an S/C width ratio of 2 : 1. x and y coordinates have been normalized for better presentation of results. (see Figure 6.1)	160
6.25	Effect of shoulder/channel ratio on the temperature variation along the normalized x-direction for different normalized y values (a) 2; (b) 2.5; (c) 3; (d) 4	161
6.26	(a) 3-D surface plot of liquid water saturation in the gas diffusion and catalyst layers for an S/C width ratio of 1 : 2; (b) Profile of liquid water saturation in the backing and catalyst layers with an S/C width ratio of 1 : 2. x and y coordinates have been normalized for better presentation of results. (see Figure 6.1)	163
6.27	(a) 3-D surface plot of liquid water saturation in the gas diffusion and catalyst layers for an S/C width ratio of 2 : 1; (b) Profile of liquid water saturation in the backing and catalyst layers with an S/C width ratio of 2 : 1 x and y coordinates have been normalized for better presentation of results. (see Figure 6.1)	164

Nomenclature

a	water activity
A	cell surface area (m^2)
A_c	cross-section area (m^2)
A_v	density of active area in the catalyst layer (m^2/m^3)
C	molar concentration (mol/m^3)
c_p	specific heat ($J/kg \cdot K$)
d_h	hydraulic diameter (m) $\equiv \frac{4A_c}{P}$
D	mass diffusivity of species (m^2/s)
E	evaporation constant (atm/s); voltage (V)
F	Faraday's constant 96487 (C/mol); force (N)
h_m	mass transfer coefficient (m/s)
h_T	heat transfer coefficient ($W/m^2 \cdot K$)
i_0^{ref}	reference exchange current density (A/m^2)
I	cell current density (A/m^2)
J	phase current density (A/m^2)
k	thermal conductivity ($W/m \cdot K$)
K_{kq}	interphase momentum exchange coefficient
\dot{M}	molar mass (kg/mol)
\dot{m}	mass flow rate (kg/s)
n	number of electrons transferred in the half cell reaction
n_d	electro-osmotic drag coefficient (H_2O/H^+)
N_u	Nusselt number
\dot{N}	molar flow rate (mol/s)
P	pressure (Pa); perimeter (m)
P_d	displacement pressure (Pa)
q	switch function; phase
Q	heat source (J/m^3) from phase change, activation losses, ohmic losses, reversible reaction
\mathcal{R}	universal gas constant 8.314 ($J/mol \cdot K$)
R	source term
RH	relative humidity
s	liquid water saturation
S	effective saturation; entropy (J/K)

S_m	maximum saturation
S_r	residual (minimum, immobile) saturation
Sh	Sherwood number
S_c	Stoichiometry
T	temperature (K)
\vec{u}	phase velocity (m/s)
V	velocity (m/s)
W	width (m)
x	molar fraction
Y	mass fraction
Δg	Gibbs free energy

Greek letters

α	transfer coefficient; volume fraction of a phase
γ	reaction order
ϵ	volume fraction
ε	porosity
ζ	loss coefficient
η	overpotential (V)
θ_c	contact angle
κ	permeability (m^2)
λ	pore size distribution
μ	viscosity ($Pa \cdot s$)
ϖ	correction factor
ρ	density (kg/m^3)
σ	conductivity (S/m); surface tension (N/m)
ϕ	phase potential (V)
χ	condensation constant ($1/s$)

Subscripts

a	anode
act	activation
b	bending
c	cathode; capillary
CL	catalyst layer
f	friction
g	gas phase
GDL	gas diffusion layer
H_2O	water
in	inlet

j	the j^{th} species
l	liquid phase
L	local
m	electrolyte membrane
mix	mixture
N_2	nitrogen
nw	non-wetting phase
ohm	ohmic
O_2	oxygen
rev	reversible
s	solid phase
sat	saturation
T	source term of temperature
w	wetting phase
0	standard conditions ($298K$ and $1atm$)

Superscripts

c	cathodic
eff	effective value
ref	reference state

Acronyms

CL	catalyst layer
GDL	gas diffusion layer
MEA	membrane electrode assembly
PEM	polymer electrolyte membrane
$PTFE$	Polytetrafluoroethylene
RH	relative humidity

Chapter 1

Introduction

Nowadays, climate change and global warming are probably two of the most used expressions among researchers, politicians, policy makers and the average person. This phenomenon has raised a great amount of debate among scientists; the most controversial being who or what is responsible for this climate change. Many attribute this change to the activities of humankind [1], while others believe it is the cause of a natural phenomenon that Earth is experiencing [2, 3]. Despite this disagreement, both agree that the levels of carbon dioxide and other greenhouse gases have increased in the atmosphere. The increase in carbon dioxide levels (or concentration) is associated with the increased energy demands in many different sectors from transportation to residential. Canada is the second largest emitter of carbon dioxide in the world on a per Capita basis [4].

In Canada and the United States, the transportation sector is very energy demanding and therefore the carbon dioxide emissions associated with it are very high. In Canada, the transportation sector was responsible for 34% of the total emissions by all sectors in year 2002 (160 million metric tonnes) [5]. In the United States, the transportation sector accounted for 32.4% of the total US energy related carbon dioxide emissions in 2003 (1874.7 million metric tonnes) [6]. Even though, there is a difference in the total carbon dioxide emitted by the transportation sector in both countries, the total percentages are very similar. In addition, studying the trend of the carbon dioxide emissions increase, it can be seen that the trend in both Canada and the United States is very similar. Since 1990, the carbon dioxide emissions related to transportation has increased at a

CHAPTER 1. INTRODUCTION

rate of 1.1 [5] and 1.4% [6] annually in Canada and the United States, respectively. The increased carbon dioxide emissions by the transportation industry in both countries have led to the need for alternative solutions.

Polymer electrolyte membrane (PEM) fuel cells are considered to be tomorrow's energy conversion and power generation devices due to their low to zero emissions and high efficiency. A full life cycle analysis for vehicles powered by internal combustion engines and by a PEM fuel cell in [7, 8] showed that the use of PEM fuel cells in vehicles leads to a decrease of emissions by 49% and a decrease of energy consumption by up to 87%. The decrease in emissions is mainly due to the low to zero emissions during operation of the vehicle. Since pure hydrogen is used as the fuel for PEM fuel cells, the byproduct of the reaction is liquid water. Similarly, the decrease in total energy consumption is mainly due to the increase in operational efficiency. The increased efficiency in turn results in the decrease of fuel needed for operation.

There are many barriers, however, that need to be addressed before PEM fuel cells can be used commercially. The cost of PEM fuel cells should be decreased from 300\$/kW to 30\$/kW in order to be able to replace the internal combustion engine [9]. Carbon monoxide (CO) poisoning of the fuel cell is another barrier to the commercialization of PEM fuel cells and its effects are seen over a substantial period of time [10]. The adsorption of carbon monoxide on the catalyst sites in the anode catalyst layer results in the decrease of available reaction sites; thus hindering the overall performance of the cell [11, 12]. One of the major technical challenges facing PEM fuel cells is the loss in cell voltage due to the slow rate of oxygen transport and weak oxygen reduction reaction at the cathode. This is further amplified by the presence of liquid water in the backing (or gas diffusion) and catalyst layers. The liquid water droplets act as barriers to the free diffusion of species in the layers to reach the reactive surfaces.

Many modeling efforts have been put forward by the research community in order to understand the mass transport in PEM fuel cells. In the next chapter a detailed literature review is given. However, some background information about PEM fuel cells is given first in the next section and followed by the objectives of this thesis and its outline.

1.1 Background

Polymer electrolyte membrane (PEM), also known as proton exchange membrane, fuel cells are electrochemical devices that run on pure hydrogen in order to produce electricity; as shown in Figure 1.1. They can be used in vast applications from portable to mobile to stationary. They are compact, quiet, quick to start, have low emissions, have high efficiency and power density and are not hazardous.

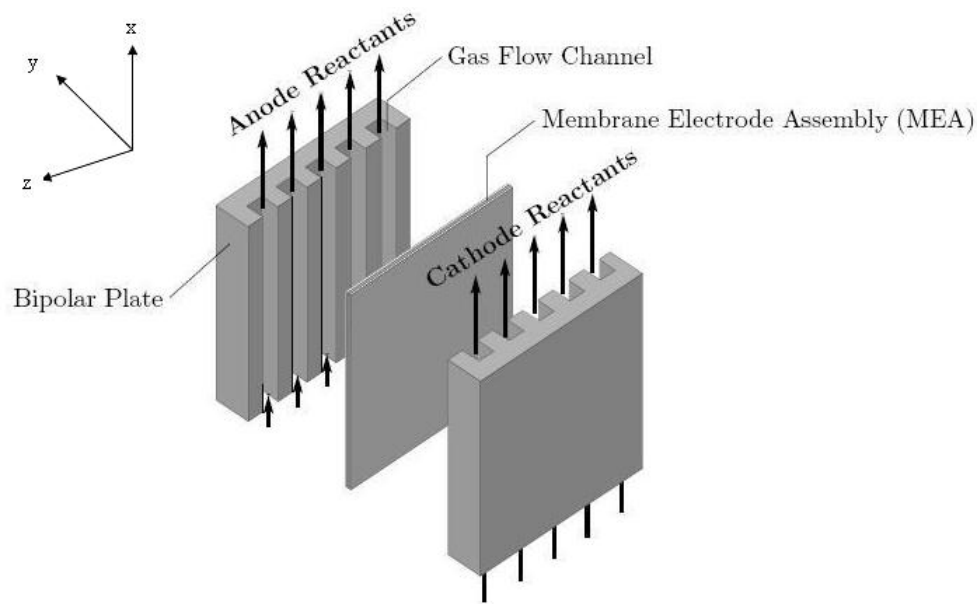


Figure 1.1: The construction of polymer electrolyte membrane (PEM) fuel cell: bipolar plate with gas channels; porous electrodes; reactive layers; polymer membrane [13]

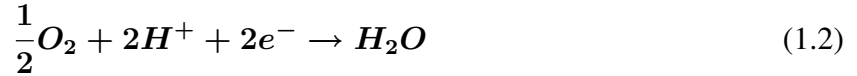
There are two sides that make up a PEM fuel cell; an anode and a cathode. At the anode side, pure hydrogen (fuel) is supplied and the electrochemical reaction that takes place is summarized by equation 1.1. Here, the hydrogen molecule is being split into protons and electrons. The protons travel through the electrolyte membrane, while the electrons are forced to travel through the external electric circuit.



Oxygen or air (oxidant) is supplied at the cathode side. The electrochemical reaction that takes

CHAPTER 1. INTRODUCTION

place at the cathode is shown in equation 1.2. Here, the oxygen combines with the protons traveling through the membrane and the electrons to produce water.



The overall reaction that takes place in a PEM fuel cell can then be represented by,

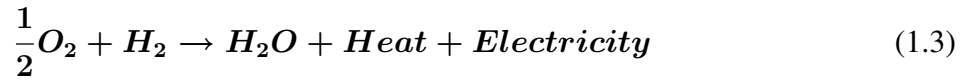


Figure 1.1 shows that the physical construction of a PEM fuel cell consists of two bipolar plates between which the membrane electrode assembly (MEA) is found. Bipolar plates provide the electrical connection between the cells in a stack. They comprise a series of grooves that are used to distribute the gases to a gas diffusion layer and to remove the reaction products. Some bipolar plates incorporate cooling channels to control the stack temperature. In addition, the bipolar plates account for about 80% of the total weight and 45% of the stack cost [14]. In order to achieve all the desired functions, the plates need to possess the following physical properties [15, 16],

- High electrical conductivity - to uniformly distribute the electrical current
- High thermal conductivity - to control the stack temperature and achieve a homogeneous temperature distribution in each cell and over the whole active area
- High corrosion resistance - low corrosion rates are needed due to the low pH levels in a fuel cell environment
- High compressive strength - to ensure that the plate does not break
- Low density - to reduce the weight of the plate
- Low cost - to reduce the overall cost of the fuel cell

To meet all the requirements for the bipolar plates, the material should be chosen carefully. There are three main materials that are under investigation and are used in bipolar plates. They are

CHAPTER 1. INTRODUCTION

non-porous graphite/electro-graphite, metals (coated and non-coated) and composites (polymer-carbon and polymer-metal). Extensive study has been published in the literature and some can be found in the following references [17-24].

The other component of a PEM fuel cell is the membrane electrode assembly (MEA). It governs the transport of species and the electrochemical reaction. The MEA is composed of three major components, a fuel electrode (anode), an oxidant electrode (cathode) and a polymer electrolyte sandwiched between the two electrodes. Each component plays a significant role in the reaction and ultimately the production of electricity. The functions of the electrode are as follows [25]:

- To provide a place for the electrochemical reaction to occur easily
- To provide a flow path for reactant supply to, and product removal from, the reaction sites
- To collect the electrons and provide a flow path for electron transfer

Since the electrode needs to fulfill many functions, it is necessary to use a porous material. In addition, the material should be chemically stable and mechanically strong in order to withstand the corrosive environment and be resistant to deformation. The electrode is composed of two parts, the gas diffusion layer and the catalyst layer. The gas diffusion layer provides a free diffusion medium in the void region for the gaseous species from and to the channel. In addition, the solid part is used as a transport medium for the electrons to and from the reaction site. The typical material used for the gas diffusion layer is carbon paper or carbon cloth wet-proofed with Teflon.

The catalyst layer is very thin and is located between the gas diffusion layer and the polymer electrolyte. It acts as the area where the electrochemical reaction occurs. It is made up of electrolyte, solid, liquid water and void region. The electrolyte is needed for the transport of protons, the solid phase is needed for the transport of electrons and the void region is used by the gaseous reactant. The electro-chemical reaction occurs at the interface between all three phases. Liquid water is normally present since the material is porous and the product of the reaction is water. Therefore, a minimum level of water will always exist in the layer.

The polymer electrolyte between the anode and the cathode is required for the following functions [25],

CHAPTER 1. INTRODUCTION

- To act as an ion conductor, so that ions can migrate from one electrode to another through the electrolyte, completing the cycle of mass transfer and electric circuit
- To act as an electron insulator, so that electrons are forced to migrate through the external circuit; thus providing electric power output
- To act as a barrier in order to separate the reactants; preventing crossover of reactants from the anode to the cathode and mixing; thus, controlling the electrochemical reaction to proceed as expected

It is important to ensure that the electrolyte is well hydrated. Liquid water in the electrolyte is needed for the transport of protons from the anode to the cathode to complete the reaction. Over hydration (flooding) or dryness of the electrolyte will result in losses in the overall performance of the cell. Typical materials used for the solid electrolyte in a PEM fuel cell are Nafion and Dow Membrane. Nafion is the most commonly used and is made of sulfonic acid polymer. Dow Membrane is a Perfluorinated sulfonic acid polymer with more sulfonate side chains than Nafion. It also has lower weight and lower electrical resistance and has higher current density capabilities than the Nafion membrane and it exhibits good performance and stability. However, its present price is too high for the transportation markets.

Figure 1.2 provides a summary of the nature of the flow in and the structure of each component of a PEM fuel cell. Both gas and liquid flow occur in the flow channels. The gas flow consists of the species flow (fuel or oxidant). The liquid flow is normally due to condensation of the water vapor used to humidify the fuel/oxidant and/or due to the removal of liquid water from the cell. In practice, the gas diffusion layer consists of a void region for diffusion of reactants (fuel and oxidant), solid phase for transport of electrons, and liquid water due to its porous nature. The void region for gaseous species diffusion, liquid water, electrolyte membrane for proton transport and solid region for electron transport make up the catalyst layer. The solid membrane is composed of liquid water and hydronium ions, hydrophobic backbone, sulfonic acid and flexible Perfluorocarbon.

Finally, the performance of the cell is normally measured using a polarization curve. The polarization curve is simply a curve of the cell voltage versus the cell current density. Using the

CHAPTER 1. INTRODUCTION

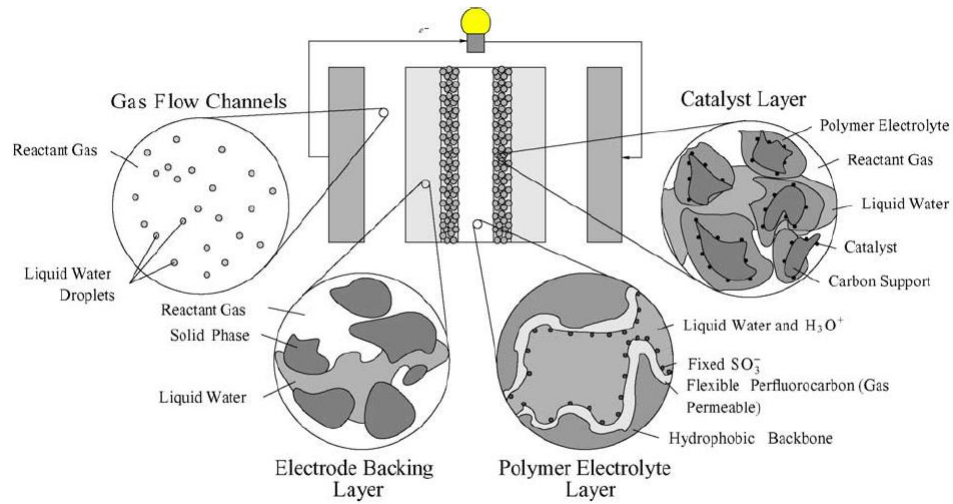


Figure 1.2: The nature of the flow in and the structure of the layers of a PEM fuel cell [13]

voltage and current density, the cell power density can be obtained. A typical polarization curve is shown in Figure 1.3.

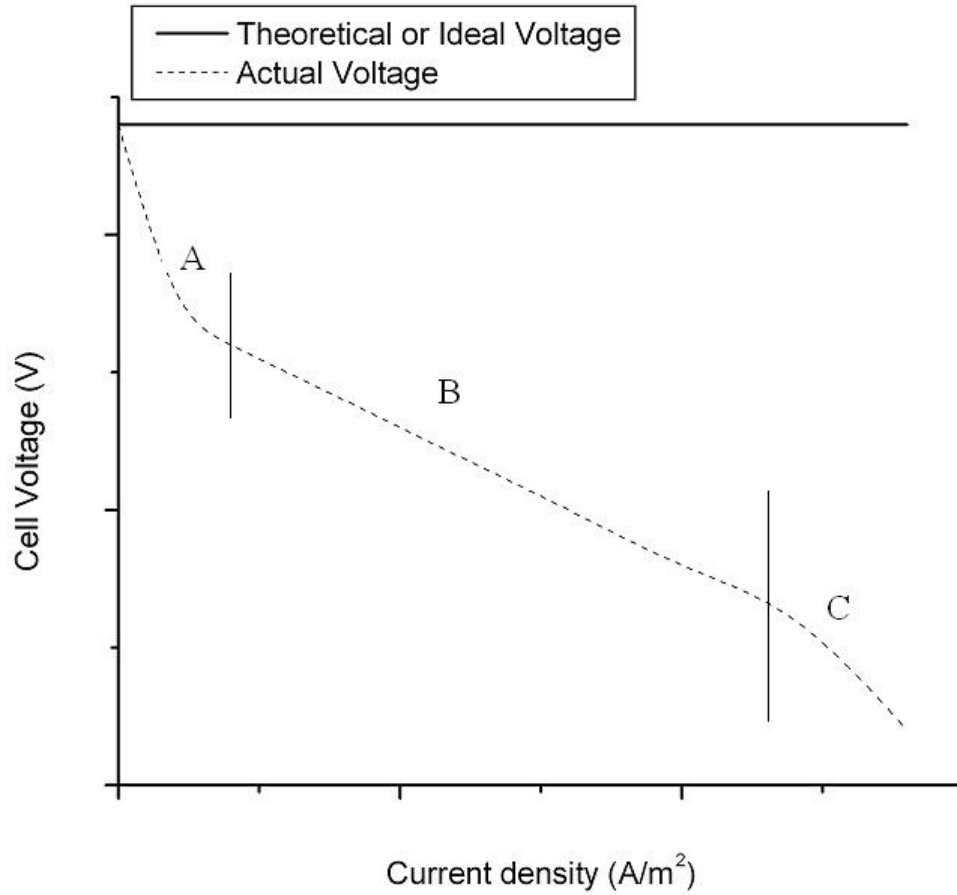


Figure 1.3: Polarization curve for a PEM fuel cell showing the regions of losses - Region A is of activation polarization, Region B is of ohmic polarization and Region C is of concentration polarization

Figure 1.3 shows that the actual cell voltage is equal to the reversible cell voltage minus the three different losses. The reversible cell voltage is dependent on the fuel, oxidant, thermodynamical properties of the product, and operating conditions, as seen in equation 1.4.

$$E_{rev} = -\frac{\Delta g(T, P)}{nF} \quad (1.4)$$

where $g(T, P)$ is the Gibbs free energy at a given temperature and pressure, n is the number of electrons, and F is Faraday's constant.

The reversible cell voltage is 1.229 V and 1.185 V when the product water is in liquid and vapor form, for PEM fuel cells at standard conditions (25°C and 1 atm) with pure hydrogen as fuel

and pure oxygen as the oxidant, respectively.

Activation loss is due to resistance to electrochemical reaction. It is zero for the anode side. On the cathode side a high energy barrier has to be overcome for the reaction to occur. The activation over-potential is dependent on the operating conditions as well as the design conditions of the catalyst layer as seen in equation 1.5.

$$\eta_{act} = \frac{\Re T}{n\alpha F} \ln \left(\frac{i^c}{i_o^{\text{ref}}} \right) \quad (1.5)$$

where, α is the transfer coefficient, i^c is the cathodic current density, and i_o^{ref} is the reference exchange current density.

The ohmic over-potential is the loss due to resistance to the flow of ions in the electrolyte and the flow of electrons in the electrode. It is dependent on the operating conditions as well as the electrode design conditions as seen in equation 1.6.

$$\eta_{ohm} = iR \quad (1.6)$$

where R is the ohmic resistance.

Finally, the concentration over-potential is due to the mass diffusion limitations especially in the cathode since the oxygen diffusion in the voids of the gas diffusion layer is slow. In addition, flooding of the electrodes will limit the free diffusion of both the fuel and the oxidant. The concentration over-potential is found using equation 3.3.

$$\eta_{concentration} = \frac{\Re T}{nF} \ln \left(\frac{i_L}{i_L - i} \right) \quad (1.7)$$

where, i_L is the local current density and i is the total current density of the cell.

1.2 Thesis Objectives

The numerical model developed for the purpose of this thesis is a two-dimensional half cell model. It is used to investigate the mass and heat transfer in the cathode of a PEM fuel cell.

CHAPTER 1. INTRODUCTION

The literature review revealed that many of the numerical models available treat the gas diffusion and catalyst layers as hydrophilic media, assume that the catalyst layer is a thin interface and therefore is just a boundary and the effects of cross flow phenomenon is lacking. Hence, the objectives of this thesis are as follows,

- To develop a comprehensive analysis of the mass and species transport as well as the electrochemical reactions in the cathode of a PEM fuel cell and their impact on the cathode performance
- To investigate the effects of cross flow, in other words, permeability on the transport of oxygen, liquid and vapor water in the cathode
- To study the effect of inlet relative humidity on the performance of the cathode
- To explore two different relations describing the dependence of capillary pressure on saturation (Leverette function and Brooks and Corey relation)
- To consider the catalyst layer as a finite domain and model the transport of species (vapor water, oxygen and liquid water)
- To study the effect of shoulder(land)/channel width ratio on species transport and leakage between neighboring channels

A single phase and multi phase models are investigated along with an isothermal and a non-isothermal model. The temperature change inside the PEM fuel cell is taken into account to show the heat transfer and its effects on mass transfer, particularly liquid water.

1.3 Outline of the Thesis

Seven chapters are put forward in this thesis in order to give a complete and comprehensive discussion.

CHAPTER 1. INTRODUCTION

1. Polymer electrolyte membrane fuel cell background is given in chapter one. In addition, the objectives of the thesis are put forward in chapter one.
2. A comprehensive discussion of the literature review is given in chapter two. The focus of the literature review is on the present state of single phase and multi-phase modeling for PEM fuel cells. A discussion of the most common multi-phase modeling techniques is also given.
3. The mathematical formulation on which the results of this thesis are based is discussed in detail in chapter three. The governing equations used to solve the single phase and multi-phase, isothermal and non-isothermal models are presented along with the boundary conditions and parameters necessary for the numerical calculation.
4. The numerical method used to solve the set of governing equations is discussed in chapter four.
5. In chapter five, the results of the isothermal single phase and multi-phase models are discussed. Further, a sensitivity analysis is carried out. The effect of permeability and pressure drop on the cross flow is shown and the effects of inlet relative humidity and shoulder(land) to channel width ratio on the performance of the cathode are examined.
6. In chapter six, the results of the non-isothermal, single phase and multi-phase models are put forward. The effect of temperature change on the cathode performance is investigated.
7. Finally, the concluding remarks along with the recommendations are given in the last chapter.

Chapter 2

Literature Review

Numerical modeling is widely used to investigate the performance of polymer electrolyte membrane fuel cells since it is fast and cheap. Since the product of the electrochemical reaction in polymer electrolyte membrane fuel cells is water, the models can be divided into single phase and multi-phase models. The single phase models are solved under the assumption that water exists in vapor form only, while in the multi-phase models, both liquid and vapor water are taken into account.

2.1 Single Phase Models

The two pioneering models in PEM fuel cell modeling and on which many other models are based, are those by Bernardi and Verbrugge [26, 27] and by Springer et al. [28, 29]. Both of these models assumed that the cell operated at steady state and was isothermal. They both carried out a one-dimensional, isothermal analysis of the species transport in the MEA and the channel.

Bernardi and Verbrugge developed a macro-homogeneous mathematical model to resemble the membrane and cathode electrode of a PEM fuel cell in [26]. Some of the parameters were adjusted in order for the model to be comparable to the experimental results obtained by Ticianelli et al. [30]. The results indicated that the contribution of the membrane to the total cell resistance was most significant at higher operating current densities when the membrane maintains full saturation.

CHAPTER 2. LITERATURE REVIEW

The resistance due to the oxygen reduction reaction appeared to be of great importance during all operating current densities. The uniformity of the rate of reaction distribution was found to be highly dependent on the current density of the catalyst layer. In their later study [27], Bernardi and Verbrugge extended their mathematical model in [26] to consider the anode catalyst layer. The focus of this study was on the factors limiting cell performance and on elucidating the mechanism of species transport. One of their major findings was that the volume fraction available for gas transport in the cathode must exceed 0.2 for better performance. The dehydration of the membrane was shown to pose some limitations on the operating current density; however, for a broad range of practical current densities there are no external water requirements. Inefficiencies due to the transport of un-reacted hydrogen or oxygen through the membrane showed to be insignificant at practical operating current densities.

Springer et al. [28] presented a numerical model that focused on simulating the performance of a complete polymer electrolyte fuel cell. To compute the results of the model, they used parameters such as diffusion coefficients, water sorption isotherms, and membrane electro-osmotic drag that were measured in their laboratory. The model was solved under the assumption that liquid water existed in the membrane only, while the water in the electrodes was in vapor form. Any excess liquid water in the electrodes was finely dispersed. One of the most significant contributions valued until today is the different relations they fitted for the water activity versus diffusion coefficients, electro-osmotic drag coefficient and electrolyte conductivity. Some of the parameters used in this thesis have been taken from [28] and will be discussed in more detail in the formulation section. In a later study [29], Springer et al. concentrated their efforts on the modeling of the losses in the cathode of a PEM fuel cell since with well humidified fuel stream losses in the anode could be negligible. From the trends observed, they deduced that gas phase transport limitations in the cathode backing determine the cell limiting current and also affect the slope of the polarization curve in the medium current density domain. There exists transport limitations in the catalyst layer in the medium current density domain and especially at low air pressures. Thus, when modeling transport limitations in the cathode the inclusion of the catalyst layer is key.

The single phase models in the literature are normally dedicated to the investigation of the elec-

CHAPTER 2. LITERATURE REVIEW

trochemical reactions and its limitations. Marr and Li [31] developed a one-dimensional, steady state model of the cathode catalyst layer. The focus of the study was on the composition and performance optimization of the cathode catalyst platinum and catalyst layer structure. They found that the electrochemical reactions occur within a thin layer, having a thickness of a few micrometers. They concluded that lower loadings of platinum are feasible for higher current densities. In addition, an optimal amount of membrane content in the void region of the catalyst layer exists for minimum cathode voltage losses due to competition between proton migration through the membrane and oxygen transfer in the void region. Jaouen et al. [32] prepared a one-dimensional, steady state agglomerate model to describe the functioning and the mass transport limitations in a PEM fuel cell. Tafel kinetics of the oxygen reduction reaction, proton migration, oxygen diffusion in the agglomerates, and diffusion of the air mixture (O_2/N_2 /water vapor) in the pores of the active layer and of the gas backing layer were analyzed. The model showed that limitation by proton migration in the active layer or by oxygen diffusion in the agglomerates led to a doubling of the Tafel slope at higher current densities. Bradean et al. [33] developed a two-dimensional steady state model with a serpentine flow field. The oxidant of choice was air saturated with water vapor. Heat transfer and mass transfer in the cathode were analyzed. It was assumed that the mass transfer is governed by Fick's law. They concluded that diffusion is the dominant transport phenomena. In addition, they found that the location of the regions of vapor over-saturation is very sensitive to design parameters such as cathode thickness, reaction rate, the graphite plate heat transfer coefficient and operating conditions. Wang et al. [34] created a one-dimensional, steady state, agglomerate model to study the effect of agglomerate size on the cell performance. They concluded that the agglomerate should be kept as small as possible to minimize the adverse effects of mass transport at high current density. They also found that only part of the electro-catalyst was effectively utilized when either the oxygen or the proton cannot fully penetrate all parts of the electrode. In another study [35], this same group investigated the effect of Nafion loading on the electrode polarization characteristics of a PEM fuel cell. A one-dimensional, macro-homogeneous, steady state model was used. They found that for a uniform layer, the best performance was obtained with a Nafion content of about 35 wt%. Therefore, in a later study [36], they investigated a three sub-layer structure

of the catalyst layer. In this study, it was found that the optimal distribution of Nafion content was a linearly increasing function through the thickness of the catalyst layer from the GDL side to the membrane side when the total platinum loading and platinum percentage are constant. In addition, the optimal distribution of platinum loading is a linearly increasing function of the thickness of the catalyst layer when the Nafion content is evenly distributed. Finally, they concluded that varying the two-variables (Nafion content and platinum loading) simultaneously, the performance of the cell does not improve compared to the performance of the optimization of the Nafion content distribution. Their main conclusion was that in the design of the catalyst layer only the optimization of Nafion content distribution needs to be considered.

2.2 Multi-phase Models

The multi-phase models are used to investigate the barriers due to liquid water. They can be compared on the basis of half cell and full cell models. The half cell models describe the transport of liquid water in the cathode side due to the nature of the electrochemical reaction at this half of the cell. He et al. [37] developed a two-dimensional, multi-phase, multicomponent transport model that uses an interdigitated gas distributor to take into account the forced flow of the gas through the porous electrode. In this model, the catalyst layer is also considered as a boundary. Therefore, water production is considered to occur at the gas diffusion layer/catalyst layer interface. In addition, they assumed that the capillary pressure (the capillary diffusion) has a constant slope across the gas diffusion layer. Natarajan et al. [38] developed a two-dimensional, multi-phase, multi-component, transient model of the cathode of the PEM fuel cell. In this model, conventional gas distributors are used and therefore, diffusion is the dominant transport process. The catalyst layer was assumed to be very thin and is considered as a boundary. The performance of the cathode was studied under different conditions. It was found that the presence of liquid water highly affects the performance of the cathode at high current densities. Increasing the operating temperature, decreasing the gas diffusion layer thickness and using shorter shoulder widths and a greater number of channels were found to enhance the liquid water removal from the cathode, in turn increasing

CHAPTER 2. LITERATURE REVIEW

its performance.

One of the most active groups in fuel cell modeling is found at Pennsylvania State University. They have developed many different models that deal with liquid water transport in the cathode of a PEM fuel cell. This group uses as the basis some of their early work done on the contamination of underground water. They developed a multi-phase mixture model to investigate infiltration and transport of nonaqueous phase liquids in the unsaturated subsurface in [39] and solved it later in [40]. This early work was then used to develop a multi-phase flow and transport of reactants and products in the cathode [41]. They assumed the gas diffusion layer to be a hydrophilic material. The capillary pressure was described by the Leverette function [42] for hydrophilic media. In the backing layer, a multi-phase region co-exists with a single-phase region. The capillary action was discovered to be the dominant mechanism for water transport inside the multi-phase zone of the hydrophilic structure. This model, like many in literature, assumes that the catalyst layer is a thin interface (boundary). The same group [43] generated a mathematical model to investigate the flooding dynamics in PEM fuel cells. The model is three dimensional and describes the multi-phase phenomena in the cathode backing layer. They also accounted for the catalyst coverage model in the catalyst layer. The capillary pressure was described by the Leverette function for a hydrophobic media (the backing layer was considered to be hydrophobic). A multi-phase [44], full cell model, was used to analyze the multi-phase transport in PEM fuel cells with bilayer cathode gas diffusion media consisting of a coarse gas diffusion layer. The effects of average pore size, wettability, thickness and porosity on the liquid water transport have been examined. They show that the back-flow of liquid water increases with increasing hydrophobicity.

Senn and Poulikakos [45] put forward a detailed model of the mass and heat transport in the backing layer of a PEM fuel cell. They assumed that the capillary pressure (driving force of liquid water in the layer) is governed by the expression developed by Leverette. The backing layer was taken as a hydrophobic medium. In addition, they considered a minimum saturation level needed for the driving force and the maximum saturation level was set to equal 1. The catalyst layer, however, was taken as a thin layer. Hence, treated as a boundary condition where the reduction reaction occurs and the electro-osmotic drag is considered. The effects of the gas

CHAPTER 2. LITERATURE REVIEW

diffusion layer thickness, number of channels and the shoulder width on the performance of the cell were investigated. Since the literature is lacking a detailed model of the distribution of species in the cathode catalyst layer, it was important for Eikerling [46] to develop such a model. The model shows that there are several vital functions for the cathode catalyst layer. It is shown that the catalyst layer is the prime medium for the conversion of liquid water to vapor and in turn determines how much water exists toward the gas diffusion layer. Therefore, modeling the catalyst layer is essential in order to be able to understand the behavior of liquid water in the cell and to optimize the cell performance.

Many full cell models are found in the literature to study the behavior of liquid water in the cell. These models take into account the anode and cathode half cells as well as the membrane. You and Liu [47] are amongst many who have created a full cell model to investigate multi-phase flow in PEM fuel cell. They investigated the transport of species and the electro-chemical reaction and compared the resultant polarization curve to experimental data. Hu et al. [48, 49] developed a three-dimensional, multi-phase flow model. The model investigates a conventional and an interdigitated flow fields. The model results show that the saturation of liquid water in the conventional flow field is less than that in the interdigitated flow field and therefore, higher ohmic losses are encountered with the interdigitated flow field. However, the humidification of the reactant gases can be used in order to lower these ohmic losses and in turn enhance the performance of the cells with an interdigitated flow field. Siegel et al. [50] developed a two-dimensional, multi-phase model. It is shown that consideration of liquid water is essential to accurately simulate the fuel cell operation. The results of the model suggest that the water transfer from the membrane to the cathode through electro-osmotic drag is very important to consider. Baschuk and Li [51], created a general formulation for a polymer electrolyte membrane fuel cell. The model formulation covers the electro-chemical reactions, proton migration and mass transport of the gaseous reactants and liquid water. The formulation can be applied to the gas channels, bipolar plate, gas diffusion and catalyst layers on the anode and the cathode sides of the fuel cell. The conservation of mass, momentum, species, and energy are applied to each phase, with the technique of volume averaging being used to incorporate the interactions between the phases as interfacial source terms. In order to avoid

CHAPTER 2. LITERATURE REVIEW

problems arising from phase discontinuities, the gas and liquid phases are considered as a mixture.

To make the numerical model more comprehensive, many models consider the temperature distribution in the PEM fuel cell. Birgersson et al. [52] presented a non-isothermal, multi-phase model to study the effects of different assumptions. Similarly, Matamoros and Brügemann [53] created a three dimensional model to simulate the water and heat transfer in a PEM fuel cell. Their work showed that the hydration of the membrane, which is affected by the inlet relative humidity, has a significant effect on the performance of the system. The saturation of the cathode is dominated by the capillary flow, or in other words the permeability. In addition, they showed that the operational temperature could have a negative effect on the performance of the cell. High operational temperatures show that the cell would have more tendencies of drying out. Wang and Wang [54] developed a multi-phase, non-isothermal model to investigate the liquid water distribution and flooding. Their results revealed that vapor-phase diffusion enhances water removal from the gas diffusion layer under the channel. They also showed that this transport mechanism aids in the heat removal through a phase change process in which water evaporates at the hotter catalyst layer, diffuses through the interstitial spaces of the gas diffusion layer and condenses on the cooler land surface. Finally, discussion of the vapor-phase and liquid-phase velocities is given and used to show that the velocity of both phases aids in the removal of water from the backing layer. Hwang and Chen [55] created a model that simultaneously calculates the solid-phase and fluid-phase temperatures inside the porous cathode of a PEM fuel cell. The distributions of the local temperature, local Nusselt number, species concentration and the current density are analyzed. In a later study, the same group, Hwang et al. [56] investigated the solid and fluid phase temperatures even further. In the catalyst layer, the energy equation is solved under the assumption that the fluid and solid temperatures are equal. They showed that the temperature of the fluid and solid phases was different due to the local thermal non-equilibrium between the two matrices. One of their major findings was that the response of the two temperatures to the electrochemical reaction rate is similar. In [57], Chao and Hwang carried out an investigation of the intrinsic heat transfer coefficient. As the intrinsic heat transfer coefficients increase, the porous electrode becomes local thermal equilibrium with a strong thermal interaction between the solid and fluid phases. Under the conditions of high

intrinsic heat transfer coefficients, the temperature difference between the solid matrices and the reactant fluids are negligible. In a more current study, Hwang [58] combined multi-phase mass transfer and heat transfer. The main conclusion of this study was that increasing the rib-shoulder temperature reduces the condensation zones since the saturation pressure is increased.

According to the literature, the multi-phase flow models in the gas diffusion and catalyst layers can be classified into three categories, multi-phase mixture model, volume of fluid model and Eulerian model. The underlying difference between these three models is the governing conservation equations of mass and momentum of the different phases making up the mixture.

2.3 Multi-phase Mixture Model

The multi-phase mixture model is solved under the assumption that the gas and liquid phases can be non-continuous and combined to form a mixture. The volume fraction of the wetting phase (liquid water in the case of PEM fuel cells) is normally solved first and then used to solve the governing equations. An iterative process is required in order to solve the governing equations.

2.4 Volume of Fluid Model

The volume of fluid model is normally used to track the interface of two or more immiscible fluids such as in stratified flow and free surface flow. Its application in PEM fuel cell modeling is normally to understand the evaporation and condensation rates and track the interface of interaction between the two phases of water (liquid and gas).

2.5 Eulerian Model

The Eulerian model is the most rigorous and accurate model, but computationally expensive. It treats each phase as its own entity. Interaction terms between the two phases are used to solve the mass and momentum equations, which add to the complexity and accuracy of the model.

2.6 Summary

The multi-phase modeling efforts put forward by the research community to-date have been mostly focused on liquid water transport under isothermal conditions and only in the gas diffusion layer. The catalyst layer is taken as a thin interface and the electro-chemical reaction is assumed to occur at the boundary of the gas diffusion and catalyst layers. The transport of liquid water in the catalyst layer is ignored. In addition, the transport of species in the porous media (gas diffusion and catalyst layers) is assumed to occur via diffusion only and the effects of convection are ignored. Thus, the effects of cross flow on liquid water removal are also ignored. Further, most of the multi-phase models in the literature are solved under the assumption that the capillary pressure is related to the saturation through the Leverette function. Finally, multi-phase modeling is presented under the assumption that the inlet relative humidity to the cell is 100% and therefore, the effects of inlet relative humidity on the total amount of water in vapor and liquid forms are neglected.

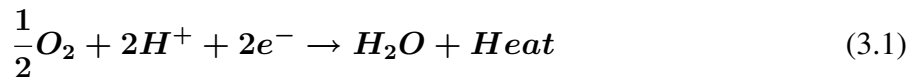
In this thesis, the catalyst layer is considered as a finite domain and therefore, the transport of species in the layer is modeled. Understanding the transport behavior of the species in the catalyst layer will ensure that the design of the layer is optimized. Further, the effects of cross flow on the transport of species and the removal of liquid water are put forward. Cross flow occurs due to the channel geometry; hence, the results of this thesis can be used to make informed decisions on the design of the channel. Further, the effects of inlet relative humidity on the performance of the cathode should be taken into account. It is obvious that lower values of inlet relative humidity will result in a lower amount of liquid water and therefore, decreases the blockage of available sites. However, liquid water is also needed to hydrate the electrolyte membrane. Hence, the relation between the electrolyte hydration and liquid water presence are presented in the thesis for better understanding of their dynamics. Finally, coupling heat and mass transfer results in a comprehensive simulation of the transport of species and the behavior of the electrochemical reaction.

Chapter 3

Model Formulation

3.1 Physical Problem

The model developed is a two dimensional model of the cathode of a PEM fuel cell. The electrochemical reaction at the cathode is known as the oxygen reduction reaction (ORR). Electrons, protons and oxygen molecules combine to produce water and heat. The reaction is described by,



Water is formed at the reaction sites as a result of the oxygen reduction. Liquid water build-up in the void region of the porous gas diffusion and catalyst layers will block oxygen diffusion. On the other hand, liquid water is needed for the hydration of the membrane for proton transport. Therefore, it is crucial to investigate the transport of liquid water in the cathode.

As mentioned earlier, the effects of cross flow on the transport of liquid water will be taken into account in this study. A comprehensive study on the cross flow phenomenon in a PEM fuel cell with a serpentine flow channel carried out by Park and Li [59] shows that due to the pressure drop along the channel flow field with a serpentine shape (Figure 3.1), the reactants can leak or cross to adjacent channels. The cross flow is found to lead to larger effective flow area altering reactant flow in the flow channel and therefore changing the flow distribution.

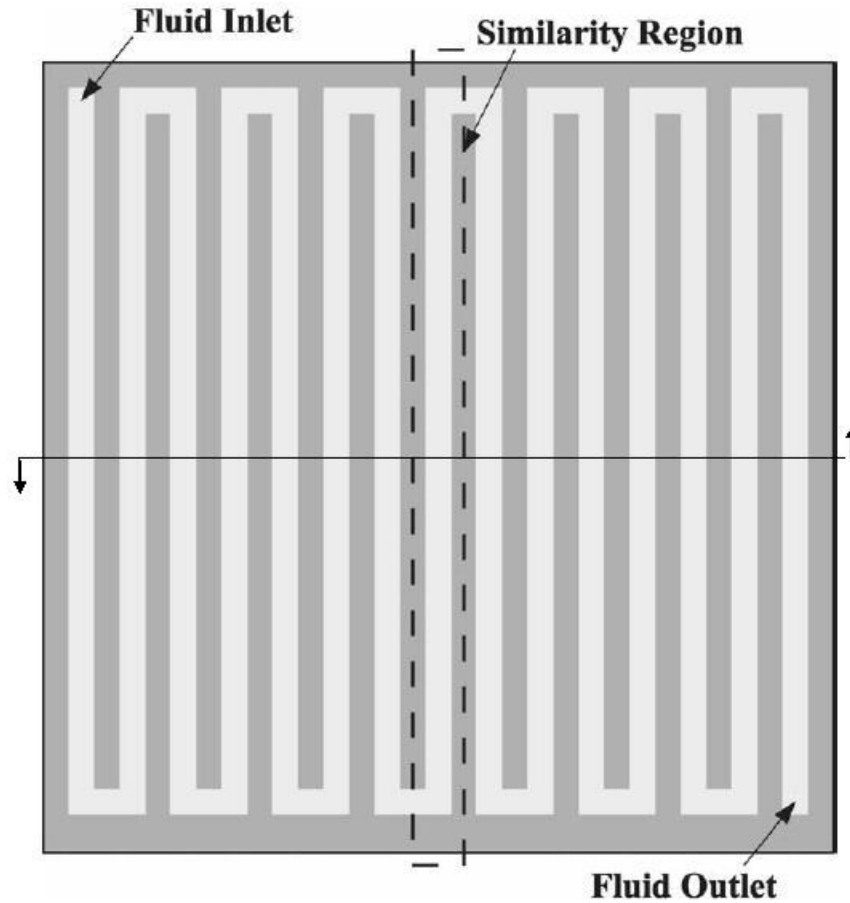


Figure 3.1: Diagram of a serpentine flow field configuration [60]

Many studies have shown that the cross flow phenomenon achieved by using a serpentine flow field leads to significant enhancement of the overall performance as well as to proper liquid water removal. Feser et al. [60] showed that the convection in the form of channel bypass results in the increase of reactant concentration and reduces product concentration in the catalyst layer; thus reducing the activation and mass-transport overpotential. Further, Kanezaki et al. [61] observed that the cross-leakage flow influences the reactant concentration at the interface between the electrode and the catalyst layer, hence the distribution of reaction rate or current density generated. In practice, this cross-leakage flow in the cathode helps drive the liquid water out of the electrode structure for effective water management, partially responsible for the good PEM fuel cell performance using the serpentine flow channels. In a later study, Li et al. [62] carried on an experimental

investigation to illustrate the effectiveness of such a flow field in water removal.

To analyze the effects of the cross flow on the transport, three channels have been modeled as shown in Figure 3.2. The x and y axes have been normalized for better presentation of results; $(0 \leq x \leq 6)$ denotes a distance of 6 mm, $(0 \leq y \leq 2)$ denotes a distance of 2 mm, $(2 \leq y \leq 3)$ denotes a distance of 150 μm and $(3 \leq y \leq 4)$ denotes a distance of 5 μm . The flow direction is in the y -direction. The flow in the channels is not modeled since the flow is fully developed and uniform; thus, the reactant concentration and pressure can be specified at the channel/gas diffusion layer interface. The electrons travel through an external electric circuit from the anode side to the cathode. They are transported via the bipolar plate to the gas diffusion layer and then to the catalyst layer. The membrane is used to transport the protons to the catalyst layer. The oxygen diffuses in the gas diffusion layer to the catalyst layer for reaction.

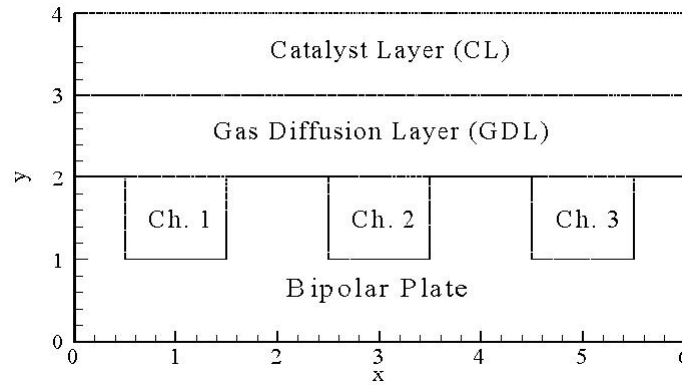


Figure 3.2: Modeling Domain - x and y axes have been normalized - flow is in the y -direction ($(0 \leq x \leq 6)$ denotes a distance of 6 mm, $(0 \leq y \leq 2)$ denotes a distance of 2 mm, $(2 \leq y \leq 3)$ denotes a distance of 150 μm and $(3 \leq y \leq 4)$ denotes a distance of 5 μm)

3.2 Oxygen Concentration Drop in the Gas Channel

The channel flow field studied in this thesis is that of a serpentine flow channel. Due to the turns in the flow field, the concentration, or in other words mass fraction, of oxygen along the flow channel decreases. The decrease of oxygen concentration is found using the following set of equations [25].

CHAPTER 3. MODEL FORMULATION

$$C_{O_2} = C_{O_2,in} \exp\left(-\frac{h_m l}{W_d V}\right) \quad (3.2)$$

where, l , is the length from the channel inlet in the flow direction along the channel, h_m is the mass transfer coefficient, W_d is the width of the channel, V is the velocity of the oxidant in the flow channel, C_{O_2} and $C_{O_2,in}$ represent the mean concentration of oxygen in the flow channel at the distance l from the channel outlet and at the channel inlet, respectively.

The inlet concentration of oxygen can be related to the inlet mole fraction of oxygen as follows,

$$C_{O_2,in} = x_{O_2,in} \left(\frac{P_g}{RT} \right) \quad (3.3)$$

where, $x_{O_2,in}$ is the inlet oxygen molar fraction. The inlet oxygen molar fraction can be found knowing that air with a known relative humidity is the oxidant. The equation set in 3.4 is used to solve for the inlet molar fractions of oxygen, nitrogen and water vapor.

$$\begin{aligned} x_{O_2,in} &= 0.25x_{N_2,in} \\ x_{H_2O,in} &= \frac{RH \cdot P_{sat}}{P_g} \\ 1 &= x_{N_2,in} + x_{O_2,in} + x_{H_2O,in} \end{aligned} \quad (3.4)$$

The mass transfer coefficient, h_m , is calculated from a correlation [63] of the Sherwood number assuming uniform surface mass flux.

$$Sh = \frac{h_m d_h}{D} = 5.39 \quad (3.5)$$

where, d_h is the hydraulic diameter of the flow channel and D is the bulk diffusion of oxygen in gas in the flow channel.

3.3 Gas Pressure Drop in the Channel

Similarly, due to the geometry of the flow channel used in this study, it is important to consider the pressure drop that occurs along the flow channel. The pressure drop is very much dependent on the mass flux of species as well as the current density of the fuel cell. It is also important to point out that the pressure drop is assumed to be linear since the flow is laminar and fully developed. The pressure drop in the flow field is governed by the following equation [64],

$$\Delta P = \frac{1}{2} \zeta \rho V^2 \quad (3.6)$$

The loss coefficient ζ consists of the coefficients for friction loss and bending loss. The friction loss coefficient ζ_f and the 90° bending loss coefficient ζ_b for a laminar flow and a square duct are given as follows,

$$\zeta = \zeta_f + 2\zeta_b \quad (3.7)$$

$$\zeta_f = \frac{56.9l}{Re_h d_h} \quad (3.8)$$

$$\zeta_b = \frac{0.21}{r_o/d_h} + 50.4 \frac{r_o}{d_h} \left(Re_h \sqrt{\frac{2r_o}{d_h}} \right)^{-\frac{2}{3}} \quad (3.9)$$

where, r_o is the bend radius of the flow channel, Re_h is the Reynolds number evaluated with the hydraulic diameter d_h .

The oxygen molar flow rate at the channel inlet is determined from the cell operating conditions including the cell average current density I , cell active area A and the stoichiometry S_c . The water vapor and nitrogen molar flow rates at the channel inlet are determined based on the species' inlet molar fraction. Equations 3.10, 3.11, and 3.12 are used to solve for the oxygen flow rate, nitrogen and water vapor molar fractions, respectively.

$$\dot{N}_{O_2} = \frac{IAS_c}{4F} \quad (3.10)$$

$$x_{N_2} = \frac{\dot{N}_{N_2}}{\dot{N}_{N_2} + \dot{N}_{O_2} + \dot{N}_{H_2O}} \quad (3.11)$$

$$x_{H_2O} = \frac{\dot{N}_{H_2O}}{\dot{N}_{N_2} + \dot{N}_{O_2} + \dot{N}_{H_2O}} \quad (3.12)$$

where, I is the cell current density, A is the cell area, S_c is the stoichiometry of the cathode, \dot{N}_{N_2} , \dot{N}_{O_2} , and \dot{N}_{H_2O} are the molar flow rates of nitrogen, oxygen and water vapor, respectively.

The total gas flow rate at the cathode channel inlet is obtained from the molar flow rate of oxygen, nitrogen and water vapor based on the inlet relative humidity. It is assumed that no liquid water exists in the inlet stream.

$$\begin{aligned} \dot{m} &= \sum \tilde{M}_j \dot{N}_j \\ V &= \frac{\dot{m}}{\rho A_c} \end{aligned} \quad (3.13)$$

where, \dot{m} is the total mass flow rate, \tilde{M}_j is the molar mass of species j , \dot{N}_j is the molar flux of the j^{th} species, V is the total velocity of the gas along the flow channel flow field, ρ is the density of the gas mixture in the channel flow field, and A_c is the cross-sectional area of the channel.

In the multi-phase model, it is assumed that liquid water is not part of the gas (oxidant) mixture in the flow channel; hence, the pressure drop calculated is applied for the conservation of gas phase pressure only. The gas pressure drop is calculated for various cell current densities and inlet relative humidity and shown in Figure 3.3. It is clear that the cell current density has a more significant effect on the pressure drop than the inlet relative humidity. In addition, the pressure drop at lower current densities seems to be almost equal for all values of inlet relative humidity. An obvious difference is seen at higher current densities. However, this difference is still small; it is within 6%.

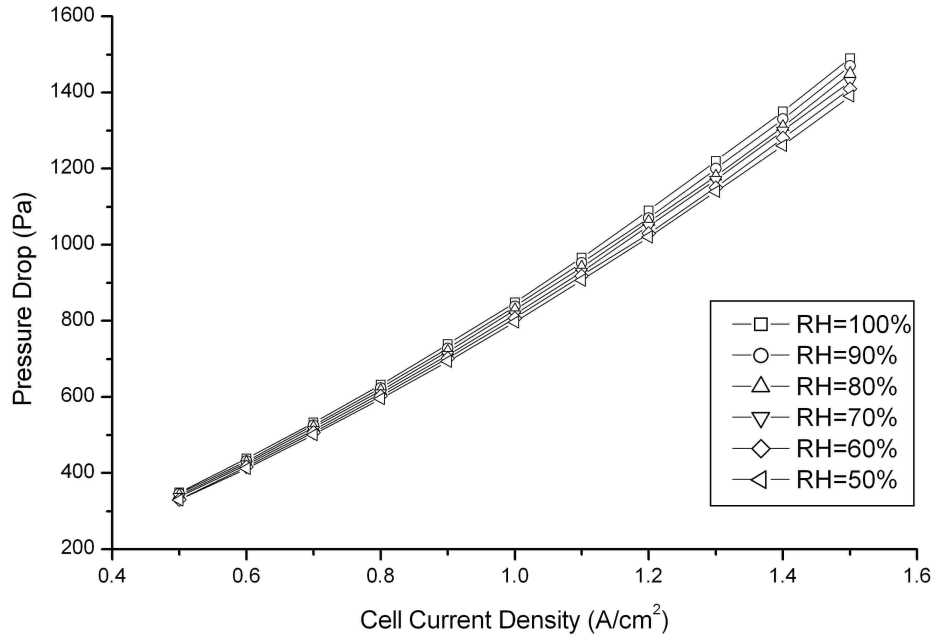


Figure 3.3: Effect of inlet relative humidity and cell current density on the pressure drop along a serpentine flow channel

3.4 Single Phase Model

The underlying assumptions along with the governing equations used to solve the isothermal and non-isothermal, single phase model are developed and presented in this section.

3.4.1 Assumptions

1. The process is steady state
2. The flow is laminar and incompressible
3. Effects of gravity are negligible
4. The model is two-dimensional - dependency in the x and y directions only with the flow in the y direction

5. The macro-homogeneous approach is considered for the gas diffusion and catalyst layers. The macro-homogeneous structure leads to the assumption that all the ingredients of the layers are evenly distributed over the layer.
6. The water is in vapor form only. The water produced due to the electro-chemical reaction in the catalyst layer is vapor water. The water transported from the membrane to the catalyst layer via electro-osmotic drag is also in vapor form.

3.4.2 Conservation of Momentum

Darcy's law is used to describe the conservation of momentum in the backing and catalyst layers due to their porous nature as given below,

$$0 = -\nabla \cdot \mathbf{P} - \frac{\mu}{\kappa} \vec{u} \quad (3.14)$$

where \mathbf{P} is the pressure, μ is the viscosity, κ is the permeability and \vec{u} is the velocity.

The conservation of momentum is applied to the control volume as shown in Figure 3.4. Forces due to shear stresses, body force and gravity are ignored.

To better understand the control volume, consider the following definitions,

$$P_{x+dx} = P_x + dx \frac{\partial P}{\partial x} \quad (3.15)$$

$$P_{y+dy} = P_y + dy \frac{\partial P}{\partial y} \quad (3.16)$$

The components of the velocity vector due to the pressure gradient are obtained as follows,

$$u = -\frac{\kappa}{\mu} \frac{dP}{dx} \quad (3.17)$$

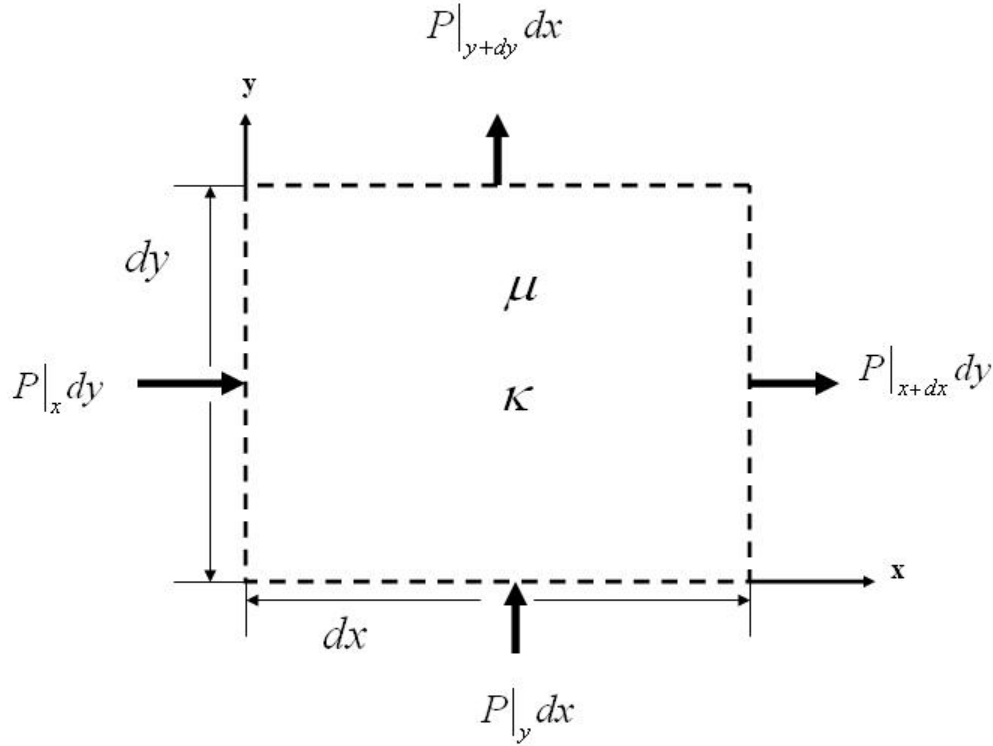


Figure 3.4: Control volume describing the conservation of momentum in the gas diffusion and catalyst layers

$$v = -\frac{\kappa}{\mu} \frac{dP}{dy} \quad (3.18)$$

3.4.3 Conservation of Species

In this study, the single phase model is used for comparison purposes. Therefore, the effect of relative humidity on the single phase model performance will not be studied. The oxidant is assumed to be fully humidified air and the transport of species in the channel is not modeled. The flow is taken to be fully developed, so the species are uniform across the channel averaged flow. The transport of species in the electrode is governed by the multi-component Stefan-Maxwell equation. Diffusion and convection are accounted for as the means of transport of the species in the electrode.

Figure 3.5 is a pictorial image of the transport of species in a control volume in the gas diffusion and catalyst layers, where R_{Y_i} is the sink source of species i . The sink source exists in the catalyst layer only due to the electrochemical reaction. Oxygen is being reduced to water via the oxygen

reduction reaction.

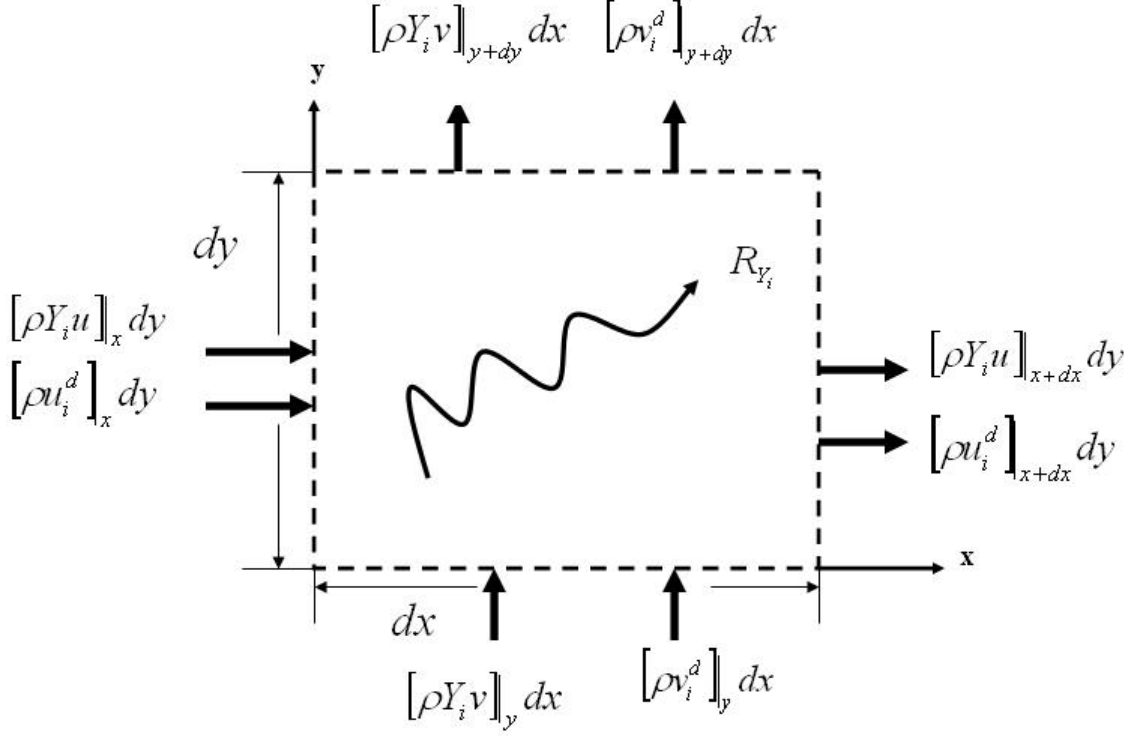


Figure 3.5: Control volume describing species transport in the gas diffusion and catalyst layers

The following information is necessary to understand the control volume terminology,

$$[\rho Y_i u]_{x+dx} = \left([\rho Y_i u]_x + \frac{\partial}{\partial x} [\rho Y_i u] dx \right) \quad (3.19)$$

$$[\rho Y_i v]_{y+dy} = \left([\rho Y_i v]_y + \frac{\partial}{\partial y} [\rho Y_i v] dy \right) \quad (3.20)$$

$$[\rho u^d]_{x+dx} = \left([\rho u^d]_x + \frac{\partial}{\partial x} [\rho u^d] dx \right) \quad (3.21)$$

$$[\rho v^d]_{y+dy} = \left([\rho v^d]_y + \frac{\partial}{\partial y} [\rho v^d] dy \right) \quad (3.22)$$

where, u^d and v^d are the diffusion velocity in the x and y directions, respectively and Y_i is the mass fraction of species i.

CHAPTER 3. MODEL FORMULATION

Since fully humidified air is used as the oxidant, the species of concern are oxygen, water vapor and nitrogen. The mass fractions of these species add up to 1; hence, the conservation is employed for only two species. The two species are oxygen and water vapor. The mass fractions of oxygen, water vapor and nitrogen are solved for using equations 3.23, 3.24 and 3.25 respectively, as follows,

$$\nabla \cdot (\rho \vec{u} Y_{O_2}) = \nabla \cdot \left(Y_{O_2} \sum D_{O_2,j}^{\text{eff}} \left[\nabla Y_{O_2} + Y_{O_2} \frac{\nabla \tilde{M}}{\tilde{M}} \right] \right) - R_{O_2} \quad (3.23)$$

where Y_{O_2} is the mass fraction of oxygen, $D_{O_2,j}^{\text{eff}}$ is the effective diffusion of oxygen in the j^{th} species.

$$\nabla \cdot (\rho \vec{u} Y_{H_2O}) = \nabla \cdot \left(Y_{H_2O} \sum D_{H_2O,j}^{\text{eff}} \left[\nabla Y_{H_2O} + Y_{H_2O} \frac{\nabla \tilde{M}}{\tilde{M}} \right] \right) + R_{H_2O} \quad (3.24)$$

where Y_{H_2O} is the mass fraction of water vapor, $D_{H_2O,j}^{\text{eff}}$ is the effective diffusion of water vapor in the j^{th} species.

$$Y_{N_2} = 1 - Y_{O_2} - Y_{H_2O} \quad (3.25)$$

where Y_{N_2} is the mass fraction of nitrogen.

Bruggemann's correction has to be used to obtain the effective diffusion coefficient of species j in the gas diffusion and catalyst layers. The correction is as follows,

$$\begin{aligned} D_{i,j}^{\text{eff}} &= \varepsilon_{GDL}^{1.5} D_{i,j} \\ D_{i,j}^{\text{eff}} &= \varepsilon_{CL}^{1.5} D_{i,j} \end{aligned} \quad (3.26)$$

In the gas diffusion layer, the source terms R_{O_2} and R_{H_2O} are equal to zero, since no reaction takes place in the gas diffusion layer. In the catalyst layer, the source term is negative in the oxygen conservation equation since oxygen is consumed in the reaction, while it is positive in the water vapor equation since water vapor is the product of the reaction. The Butler-Volmer equation is used to describe the reaction rates of oxygen and water in the catalyst layer as given by,

$$R_{O_2} = \frac{\tilde{M}_{O_2}}{4F} |J| \quad (3.27)$$

$$R_{H_2O} = \frac{\tilde{M}_{H_2O}}{2F} |J| \quad (3.28)$$

$$J = A_v i_o^{\text{ref}} \left(\frac{C_{O_2}}{C_{O_2}^{\text{ref}}} \right)^{\gamma_{O_2}} \left\{ \exp \left[\frac{\alpha F}{\Re T} (\phi_s - \phi_m) \right] - \exp \left[-\frac{\alpha F}{\Re T} (\phi_s - \phi_m) \right] \right\} \quad (3.29)$$

where A_v is the density of active area in the catalyst layer, $C_{O_2}^{\text{ref}}$ is the reference concentration of oxygen, γ_{O_2} is the order of reaction, ϕ_s is the solid potential and ϕ_m is the electrolyte potential.

3.4.4 Conservation of Charge

The control volume used to obtain the governing equation for the conservation of charge is shown in Figure 3.6. This figure is a general figure for the transport of electrons and protons in the cell. Keep in mind that in the bipolar plate and gas diffusion layer the current due to proton transport is equal to zero since protons do not travel in the bipolar plate and the gas diffusion layer. The source term due to the electrochemical reaction is illustrated in the figure as R_i and exists in the catalyst layer only. In the figure, I_x and I_y show the direction of the current. The current flows in the opposite direction to the flow of electrons; thus, it is flowing in the negative x and y directions.

The terminology used in the figure is defined as follows,

$$[i_p]_{x+dx} = \left([i_p]_x + \frac{\partial}{\partial x} [i_p] dx \right) \quad (3.30)$$

$$[i_p]_{y+dy} = \left([i_p]_y + \frac{\partial}{\partial y} [i_p] dy \right) \quad (3.31)$$

$$[i_s]_{x+dx} = \left([i_s]_x + \frac{\partial}{\partial x} [i_s] dx \right) \quad (3.32)$$

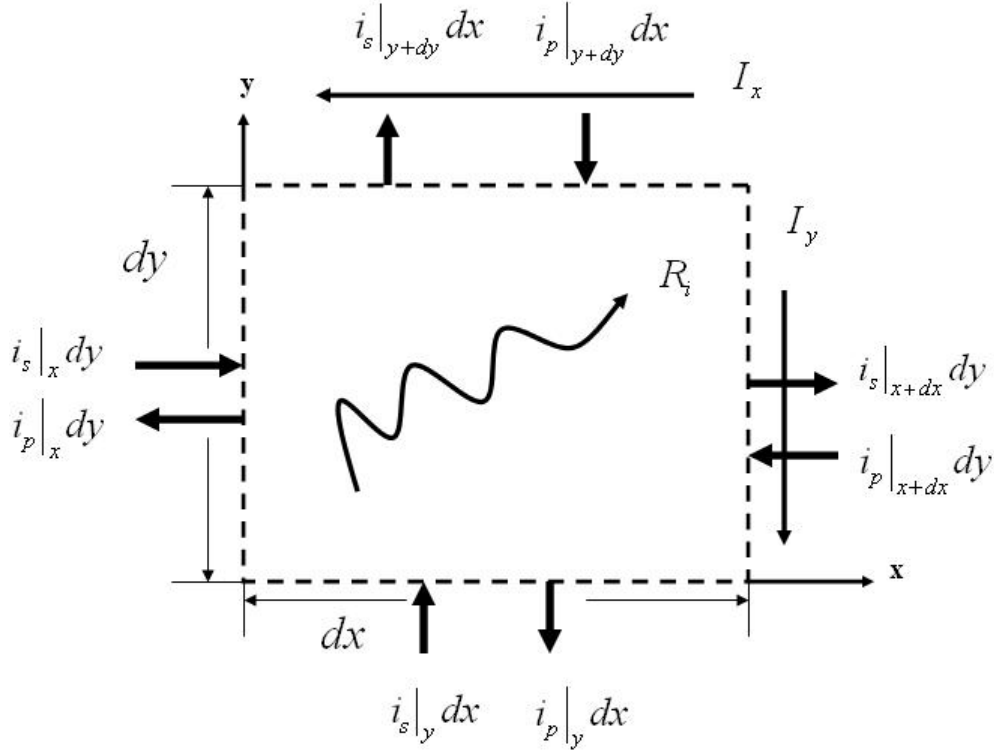


Figure 3.6: Control volume applied to the conservation of charge

$$[i_s]_{y+dy} = \left([i_s]_y + \frac{\partial}{\partial y} [i_s] dy \right) \quad (3.33)$$

where, i_p and i_s are the currents due to proton and electron transfer, respectively.

In this thesis, the ionic charge due to the proton and electron transport are taken into account. Electron transport is related to the solid potential and is described by,

$$\nabla \cdot i_s = \nabla \cdot (-\sigma_s^{\text{eff}} \nabla \phi_s) = -J \quad (3.34)$$

where σ^{eff} is the effective electrical conductivity.

Electron transport is modeled in the bipolar plate, the gas diffusion layer and the catalyst layer. The electron travels from the bipolar plate to the gas diffusion layer to the catalyst layer where the reaction occurs. In the catalyst layer, the generation of ionic current has to be considered. The rate of generation is simply the rate of reaction at the cathode side and is given by the Butler-Volmer

equation in equation 3.29.

Due to the porous nature of the gas diffusion and catalyst layers, the conductivity has to be corrected and the effective conductivity is found as follows,

$$\sigma_s^{\text{eff}} = \begin{cases} \sigma_s (1 - \varepsilon_{GDL})^{1.5} & \text{in the GDL} \\ \sigma_s (\epsilon_s)^{1.5} & \text{in the CL} \end{cases} \quad (3.35)$$

where ε_{GDL} is the void region in the gas diffusion layer, ϵ_s is the solid phase fraction in the catalyst layer.

Similarly, the ionic charge due to proton transfer has to be considered. It is normally referred to as the electrolyte potential and is found as follows,

$$\nabla \cdot i_m = \nabla \cdot (-\sigma_m^{\text{eff}} \nabla \phi_m) = J \quad (3.36)$$

where σ_m^{eff} is the effective electrolyte conductivity.

The electrolyte potential exists in the catalyst layer only since protons do not travel through the gas diffusion layer or the bipolar plate.

Again, since the catalyst layer is a porous material the electrolyte conductivity has to be corrected as follows,

$$\sigma_m^{\text{eff}} = \sigma_m (\varepsilon_{CL} \epsilon_m)^{1.5} \quad (3.37)$$

where ε_{CL} is the void region in the catalyst layer, ϵ_m is the electrolyte fraction in the catalyst layer and σ_m is the bulk conductivity for the electrolyte membrane.

3.4.5 Conservation of Energy

The conservation of energy in the bipolar plate and gas diffusion and catalyst layers can be generalized in the control volume shown in Figure 3.7. Energy is transferred in the three domains through conduction following Fourier's Law. The heat source and the internal energy are represented by the term R_q shown in the figure. The internal energy accounts for the enthalpy and therefore, the

transfer of heat through convection. Note that the effects of shear forces along with body forces on the energy equation are not taken into account in this thesis.

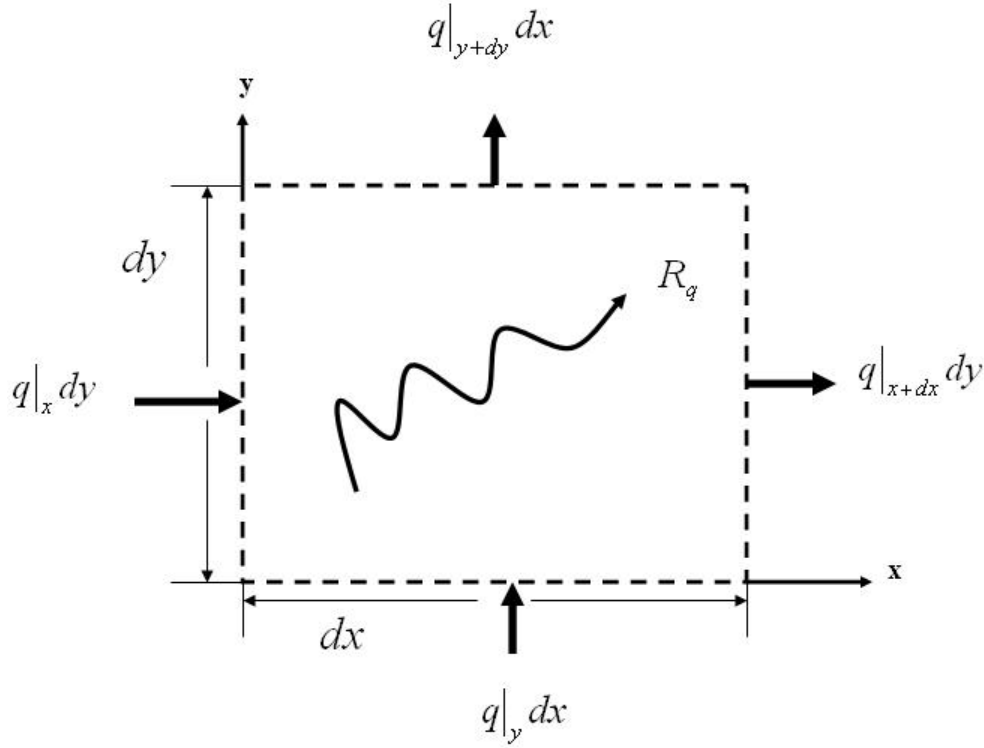


Figure 3.7: Control volume of conservation of energy in the bipolar plate and gas diffusion and catalyst layers

$$[q]_{x+dx} = \left([q]_x + \frac{\partial}{\partial x} [q] dx \right) \quad (3.38)$$

$$[q]_{y+dy} = \left([q]_y + \frac{\partial}{\partial y} [q] dy \right) \quad (3.39)$$

In the cathode of a PEM fuel cell heat is generated due to the transport of electrons, protons and the electrochemical reaction. The conservation of energy can be written as follows,

$$(\rho c_p)^{\text{eff}} \vec{u} \cdot \nabla T = \nabla \cdot (k^{\text{eff}} \nabla T) + \dot{Q} \quad (3.40)$$

CHAPTER 3. MODEL FORMULATION

where $(\rho c_p)^{\text{eff}}$ represents the effective heat capacity of each layer. A general equation to find the effective heat capacity in the three domains, bipolar plate, backing layer, and catalyst layer, is given by

$$(\rho c_p)^{\text{eff}} = \epsilon_g (\rho c_p)_g + \epsilon_s (\rho c_p)_s + \epsilon_l (\rho c_p)_l + \epsilon_m (\rho c_p)_m \quad (3.41)$$

The effective value is determined by the volume fraction of each phase in the layer. The specific heat (c_p) of a Nafion membrane is unavailable. The specific heat of a PTFE based structure is used instead. Similarly, the effective thermal conductivity, k^{eff} , is evaluated for each layer as

$$k^{\text{eff}} = \epsilon_l k_l + \epsilon_m k_m + \epsilon_s k_s + \epsilon_g k_g \quad (3.42)$$

where ϵ_l , ϵ_m , ϵ_s , and ϵ_g represent the volume fraction of liquid water, membrane electrolyte, solid matrix and the gas pore, respectively. Hence, the summation of the ϵ terms equals 1.

The last term \dot{Q} in equation 3.40 represents the heat source. The total heat generation in a PEM fuel cell is comprised of reversible and irreversible heat releases. The irreversible heat release can be further divided into activation heat generation and ohmic heating, since in the present formulation the activation polarization actually includes the overpotential due to the mass transfer. Therefore, the total heat generation is:

$$\begin{aligned} \dot{Q} &= \dot{Q}_{\text{rev}} + \dot{Q}_{\text{act}} + \dot{Q}_{\text{ohm}} \\ &= \underbrace{\left[\frac{J}{nF} \right] (T \Delta S)}_{\text{rev}} + \underbrace{[\eta J]}_{\text{act}} + \underbrace{\frac{J_s^2}{\sigma_s^{\text{eff}}} + \frac{J_m^2}{\sigma_m^{\text{eff}}}}_{\text{ohm}} \end{aligned} \quad (3.43)$$

where ΔS represents the entropy change of the overall reaction, η is the activation overpotential, J is the reaction rate, σ_s and σ_m are the electronic and protonic conductivities, respectively, J_s and J_m are the electronic and protonic current densities, respectively.

The reversible and activation heat generation terms are related to the electrochemical reaction and, hence, only valid in the catalyst layer. The protonic ohmic heating source terms are considered only in the catalyst layer. Similarly, the electronic ohmic heating term is considered in the bipolar plate, backing and catalyst layers. The different source terms can be summarized as follows,

Table 3.1: Summary of source term in energy equation in the different domains for the single phase model

Domain	Source Term
Bipolar Plate	$\frac{J_s^2}{\sigma_s^{\text{eff}}}$
Gas Diffusion Layer	$\frac{J_s^2}{\sigma_s^{\text{eff}}}$
Catalyst Layer	$\left \frac{J}{4F} \right (T \Delta S) + \eta J + \frac{J_s^2}{\sigma_s^{\text{eff}}} + \frac{J_m^2}{\sigma_m^{\text{eff}}}$

3.5 Multi-Phase Model

In this section a detailed discussion of the governing equations for the multi-phase, isothermal and non-isothermal model is presented.

3.5.1 Assumptions

1. The process is steady state
2. The flow is laminar and incompressible
3. Effects of gravity are negligible
4. The model is two-dimensional - dependency in the x and y directions only
5. The macro-homogeneous approach is considered for the gas diffusion and catalyst layers.
6. The gas diffusion and catalyst layers are hydrophobic (i.e. the contact angle is greater than 90°)
7. Both vapor and liquid phases co-exist in the gas diffusion and catalyst layers
8. The production of water in the catalyst layer is in liquid form

3.5.2 Conservation of Momentum

Darcy's law is used to describe the relative velocity of species given that the flow of species in the gas diffusion layer and the catalyst layer is expected to be small. Thus, the velocity and pressure of the phases can be solved for using the generalized Darcy term as follows [65, 66],

$$0 = -\nabla \cdot \mathbf{P}_k - \frac{\mu_k}{\kappa \kappa_{rk}} \vec{u}_k \quad (3.44)$$

where \mathbf{P}_k is the pressure of phase k , κ is the bulk permeability of the porous medium, μ_k is the viscosity of phase k , κ_{rk} is the relative permeability of phase k and \vec{u}_k is the relative velocity of phase k .

The conservation equation is obtained in a similar fashion as that for the single phase model. Refer back to Figure 3.4 for the control volume used to obtain the conservation of momentum equation.

Here the phase pressure is dependent on the phase velocity, viscosity and permeability. The permeability is independent of the fluid, where as the relative permeability of the phase is dependent on the liquid water saturation in the layers. In addition, the relative permeability is dependent on the capillary pressure, which is the difference between the gas and liquid pressures,

$$P_c = P_g - P_l \quad (3.45)$$

Normally a liquid water droplet is taken to be in the shape of a cylindrical pore. For a cylindrical pore, the capillary pressure can be written in the following general form as a function of the pore size, contact angle and surface tension [67]

$$P_c = -\frac{2\sigma \cos \theta_c}{r} \quad (3.46)$$

where σ is the surface tension, θ_c is the contact angle of the wetting phase with the solid phase in the porous media, and r is the radius of the cylindrical pore.

For a hydrophilic media, the wetting phase is the gas phase and therefore the gas-phase satura-

tion is used to express the capillary pressure and is solved for. The contact angle for a hydrophilic media is less than 90° . While, in a hydrophobic media the liquid phase becomes the wetting phase and therefore the liquid-phase saturation is used. The contact angle for a hydrophobic media is greater than 90° . This information is also illustrated through Figure 3.8.

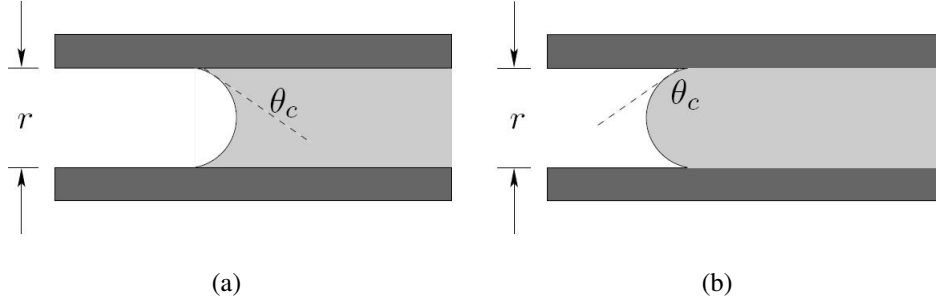


Figure 3.8: Pore with (a) hydrophilic; (b) hydrophobic characteristics

A porous medium can possess both hydrophobic and hydrophilic properties. When studying the gas diffusion and catalyst layers (porous media) in this thesis, it can be assumed that they are either completely hydrophobic or completely hydrophilic since the study is on a macro level. Yu et al. [68] used environmental scanning electron microscopy (ESEM) to measure the hydrophilicity and hydrophobicity in the catalyst layer. Their findings are shown in Figure 3.9. Many other studies for measuring the contact angle are also reported in the literature, see [69-72]. From all these studies it can be safely assumed that the gas diffusion and catalyst layers possess hydrophobic properties.

After studying the contact angle, it is necessary to investigate the relationship between the capillary pressure and the saturation. According to Ustohal et al. [73], there exists a minimum (residual) saturation at which the capillary pressure approaches infinity. At the same time, there exists a maximum saturation at which the capillary pressure approaches negative infinity. One can think of the residual saturation as the saturation at which the fluid loses its capability to move [74]. A general correlation for the capillary pressure is given below [75],

$$P_c = 2\varpi\sigma\theta_c\sqrt{\frac{\varepsilon}{\kappa}}f(S) \quad (3.47)$$

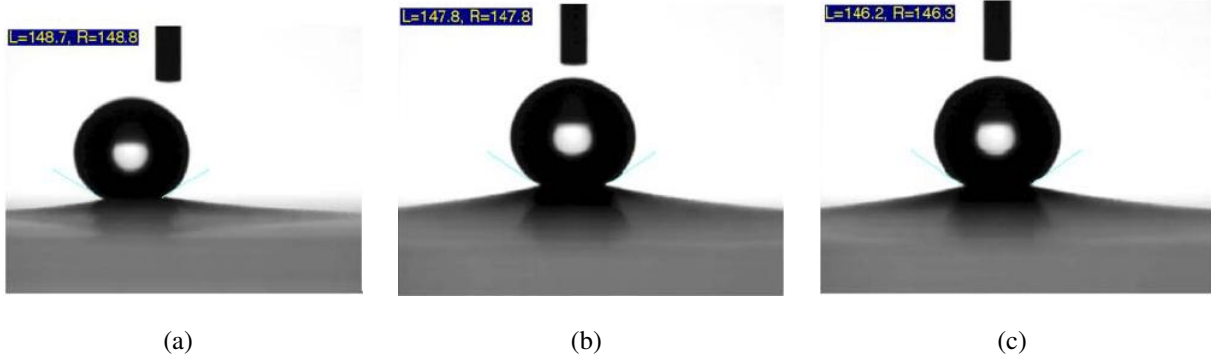


Figure 3.9: The time dependent contact angle of a catalyst layer with wetting process (a) (0 s) The first attachment of the water droplet at the catalyst layer surface. The contact angle is 148.7° ; (b)(60 s), the measured contact angle is 147.8° ; (c) (100 s), the measured contact angle is 146.2° [68]

where P_c is the capillary pressure, ϖ is the correction factor to account for the change in contact angle due to roughness, θ_c is the contact angle of the wetting fluid to the solid, $f(S)$ is a function of the effective saturation of the wetting fluid.

For the purpose of this thesis, two different relationships that describe the capillary pressure will be used and discussed. The most widely used relationship in the fuel cell literature is that relationship derived by Leverette and simply known as the Leverette function [42]

$$P_c = \sigma \cos(\theta_c) \left(\frac{\varepsilon}{\kappa} \right)^{0.5} f(S) \quad (3.48)$$

where the expression of the Leverette function is dependent on the contact angle as follows,

$$f(S) = \begin{cases} 1.417(1 - S) - 2.120(1 - S)^2 + 1.263(1 - S)^3 & \text{if } 0^\circ \leq \theta_c < 90^\circ \\ 1.417S - 2.120S^2 + 1.263S^3 & \text{if } 90^\circ < \theta_c < 180^\circ \end{cases} \quad (3.49)$$

As seen above, the Leverette function varies depending on the contact angle, θ_c , which in turn depends on the nature of the porous media.

The other relationship that will be used in this thesis is known as the Brooks and Corey rela-

tionship for a porous media and is described by equation [76].

$$P_c = \begin{cases} \frac{P_d}{(S)^{\frac{1}{\lambda}}} & \text{if } 0^\circ \leq \theta_c < 90^\circ \\ \frac{P_d}{(1 - S)^{\frac{1}{\lambda}}} & \text{if } 90^\circ < \theta_c < 180^\circ \end{cases} \quad (3.50)$$

where P_d is the displacement pressure and λ is the pore size distribution.

Brooks and Corey found that for a specific material and fluid the change in the displacement pressure and the pore size distribution is independent of the material properties. Ustohal et al. prepared an experiment which resulted in the values of P_d and λ through curve fitting for a liquid, gas mixture and TEFLON material in [73]. The values found by this experiment are used in this thesis. According to the Leverette function, the capillary pressure is very much dependent on the permeability of the backing layer, while with the Brooks and Corey relation, the capillary pressure is only dependent on the effective saturation. This difference is shown in Figure 3.10. For the Leverette function, the capillary pressure seems to be less dependent on the permeability of the material at high permeability values. The trend of capillary pressure versus effective saturation using the Brooks and Corey relation is very similar to that using the Leverette function at permeability values higher than $5.5 \times 10^{-12} m^2$.

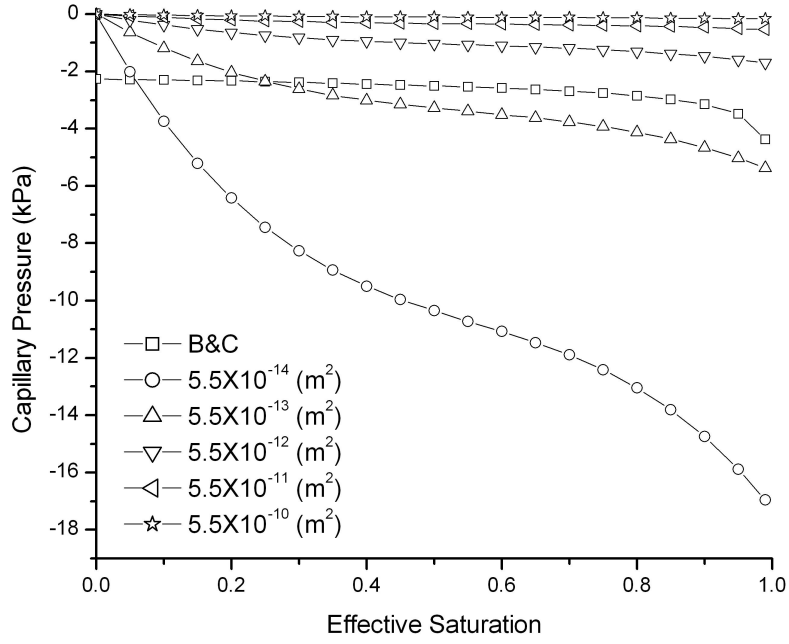


Figure 3.10: Capillary pressure versus effective saturation for different permeability values evaluated with the Leverette function and Brooks & Corey relation with permeability as the parameter given in the legend

The effective saturation is needed to solve the momentum equation and is defined as,

$$S = \frac{s - S_r}{S_m - S_r} \quad (3.51)$$

where S_r and S_m are the residual and maximum saturation, respectively, of the wetting fluid. Their values have been found by Ustohal et al. [73].

Many models have been developed to predict the relative permeability of the wetting and non-wetting phases. These models have been developed from conceptual models of flow in capillary tubes combined with models of pore-size distribution [77]. Some of the most common models are the Burdine, Mualem, and Power models shown below [78]:

$$\kappa_{rw} = S^2 \left[\frac{\int_0^S \frac{dS}{P_c^2}}{\int_0^1 \frac{dS}{P_c^2}} \right] \quad \kappa_{rnw} = (1 - S)^2 \left[\frac{\int_S^1 \frac{dS}{P_c^2}}{\int_0^1 \frac{dS}{P_c^2}} \right] \quad (3.52)$$

$$\kappa_{rw} = S^\eta \left[\frac{\int_0^S \frac{dS}{P_c^2}}{\int_0^1 \frac{dS}{P_c^2}} \right]^2 \quad \kappa_{rnw} = (1 - S)^\eta \left[\frac{\int_S^1 \frac{dS}{P_c^2}}{\int_0^1 \frac{dS}{P_c^2}} \right]^2 \quad (3.53)$$

$$\kappa_{rw} = S^n \quad \kappa_{rnw} = (1 - S)^n \quad (3.54)$$

where equation 3.52 is the Burdine model, equation 3.53 is the Mualem model and equation 3.54 is the Power model, κ_{rw} and κ_{rnw} denote the relative permeability of the wetting and non-wetting phases, respectively.

For the purpose of this thesis, the power law is used to describe the relative permeability of the wetting and non-wetting phases [41].

$$\kappa_{rw} = S^3 \quad \kappa_{rnw} = (1 - S)^3 \quad (3.55)$$

3.5.3 Conservation of Mass

Figure 3.11 shows the control volume used to generate the equation of conservation of liquid water mass. The control volume is a representation of mass transfer in the gas diffusion and catalyst layers. The sink source shown as, R_{rn} , is due to evaporation and/or condensation of liquid water in both layers. In the catalyst layer, the sink source takes care of the addition of liquid water through the electrochemical reaction.

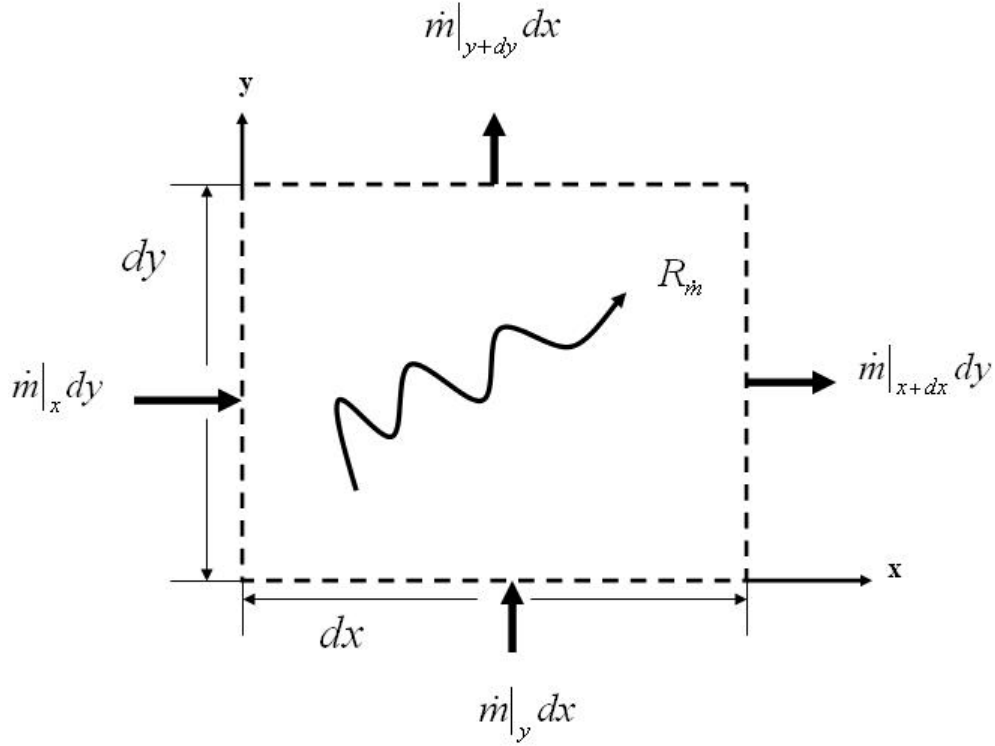


Figure 3.11: Control volume representing the conservation of liquid water mass in the gas diffusion and catalyst layers

$$[\dot{m}]_{x+dx} = \left([\dot{m}]_x + \frac{\partial}{\partial x} [\dot{m}] dx \right) \quad (3.56)$$

$$[\dot{m}]_{y+dy} = \left([\dot{m}]_y + \frac{\partial}{\partial y} [\dot{m}] dy \right) \quad (3.57)$$

The conservation of mass equation that is applied in this thesis to solve the liquid phase is described below.

$$\nabla \cdot (\rho_l \vec{u}_l) = \text{Change in Mass} \quad (3.58)$$

From equation 3.44, the liquid and gas pressures can be related to their perspective velocities and relative permeability as follows,

$$0 = -\nabla \cdot P_l - \frac{\mu_l}{\kappa \kappa_{rl}} \vec{u}_l \quad (3.59)$$

$$0 = -\nabla \cdot P_g - \frac{\mu_g}{\kappa \kappa_{rg}} \vec{u}_g \quad (3.60)$$

Using the definition of capillary pressure, liquid pressure and gas pressure as described by 3.45, 3.59 and 3.60, respectively, the conservation of the liquid phase mass can be rewritten in terms of the capillary pressure as follows,

$$\nabla \cdot \left(\rho_l \left[-D_c \nabla S + \frac{\mu_g \kappa_{rl}}{\mu_l \kappa_{rg}} \vec{u}_g \right] \right) = R_{v \leftrightarrow l} + (R_{H_2O})_l \quad (3.61)$$

$$D_c = \frac{\kappa_l}{\mu_l} \frac{dP_c}{dS} \quad (3.62)$$

where κ_l is $\kappa \kappa_{rl}$.

The two source terms in the mass conservation equation of liquid water describe the condensation or evaporation of liquid water due to phase change from vapor to liquid or vice versa in the gas diffusion and catalyst layers and the addition of liquid water via the electrochemical reaction in the catalyst layer. The condensation, evaporation term is evaluated as follows [41],

$$R_{v \leftrightarrow l} = \chi \varepsilon \frac{x_{H_2O}}{\mathfrak{RT}} (x_{H_2O} P_g - P_{sat}) \tilde{M}_{H_2O} (1 - S) q + E \varepsilon \rho_l S (x_{H_2O} P_g - P_{sat}) (1 - q) \quad (3.63)$$

where χ is the condensation rate, E is the evaporation rate and q is the switch function and is dependent on the relative humidity inside the gas diffusion and catalyst layers as defined below.

$$q = \begin{cases} 0 & \text{if } \frac{x_{H_2O} P_g}{P_{sat}} \leq 1 \\ 1 & \text{if } \frac{x_{H_2O} P_g}{P_{sat}} > 1 \end{cases} \quad (3.64)$$

It is important to note that the effective saturation is used to describe the condensation and evaporation terms in equation 3.63. There exists a minimum (or residual) saturation level, as mentioned previously, which will be trapped liquid water and will be immobile. The capillary

CHAPTER 3. MODEL FORMULATION

pressure (or force) will not be strong enough in order to break the ties between the molecules; thus, this minimum level will not evaporate.

The saturation pressure in atmospheres is estimated using the correlation obtained by Springer et al. [28] given by equation 3.65. This correlation is obtained for a temperature range of 0 – 100°C. The error of this function is less than 1%. For instance, the saturation pressure obtained using the correlation at 80°C is 47.3 kPa, while the actual saturation pressure at 80°C is 47.37 kPa [79].

$$\log_{10} P_{sat} = -2.1794 + 0.02953(T - 273) - 9.1837 \times 10^{-5}(T - 273)^2 + 1.4454 \times 10^{-7}(T - 273)^3 \quad (3.65)$$

The addition of liquid water through the electrochemical reaction is evaluated in the catalyst layer only. It is equal to zero in the gas diffusion layer since no reaction takes place. The source term in this model is very much similar to that introduced earlier in the single phase model using equation 3.28. In the multi-phase model, however, the liquid water will act as a barrier to the reaction; hence, the reaction sites will be decreased. The decrease in reaction sites will in turn affect the expression of the current density described by the Butler-Volmer equation given in 3.29. The production of water will follow the subsequent expression,

$$(R_{H_2O})_l = \frac{\tilde{M}_{H_2O}}{2F} (1 - S) A_v i_o^{\text{ref}} \left(\frac{C_{O_2}}{C_{O_2}^{\text{ref}}} \right)^{\gamma_{O_2}} \cdot \left| \left(\exp \left[\frac{\alpha F}{\Re T} (\phi_s - \phi_m) \right] - \exp \left[-\frac{\alpha F}{\Re T} (\phi_s - \phi_m) \right] \right) \right| \quad (3.66)$$

3.5.4 Conservation of Species

In order to solve for the oxygen and water vapor concentrations in the gas diffusion and catalyst layers, the species conservation should be applied. The conservation of species will be similar to that described for the single phase model in section 3.4 and can be also represented by the control volume shown in Figure 3.5. Here, the diffusion of the gaseous species will be affected by the

presence of liquid water in the porous medium. Therefore, the saturation of liquid water has to be taken into account when writing the conservation of species. The conservation of oxygen and water vapor are described by equations 3.67 and 3.69 below.

$$\nabla \cdot (\rho \vec{u} Y_{O_2}) = \nabla \cdot \left(Y_{O_2} \sum (1 - S)^{1.5} D_{O_2,j}^{\text{eff}} \left[\nabla Y_{O_2} + Y_{O_2} \frac{\nabla \tilde{M}}{\tilde{M}} \right] \right) - R_{O_2} \quad (3.67)$$

Similar to the single phase model, the source term in equation 3.67 is equal to zero in the gas diffusion layer since there is no sink source. In the catalyst layer, the rate of oxygen reaction is as follows,

$$R_{O_2} = \frac{\tilde{M}_{O_2}}{4F} (1 - S) A_v i_o^{\text{ref}} \left(\frac{C_{O_2}}{C_{O_2}^{\text{ref}}} \right)^{\gamma_{O_2}} \cdot \left| \left(\exp \left[\frac{\alpha F}{\Re T} (\phi_s - \phi_m) \right] - \exp \left[-\frac{\alpha F}{\Re T} (\phi_s - \phi_m) \right] \right) \right| \quad (3.68)$$

The conservation of water vapor in the gas diffusion and catalyst layers is presented in equation 3.69. The source term, $R_{v \leftrightarrow l}$, is present in the gas diffusion and catalyst layers and used to evaluate the vapor water that will condense or evaporate.

$$\nabla \cdot (\rho \vec{u} Y_{H_2O}) = \nabla \cdot \left(Y_{H_2O} \sum (1 - S)^{1.5} D_{H_2O,j}^{\text{eff}} \left[\nabla Y_{H_2O} + Y_{H_2O} \frac{\nabla \tilde{M}}{\tilde{M}} \right] \right) - R_{v \leftrightarrow l} \quad (3.69)$$

Bruggemann's correction is used here again to obtain the effective diffusion coefficient. It is similar to that given in equation 3.26.

3.5.5 Conservation of Charge

The conservation of charge for the multi-phase model is very similar to that of the single phase model, refer back to the control volume in Figure 3.6. The ionic charge due to proton and electron transfer should be taken into account. The charge due to electron and proton transfer are described

by equations 3.34 and 3.36, respectively. The major difference between the single phase and multi-phase models is the presence of liquid water in the catalyst layer. Liquid water will block some of the available sites for the reaction; hence, the Butler-Volmer equation will have to be modified to take into consideration the liquid water presence. The source term in equations 3.34 and 3.36 will be modified and should be written as follows,

$$J = (1 - S) A_v i_o^{\text{ref}} \left(\frac{C_{O_2}}{C_{O_2}^{\text{ref}}} \right)^{\gamma_{O_2}} \left(\exp \left[\frac{\alpha F}{\Re T} (\phi_s - \phi_m) \right] - \exp \left[-\frac{\alpha F}{\Re T} (\phi_s - \phi_m) \right] \right) \quad (3.70)$$

Again, since the gas diffusion and catalyst layers are porous media, the solid and electrolyte conductivity should be corrected as shown earlier in equations 3.35 and 3.37

3.5.6 Conservation of Energy

Heat is generated due to the electrochemical reaction and resistance to species transport. The heat generation will in turn have a noticeable effect on the overall performance of the cell. The control volume describing the energy transport in the cathode is shown in Figure 3.7. The energy equation that will be employed is written as follows,

$$(\rho c_p)^{\text{eff}} \vec{u}_{mix} \nabla \cdot T = \nabla \cdot (k^{\text{eff}} \nabla T) + \dot{Q} \quad (3.71)$$

where $(\rho c_p)^{\text{eff}}$ represents the effective heat capacity of each layer and a general form was given earlier in equation 3.41. Similarly, the effective thermal conductivity, k^{eff} , is evaluated for each layer as shown earlier in equation 3.42.

It is important to note that the mixture velocity is being used to solve the energy equation. This follows the assumption that the liquid and gas phase temperatures are equal that is a local thermodynamic equilibrium exists. The mixture velocity can be found using the mixture properties as shown below

$$\rho_{mix} \vec{u}_{mix} = \rho_l \vec{u}_l + \rho_g \vec{u}_g$$

$$\rho_{mix} = \rho_l + \rho_g(1 - S) \quad (3.72)$$

The last term \dot{Q} in equation 3.71 represents the heat source. The total heat generation in a PEM fuel cell is comprised of reversible and irreversible heat releases. The irreversible heat release can be further divided into activation heat generation and ohmic heating, since in the present formulation the activation polarization actually includes the overpotential due to the mass transfer. Therefore, the total heat generation is:

$$\begin{aligned} \dot{Q} &= \dot{Q}_{rev} + \dot{Q}_{act} + \dot{Q}_{ohm} + \dot{Q}_{phase} \\ &= \underbrace{\left| \frac{J}{nF} \right| (T\Delta S)}_{rev} + \underbrace{|\eta J|}_{act} + \underbrace{\frac{J_s^2}{\sigma_s^{eff}} + \frac{J_m^2}{\sigma_m^{eff}}}_{ohm} + \underbrace{h_{fg}R_{v \leftrightarrow l}}_{phase} \end{aligned} \quad (3.73)$$

where h_{fg} is the enthalpy of vaporization of water.

The reversible and activation heat generation terms are related to the electrochemical reaction and, hence, only valid in the catalyst layer. The protonic ohmic heating source terms are considered only in the catalyst layer. Similarly, the electronic ohmic heating term is considered in the bipolar plate, backing and catalyst layers. The different source terms can be summarized in Table 3.2.

Table 3.2: Summary of source term in energy equation in the different domains for the multi-phase model

Domain	Source Term
Bipolar Plate	$\frac{J_s^2}{\sigma_s^{eff}}$
Gas Diffusion Layer	$\frac{J_s^2}{\sigma_s^{eff}} + h_{fg}R_{v \leftrightarrow l}$
Catalyst Layer	$\left \frac{J}{4F} \right (T\Delta S) + \eta J + \frac{J_s^2}{\sigma_s^{eff}} + \frac{J_m^2}{\sigma_m^{eff}} + h_{fg}R_{v \leftrightarrow l}$

3.6 Boundary Conditions

This section is designed to explain the boundary conditions employed to solve the single phase and multi-phase models. The major difference between the two models is the addition of the saturation equation (liquid water mass conservation) to the multi-phase model. Before studying the boundary conditions, recall the modeling domain shown earlier and is shown again in Figure 3.12.

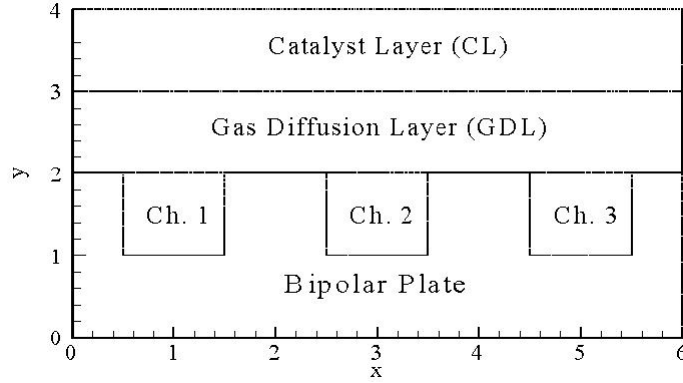


Figure 3.12: Modeling Domain - x and y axes have been normalized - flow is in the y -direction (($0 \leq x \leq 6$) denotes a distance of 6 mm , ($0 \leq y \leq 2$) denotes a distance of 2 mm , ($2 \leq y \leq 3$) denotes a distance of 150 μm and ($3 \leq y \leq 4$) denotes a distance of 5 μm)

- $Y_{O_2}|_{\text{At the inlet of Channel 1}} = Y_{O_{2,in}}$

At the gas diffusion layer/Channel 1 inlet interface, the mass fraction of oxygen is specified. It is assumed that the flow in the channel is fully developed and uniform; thus, the mass fraction can be calculated knowing the inlet relative humidity and that the reactant gas is air.

- $Y_{O_2}|_{\text{At the inlet of Channel 2 \& 3}} = Y_{O_{2,in}} - \Delta Y_{O_2}$

At the gas diffusion layer/Channel 2 and 3 interfaces, the mass fraction of oxygen is specified. There is loss in concentration of the reactant gas along the flow field due to the shape of the flow field. The calculation for the concentration drop presented earlier in equation 3.2 is used and then the concentration drop is changed to a decrease in mass fraction assuming that there is no loss in relative humidity along the channel flow field.

CHAPTER 3. MODEL FORMULATION

- $\vec{n} \cdot (\nabla Y_{O_2})|_{\text{At all other boundaries}} = 0$

At all the other boundaries the symmetry boundary condition is used.

- $P_g|_{\text{At the inlet of Channel 1}} = P_{cathode}$

The Darcy's Law governs the gaseous pressure distribution in the gas diffusion layer and catalyst layers. At the gas diffusion layer/Channel 1 interface, the gas pressure is specified. This can be done since it is assumed that the flow is fully developed.

- $P_g|_{\text{At the inlet of Channel 2 \& 3}} = P_{cathode} - \Delta P_g$

At the gas diffusion layer/Channel 2 and 3 interfaces, the gas pressure is specified. From equation 3.6, the pressure drop from one channel to another is found.

- $\vec{n} \cdot (\nabla P_g)|_{\text{At all other boundaries}} = 0$

The symmetry boundary condition is used at all the other boundaries.

- $\phi_s|_{y=0} = \phi_{cathode}$

The solid potential due to electron transfer from the anode to the cathode is specified at the bipolar plate boundary.

- $\vec{n} \cdot (\nabla \phi_s)|_{\text{At all the other boundaries}} = 0$

At all the other boundaries, the insulation boundary condition is used to solve for the solid potential. It implies that electrons cannot travel through that boundary condition; the corresponding current density would equal zero.

- $\phi_m|_{y=4} = 0$

The electrolyte potential due to the proton transfer from the membrane to the cathode is specified at the catalyst layer/membrane interface. It is assumed to be uniform along this boundary and to be equal to zero Volt.

- $\vec{n} \cdot (\nabla \phi_m)|_{\text{At all the other boundaries}} = 0$

At all the other boundaries, the insulation boundary condition is used to solve for the electrolyte potential. It implies that electrons cannot travel through that boundary condition; the corresponding current density would equal zero.

CHAPTER 3. MODEL FORMULATION

- $Y_{H_2O}|_{\text{At the inlet of Channel 1, 2 \& 3}} = Y_{H_2O}$

The mass fraction of water vapor is specified at the inlet of the three channels. The inlet mass fraction can be calculated using the inlet relative humidity.

- $\vec{n} \cdot (D_{H_2O} \nabla Y_{H_2O})|_{y=4} = \frac{n_d i|_{y=4} \tilde{M}_{H_2O}}{F}$

$$i|_{y=4} = i_o^{\text{ref}} \left(\frac{C_{O_2}}{C_{O_2}^{\text{ref}}} \right)^{\gamma_{O_2}} \left(\exp \left[\frac{\alpha F}{\Re T} (\phi_s - \phi_m)|_{y=4} \right] - \exp \left[-\frac{\alpha F}{\Re T} (\phi_s - \phi_m)|_{y=4} \right] \right)$$

At the catalyst layer/membrane interface, a liquid water flux is specified. This flux is due to the electro-osmotic force.

NOTE: THIS BOUNDARY CONDITION IS EMPLOYED FOR SINGLE PHASE MODEL ONLY FOR THE MULTI-PHASE MODEL THE FLUX AT ($Y = 4$) IS EQUAL TO ZERO

- $\vec{n} \cdot (\nabla Y_{H_2O})|_{\text{At all other boundaries}} = 0$

The symmetry boundary condition is used at all other boundaries.

- $S|_{\text{At the inlet of channels 1,2 \& 3}} = 0$

The effective saturation is specified at the gas diffusion layer/Channel 1, 2 and 3 interfaces.

- $\vec{n} \cdot (D_c \nabla S)|_{y=4} = \frac{n_d i|_{y=4} \tilde{M}_{H_2O}}{F \rho_l S \varepsilon_{CL}}$

$$i|_{y=4} = (1 - S) i_o^{\text{ref}} \left(\frac{C_{O_2}}{C_{O_2}^{\text{ref}}} \right)^{\gamma_{O_2}} \cdot \left(\exp \left[\frac{\alpha F}{\Re T} (\phi_s - \phi_m)|_{y=4} \right] - \exp \left[-\frac{\alpha F}{\Re T} (\phi_s - \phi_m)|_{y=4} \right] \right)$$

At the catalyst layer/membrane interface, a liquid water flux is specified. This flux is due to the electro-osmotic force.

- $\vec{n} \cdot (\nabla S)|_{\text{At all other boundaries}} = 0$

The symmetry boundary condition is employed at all the other boundary conditions.

- $T|_{y=0} = T_o$

At the bipolar plate boundary, the temperature is specified to some temperature. In this case,

T_o is equal to 353 K.

- $\vec{n} \cdot (k^{\text{eff}} \nabla T) \big|_{\text{solid side}} = h_T (T_o|_{\text{channel side}} - T|_{\text{solid side}})$

This boundary condition is applied to all the gas channel boundaries. It represents the convective heat transfer from the gas in the channel. h_T is the convective heat transfer coefficient, which can be derived from the Nusselt number correlation [63] given by $Nu \equiv \frac{h_T d_h}{k_i} = 3.61$.

- $\vec{n} \cdot (\nabla T) \big|_{\text{At all other boundaries}} = 0$

Thermal insulation boundary condition is applied to the remaining boundaries.

3.7 Parameters

For a comprehensive discussion of the results, it is crucial to state the parameters used. A study conducted by Tao et al. [80] and Min et al. [81] showed that there are 11 major parameters that can affect the results and they vary from one study to another. A sensitivity analysis showed that the parameters on the cathode side have a stronger influence on the overall cell performance. Therefore, this section is designed to give a detailed description of the parameters used to solve the mathematical models described in sections 3.4 and 3.5.

The electrolyte conductivity is dependant on the activity of water inside the catalyst layer [28].

$$\sigma_m = -100 \exp \left[1268 \left(\frac{1}{303} - \frac{1}{T} \right) \right] [0.00326 - 0.005139\lambda] \quad (3.74)$$

$$\lambda = 0.3 + 6a [1 - \tanh(a - 0.5)] + 3.9\sqrt{a} \left[1 + \tanh \left(\frac{a - 0.89}{0.23} \right) \right] \quad (3.75)$$

$$a = \frac{x_{H_2O} P}{P_{sat}} \quad (3.76)$$

The electro-osmotic drag coefficient of water molecules through the electrolyte membrane is

CHAPTER 3. MODEL FORMULATION

also dependent on the water activity [82, 83].

$$n_d = \begin{cases} 1.0 & \text{if } \lambda < 9 \\ 0.117\lambda - 0.053 & \text{if } \lambda \geq 9 \end{cases} \quad (3.77)$$

The reference exchange current density is obtained using the following correlation [84],

$$\log_{10}(i_o^{\text{ref}}) = 3.507 - \frac{4001}{T} \quad (3.78)$$

Water diffusion through the electrolyte in m^2/s is found using the following correlation [85],

$$D_{l-m} = 4.1 \times 10^{-10} \left(\frac{\lambda}{0.25} \right)^{0.15} \left[1 + \tanh \left(\frac{\lambda - 2.5}{1.4} \right) \right] \quad (3.79)$$

The operating and physical conditions are summarized in Table 3.3. These properties are used to solve the governing equations unless otherwise stated. In the results section a sensitivity analysis will be presented; thus, some of the operating and physical parameters will be varied to investigate their effects. The operating temperature and pressure were chosen as is, since it has been shown that higher operating conditions lead to better performance of the cell. An experiment done by Song et al. in [86] showed that a temperature of 80°C accompanied with high pressure gives the best performance for a wide range of operating current densities. Before studying the parameters in Table 3.3, consider Figure 3.13.

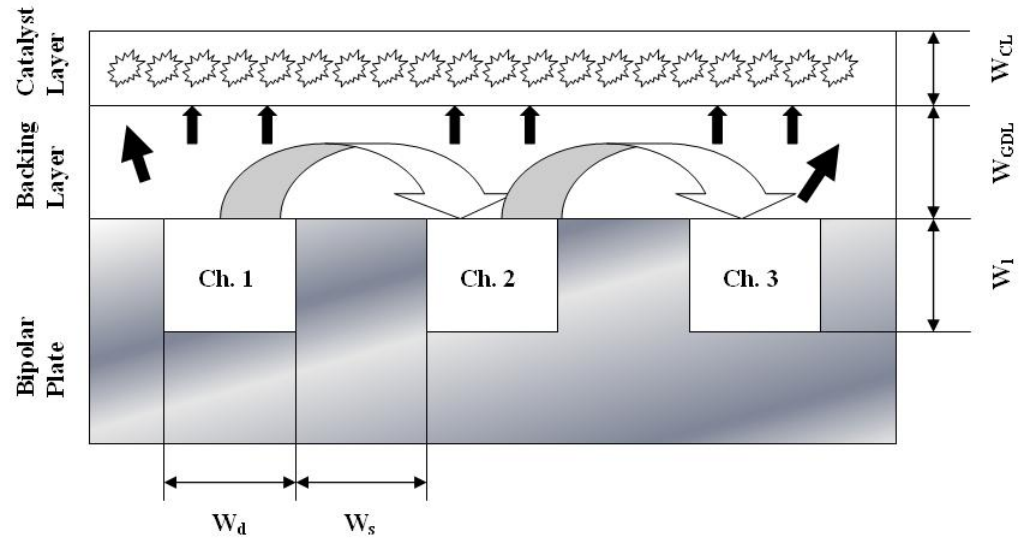


Figure 3.13: Geometry of the cathode

Thermal and physical properties needed to solve the heat transfer equation (energy equation) are given in Table 3.4.

Table 3.3: Operating and physical conditions

Parameter	Value	Unit
Operating Pressure (P)	5	atm
Operating Temperature (T)	353	K
Cell Voltage	0.7	V
Stoichiometry, (S_c)	2	
Cell Surface Area, (A)	100	cm^2
Channel Width (W_d)	1	mm
Channel Length (W_l)	1	mm
Shoulder Width (W_s)	1	mm
Gas Diffusion Layer Width (W_{GDL})	150	μm
Catalyst Layer Width (W_{CL})	5	μm
Gas Diffusion Layer Porosity (ϵ_{GDL})	0.5	
Catalyst layer Porosity (ϵ_{CL})	0.4	
Electrolyte Fraction in Catalyst Layer (ϵ_m)	0.15	
Solid Fraction in Catalyst Layer (ϵ_s)	0.3	
Permeability (κ)	5.5×10^{-11}	m^2
Electronic Conductivity (σ_s)	115	S/m
Oxygen Reference Concentration ($C_{O_2}^{ref}$)	3.38	mol/m^3
Order of Reaction (γ_{O_2})	1.0	
Minimum Saturation Level (S_r)	0.102	
Maximum Saturation Level (S_m)	0.924	
Evaporation Rate (E)	100	$atm^{-1} s^{-1}$
Condensation Rate (χ)	100	$1/s$
Displacement Pressure (P_d)	-2266.11	Pa
Pore Size Distribution (λ)	7.2	
Surface Tension (σ)	0.062	(N/m)
Contact Angle (θ_c)	100°	

Table 3.4: Thermal and physical properties of some materials @ 353 K [87][88]

	Density (kg/m^3)	Thermal conductivity ($W/m \cdot K$)	Specific heat ($J/kg \cdot K$)
Bipolar plate	1900	21	710
Electrode support (PTFE)	2200	1.3 (Ballard AvCarb [®] P150)	1050
Catalyst layer	2100	0.8725	1050
Membrane (Nafion)	1980	0.445	1050 (PTFE)
Air	0.9950	0.03	1010
Water vapor	0.632	0.023	1960
Liquid water	972	0.67	4197

Chapter 4

Numerical Method

The set of governing equations presented have been all solved using a commercial software, COMSOL Multiphysics (FEMLAB 3.2b). This chapter is designed to give some background on the commercial software and how it has been utilized in order to solve the problem at hand for this thesis.

FEMLAB is an interactive environment used for modeling and solving scientific and engineering problems based on partial differential equations. Once the user defines the modules (or in other words the engineering equations) in conjunction with the proper constants and boundary conditions, FEMLAB internally compiles a set of partial differential equations representing the problem.

The underlying mathematical structure with which FEMLAB operates is a system of partial differential equations. In FEMLAB, partial differential equations can be represented in three ways: coefficient form (suitable for linear or nearly linear problems), general form (intended for nonlinear problems), and weak form (that works as a high-level finite element modeling language).

When solving the partial differential equations that describe a model, FEMLAB applies the finite element method (FEM). FEMLAB runs that method in conjunction with adaptive meshing and error control as well as with a variety of numerical solvers.

More information regarding this software is provided through its web site at www.comsol.com.

4.1 Integrating the Math Model into COMSOL Multiphysics

In order to solve the governing equations, the built-in modules along with the coefficient PDE have been used.

- The Stefan-Maxwell equation module is used to solve for the species. The species specified are oxygen, water vapor, and nitrogen.

This module exists in two domains out of the three computational domains, gas diffusion layer and catalyst layer. It is set to inactive in the bipolar plate domain since no gaseous species' transport occurs in the plate. It is important to choose oxygen as the main species, followed by water vapor and then nitrogen. Since nitrogen is not involved in any reactions, its mass fraction is computed using the knowledge that summation of species' mass fractions would equal one.

- The AC/DC Module is employed to solve for the solid and electrolyte potentials.

Two modules are needed to solve for the potentials; one represents the solid potential while the other represents the electrolyte potential. The solid potential applies to all three domains, while the electrolyte potential has to be set as inactive in the bipolar plate and gas diffusion layer since protons do not travel through these two domains.

- The Darcy equation found under the chemical engineering module is used to solve for the gas velocities.

The Darcy equation is applied to the gas diffusion and catalyst layers, while it is set to inactive in the bipolar plate domain.

- The coefficient PDE is used to define the mass transfer of liquid water in the gas diffusion and catalyst layers and is set to inactive in the bipolar plate domain.

A numerical error occurred when solving this equation due to the capillary diffusion coefficient. The capillary diffusion coefficient is equal to zero when the effective liquid saturation is zero, recall equation 3.61. The capillary diffusion coefficient is dependent on the relative permeability of liquid water in the layers defined by equation 3.55. A constant was used in

order to fix this numerical problem. The relative permeability of liquid water was therefore changed to the following form, $\kappa_l = \underbrace{\kappa S^3}_{\kappa_{r,l}} + \tau$, where τ is a constant used to ensure convergence when the effective saturation is equal to zero. A value of 0.01 was first chosen for τ to compute the saturation in the layers. The value was then decreased to ensure that it did not have any effect on the final result. It was seen that the solution becomes independent of τ with a value of 1×10^{-6} . A similar approach was taken by Vynnycky [89].

- The energy equation found under the chemical module is used to define the heat transfer in the cell.

In order to be able to apply the convective heat transfer from the channel to the surrounding solid areas, the conduction module has to be used. Thus, to incorporate the convection term in the energy equation, a source term is used. The source term defines the transfer of heat through convection in the gas diffusion and catalyst layers. It is defined as the velocity times the gradient of temperature.

4.2 Inputs

There are many ways of inputting necessary information into FEMLab. The constants option was used to define all the physical and thermal parameters given in Tables 3.3 and 3.4. Each parameter was given a name and a corresponding value. This option is very useful if the parameter does not change in value with the change of one of the unknown variables.

The domain expressions option was used to define the expressions that are dependent on the variables solved by the governing equations. Some of these expressions include the rate of reaction, relative humidity (water activity), saturation pressure, interaction of liquid water and vapor water, electrolyte conductivity, capillary pressure, and relative gas and liquid permeability.

The boundary expressions option was used to define the boundary expressions dependent on the variables being solved. Some of these expressions include the electro-osmotic drag coefficient, the local current density and the inlet mass fraction of water vapor.

Finally, the user interface provided by the software enables the user to indicate the boundary

condition at each boundary. The boundary conditions listed earlier in section 3.6, were specified at each corresponding boundary.

4.3 Validation of the Model

The validation of the numerical model is important since the results of this thesis are dependent on it. The numerical model in this thesis is used to solve the half cell of a PEM fuel cell. In the PEM fuel cell field, experiments are normally done on the entire cell. Thus, available experimental data is of the performance of the entire cell. Normally, the polarization curve is used to verify that a numerical model is correct.

For the purpose of this thesis, the verification of the COMSOL Multiphysics is used to verify the numerical model since the governing equations are all solved using the built-in modules. Thus, it is important to verify that the software is correctly assigning and solving the matrices. The verification is carried out as follows,

1. First, each term in the built-in modules is verified. Let us take the Stefan-Maxwell equation module as an example. In this module, there exists a diffusion term, a convection term and a source term. First the diffusion term is turned on while the convection and source terms are turn off. This is done to ensure that the diffusion term is working properly. It is seen that the transport of species is purely due to diffusion and there exists no sink source since the reaction (source) term does not exist at this moment. Then, the convection term is turned on while keeping the source term off. For this test, two velocity gradients are used, a zero velocity gradient and a velocity gradient of 1 (m/s). Remember in PEM fuel cells the velocity gradient is in the laminar region. This test was done to ensure that the convection term is working. It is important to test this term since a part of this thesis covers the effects of the velocity gradient on the species' transport. Finally, a sink source is added. A positive, negative and a zero source terms are used to ensure that the source term is working properly. Finally, similar tests are done on the boundary conditions to ensure that a proper solution is obtained. All the tests mentioned above were carried out for all the built-in modules.

2. The second stage of verification was to find some numerical models of a full PEM fuel cell, which use COMSOL Multiphysics. Ziegler et al. [90] created a model for planar self-breathing PEM fuel cells using COMSOL Multiphysics. They solved the transport of mass and heat in the full cell (anode, cathode and membrane) using the built-in modules in the software. They were able to solve for the three kinds of polarization overpotential described earlier in the introduction section. Activation, ohmic and concentration polarization overpotential. Thus, they created a polarization curve and were able to validate their curve with that of experimental data. They found very close agreement between the model and the experimental data. Consequently, it can be said that COMSOL Multiphysics is capable of solving the governing equations of a PEM fuel cell system. In addition, Wu [91] used COMSOL Multiphysics to solve a two and three dimensional models of a full PEM fuel cell for his masters thesis. He solved the mass and heat transfer in the cell. He was then able to validate the resultant polarization curve to that of experimental data and found a good agreement between the numerical model and the experimental model. Again, this shows that COMSOL Multiphysics is capable of solving a PEM fuel cell system.
3. To ensure the proper formulation of solution matrices using the specified boundaries, boundary conditions were imposed on multiple boundaries.

4.4 Meshing and Grid Independency

The mesh type used is a non-uniform, triangular mesh. The element size in the gas diffusion and catalyst layers is refined to 1/10 of the layers' thickness. At the channel inlet boundaries, the mesh size is further decreased. This decrease is necessary in order to ensure the convergence of the solution. In the bipolar plate, the solution is independent of the mesh size since the thickness of the plate is very big compared to that of the gas diffusion and catalyst layers. In order to ensure that the solution is grid independent, 88332 elements were used. Analysis was carried out in order to study the effect of decreasing element number on the solution. Figure 4.1 is constructed to show the relation between the error and the number of meshing elements. The error was tabulated using

equation 4.1.

$$\text{error} = \frac{|J_{2N} - J|}{J_{2N}} \times 100\% \quad (4.1)$$

where J_{2N} is the current density when the number elements is doubled.

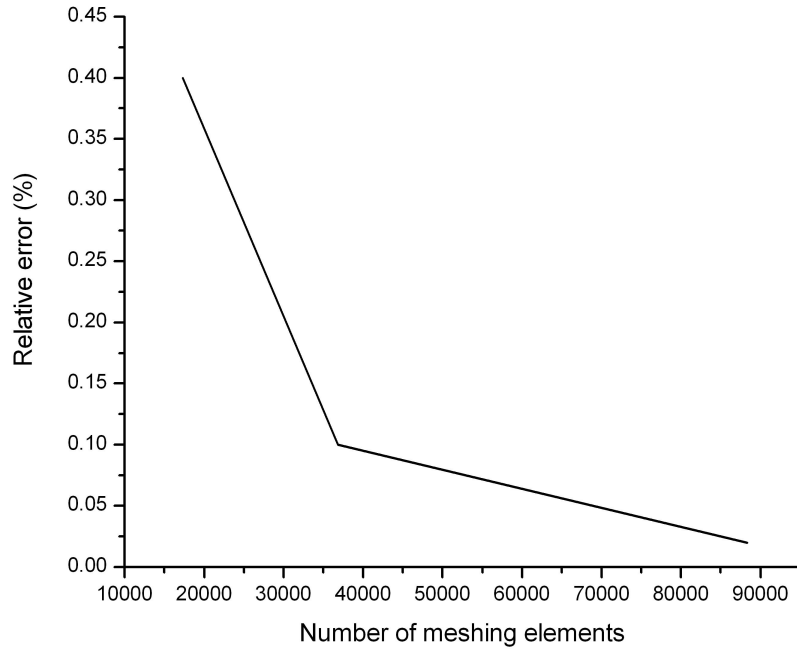


Figure 4.1: Error in the average current density vs. the number of meshing elements

Chapter 5

Isothermal Model Results

The discussion of this chapter deals with the results based on the assumption that the fuel cell is isothermal (temperature does not change throughout the computational domain); hence, the energy equation can be omitted and is not solved for. The first three sections in this chapter are dedicated to studying species transport and the electrochemical reaction in the cell. Detailed analysis will be conducted on the single phase and multi-phase models in the first two sections and then a comparison of the two models will be put forward. The last section of this chapter deals with a sensitivity analysis using the multi-phase, isothermal model. The effect of inlet relative humidity, pressure drop, permeability of layers and shoulder(land)/channel width ratio will be investigated. It is necessary to note here that the words shoulder and land will be used interchangeably in the later sections. They both describe the same area, which is the area between two adjacent channels. To better understand the results, recall the modeling domain, which is shown in Figure 5.1

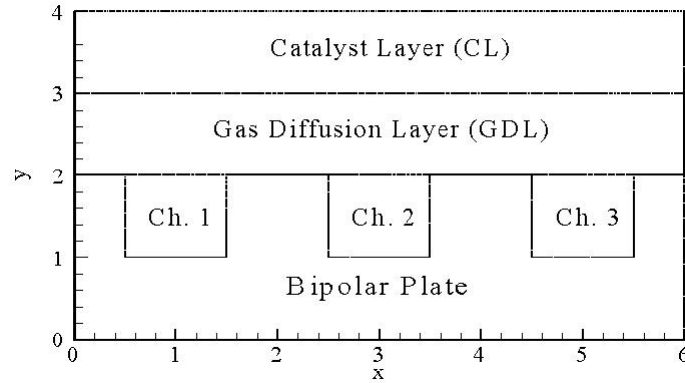


Figure 5.1: Modeling Domain - x and y axes have been normalized - flow is in the y -direction ($(0 \leq x \leq 6)$ denotes a distance of 6 mm , $(0 \leq y \leq 2)$ denotes a distance of 2 mm , $(2 \leq y \leq 3)$ denotes a distance of $150 \mu\text{m}$ and $(3 \leq y \leq 4)$ denotes a distance of $5 \mu\text{m}$)

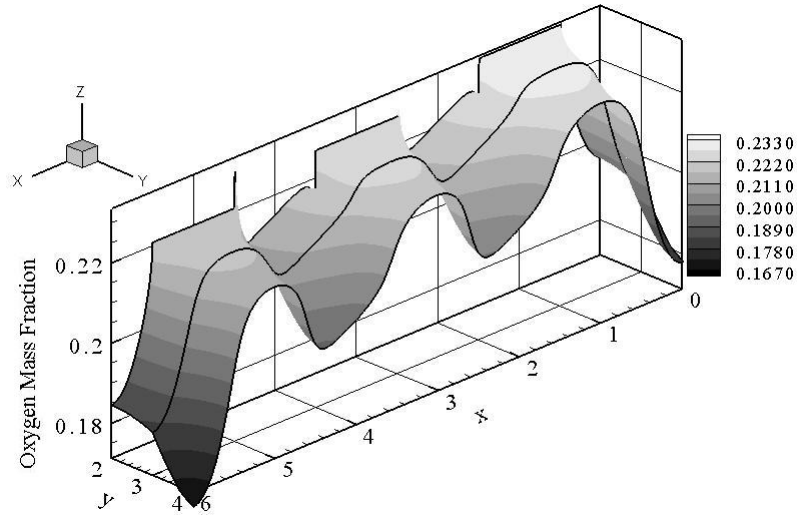
5.1 Single Phase Model Results

In this section, the results of the single phase model are put forward. The results discussed are based on an inlet relative humidity of 100%, a pressure drop of 349 Pa along the channel flow field, a gas diffusion and catalyst layers permeability of $5.5 \times 10^{-11} \text{ m}^2$, the gas temperature is 80°C and the operating pressure is 5 atm.

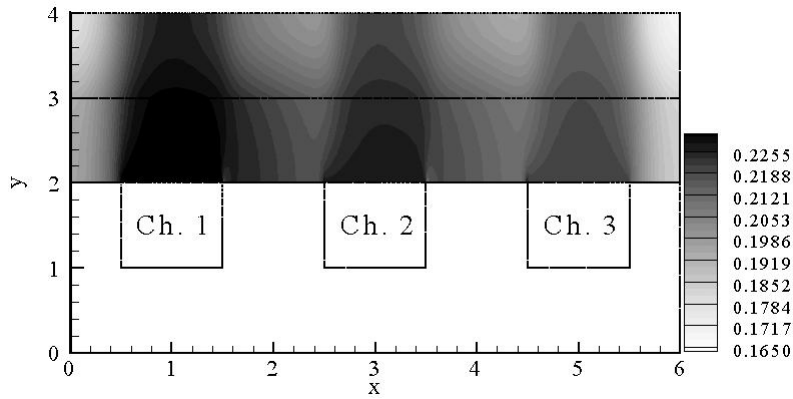
The distribution of oxygen concentration in the backing and catalyst layers is used to show how the reactant is transported and to understand the reaction mechanism in the catalyst layer. The distribution of oxygen mass fraction in the GDL and CL is shown in Figure 5.2. Due to the pressure drop along the channel flow field, the cross flow of oxygen is apparent. The transport of oxygen through the GDL is very much enhanced. Further, it is important to notice the reduction in oxygen mass fraction at the land on the left of channel 1 and on the right of channel 3. This occurs since there is no cross flow at these two locations. The mass fraction decrease is also seen between channels; there is a concentration drop as mentioned earlier in section 3.2. Finally, the other important piece of information provided by the mass fraction distribution is the reaction location. It is seen that the distribution is very much two-dimensional. In the x -direction, it is apparent that there is a variation in the concentration of oxygen. It is higher under the channel areas than under

CHAPTER 5. ISOTHERMAL MODEL RESULTS

the land areas. This implies that more reaction takes place under the land areas. In addition, the variation in the y -direction is seen. The concentration of oxygen decreases along the thickness of the catalyst layer. It is seen that the concentration is lower at the catalyst layer/membrane interface ($y = 4$) than at the gas diffusion layer/catalyst layer interface ($y = 3$); reaction is higher at ($y = 4$).



(a)



(b) Oxygen mass fraction

Figure 5.2: (a) 3-D surface plot of oxygen mass fraction in the gas diffusion and catalyst layers. Note that $y = 4$ is the catalyst layer/membrane interface; (b) Distribution of oxygen mass fraction in the gas diffusion and catalyst layers for the single phase model. x and y coordinates have been normalized for better presentation of results (see Figure 5.1)

CHAPTER 5. ISOTHERMAL MODEL RESULTS

In order to better explain the cross flow phenomenon, the velocity distribution at different cross sections in the gas diffusion and catalyst layers should be examined. Figures 5.3 and 5.4 show the velocity distribution at different cross sections in the gas diffusion and catalyst layers, respectively. It is apparent that the magnitude of the velocity decreases along the layers' thickness. This implies that transport limitations and losses exist in the cell. Another interesting observation is the x-component of the velocity. In the gas diffusion layer, the x-component of the velocity changes in magnitude and shape along the thickness. It is much different in the catalyst layer, where the magnitude and shape of the x-component is the same along the thickness. The y-component is the main contributor to the convective flux of species towards the reaction site in both layers, whereas, the x-component of the velocity is the main contributor to the convective flux of species from one channel to the adjacent channel. In other words, the x-component of the velocity vector is the driving force for the cross flow phenomenon and is the main determinant of its magnitude. From Figures 5.3 and 5.4, it is clear that convection plays a more significant part in transporting species in the gas diffusion layer. Diffusion is the more dominant means of species transport in the catalyst layer. Thus, the overall species transport is much faster in the gas diffusion layer. Further, from the velocity figures, it can be expected that the product removal from the gas diffusion will be enhanced due to the leakage between channels. Water will be transported from the gas diffusion layer to the channel flow fields more effectively due to the cross flow phenomenon.

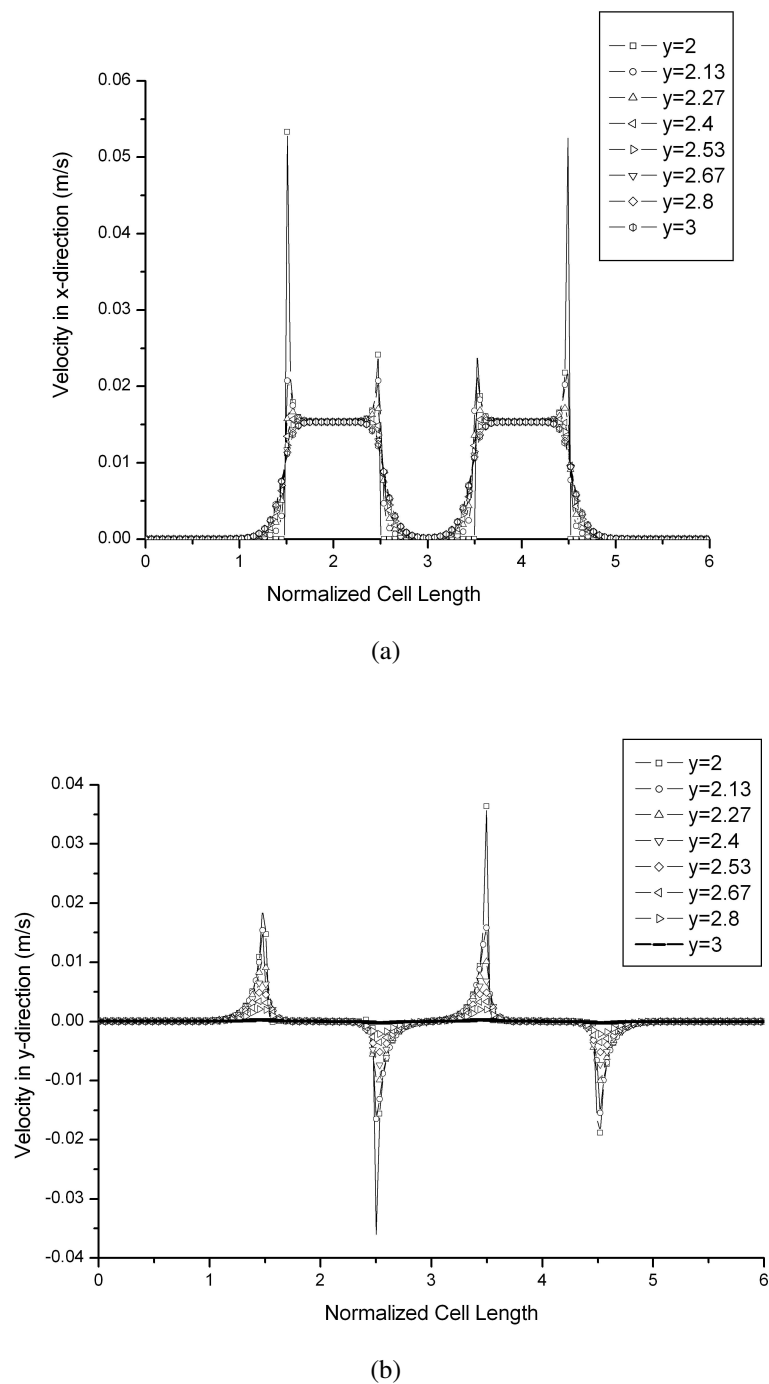


Figure 5.3: Velocity distribution in the gas diffusion layer at different points along the gas diffusion layer thickness (m/s) (a) x-component; (b) y-component

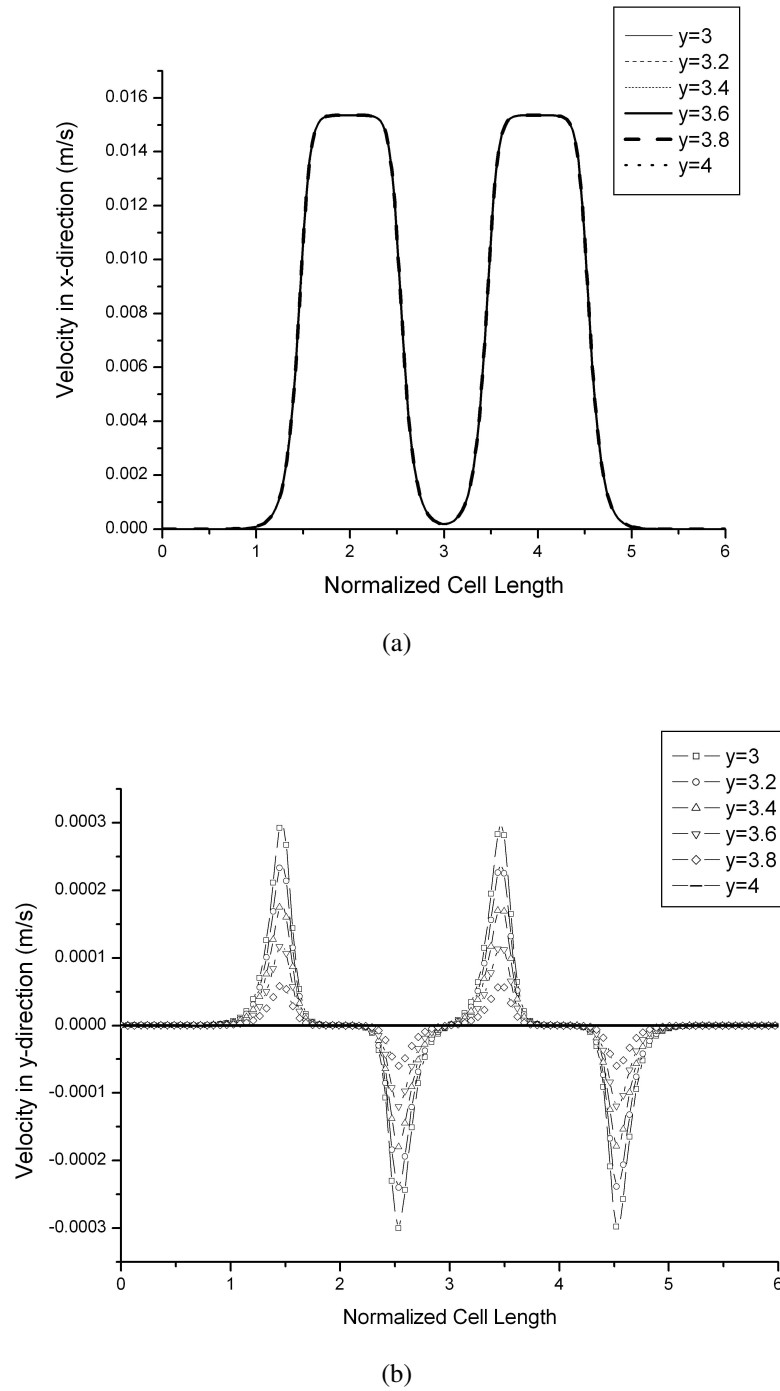


Figure 5.4: Velocity distribution in the catalyst layer at different points along the catalyst layer thickness (m/s) (a) x-component; (b) y-component

CHAPTER 5. ISOTHERMAL MODEL RESULTS

Further to explain the distribution of the oxygen concentration in the catalyst layer it is necessary to investigate the rate of reaction. Figure 5.5 shows the two-dimensional distribution of the rate of oxygen consumption in the catalyst layer. It is apparent that the rate of reaction is at its highest value under the land area and at the catalyst layer/membrane interface. In addition, it increases along the catalyst layer thickness explaining the increased consumption rate of oxygen. This piece of information suggests that future enhancements of the catalyst layer should be focused on the area closest to the membrane.

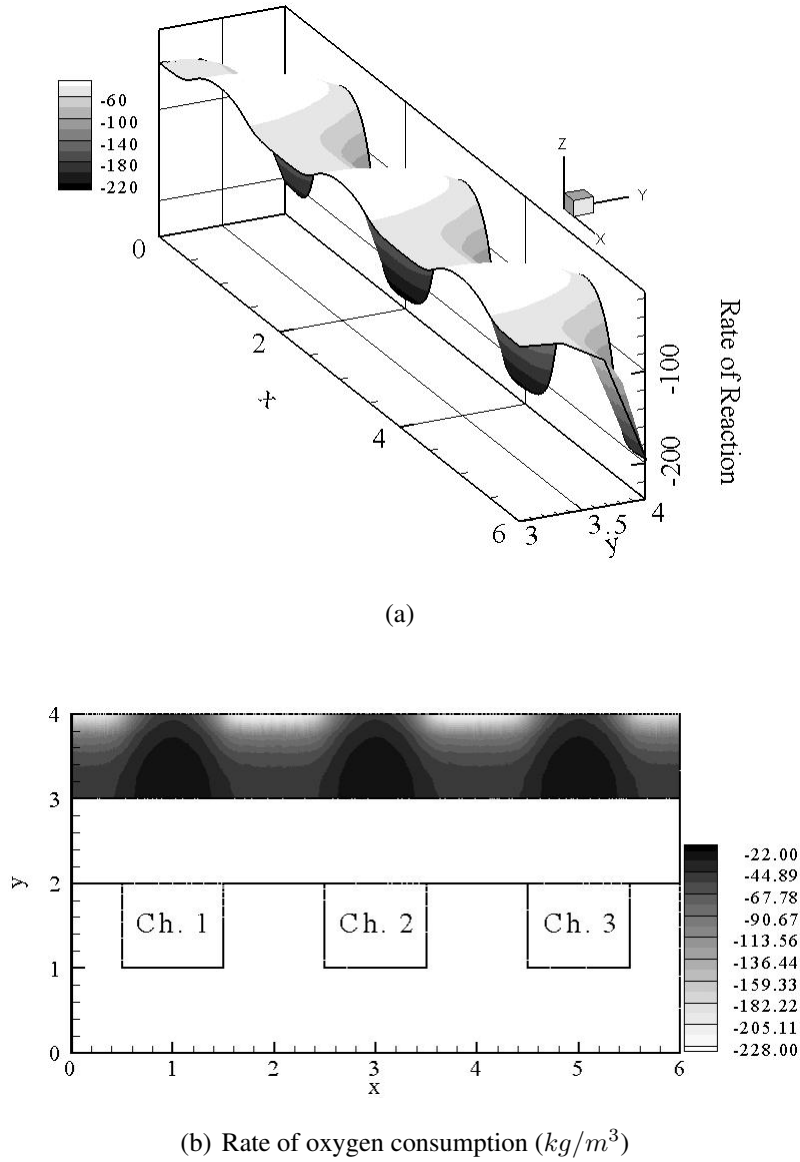


Figure 5.5: (a) 3-D surface plot of oxygen consumption rate in the catalyst layer. Note that $y = 4$ is the catalyst layer/membrane interface; (b) Rate of oxygen consumption in the catalyst layer (kg/m^3) for the single phase model. x and y coordinates have been normalized for better presentation of results. (see Figure 5.1)

CHAPTER 5. ISOTHERMAL MODEL RESULTS

It is interesting to note that even though oxygen is readily available under the channel areas, the consumption rate is lower at those areas. This trend can be explained by simply examining the Butler-Volmer equation in equation 3.29. From this equation it is seen that the rate of reaction is dependent not only on the mass fraction of oxygen but also on the cathode over-potential. Unlike its linear relationship with the oxygen mass fraction, the reaction rate has an exponential relationship with the over-potential. This implies that any small variation of the over-potential in the catalyst layer will highly influence the rate of reaction. In order to explain the distribution of the reaction rate in the catalyst layer, the cathode over-potential in the catalyst layer should be observed and is shown in Figure 5.6.

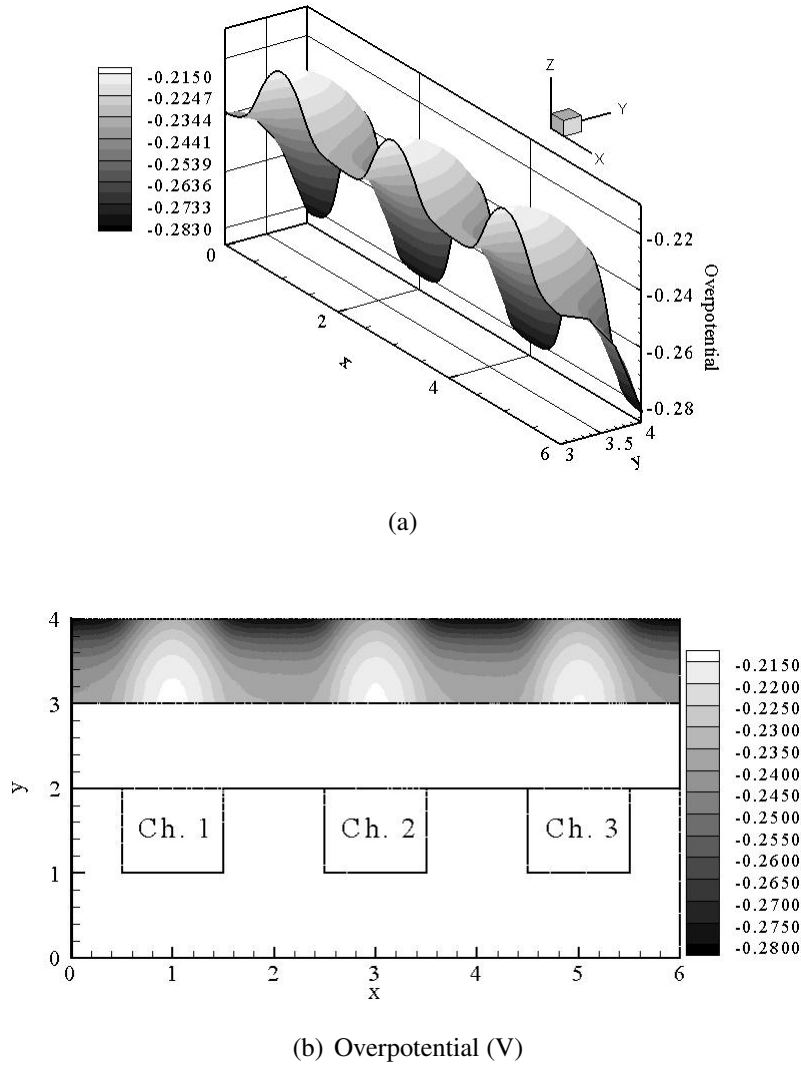


Figure 5.6: (a) 3-D surface plot of overpotential in the catalyst layer. Note that $y = 4$ is the catalyst layer/membrane interface; (b) Overpotential in the catalyst layer (V) for the single phase model. x and y coordinates have been normalized for better presentation of results. (see Figure 5.1)

The over-potential is a result of the transfer of electrons and protons. It is the energy required for the reaction to proceed and it is equal to the difference between the electronic (solid) potential and protonic (electrolyte) potential, $\eta_c = \phi_s - \phi_m$. Thus, it is important to investigate the two potentials.

The solid potential exists in the bipolar plate and gas diffusion and catalyst layers. Electrons are transported to the cathode bipolar plate via the external electric circuit, they then travel through

the solid phase in the backing layer in order to reach the reaction sites in the catalyst layer. Electrons do not travel in the channel since they need a solid phase as means of their transportation. Figure 5.7 is a visual representation of the path taken by the electrons once they enter the cathode from the electric circuit. The distribution of the solid potential is shown in Figures 5.8 and 5.9. Figure 5.8 gives a two-dimensional surface representation of the solid potential in the three modeling domains, while Figure 5.9 is a 3-D surface plot of the solid potential in the three modeling domains. Figure 5.8(a) shows the overall distribution of the solid potential in the cathode, while Figures 5.8(b), 5.8(c) and 5.8(d) show the distribution of the solid potential in the bipolar plate, gas diffusion layer, catalyst layer, respectively. The decrease of solid potential in the bipolar plate is very low due to the high electric conductivity of the plate. The potential drop is higher in the gas diffusion and catalyst layers. Further examination of the distribution of the solid potential shows that the potential is higher under the land area than under the channel. This can be explained by the path the electrons need to travel. Since they do not travel through the channel, they need to travel a longer distance to reach the areas under the channel.

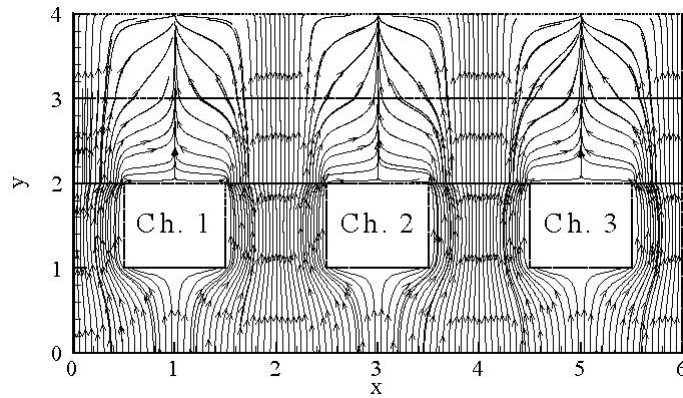
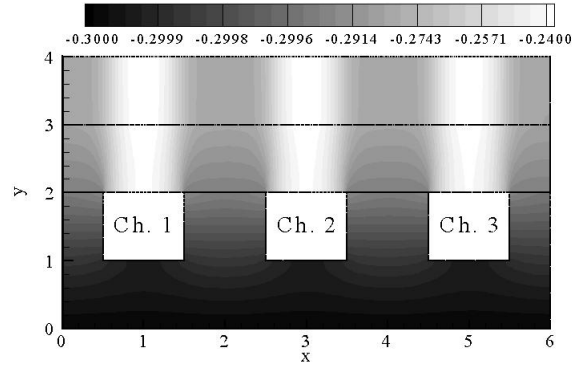
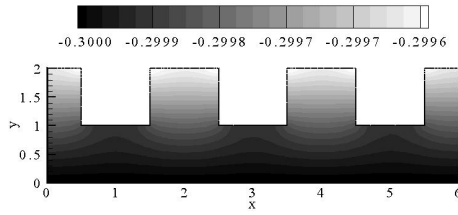


Figure 5.7: Streamline plot of the path taken by the electrons in the bipolar plate, gas diffusion and catalyst layers. x and y coordinates have been normalized for better presentation of results. (see Figure 5.1)

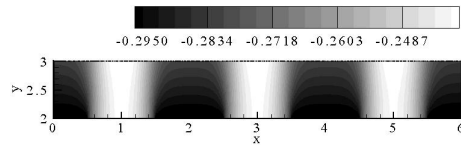
CHAPTER 5. ISOTHERMAL MODEL RESULTS



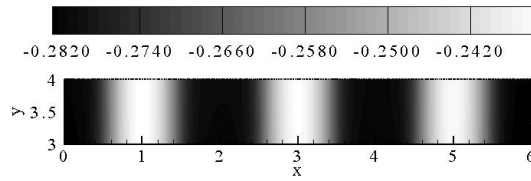
(a) Solid potential (V)



(b) Solid potential in bipolar plate (V)



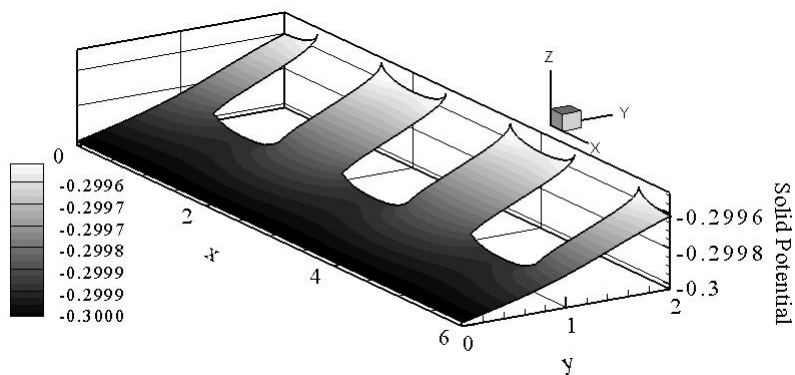
(c) Solid potential in GDL (V)



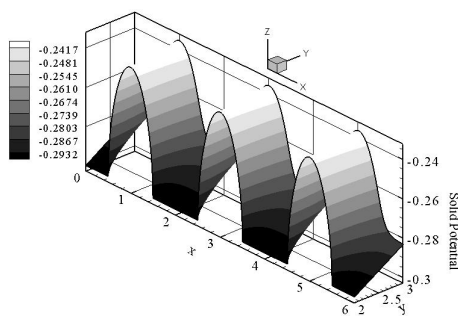
(d) Solid potential in CL (V)

Figure 5.8: Solid potential (V) distribution in the (a) cathode; (b) bipolar plate; (c) gas diffusion layer; (d) catalyst layer for the single phase model. x and y coordinates have been normalized for better presentation of results. (see Figure 5.1)

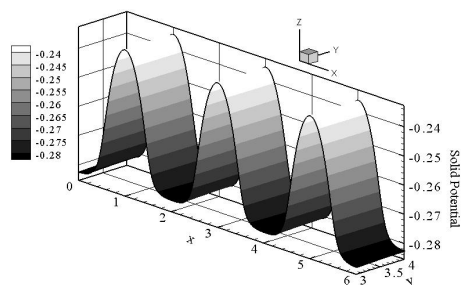
CHAPTER 5. ISOTHERMAL MODEL RESULTS



(a)



(b)



(c)

Figure 5.9: 3-D surface plot of the solid potential in the (a) bipolar plate; (b) gas diffusion layer; (c) catalyst layer.

CHAPTER 5. ISOTHERMAL MODEL RESULTS

The losses that occur in the solid potential can be better explained by the examination of the solid current density. Figure 5.10 shows the distribution of the solid current density in the x and y directions, respectively. The current density is a vector quantity. Only the component in the y-direction (width of the catalyst layer) is useful. It contributes to the power output of the cell while the x-direction (length of the cell) component contributes to the losses of the cell and should be minimized. Examination of the current density in the x-direction demonstrates that losses due to electron transfer occur in the gas diffusion and catalyst layers and specifically in the areas under the channel. This is seen again in the behavior of the current density in the y-direction. In addition, it can be seen that there is a current build-up around the channel edges. This can be explained by the sharp edges of the channel. Therefore, a study should be put forward to examine the channel geometry and its effects.

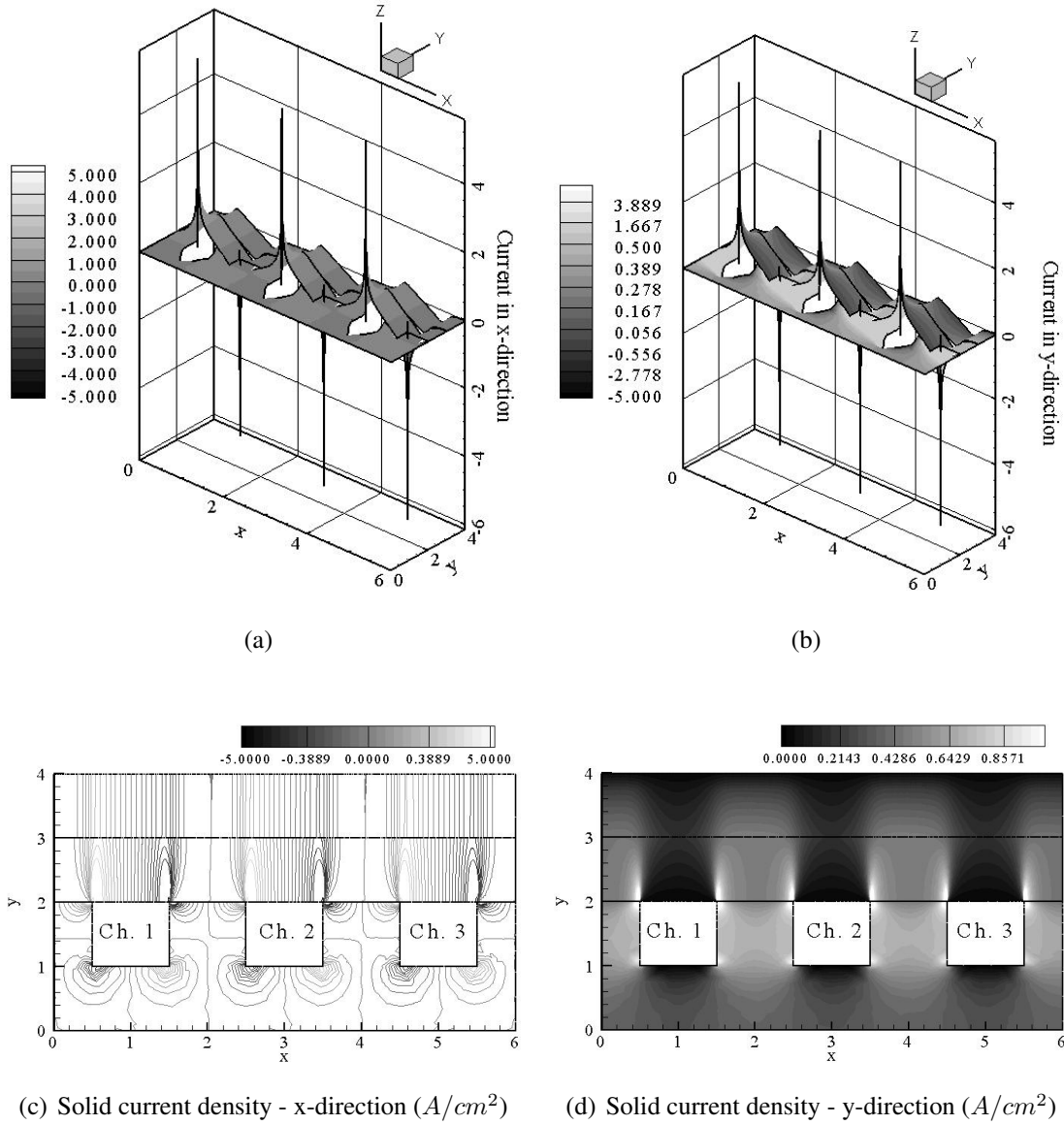


Figure 5.10: 3-D surface plot of the solid potential current density in the bipolar plate and gas diffusion and catalyst layers in the (a) x-direction; (b) y-direction. Solid potential current density (A/cm^2) in the (c) x-direction; (d) y-direction for the single phase model. x and y coordinates have been normalized for better presentation of results. (see Figure 5.1)

CHAPTER 5. ISOTHERMAL MODEL RESULTS

The proton transfer contributes to the electrolyte potential which is the other piece of the puzzle that affects the behavior of the over-potential. Protons travel through the electrolyte membrane to reach the reaction site in the catalyst layer. The electrolyte potential is shown in Figure 5.11. The electrolyte potential increases along the catalyst layer thickness from the membrane interface to the GDL interface. This is expected since the over-potential decreases from the membrane interface to the GDL interface.

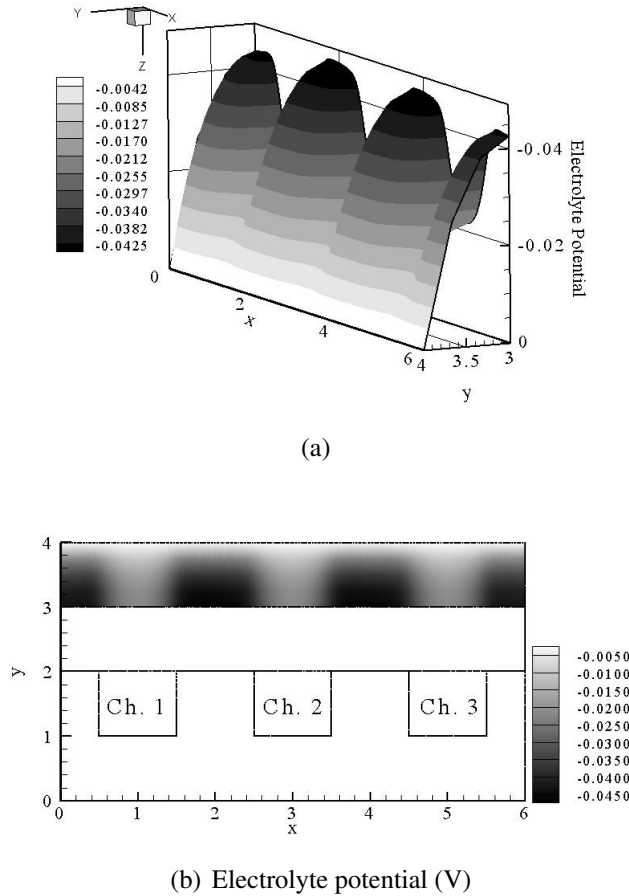


Figure 5.11: (a) 3-D surface plot of electrolyte potential in the catalyst layer. Note that $y = 4$ is the catalyst layer/membrane interface; (b) Electrolyte potential (V) distribution in the catalyst layer for the single phase model. x and y coordinates have been normalized for better presentation of results. (see Figure 5.1)

CHAPTER 5. ISOTHERMAL MODEL RESULTS

Similarly, current is generated due to the transfer of protons through the catalyst layer. The electrolyte current density distribution is also a two-dimensional distribution with x and y components, which are shown in Figure 5.12. It is seen here that the useful current (y-component) has its highest value at the catalyst layer/membrane interface. The consumption of protons, in other words the reaction, is higher around the catalyst layer/membrane interface. In addition, it is apparent that the losses due to proton transfer are much smaller than the losses due to the electron transfer. This is shown through the x-component of the electrolyte current density.

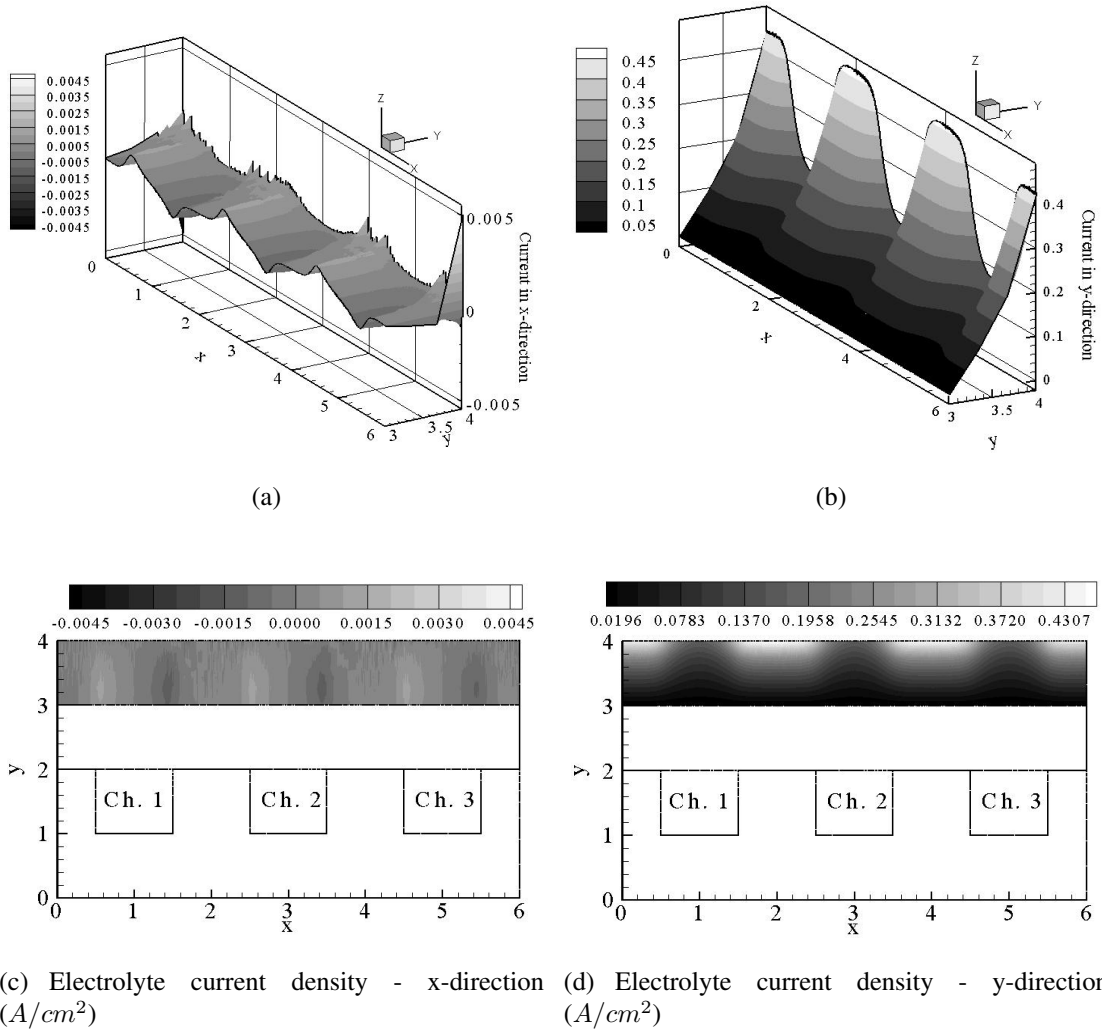


Figure 5.12: 3-D surface plot of the electrolyte potential current density in the catalyst layer in the (a) x-direction; (b) y-direction. Electrolyte potential current density (A/cm^2) in the (c) x-direction; (d) y-direction for the single phase model. x and y coordinates have been normalized for better presentation of results. (see Figure 5.1)

CHAPTER 5. ISOTHERMAL MODEL RESULTS

Finally, it is very important to study the relative humidity in the gas diffusion and catalyst layers to understand the behavior of water transport in the fuel cell. The relative humidity can be calculated from the properties of the mixture. It is the ratio of the partial pressure of water vapor and the saturation pressure of water at a given temperature. The ratio is defined as follows,

$$RH = \frac{P_{H_2O}}{P_{sat}(T)} \quad (5.1)$$

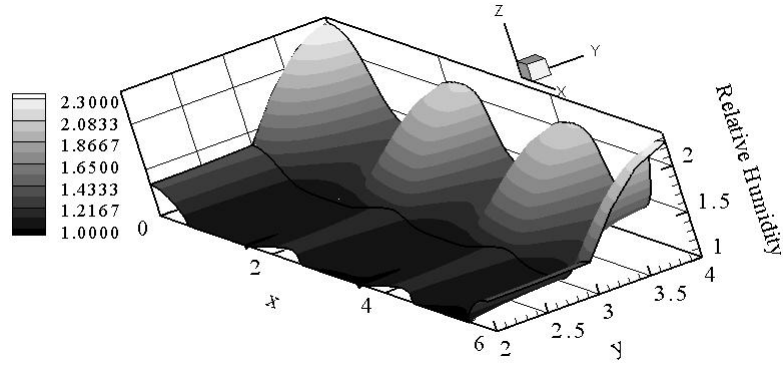
The partial pressure of water vapor is simply the product of the molar fraction of water vapor and the total pressure of the gas mixture and is obtained as follows,

$$P_{H_2O} = x_{H_2O} P_g \quad (5.2)$$

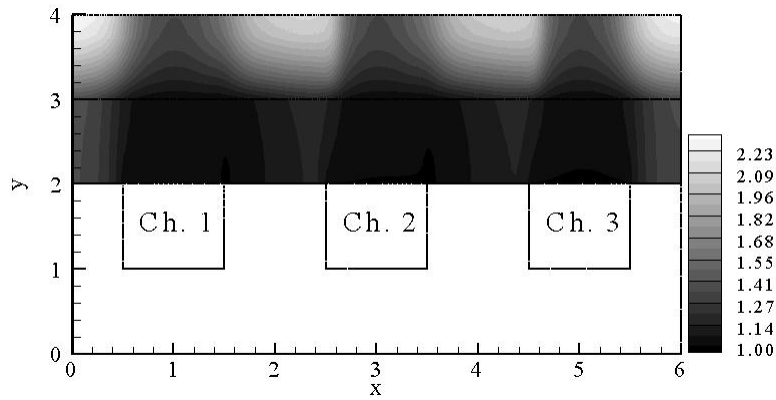
$$x_{H_2O} = \frac{\frac{Y_{H_2O}}{\bar{M}_{H_2O}}}{\frac{Y_{H_2O}}{\bar{M}_{H_2O}} + \frac{Y_{O_2}}{\bar{M}_{O_2}} + \frac{Y_{N_2}}{\bar{M}_{N_2}}} \quad (5.3)$$

The relative humidity can be used as a qualitative measure to know whether water will condense or evaporate. A relative humidity higher than 100% implies that water has to condense and liquid water will be present, while a relative humidity smaller than 100% indicates that any liquid water present will evaporate. The presence of inert gases in the mixture, in a strict sense, changes the saturation pressure of water by a very small amount, which is less than 1% for conditions typically encountered in fuel cell operation and thus negligible in engineering calculations [25]. In addition, the saturation pressure for this part of the study is assumed to be constant since the fuel cell is assumed to be isothermal.

With the assumption that water is in the vapor state only and the inlet relative humidity is 100%, it is expected that the relative humidity will be above 100% due to water production as seen in Figure 5.13. In addition, the cross flow phenomenon is very apparent. The cross flow helps with the water removal from the cell.



(a)



(b) Relative humidity

Figure 5.13: (a) 3-D surface plot of relative humidity in the gas diffusion and catalyst layers. Note that $y = 4$ is the catalyst layer/membrane interface; (b) Relative humidity (or water vapor) in the gas diffusion and catalyst layers for the single phase model. x and y coordinates have been normalized for better presentation of results. (see Figure 5.1)

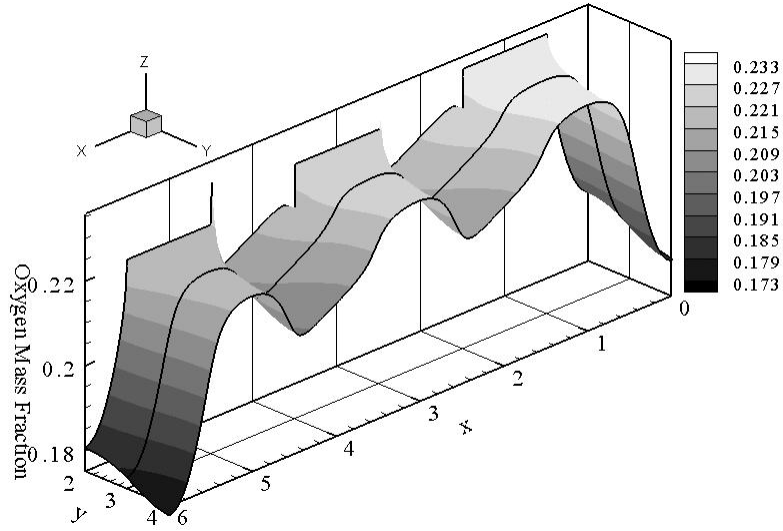
5.2 Multi-Phase Model Results

The discussion of the single phase model given earlier raises the need for the consideration of liquid water (i.e. the introduction of a multi-phase model). It was concluded that with the production of water, the relative humidity in the gas diffusion and catalyst layers will be higher than 1. This section is designed to discuss the results of the multi-phase isothermal model. In order to be able to make a coherent comparison between the single phase and multi-phase models, the

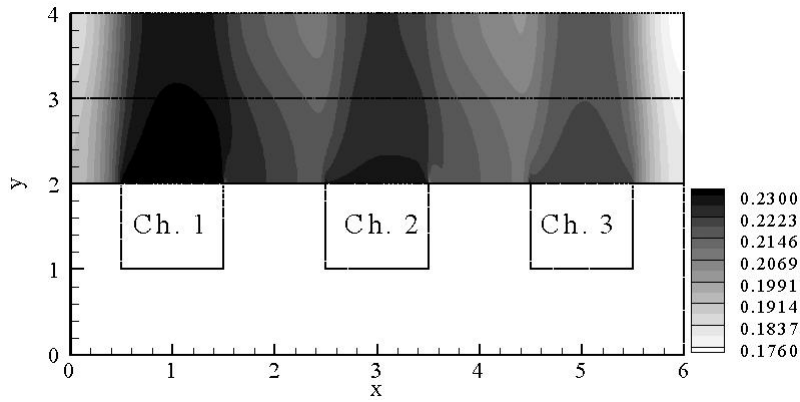
CHAPTER 5. ISOTHERMAL MODEL RESULTS

results discussed in this section are based on an inlet relative humidity of 100%, a pressure drop of 349Pa along the channel flow field, a permeability of $5.5 \times 10^{-11}\text{m}^2$ for the backing and catalyst layers and operating conditions of 80°C and 5atm . Further, the case presented in this section is considered as the base case to be compared to all the other cases presented in later sections. The Leverette function is used to describe the capillary pressure in the backing and catalyst layers. The gas diffusion and catalyst layers are assumed to be hydrophobic media.

The oxygen mass fraction, concentration, in the backing and catalyst layers for the multi-phase model is shown in Figure 5.14. The profile of the oxygen distribution in the backing and catalyst layers is two-dimensional and similar to that of the single phase model. The oxygen concentration decreases along the catalyst layer thickness since its rate of consumption is increasing. Further, the oxygen concentration in the areas under the channel is higher than those under the land. Oxygen is readily supplied to the areas under the channel.



(a)

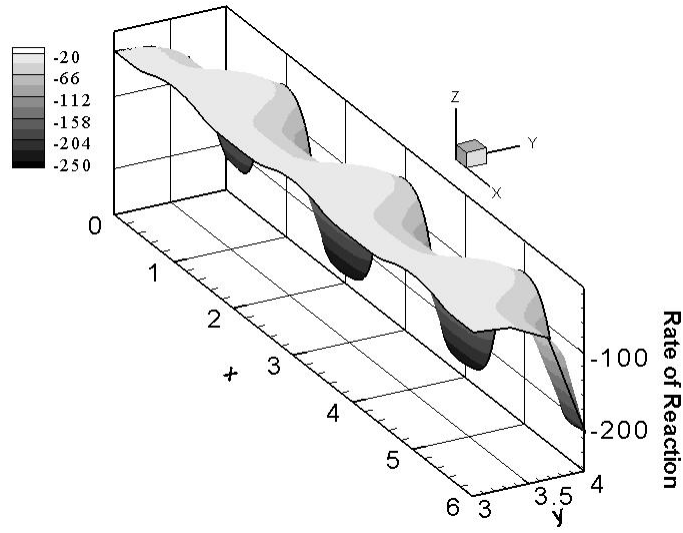


(b) Oxygen mass fraction

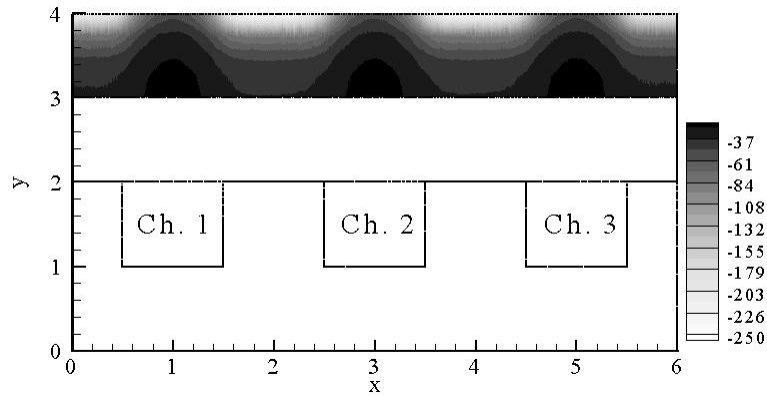
Figure 5.14: (a) 3-D surface plot of oxygen mass fraction for the multi-phase model. Note $y = 4$ is the catalyst layer/membrane interface; (b) Contour plot of oxygen mass fraction profile in the gas diffusion and catalyst layers for the multi-phase model. x and y coordinates have been normalized for better presentation of results. (see Figure 5.1)

CHAPTER 5. ISOTHERMAL MODEL RESULTS

As mentioned earlier, the oxygen distribution in the catalyst layer is not only dependent on the rate of transport of oxygen in the gas diffusion layer but it is also highly dependent on the rate of reaction occurring in the catalyst layer. The two-dimensional distribution of the reaction rate in the catalyst layer for the multi-phase model is shown in Figure 5.15. The trend seen here is similar to that of the single phase model. It is higher under the land areas. In addition, the consumption appears to happen closer to the catalyst layer/membrane interface.



(a)



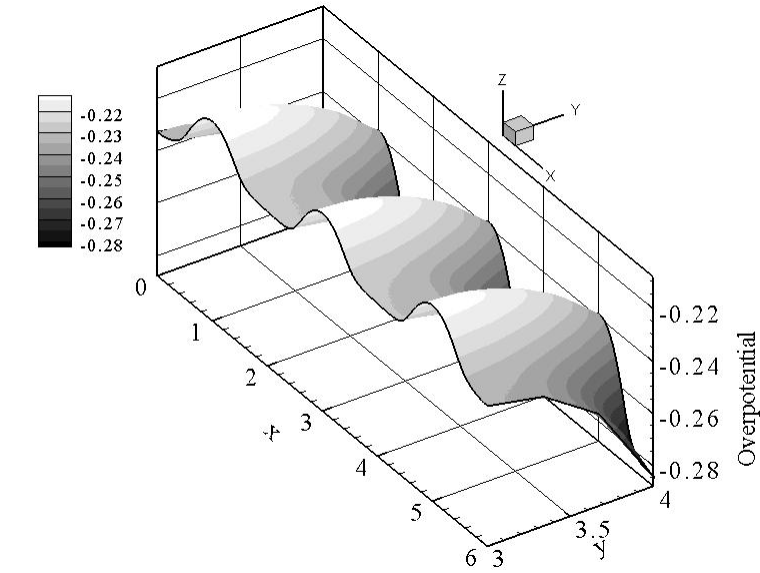
(b) Rate of oxygen consumption (kg/m^3)

Figure 5.15: (a) 3-D surface plot of oxygen consumption rate. Note $y = 4$ is the catalyst layer/membrane interface; (b) Contour plot of rate of oxygen consumption in the catalyst layer (kg/m^3) for the multi-phase model. x and y coordinates have been normalized for better presentation of results. (see Figure 5.1)

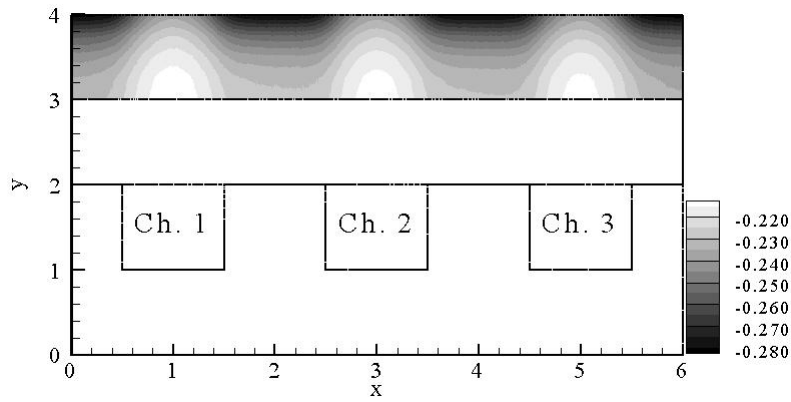
CHAPTER 5. ISOTHERMAL MODEL RESULTS

Due to the exponential dependency of the rate of reaction on the overpotential, Figure 5.16 has been constructed to show the distribution of the over-potential in the catalyst layer for the multi-phase model. The overpotential increases along the catalyst layer thickness from the GDL interface towards the membrane interface. It is also higher under the land areas than under the channel areas. To understand this trend, the solid and electrolyte potentials should be examined.

Examining Figure 5.17, it is apparent that the losses in the bipolar plate due to electron transfer are minimal and are approximately equal to that in the single phase model. This is expected since the bipolar plate is considered as 100% solid material and would be the same in both cases. In addition, it is seen that the solid potential is higher under the land areas since the electrons are readily available to these sites. This suggests that the path taken by the electrons governs the overall trend of the overpotential and in turn the reaction rate.



(a)



(b) Overpotential (V)

Figure 5.16: (a) 3-D surface plot of overpotential in the catalyst layer. Note $y = 4$ is the catalyst layer/membrane interface; (b) Contour plot of overpotential (V) in the catalyst layer for the multi-phase model. x and y coordinates have been normalized for better presentation of results. (see Figure 5.1)

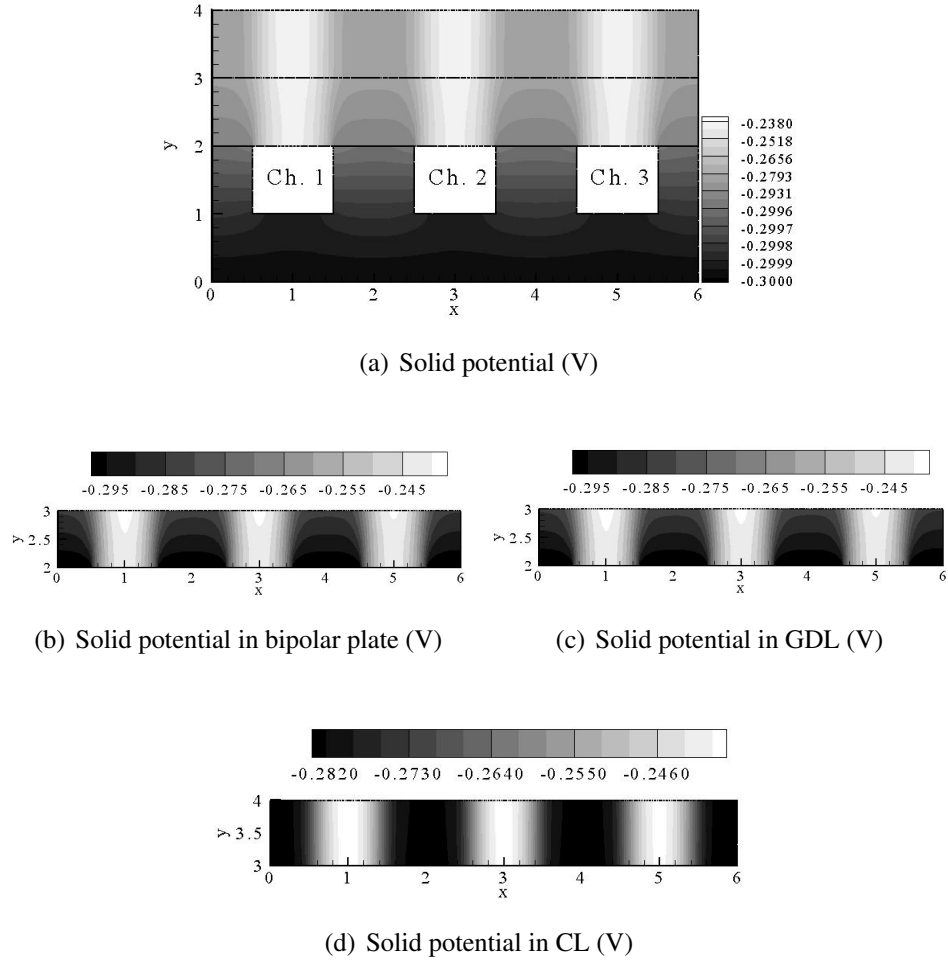
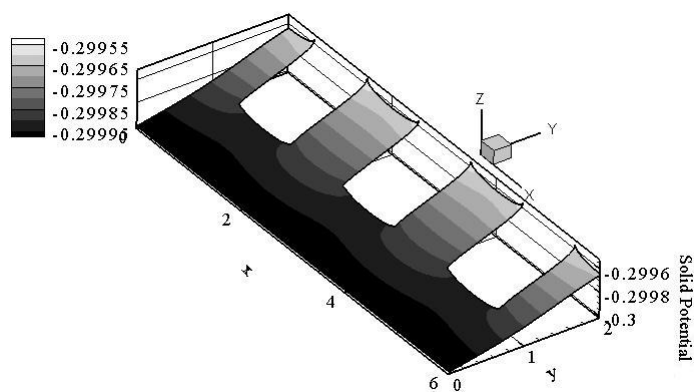
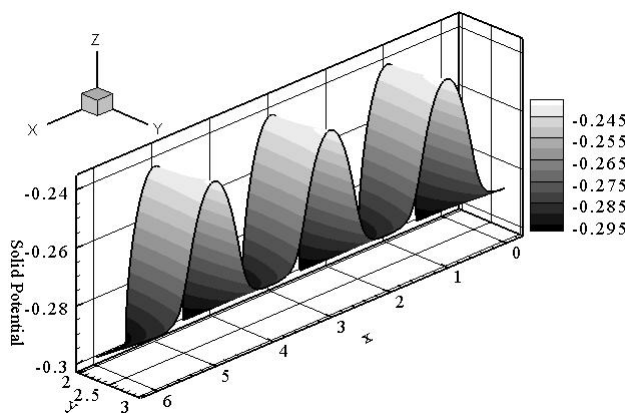


Figure 5.17: Solid potential (V) distribution in the (a) cathode; (b) bipolar plate; (c) gas diffusion layer; (d) catalyst layer for the multi-phase model. x and y coordinates have been normalized for better presentation of results. (see Figure 5.1)

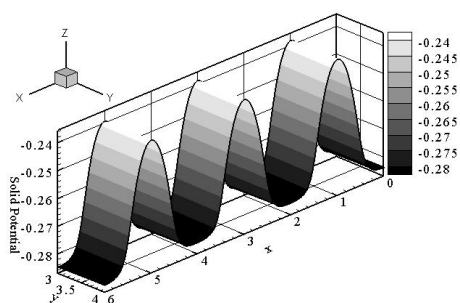
CHAPTER 5. ISOTHERMAL MODEL RESULTS



(a)



(b)



(c)

Figure 5.18: 3-D surface plot of solid potential in (a) bipolar plate; (b) gas diffusion layer; (c) catalyst layer for the multi-phase model.

CHAPTER 5. ISOTHERMAL MODEL RESULTS

The losses that occur due to electron transport are shown through the solid current density in Figure 5.19. Again, the current density in the x-direction expresses the magnitude of the losses, while that in the y-direction is the useful current density. The trend here is very similar to that of the single phase model. The losses due to electron transport in the backing and catalyst layers is very meaningful. In addition, there is a current build-up at the corner of the flow channel due to the sharp edges.

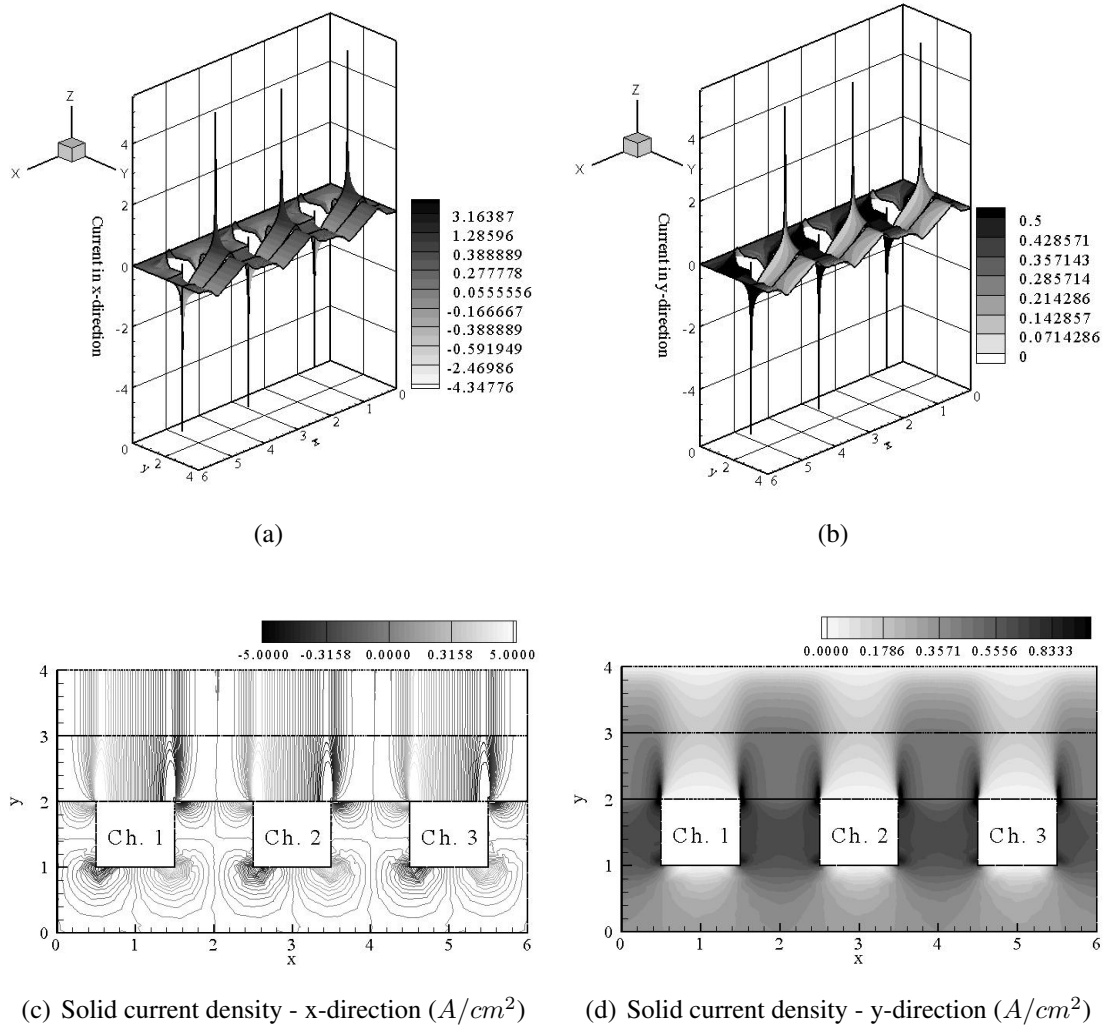


Figure 5.19: 3-D surface plot of the solid potential current density in the bipolar plate and gas diffusion and catalyst layers in the (a) x-direction; (b) y-direction. Solid potential current density (A/cm^2) in the (c) x-direction; (d) y-direction for the multi-phase model. x and y coordinates have been normalized for better presentation of results. (see Figure 5.1)

CHAPTER 5. ISOTHERMAL MODEL RESULTS

Figure 5.20 is of the electrolyte potential distribution in the catalyst layer for the two phase model. It is seen here, that the electrolyte potential has a two-dimensional distribution in one half of the catalyst layer and a one-dimensional distribution in the other half. The electrolyte potential increases in magnitude in the negative y-direction (from the membrane interface to the gas diffusion layer interface). Current is being generated due to proton transport from the membrane towards the gas diffusion layer. Current generation results in the increase of electrolyte potential.

The current density produced due to the proton transfer in the catalyst layer is shown in Figure 5.21. It is seen here as well that this quantity is a vector quantity with x and y components. The losses due to proton transfer are very small. The overall distance traveled by the protons in the catalyst layer is small. Further, unlike the electrons, the protons are not required to travel around any areas.

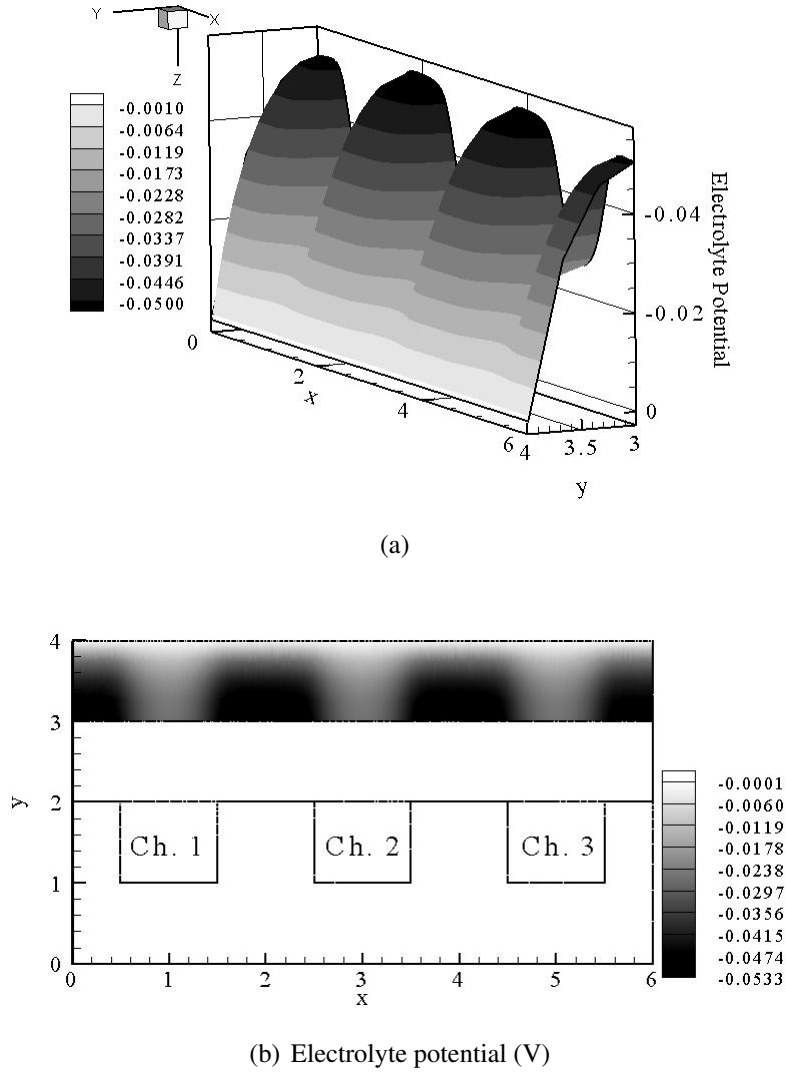


Figure 5.20: (a) 3-D surface plot of electrolyte potential in the catalyst layer. Note $y = 4$ is the catalyst layer/membrane interface; (b) Contour plot of electrolyte potential (V) in the catalyst layer for the multi-phase model. x and y coordinates have been normalized for better presentation of results. (see Figure 5.1)

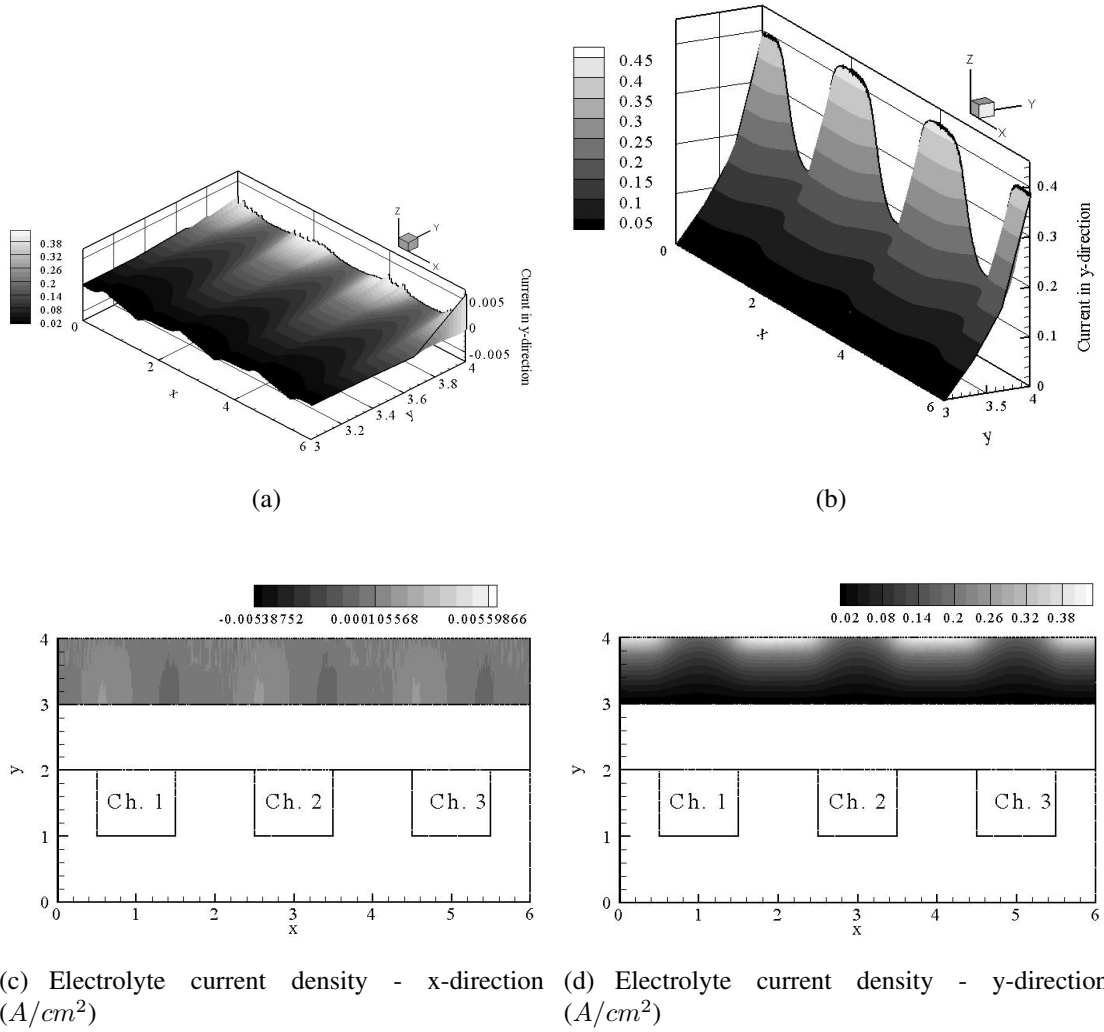


Figure 5.21: 3-D profile of the electrolyte potential current density in catalyst layer in the (a) x-direction; (b) y-direction. Electrolyte potential current density (A/cm^2) in the (c) x-direction; (d) y-direction for the multi-phase model. x and y coordinates have been normalized for better presentation of results. (see Figure 5.1)

CHAPTER 5. ISOTHERMAL MODEL RESULTS

The introduction of liquid water in this model was necessary to ensure that the relative humidity in the two layers does not exceed 1. In fact, the relative humidity in the gas diffusion and catalyst layers is 1 everywhere; thus, there is no need to show this fact on a figure. The distribution of the saturation level in the gas diffusion and catalyst layers is used as a measure of liquid water presence. Saturation increases along the thickness of the backing and catalyst layers as seen in Figure 5.22. The effect of the cross flow phenomenon is apparent. It is clearly seen that due to the pressure drop in the flow field, the removal of liquid water is enhanced. The accumulation of liquid water in the areas under the land is decreased. However, at the two boundaries ($x = 0$ & $x = 6$), it is seen that there is water accumulation since there is no pressure drop at these two boundaries. Further, the saturation level is slightly higher under the land area in the gas diffusion and catalyst layer since there is a higher reaction rate at the areas under the land.

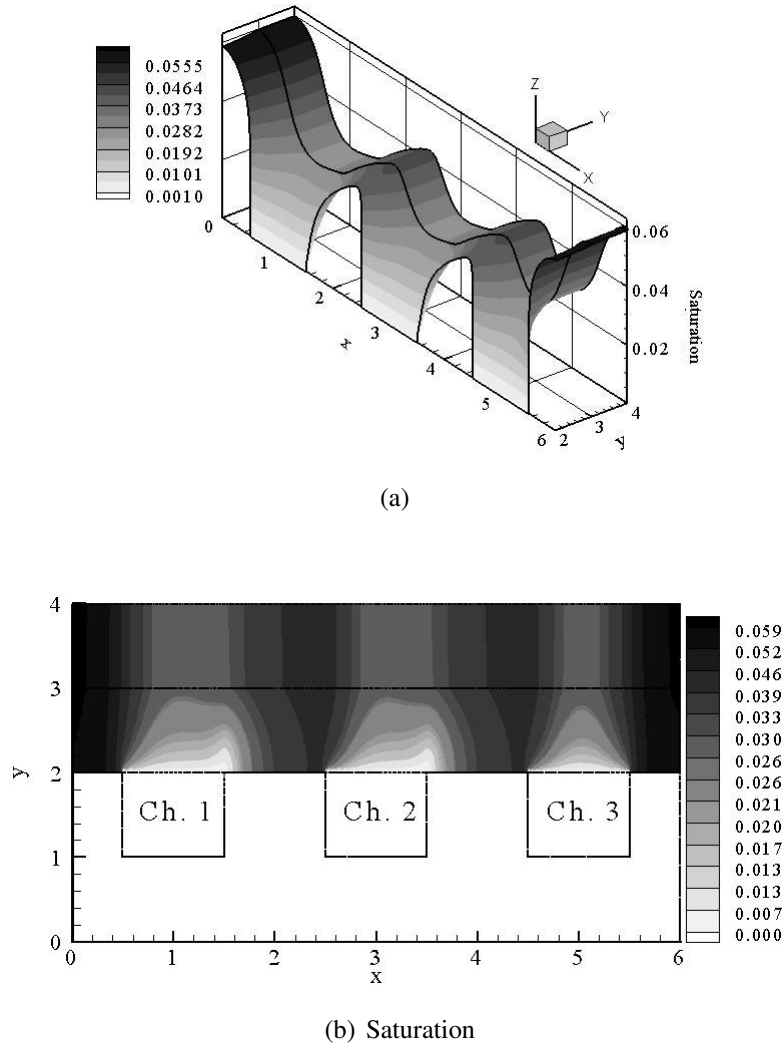


Figure 5.22: (a) 3-D surface plot of liquid water saturation in the gas diffusion and catalyst layers. Note $y = 4$ is the catalyst layer/membrane interface; (b) Contour plot of liquid water saturation profile in the gas diffusion and catalyst layers for the multi-phase model. x and y coordinates have been normalized for better presentation of results. (see Figure 5.1)

The water removal can also be displayed by examining the streamline plot of the liquid water velocity shown in Figure 5.23. It is very apparent that convection plays an important role in the removal of water from the backing and catalyst layers of the cell. This results in a decreased amount of liquid water build-up under the land areas.

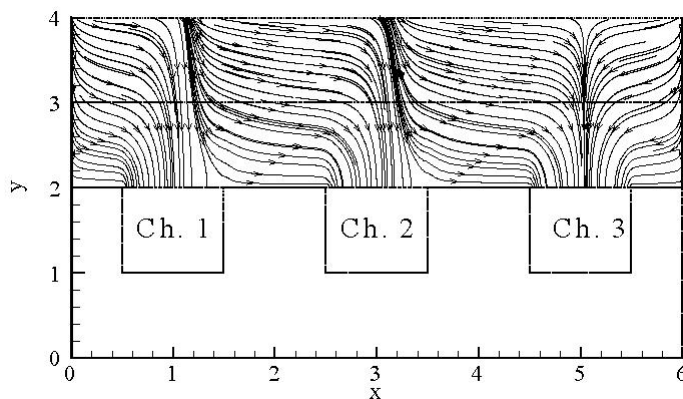


Figure 5.23: Streamline plot of the liquid water velocity with pressure drop along the flow channel field. x and y coordinates have been normalized. (see Figure 5.1)

5.3 Comparison of Single Phase and Multi-Phase Models

The detailed discussion of the single phase and multi-phase models in the previous sections reveals that in both cases the species transport and electrochemical reaction occur in a similar fashion. The overall two-dimensional distribution of oxygen in the backing and catalyst layers is similar in both cases. The concentration is higher under the channel areas where it is readily provided, while it is lower under the land areas due to the longer distance oxygen needs to be transported. However, the oxygen transport is hindered by the presence of liquid water since some of the void region is blocked. Figure 5.24 is used in order to compare the oxygen mass fraction distribution in the catalyst layer of the single phase and multi-phase models. The oxygen mass fraction is evaluated along the CL/membrane ($y = 4$) and GDL/CL ($y = 3$) interfaces for both models and it is plotted along the normalized cell length (in other words along the normalized x -direction). It is apparent, that at the interface $y = 3$, the mass fraction of oxygen is higher for the single phase model. This happens since the presence of liquid water in the gas diffusion layer in the multi-phase model will

block some of the void region available for the free diffusion of oxygen. At the interface $y = 4$, the mass fraction of oxygen in the multi-phase model is higher. In the multi-phase model, it is assumed that water is produced in liquid form only. Since the inlet relative humidity is 100% and the cell is isothermal, little liquid water will evaporate; hence, an accumulation of liquid water in the catalyst layer will occur. This results in the blockage of the void region in the catalyst layer and further hindering of the diffusion of oxygen in the layer and its reaction rate.

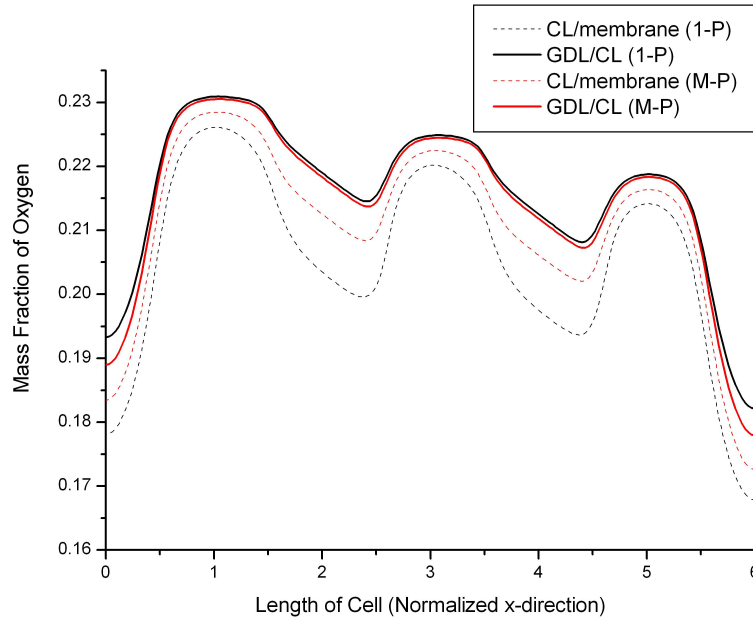


Figure 5.24: Comparison of the oxygen mass fraction in the catalyst layer of the single phase and multi-phase models at different y positions along the catalyst layer. 1-P \equiv single phase, M-P \equiv multi-phase.

Further, the oxygen consumption seems to occur in a similar fashion in both cases. It is higher under the land areas. The reaction rate reaches its highest magnitude at the catalyst layer/membrane interface and it's lowest value is at the gas diffusion layer/catalyst layer interface. The rate of oxygen consumption in the catalyst layer for the multi-phase model is reduced due to the reduced reaction sites by the presence of liquid water. Figure 5.25 is constructed to compare the rate of oxygen consumption in the catalyst layer of the single phase and multi-phase models. The rate of oxygen consumption is evaluated along the CL/membrane ($y = 4$) and GDL/CL ($y = 3$) interfaces for both models and it is plotted along the normalized cell length (in other words along

the normalized x-direction). It is seen that the rate of oxygen consumption at both interfaces is higher for the single phase model than the multi-phase model. The liquid water presence results in the decrease of catalyst sites and therefore the decrease of oxygen consumption. Studying the overpotential for both models will help explain this trend.

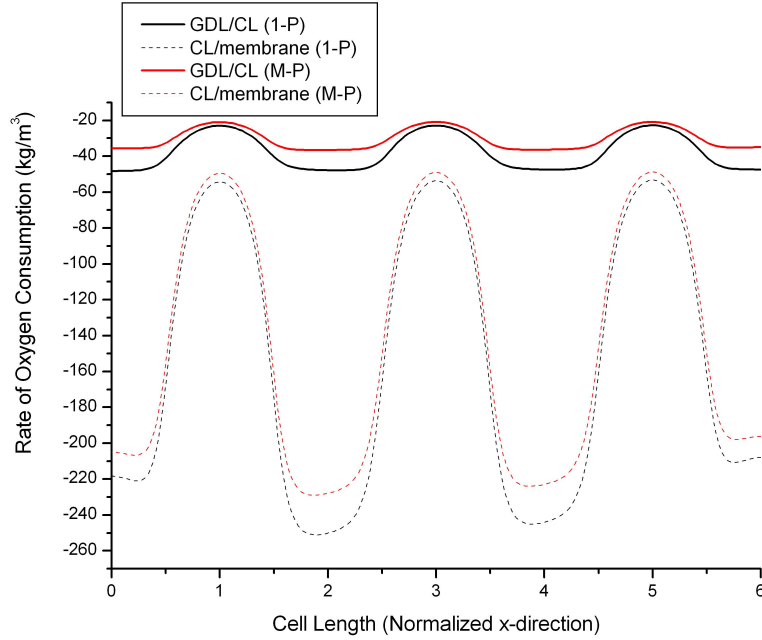


Figure 5.25: Comparison of the rate of oxygen consumption (kg/m^3) in the catalyst layer of the single phase and multi-phase models at different y positions along the catalyst layer. 1-P \equiv single phase, M-P \equiv multi-phase.

As stated many times before, the rate of reaction is very much dependent on the overpotential in the catalyst layer. Therefore, Figure 5.26 is used to compare the overpotential distribution in the catalyst layer of the single phase and multi-phase models. The overpotential is evaluated along the CL/membrane and GDL/CL interfaces for both models and it is plotted along the normalized cell length (in other words along the normalized x-direction). It is clear here, that in both models, the distribution is two-dimensional and the trend is very similar. The highest value of the overpotential is obtained at the CL/membrane interface. It is clear here, that the overpotential value at the CL/membrane interface for the multi-phase model is slightly lower than that of the single phase model. Visiting the Butler-Volmer equation, equation 3.29, shows that the dependency of the reaction rate on the overpotential is exponential.

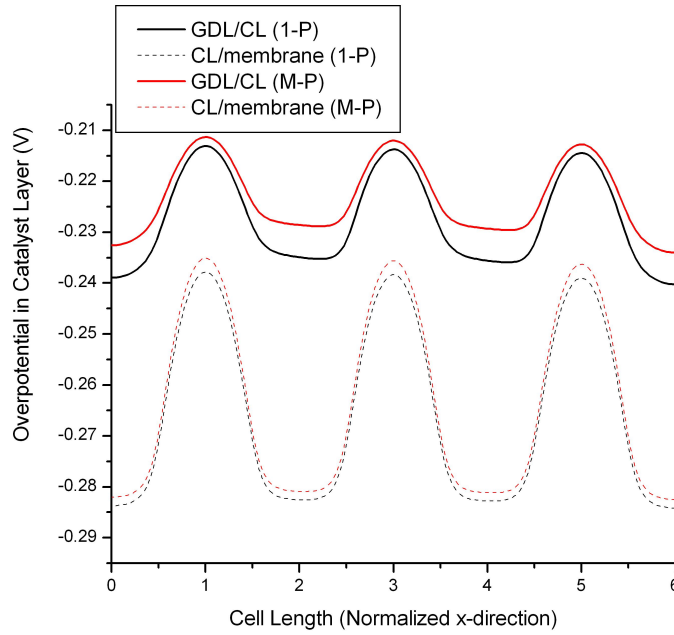


Figure 5.26: Comparison of the overpotential (V) in the catalyst layer of the single phase and multi-phase models at different y positions along the catalyst layer. 1-P \equiv single phase, M-P \equiv multi-phase.

The major losses in both models occur due to the electron transport in the backing and catalyst layers. Small losses can be attributed to proton transport. Finally, the overall current density produced in the catalyst layer for the single phase model is 4166 A/m^3 , while it is 3899 A/m^3 for the multi-phase model, a decrease of 7%.

5.4 Sensitivity Analysis for Multi-Phase Model

5.4.1 Effect of Inlet Relative Humidity

In this section, the effect of the inlet relative humidity on the overall performance of the cathode will be studied. It is important to study this parameter since it is controlled by the operator and can be easily changed. In PEM fuel cells, the inlet relative humidity is used to control the amount of vapor water entering the cell; hence, affecting the hydration of the membrane. Vapor water will condense once the relative humidity in the gas diffusion and catalyst layers reaches 1 and in turn

CHAPTER 5. ISOTHERMAL MODEL RESULTS

liquid water will evaporate when the relative humidity inside the layers is less than 1. In addition, as seen in equation 3.74, the electrolyte conductivity is directly influenced by the relative humidity, in other words water activity, in the catalyst layer. The electrolyte conductivity is important in determining the current density.

In order to determine the effect of the inlet relative humidity on the performance of the cathode, six different values for the inlet relative humidity will be examined (100%, 90%, 80%, 70%, 60%, 50%). In addition, the comparison will be carried out for the Leverette function and the Brooks and Corey relation for the capillary function.

Figure 5.27 shows the effect of the inlet relative humidity on the current density (performance) and the electrolyte conductivity in the cathode catalyst layer. The Leverette function is used to describe the relationship of the capillary pressure versus the effective saturation. It is clear that the best performance is reached with an inlet relative humidity of 90%. However, this performance does not correspond to the highest electrolyte conductivity. It is also interesting to note here, that an inlet relative humidity of 80% leads to a slightly higher performance than an inlet relative humidity of 100% even though it corresponds to a lower electrolyte conductivity. Further examination of the figure shows that the variation in current density with the inlet relative humidity is very small.

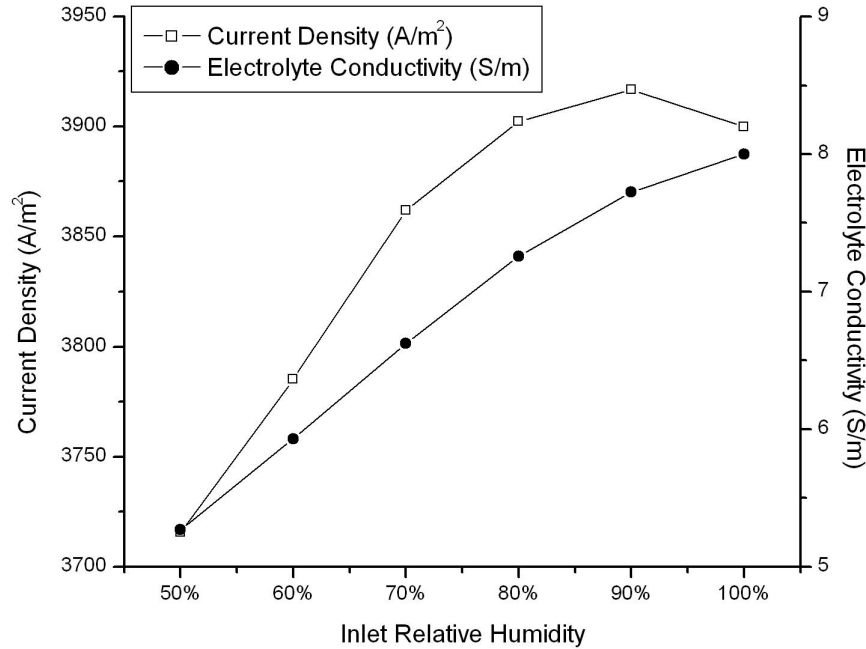


Figure 5.27: Effect of inlet relative humidity on the performance of the cathode and the electrolyte conductivity using the Leverette function

In order to be able to explain the behavior of the current density versus the inlet relative humidity, Figures 5.28 and 5.30 should be examined. The relative humidity in the backing and catalyst layers for different inlet relative humidity values is described by Figure 5.28, while Figure 5.30 shows the effective liquid water saturation in the backing and catalyst layers. The corresponding plots for an inlet relative humidity of 100% are not presented. The relative humidity in the backing and catalyst layers for an inlet relative humidity of 100% is 1 everywhere and the saturation distribution is given earlier by Figure 5.22. The relative humidity in the backing layer for all the values of inlet relative humidity seems to vary between the inlet relative humidity and 100%. Meanwhile, in the catalyst layer, the relative humidity is close to 100%. This is so since the evaporation term is much higher in the catalyst layer due to the presence of more liquid water that is readily available for evaporation. This helps explain the high electrolyte conductivity with an inlet relative humidity of 80% and 90%. Also, as expected, the saturation levels are higher with higher inlet relative humidity.

CHAPTER 5. ISOTHERMAL MODEL RESULTS

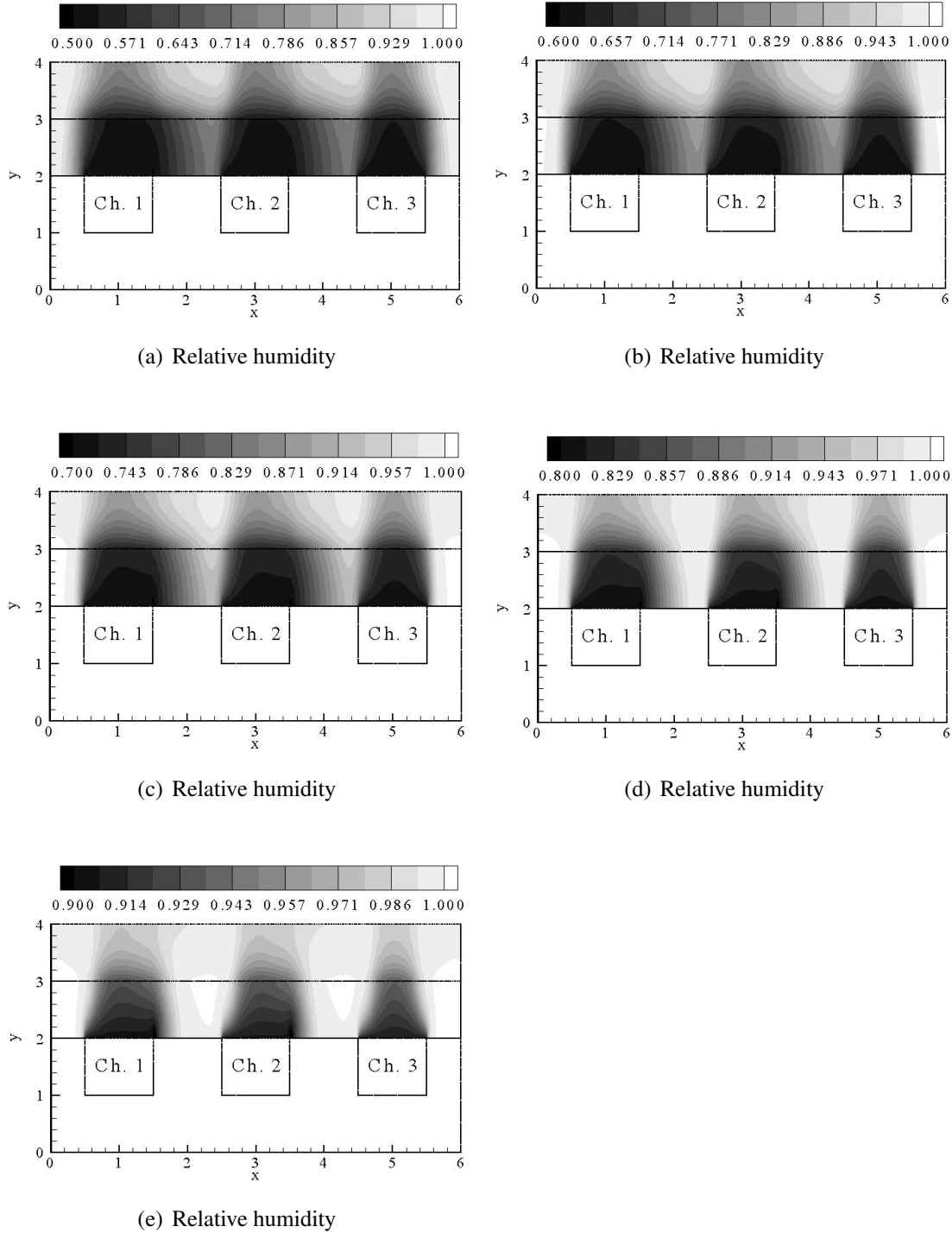


Figure 5.28: Relative humidity in the backing and catalyst layers for inlet relative humidity of (a) 50%; (b) 60%; (c) 70%; (d) 80%; (e) 90% - using the Leverette function. x and y coordinates have been normalized for better presentation of results. (see Figure 5.1)

CHAPTER 5. ISOTHERMAL MODEL RESULTS

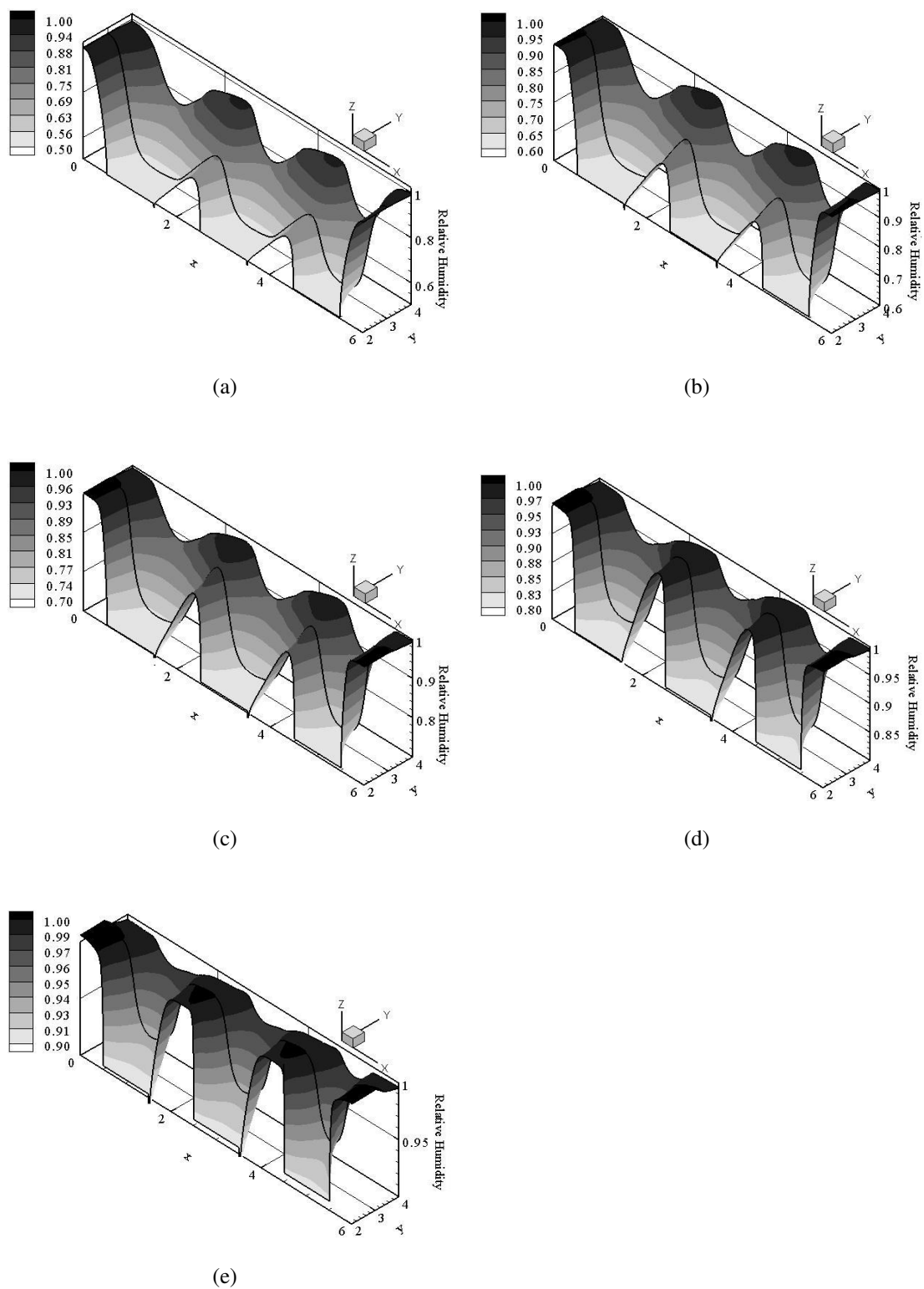


Figure 5.29: Liquid water saturation in the backing and catalyst layers for inlet relative humidity of (a) 50%; (b) 60%; (c) 70%; (d) 80%; (e) 90% - using the Leverette function.

CHAPTER 5. ISOTHERMAL MODEL RESULTS

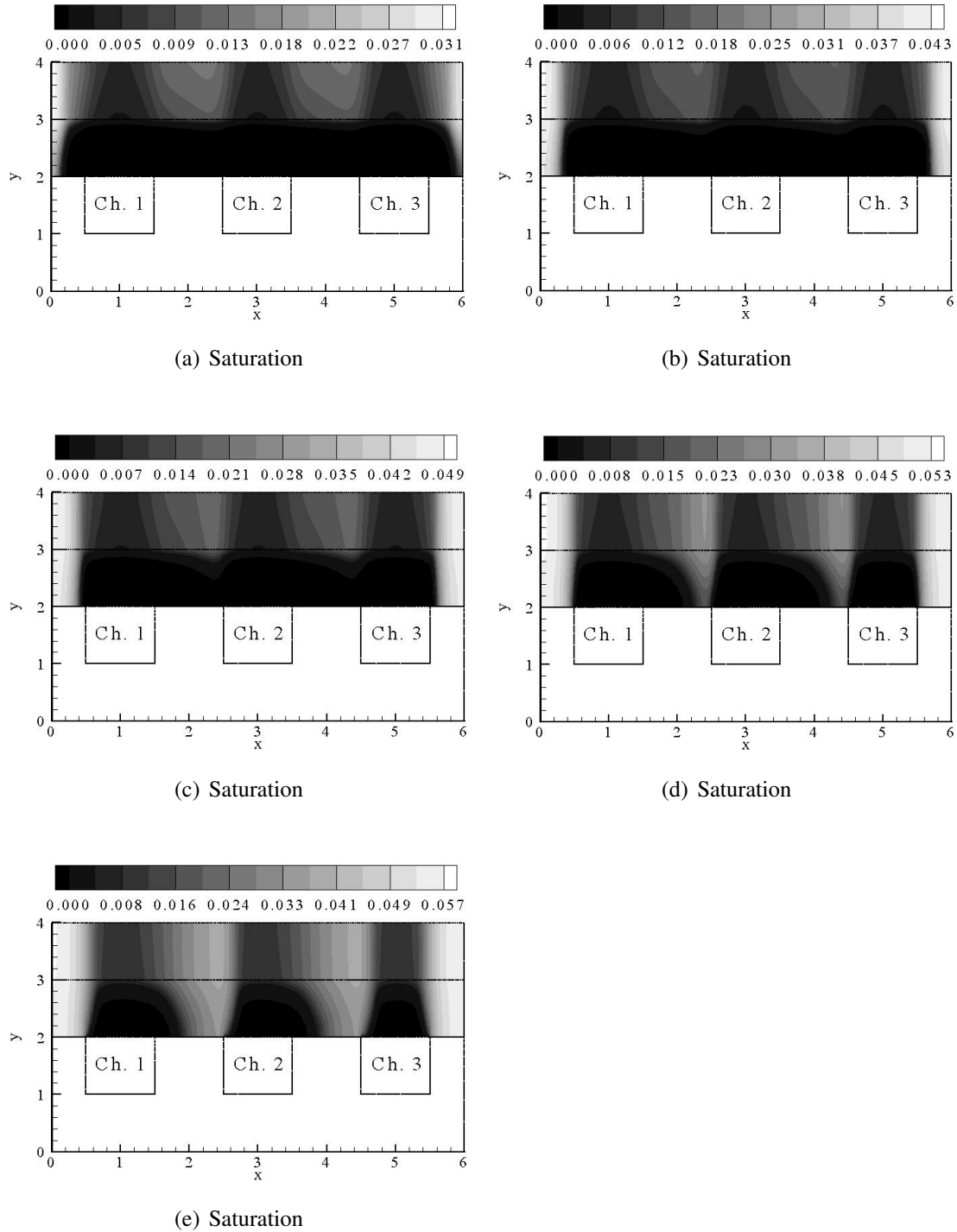


Figure 5.30: Liquid water saturation in the backing and catalyst layers for inlet relative humidity of (a) 50%; (b) 60%; (c) 70%; (d) 80%; (e) 90% - using the Leverette function. x and y coordinates have been normalized for better presentation of results. (see Figure 5.1)

CHAPTER 5. ISOTHERMAL MODEL RESULTS

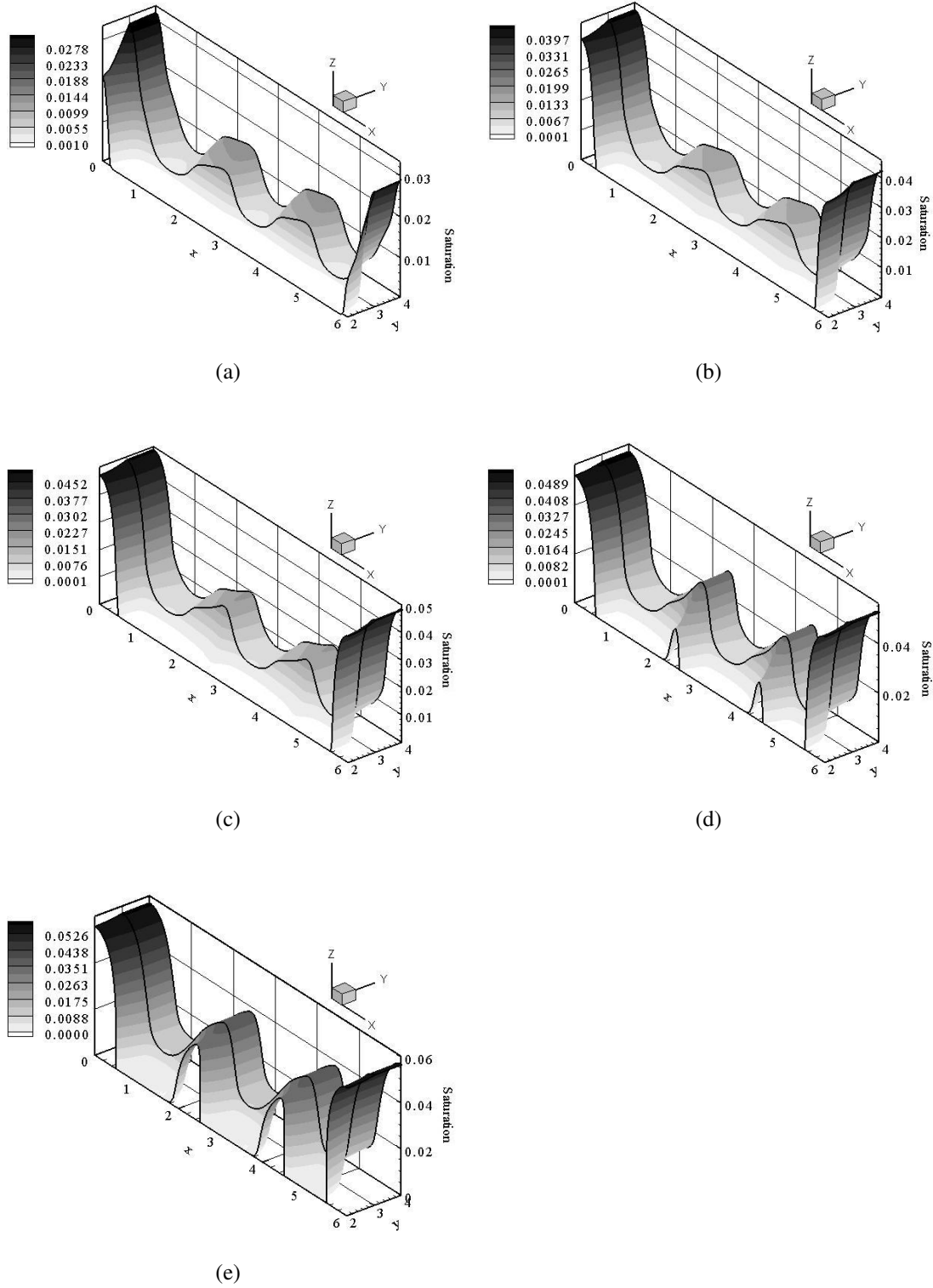


Figure 5.31: Liquid water saturation in the backing and catalyst layers for inlet relative humidity of (a) 50%; (b) 60%; (c) 70%; (d) 80%; (e) 90% - using the Leverette function

CHAPTER 5. ISOTHERMAL MODEL RESULTS

The information gathered from Figures 5.27, 5.28 and 5.30 leads to the important conclusion that electrolyte conductivity has a significant effect on the performance up to a point. It seems that after the electrolyte conductivity reaches 7.7 S/m , the saturation becomes more significant.

A similar analysis is done using the Brooks and Corey relation. Figure 5.32 summarizes the relation between the current density and the electrolyte conductivity in the catalyst layer versus the inlet relative humidity. The trend is very much similar to that for the Leverette function. It seems here that with inlet relative humidity of 80% and 90% the performance is very similar. It can be said that the optimum performance is reached with either inlet relative humidity.

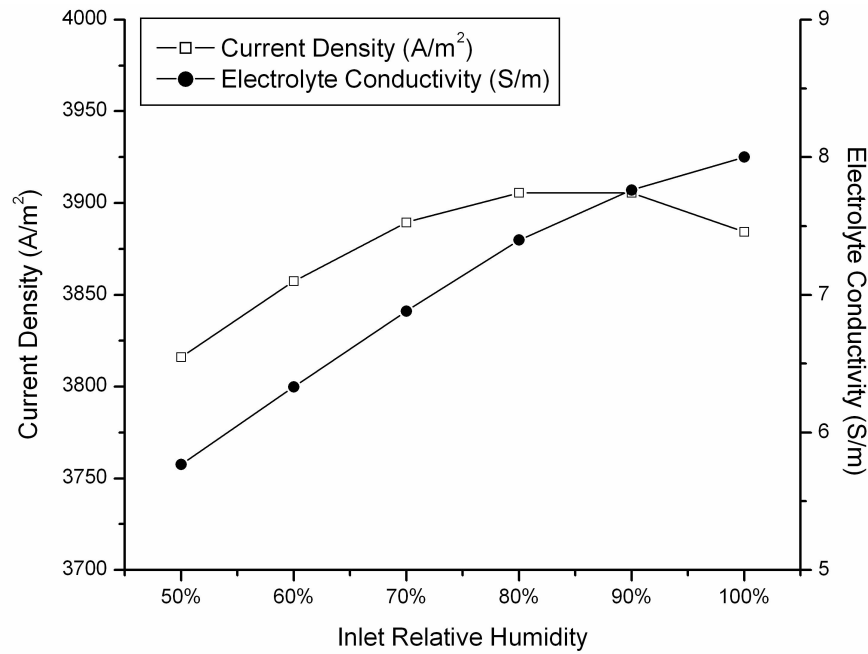


Figure 5.32: Effect of inlet relative humidity on the performance of the cathode and the electrolyte conductivity using the Brooks and Corey relation

Similarly, the relative humidity and the effective liquid saturation in the backing and catalyst layers have been examined and are shown in Figures 5.33 and 5.35. The relative humidity in the backing and catalyst layers corresponding to an inlet relative humidity of 100% is not presented since it will have a value of 100% everywhere.

CHAPTER 5. ISOTHERMAL MODEL RESULTS

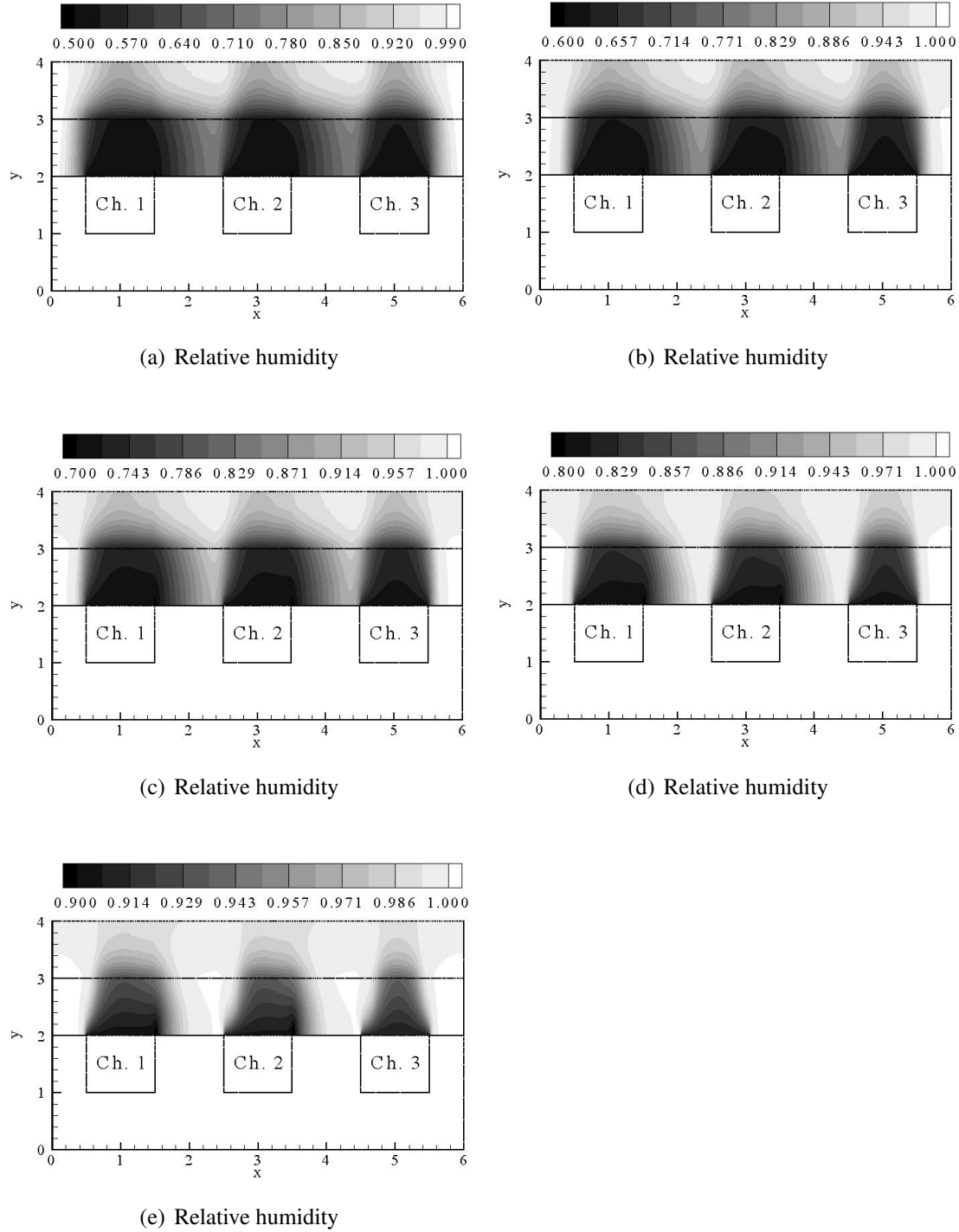


Figure 5.33: Relative humidity in the backing and catalyst layers for inlet relative humidity of (a) 50%; (b) 60%; (c) 70%; (d) 80%; (e) 90% - using Brooks and Corey relation. x and y coordinates have been normalized for better presentation of results. (see Figure 5.1)

CHAPTER 5. ISOTHERMAL MODEL RESULTS

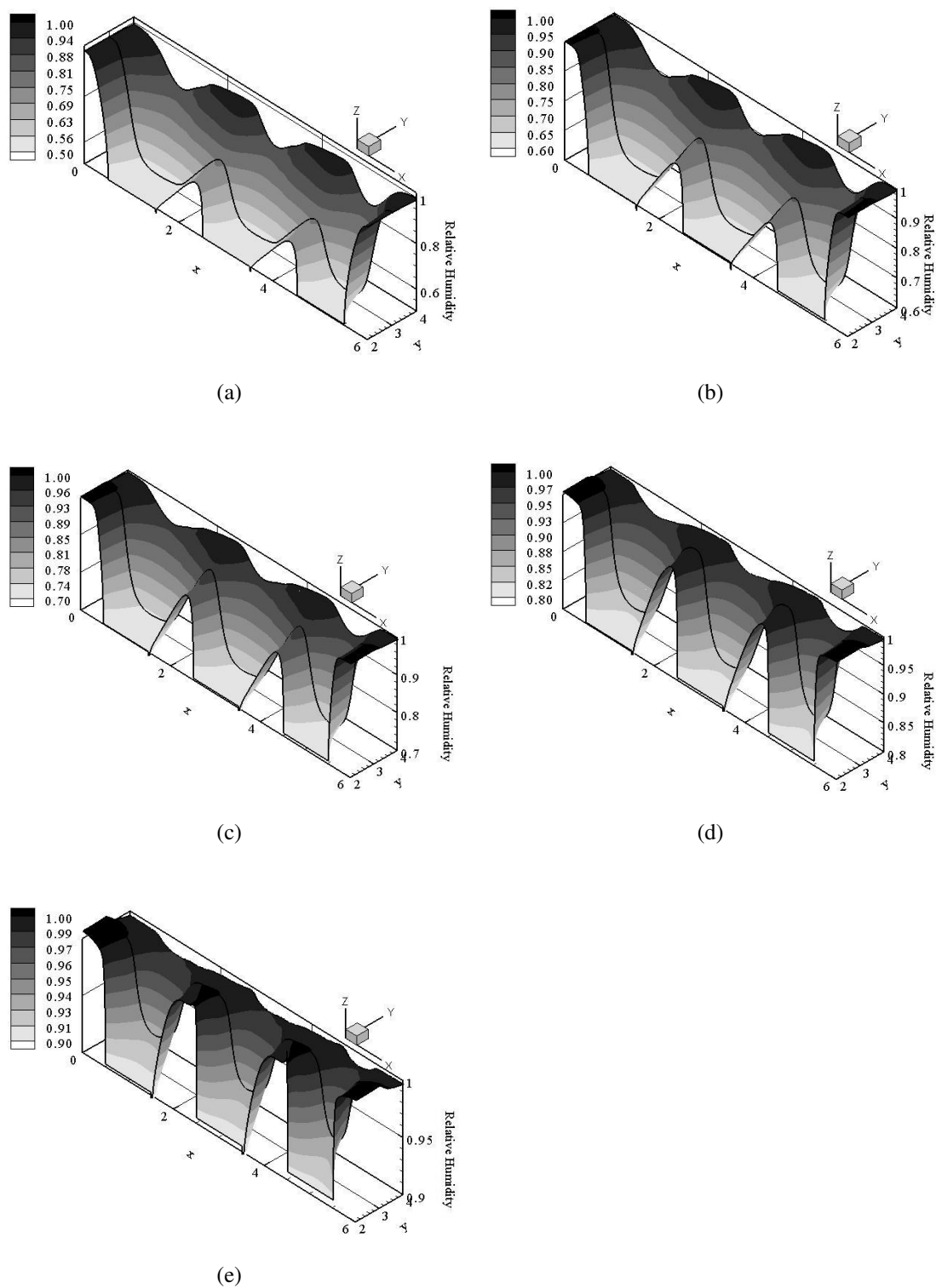


Figure 5.34: Relative humidity in the backing and catalyst layers for inlet relative humidity of (a) 50%; (b) 60%; (c) 70%; (d) 80%; (e) 90% - using Brooks and Corey relation

CHAPTER 5. ISOTHERMAL MODEL RESULTS

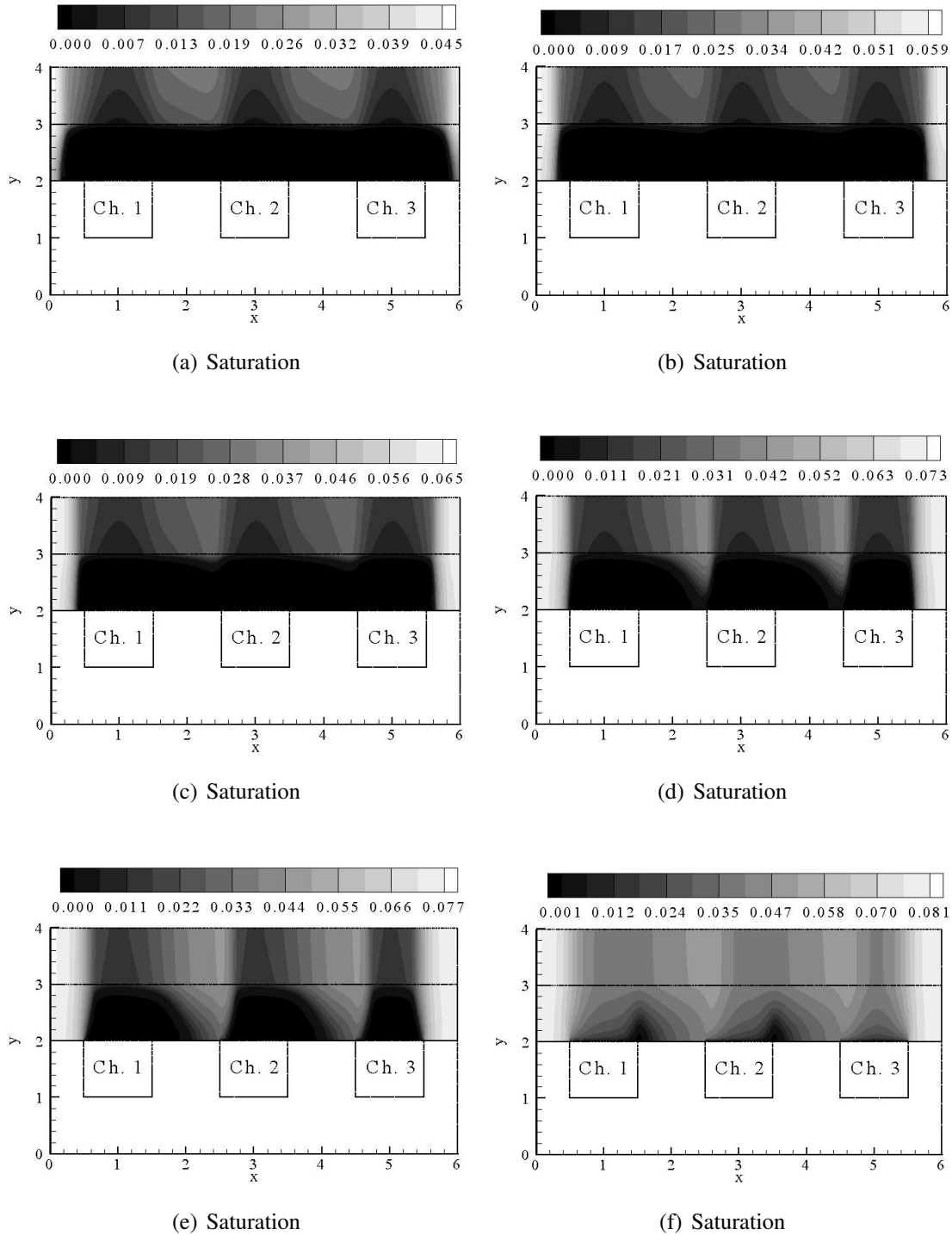


Figure 5.35: Liquid water saturation in the backing and catalyst layers for inlet relative humidity of (a) 50%; (b) 60%; (c) 70%; (d) 80%; (e) 90%; (f) 100% - using the Brooks and Corey relation. x and y coordinates have been normalized for better presentation of results. (see Figure 5.1)

CHAPTER 5. ISOTHERMAL MODEL RESULTS

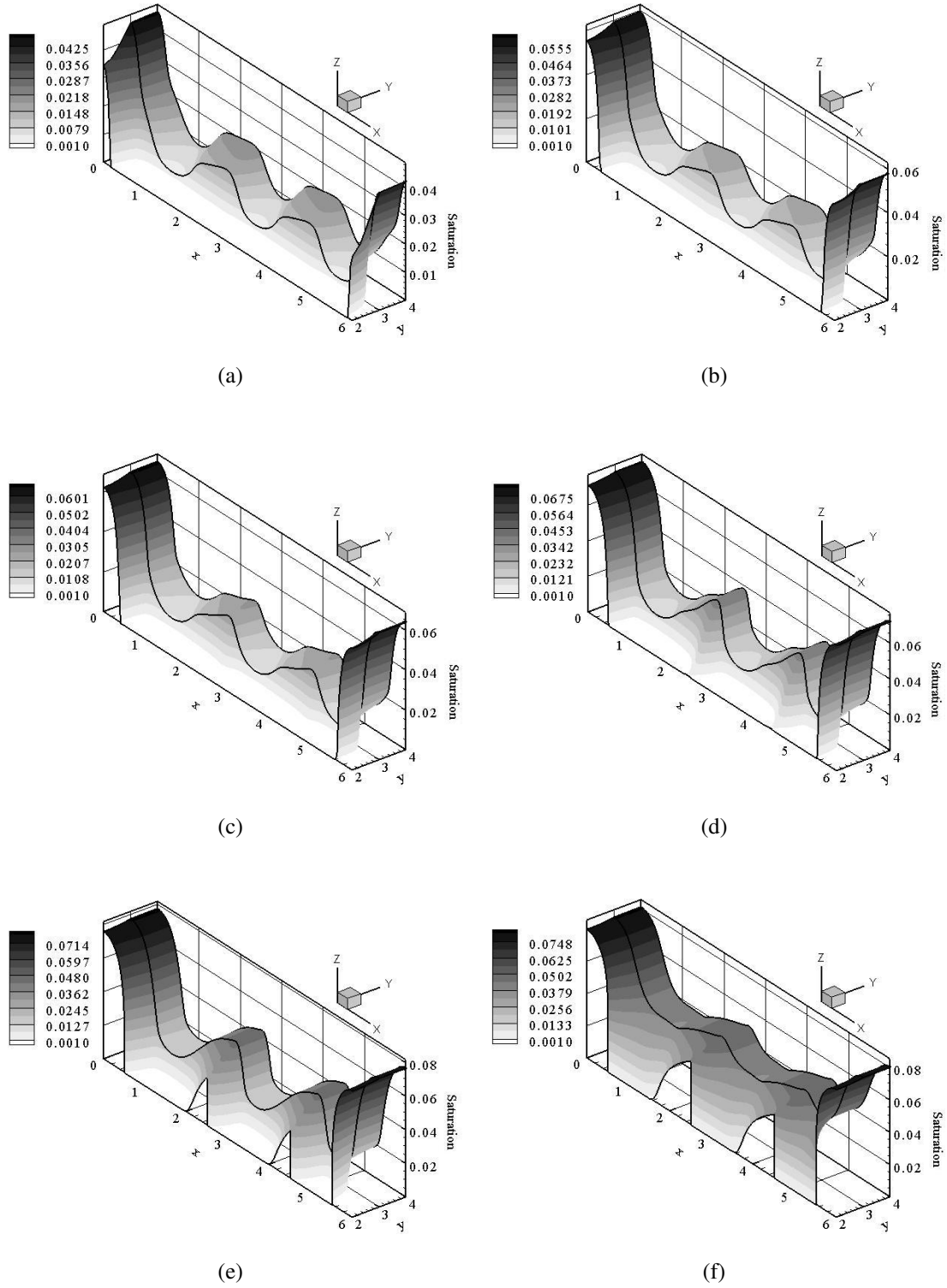


Figure 5.36: Liquid water saturation in the backing and catalyst layers for inlet relative humidity of (a) 50%; (b) 60%; (c) 70%; (d) 80%; (e) 90%; (f) 100% - using the Brooks and Corey relation

CHAPTER 5. ISOTHERMAL MODEL RESULTS

Finally, a comparison of the results obtained with the Leverette function and Brooks and Corey relation lead to the following observations:

- With the Brooks and Corey relation, effective liquid water saturation in the backing and catalyst layers is higher than that obtained with the Leverette function. This can be explained by referring back to Figure 3.10. The Brooks and Corey relation leads to a higher capillary pressure; thus, the capillary diffusion coefficient, D_c , will be lower affecting the liquid water removal.
- With an inlet relative humidity of 90%, 80%, 70%, 60% and 50%, the corresponding electrolyte conductivity is higher with the Brooks and Corey relation and the performance is slightly higher. This occurs since more liquid water is available for evaporation; thus, the relative humidity in the catalyst layer is increased. However, for an inlet relative humidity of 100%, the performance using the Leverette function seems to be better. This is so since for both relations the relative humidity in the catalyst layer is 1, but the saturation level is higher for the Brooks and Corey relation. Therefore, the available sites for reaction are reduced.
- Finally, the overall trend of performance in the catalyst layer using both relations seems to be similar. The electrolyte conductivity has a significant effect on the performance up to a point.

At the end of this section it is important to note that the catalyst layer plays a very important role in controlling the water concentration in the cell both in vapor and liquid forms. The evaporation of liquid water seems to mostly occur in the catalyst layer. This is expected since the production of water occurs in the catalyst layer; hence, depending on the thermodynamic properties of the cell at the time of water production, water will either evaporate or condense before leaving the catalyst layer. This piece of information is in agreement with the conclusions made by Eikerling [46].

5.4.2 Effect of Pressure Drop

As mentioned earlier, a comprehensive study on the cross flow phenomenon in a PEM fuel cell with a serpentine flow channel has been carried out by Park and Li [59]. Due to the cross leakage

CHAPTER 5. ISOTHERMAL MODEL RESULTS

between neighboring channels with a serpentine flow field, liquid water is ensured to be properly removed from the cell. This section is designed to discuss the effect of the pressure drop on liquid water removal.

The base case discussed earlier has a pressure drop of 349 Pa and an inlet relative humidity of 100%. The case presented here and discussed is based on the assumption that the pressure drop is zero. None of the other parameters pertaining to the base case have been altered. The cell voltage is 0.7 V, the operating conditions are 80°C and the permeability of the porous media is $5.5 \times 10^{-11} \text{m}^2$. The effective saturation level in the gas diffusion and catalyst layers is shown in Figure 5.37 using the Leverette function and the Brooks and Corey relation. Liquid water seems to accumulate in the areas under the land. Due to no pressure drop, the fluid is not allowed to pass from one channel to another unlike in Figure 5.22. It is interesting to notice though that the highest saturation level in both cases is the same. Recall that the permeability of the backing layer plays a significant role in obtaining the saturation level and it is the same in both cases.

CHAPTER 5. ISOTHERMAL MODEL RESULTS

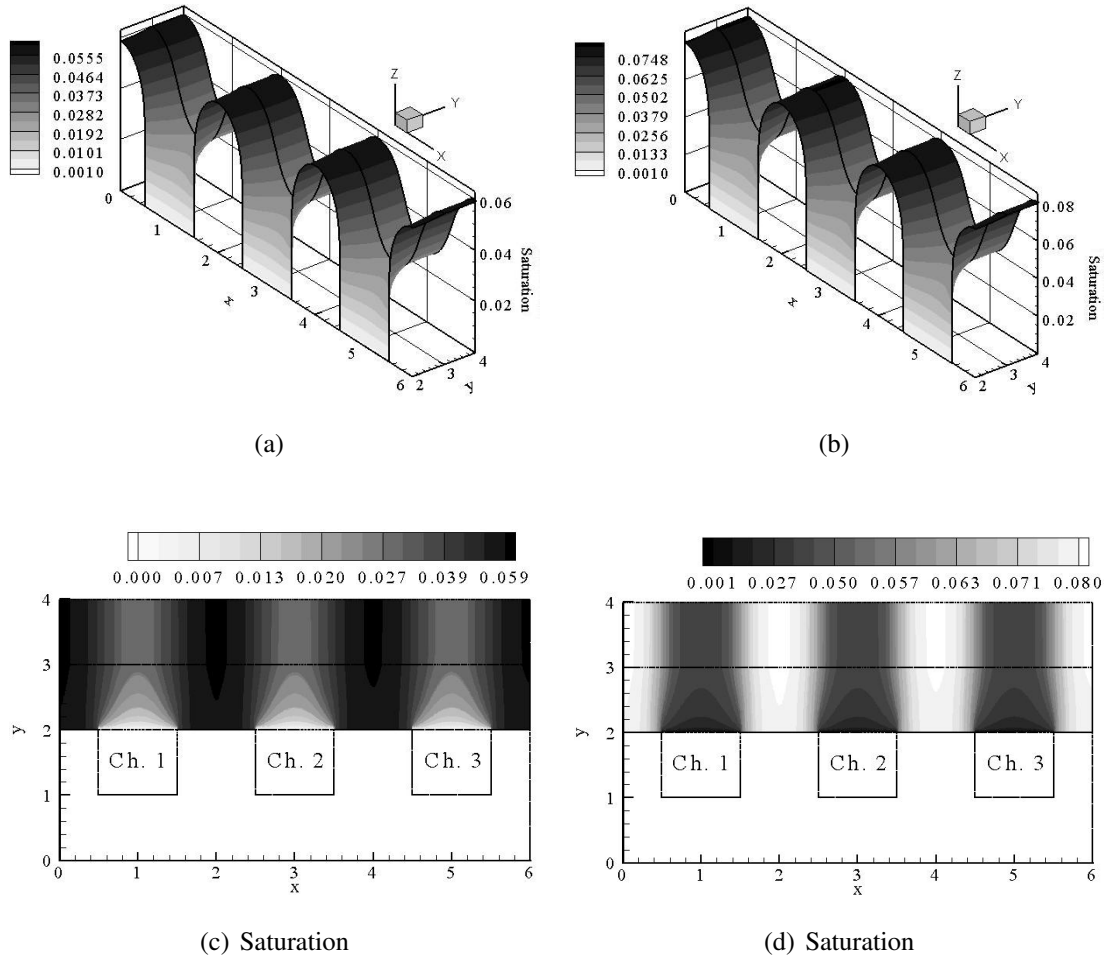


Figure 5.37: 3-D surface plot of liquid water saturation in the gas diffusion and catalyst layers with the capillary pressure represented using (a) Leverette function; (b) Brooks & Corey relation. Liquid water saturation in the backing and catalyst layers with $\Delta P = 0$ - (c) Leverette Function; (d) Brooks and Corey Relation.

Figure 5.38 is a pictorial illustration of how diffusion is the only means of water removal from the cell with no pressure gradient along the channel flow field.

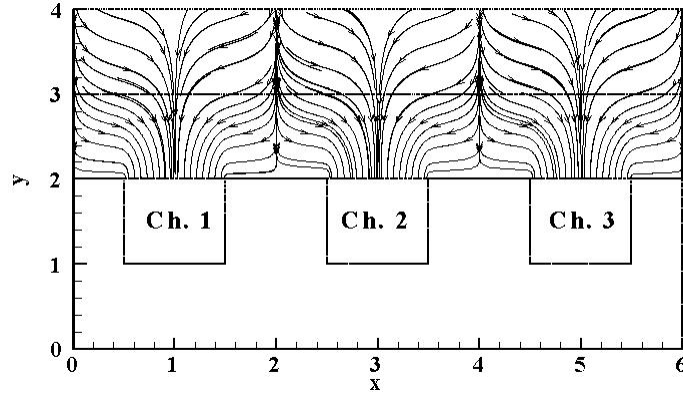


Figure 5.38: Plot of liquid water velocity streamlines with $\Delta P = 0$ along the channel flow field. x and y coordinates have been normalized for better presentation of results. (see Figure 5.1)

The corresponding velocity gradient for the gas is zero, since there is no pressure gradient along the channel flow field. Revisiting the definition of the liquid water velocity, its dependency on the gas phase velocity is obvious.

$$\vec{u}_l = \frac{\mu_g \kappa_l}{\mu_l \kappa_g} \vec{u}_g - D_c \nabla S \quad (5.4)$$

where \vec{u}_l is the liquid phase velocity and \vec{u}_g is the gas phase velocity.

Thus, the presence of cross flow, or in other words a gas phase velocity, will aid in the removal of liquid water from the cell as seen previously in Figure 5.23. With the presence of cross flow, liquid water is removed from the cell via capillary diffusion and the gas pressure difference.

The corresponding current density in the catalyst layer for this case is 3833 and 3809 A/m^2 using the Leverette function and the Brooks and Corey relation, respectively; a decrease of 2% compared to the presence of cross flow.

Finally, it should be pointed out here that even though a high permeability value is used to generate the results of this section, the lack of a pressure gradient along the flow field results in a decrease in performance. Consequently, for a better performance, a high pressure drop accompanied with a high permeability should be used.

5.4.3 Effect of Permeability

The discussion of this section will be focused on how the permeability affects the liquid water distribution in the cell. It is vital to consider the effects of permeability since it is a measure of the ability of the material to transmit fluids. Therefore, it will be an important measure of how liquid water is being transported in the layers and of the cross flow phenomenon. In addition, the permeability plays a significant role in determining the relative permeability of the gas and liquid phases; hence, affecting the velocity of both phases. Further, the permeability will have a significant effect on the capillary diffusion coefficient, D_c , described by equation 3.62. The capillary diffusion coefficient is a measure of how fast liquid water will be transferred in the backing and catalyst layers. The permeability affects the capillary diffusion coefficient not just directly through the relative permeability of liquid water, but also through the capillary pressure. The capillary pressure is expressed through the Leverette function and the Brooks and Corey relation.

In this section, two permeability values will be considered for comparison. The permeability values used to generate the results of this subsection are $5.5 \times 10^{-13} \text{ m}^2$ and $5.5 \times 10^{-10} \text{ m}^2$. The inlet relative humidity is 100%, the pressure drop along the channel flow field is 349 Pa and all the other parameters are kept the same as the base case discussed in section 5.2. With a low permeability value, the cross flow phenomenon is not observed even with a pressure drop along the channel flow field as shown in Figure 5.39. It is clear that there is water build-up in the areas under the land between the channels. The only means of liquid water removal is through diffusion. In addition, it is important to notice that with a low permeability value, the highest level of liquid water saturation is higher than that of the base case.

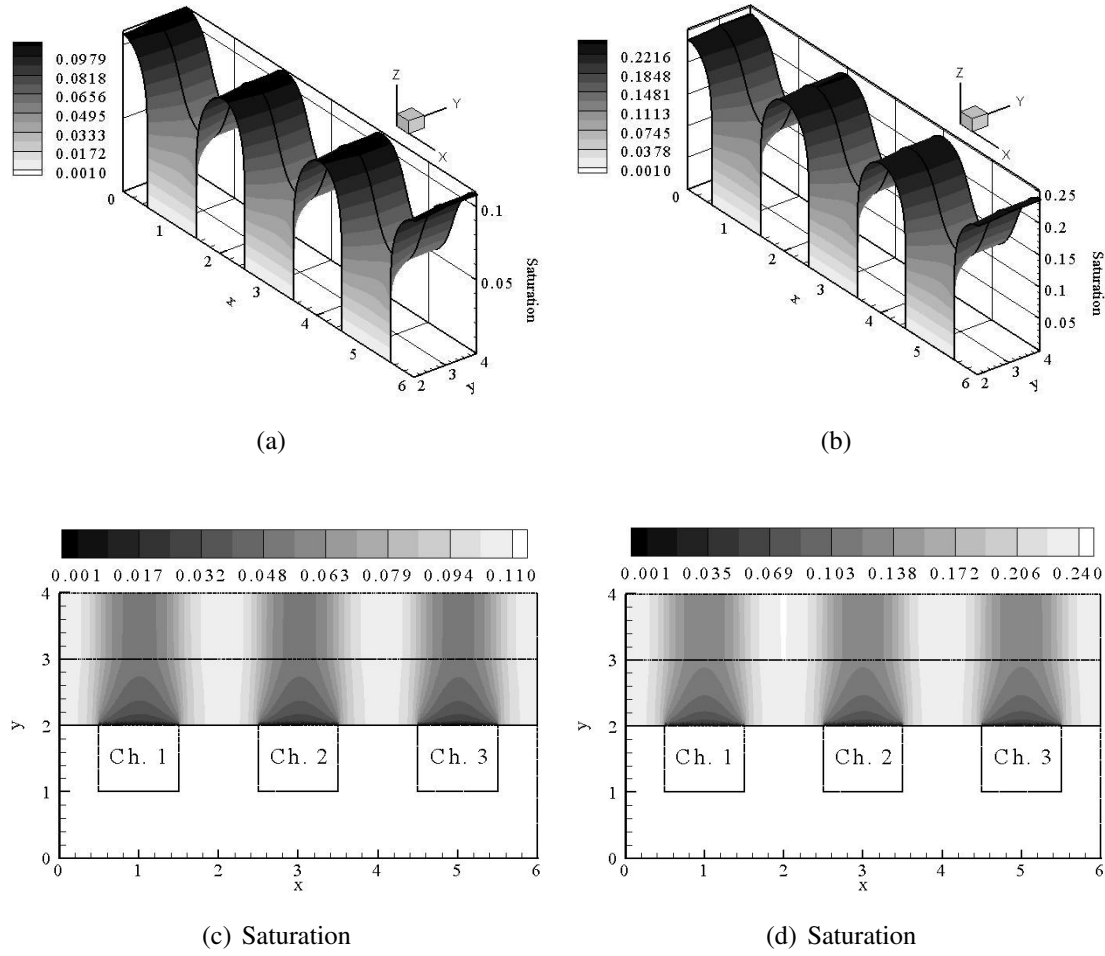


Figure 5.39: 3-D surface plot of liquid water saturation with $\kappa = 5.5 \times 10^{-13} m^2$ - (a) Leverette function; (b) Brooks & Corey relation. Liquid water saturation in the backing and catalyst layers for $\kappa = 5.5 \times 10^{-13} m^2$ - (c) Leverette Function; (d) Brooks and Corey Relation. x and y coordinates have been normalized for better presentation of results. (see Figure 5.1)

With a high permeability value, the cross flow phenomenon is observed in Figure 5.40. Compared to the base case, the liquid water removal is much more improved and the highest liquid water saturation is decreased.

CHAPTER 5. ISOTHERMAL MODEL RESULTS

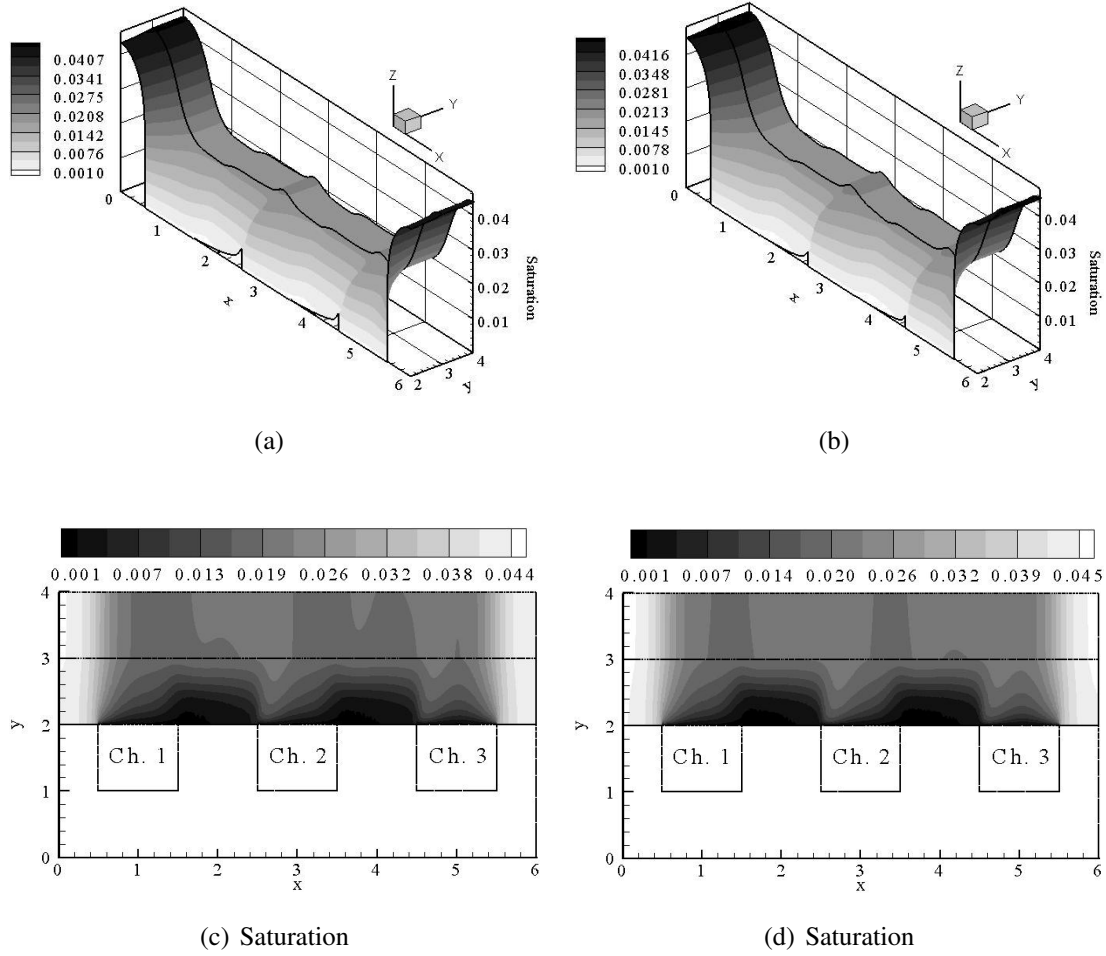


Figure 5.40: 3-D surface plot of liquid water saturation for $\kappa = 5.5 \times 10^{-10} m^2$ - (a) Leverette function; (b) Brooks & Corey relation. Liquid water saturation in the backing and catalyst layers for $\kappa = 5.5 \times 10^{-10} m^2$ - (c) Leverette Function; (d) Brooks and Corey Relation. x and y coordinates have been normalized for better presentation of results. (see Figure 5.1)

With low permeability value, the current density in the catalyst layer is 3777 and 3610 A/m^2 with the Leverette function and Brooks and Corey relation, respectively. With a high permeability value, the current density in the catalyst layer is 3942 and 3941 A/m^2 with the Leverette function and the Brooks and Corey relation, respectively.

Finally, the x-direction velocity component will be investigated to better comprehend the effect of permeability on the cross flow or leakage phenomenon in the fuel cell. The x component of the velocity is an indicator of the flow rate between adjacent channels. In Figure 5.41 a comparison of

the x-velocity magnitude for the three different permeability values, $5.5 \times 10^{-13} \text{ m}^2$, $5.5 \times 10^{-11} \text{ m}^2$ and $5.5 \times 10^{-10} \text{ m}^2$, is shown. The velocity is plotted against the normalized y direction at a normalized x value of 4. It is obvious that the velocity increases with an increase of permeability. At a permeability of $5.5 \times 10^{-13} \text{ m}^2$ the velocity is almost negligible. Further investigation of the x-component of the velocity illustrates the convection effects between channels. In Figure 5.41, the x-velocity is plotted against the normalized x-direction at the mid point of the gas diffusion layer for three permeability values. With a permeability value of $5.5 \times 10^{-13} \text{ m}^2$, the magnitude of the velocity is zero everywhere; thus, convection is negligible. Moreover, comparison of the corresponding velocity magnitudes for permeability values of $5.5 \times 10^{-11} \text{ m}^2$ and $5.5 \times 10^{-10} \text{ m}^2$, shows that the magnitude increase is proportional to the increase of permeability.

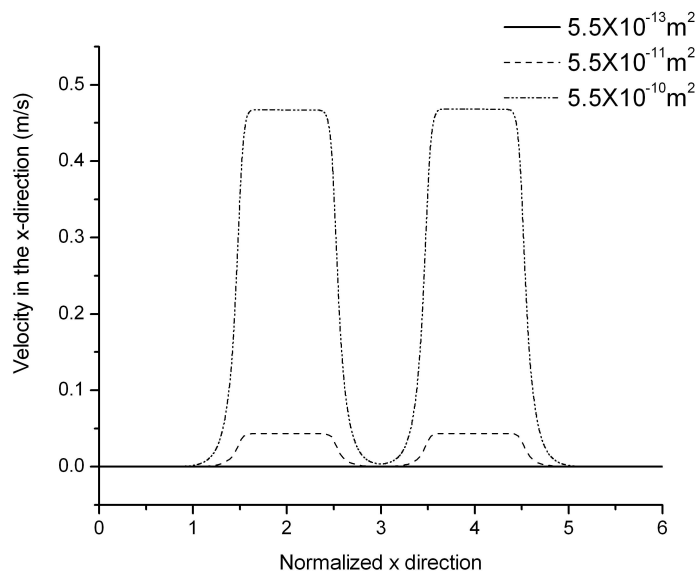


Figure 5.41: x-component of the velocity in m/s against the normalized x direction for different permeability values plotted at a normalized y value of 2.5.

5.4.4 Effect of Shoulder(Land)/Channel (S/C) Width Ratio

The shoulder(land) to channel width ratio is another important parameter to be investigated. The channel width controls the amount of oxidant being supplied, while the shoulder(land) width controls the area available for electron transfer through the bipolar plate. In this section, four different

CHAPTER 5. ISOTHERMAL MODEL RESULTS

ratios are compared to the base case (ratio is 1:1). The width ratio is calculated as follows,

$$\frac{\text{Shoulder}}{\text{Channel}} = \frac{W_s}{W_d} \quad (5.5)$$

where, W_s is the width of the shoulder and W_d is the channel width. Figure 5.42 gives a pictorial illustration of the two parameters; W_s and W_d .

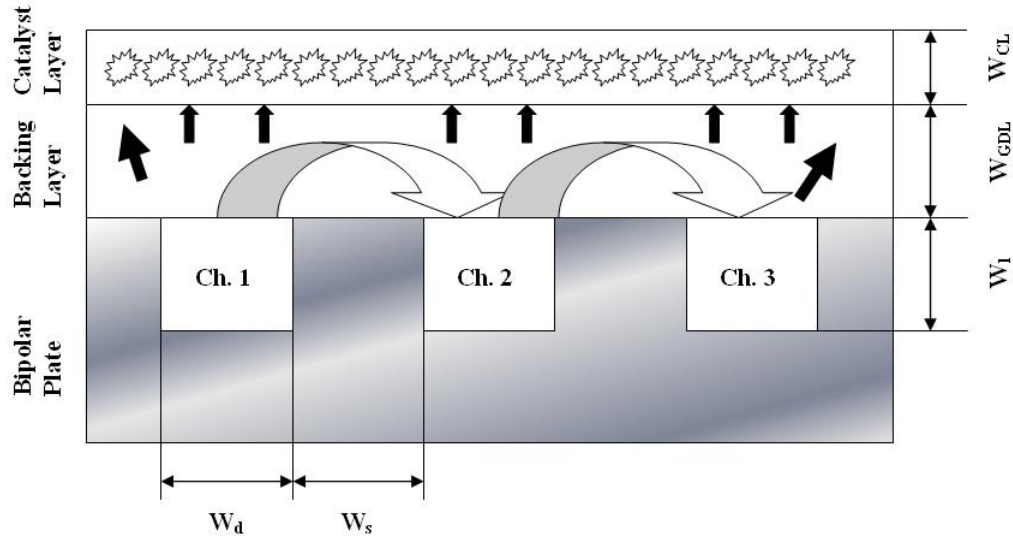


Figure 5.42: Illustration of shoulder to channel width ratio

The results are summarized in Tables 5.1 and 5.2. When the shoulder(land) to channel width ratio decreases, the channel area is increased and therefore, the amount of oxidant being supplied to the cell is increased.

Table 5.1: Effect of shoulder/channel width ratio on the performance of the cathode using the Leverette function

Ratio	Current Density (A/m^2)
2:1	3764
1:2	4170
1:1	3899
3:1	3551
1:3	4194

CHAPTER 5. ISOTHERMAL MODEL RESULTS

Table 5.2: Effect of shoulder/channel width ratio on the performance of the cathode - Brooks and Corey relation

Ratio	Current Density (A/m^2)
2:1	3749
1:2	4145
1:1	3884
3:1	3539
1:3	4166

The decrease in the width ratio results in an increase in the total current density in the catalyst layer. The gain in current density with the decrease of the ratio is attributed to the increase of oxidant flow into the cell. On the other hand, when the ratio is increased, the overall performance of the cathode decreases due to a lower gas flow rate. This is also illustrated in Figure 5.43. The total current density along the normalized cell length for different parts of the catalyst layer is shown. It is apparent that with the decrease of the width ratio, the overall current density increases and the difference is most apparent around the catalyst layer/membrane interface. Thus, to get higher performance, a shorter shoulder width is preferred. However, it should be noted that the shoulders are needed for current collection. Decreasing the shoulder/channel width ratio even further might result in higher cell ohmic resistance and therefore higher losses. This helps explain the small difference in performance gain when the width ratio is decreased from 1:2 to 1:3.

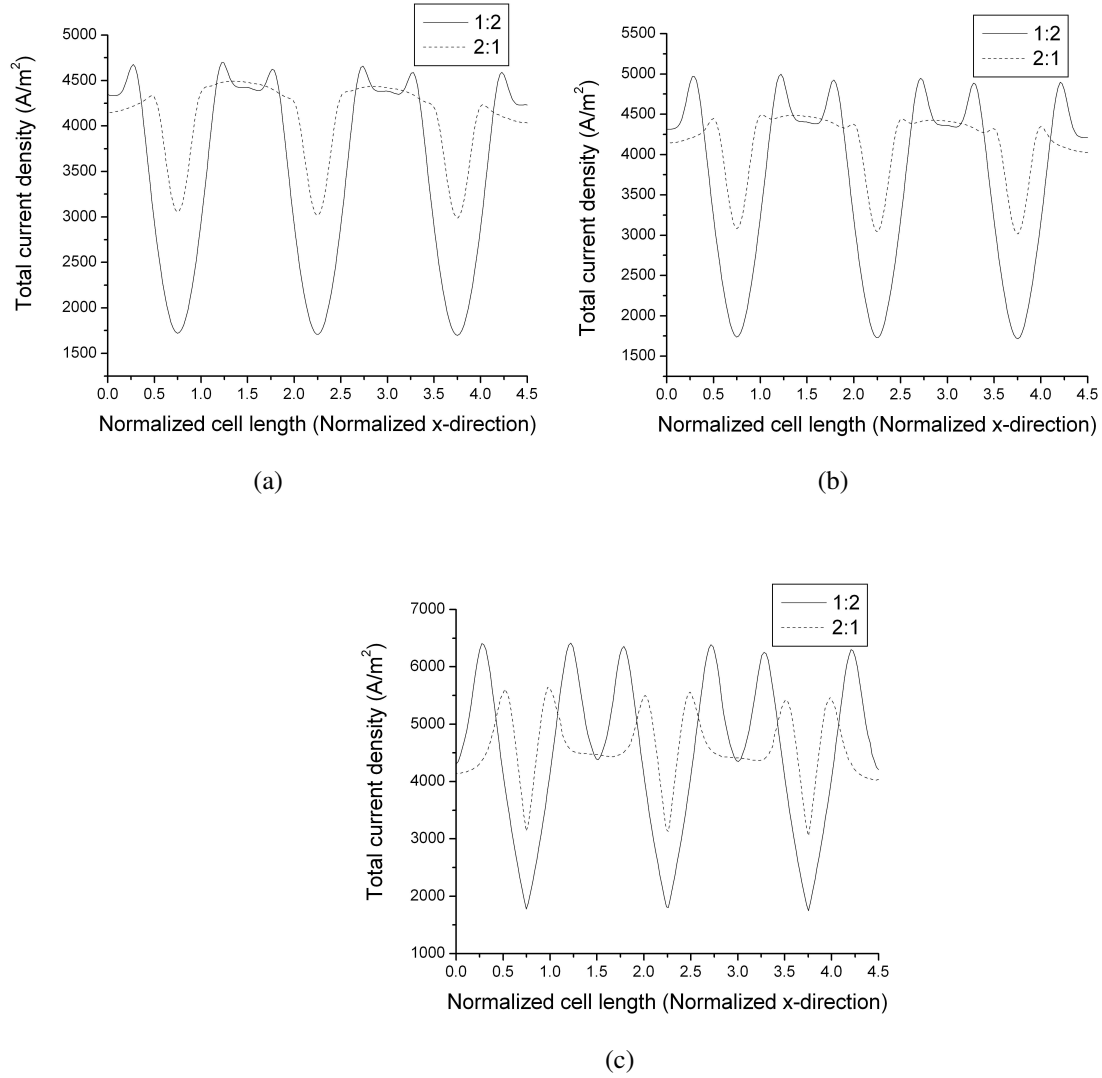


Figure 5.43: Total current density in the catalyst layer (A/m^2) along the normalized x-direction at different y positions (a) 3; (b) 3.5; (c) 4; with an S/C ratio of 1:2 and 2:1 and the capillary pressure is represented by the Leverette function

CHAPTER 5. ISOTHERMAL MODEL RESULTS

The effect of the shoulder/channel width ratio on the cross flow phenomenon should also be mentioned in this section. Figure 6.27 a & b is of the liquid water saturation profile in the backing and catalyst layers with an S/C width ratio of 2:1 and 1:2, respectively. The cross flow between two adjacent channels is decreased with an increase in S/C width ratio. The species (liquid water, vapor water and oxygen) need to travel a longer distance from one channel to reach the adjacent channel. However, when the S/C ratio is 1:2, the distance between two adjacent channels is decreased and therefore, the cross flow is enhanced. This is also illustrated through the velocity in the x-direction as seen in Figure 5.45. The magnitude of the velocity is halved with the doubling of the S/C width ratio. Therefore, the mass flow rate of liquid water is halved with the doubling of the S/C width ratio. This implies that the pressure gradient created is increased with the increase of the channel width.

CHAPTER 5. ISOTHERMAL MODEL RESULTS

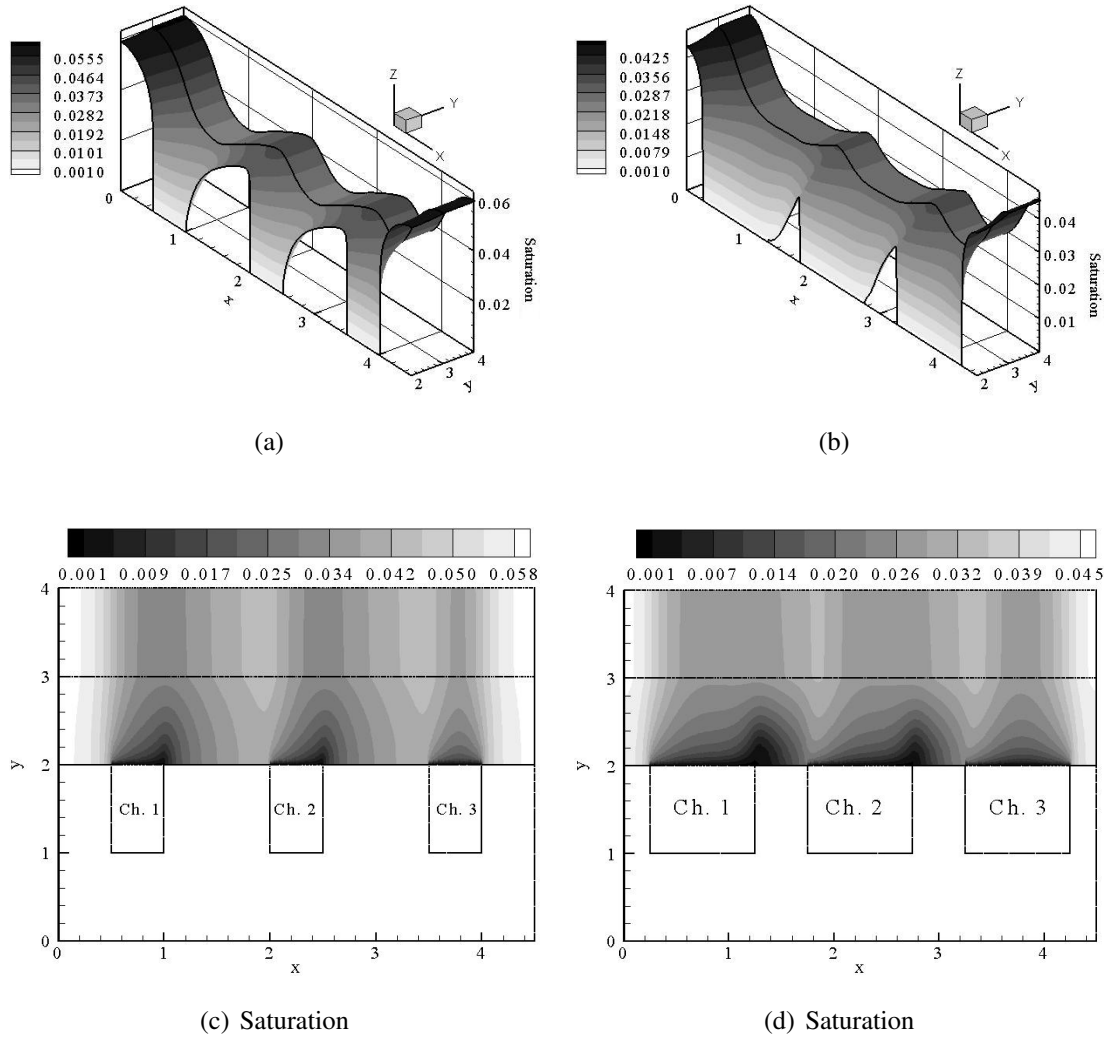


Figure 5.44: 3-D surface plot of liquid water saturation in the gas diffusion and catalyst layers using the Leverette function and an S/C width ratio of (a) 2 : 1; (b) 1 : 2. Profile of liquid water saturation in the backing and catalyst layers with a S/C width ratio of (c) 2 : 1; (d) 1 : 2 using the Leverette function. x and y coordinates have been normalized for better presentation of results. (see Figure 5.1)

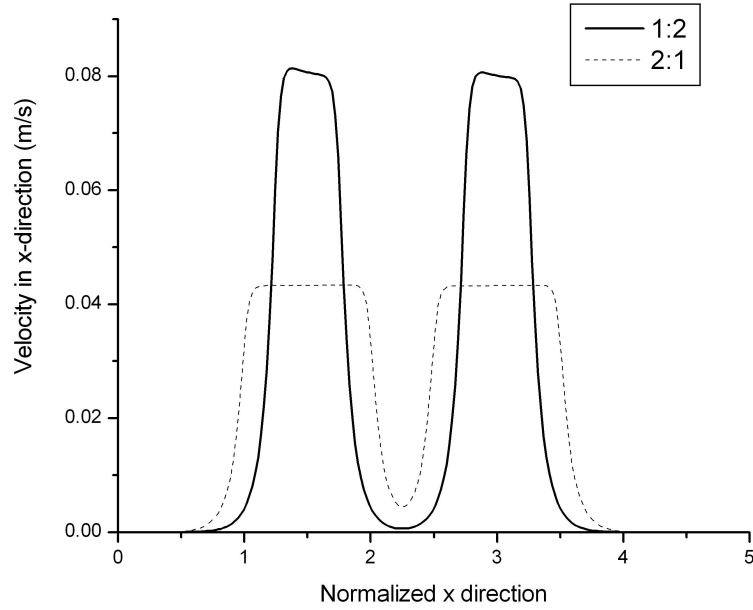


Figure 5.45: x-component of the velocity in m/s against the normalized x direction for an S/C width ratios of 1:2 and 2:1 plotted at a normalized y value of 2.5.

Finally, studying the saturation profiles in Figure 6.27 demonstrates that a decrease in shoulder/channel width ratio results in better removal of liquid water from the cell. The total liquid water saturation in the cathode with an S/C width ratio of 1:2 is lower than that with an S/C width ratio of 2:1. This is attributed to the increased channel area; consequently, an increased area for liquid water removal.

Chapter 6

Non-Isothermal Model Results

The purpose of this chapter is to put forward a discussion of the heat transfer in the cathode of a polymer electrolyte membrane fuel cell and its effects on species transport and the electrochemical reaction. The temperature profile as well as the water distribution in the cathode will be examined. In the first section of this chapter, the single phase, non-isothermal model results are discussed. The temperature distribution, the effect of heat generation on the water vapor distribution, cross flow phenomenon and the electrochemical reaction are investigated. In addition, some differences between the single phase, isothermal and non-isothermal models are examined. The second section deals with the multi-phase, non-isothermal model results. The temperature profile along with the liquid water saturation profiles are considered. Further, the effect of heat addition on the evaporation rate of liquid water is studied. The last section is dedicated to a sensitivity study. The effects of the permeability, inlet relative humidity and shoulder(land)/channel width ratio on the temperature are examined. To better understand the results of this section, recall the modeling domain shown in Figure 6.1.

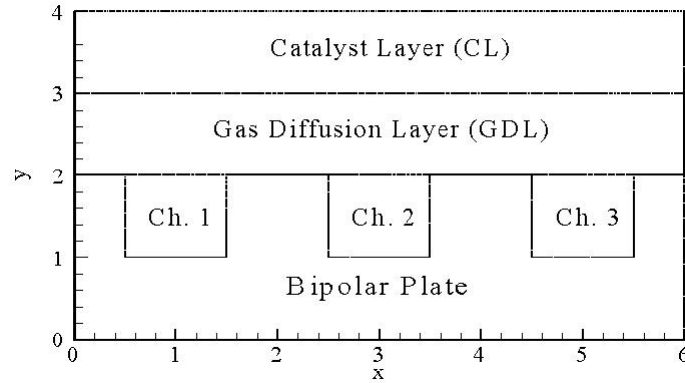


Figure 6.1: Modeling Domain - x and y axes have been normalized - flow is in the y -direction ($(0 \leq x \leq 6)$ denotes a distance of 6 mm , $(0 \leq y \leq 2)$ denotes a distance of 2 mm , $(2 \leq y \leq 3)$ denotes a distance of $150 \mu\text{m}$ and $(3 \leq y \leq 4)$ denotes a distance of $5 \mu\text{m}$)

6.1 Single Phase Model Results

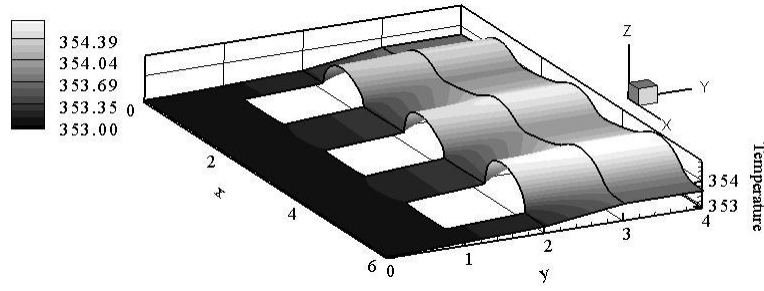
The single phase, isothermal model presented in the last chapter led to the need for a multi-phase model since the relative humidity in the backing and catalyst layers was shown to be above 1. In real life applications of PEM fuel cells, the generation of heat takes place and therefore, the temperature of the cell varies affecting its thermodynamic properties. In this thesis, the saturation pressure is of great interest since it directly affects the relative humidity in the layers and governs the evaporation and condensation of water. This section is designed to show the results of a single phase, non-isothermal model and proper conclusions are made. In order to be able to carry out a comparison of the isothermal and non-isothermal cases, the oxidant is fully humidified air, there exists some pressure drop of 349 Pa along the channel flow field due to its geometry, the operating conditions of the cell are 80°C and 5 atm and the cell voltage is kept at 0.7 V .

The variation of temperature in the bipolar plate, gas diffusion layer and catalyst layer is shown in Figure 6.2. The temperature variation in the bipolar plate is very small due to its high thermal conductivity. High thermal conductivity is necessary for uniform distribution of temperature and eventually for being able to control the stack temperature; see section 1.1. In the gas diffusion layer, the transfer of heat through convection is very apparent. In addition, it is important to note

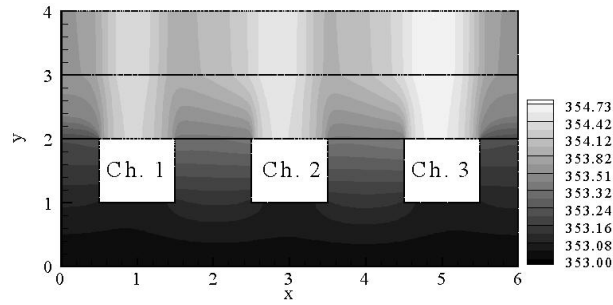
CHAPTER 6. NON-ISOTHERMAL MODEL RESULTS

that the temperature is higher under the channel areas than the areas under the land. This can be explained by examining the boundary conditions. The temperature at the bipolar plate ($y = 0$) is specified at $80^{\circ}C$, while convective heat transfer occurs at the channel boundaries with the gas temperature being $80^{\circ}C$. Therefore, it seems that heat addition through convection is significant. Further, the average temperature over the catalyst layer is higher than that over the gas diffusion layer due to the heat addition through the electrochemical reaction.

CHAPTER 6. NON-ISOTHERMAL MODEL RESULTS



(a)



(b) Temperature (K)

Figure 6.2: (a) 3-D surface plot of temperature in the bipolar plate and gas diffusion and catalyst layers. Note that $y = 4$ is the catalyst layer/membrane interface; (b) Temperature (K) profile in the cathode bipolar plate and backing and catalyst layers for the single phase, non-isothermal model. x and y coordinates have been normalized for better presentation of results. (see Figure 6.1)

CHAPTER 6. NON-ISOTHERMAL MODEL RESULTS

Next, the saturation pressure in the gas diffusion and catalyst layers is investigated and its profile is presented through Figure 6.3. Since the saturation pressure is temperature dependent, its distribution follows that of the temperature very closely. At high temperature values a high saturation pressure is reached.

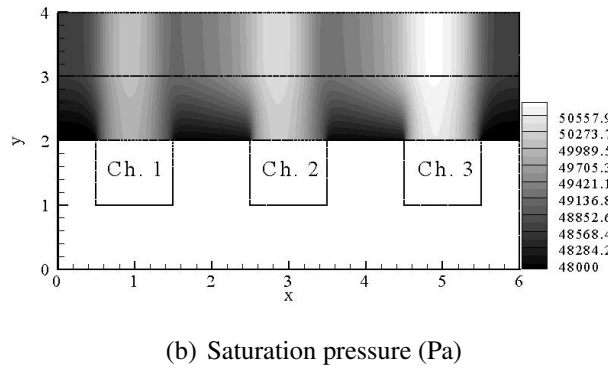
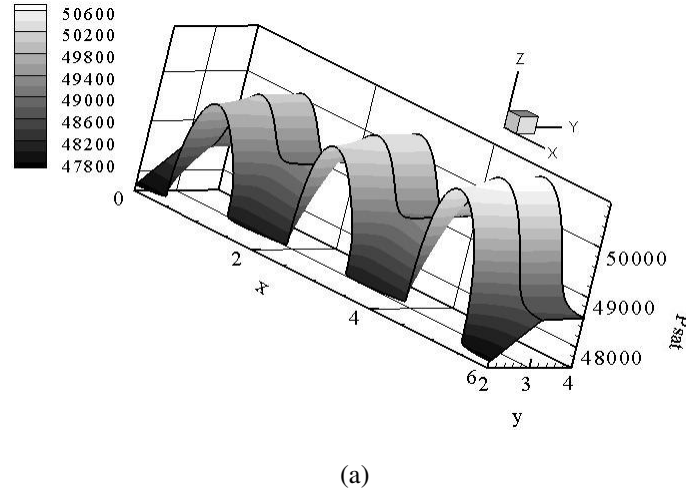
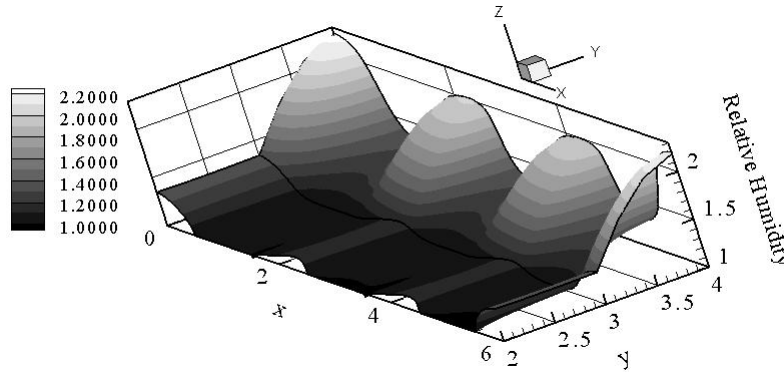


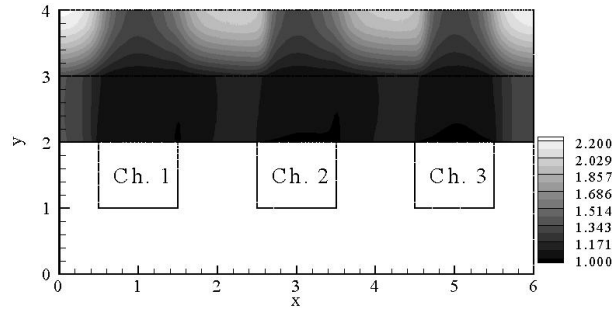
Figure 6.3: (a) 3-D surface plot of saturation pressure in the gas diffusion and catalyst layers. Note that $y = 4$ is the catalyst layer/membrane interface; (b) Saturation pressure (Pa) profile in the cathode backing and catalyst layers for the single phase, non-isothermal model. x and y coordinates have been normalized for better presentation of results. (see Figure 6.1)

In order to investigate the electrochemical reaction, the relative humidity in the backing and catalyst layers is plotted in Figure 6.4. The production of water is higher under the land areas than under the channel areas implying that the reaction takes place under the land areas. Further, the

highest rate of water production is reached at the catalyst layer/membrane interface. Figure 6.5 can be used to further explain this trend.



(a)



(b) Relative humidity

Figure 6.4: (a) 3-D surface plot of relative humidity in the gas diffusion and catalyst layers. Note that $y = 4$ is the catalyst layer/membrane interface; (b) Relative humidity profile in the cathode backing and catalyst layers for single phase, non-isothermal model. x and y coordinates have been normalized for better presentation of results. (see Figure 6.1)

Figure 6.5 shows the two-dimensional distribution of the relative humidity, or water vapor. Relative humidity along the cell length is plotted at different normalized y values. $y = 2.5$ corresponds to the mid point of the gas diffusion layer, $y = 3$ corresponds to the gas diffusion layer/catalyst layer interface and $y = 4$ corresponds to the catalyst layer/membrane interface. The trend again shows that the water production is increased under the land areas and its highest value is reached at the catalyst layer/membrane interface.

CHAPTER 6. NON-ISOTHERMAL MODEL RESULTS

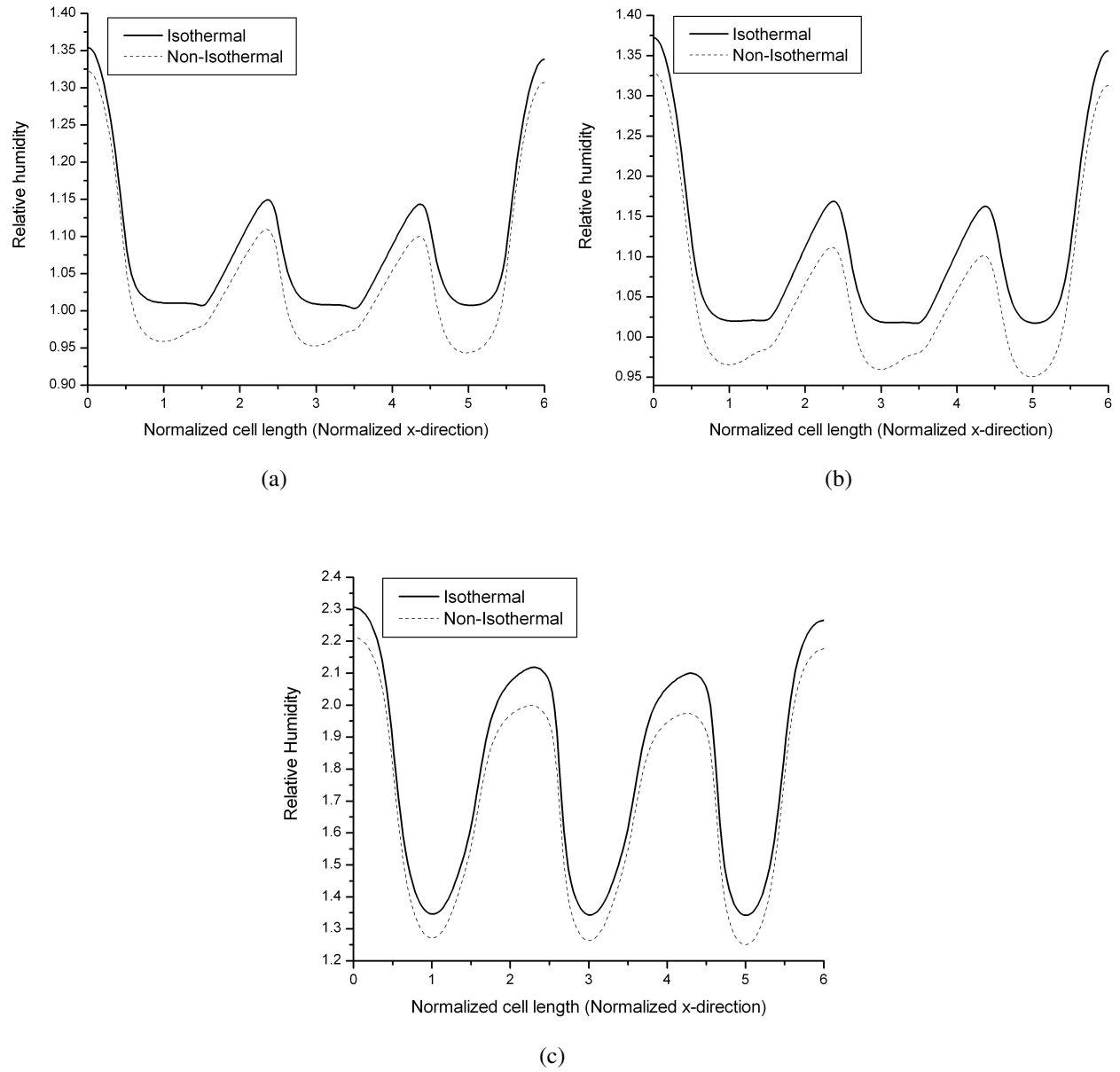


Figure 6.5: Relative humidity for the single phase isothermal and non-isothermal cases along the normalized x-direction for different normalized y values (a) 2.5; (b) 3; (c) 4

CHAPTER 6. NON-ISOTHERMAL MODEL RESULTS

Figure 6.5 is also used to compare the relative humidity in the backing and catalyst layers for both the isothermal and non-isothermal cases. It is apparent that with the inclusion of the energy equation, the relative humidity decreases. This is so since the relative humidity is dependent on the saturation pressure, which in turn is dependent on the temperature. The average relative humidity is decreased by 5% with the variation of temperature. Also, it is important to note that the trend is very similar in both cases. This implies that the temperature does not affect the species transport in the gas diffusion and catalyst layers. In order to investigate this point even further, the rate of water production is investigated for both the isothermal and non-isothermal cases and is presented in Figure 6.6. The rate of water production is plotted against the normalized cell length at different points along the catalyst layer thickness. For both cases, the rate of water production increases along the thickness of the catalyst layer. In addition, it is higher under the land areas, implying that the reaction occurs more readily under these sites. Further, it should be mentioned that the production of water is lowered with the variation of temperature. In fact, comparing the resultant current density in the catalyst layer for both cases reveals that heat production leads to a slight decrease in performance (around 1%). Revisiting the Butler Volmer equation, equation 3.29, this decrease is expected due to the dependency of the current density in the catalyst layer on temperature. However, the temperature change is not large enough to create a more significant difference. The slight decrease in the average current density due to heat addition is also seen in Figure 6.7.

CHAPTER 6. NON-ISOTHERMAL MODEL RESULTS

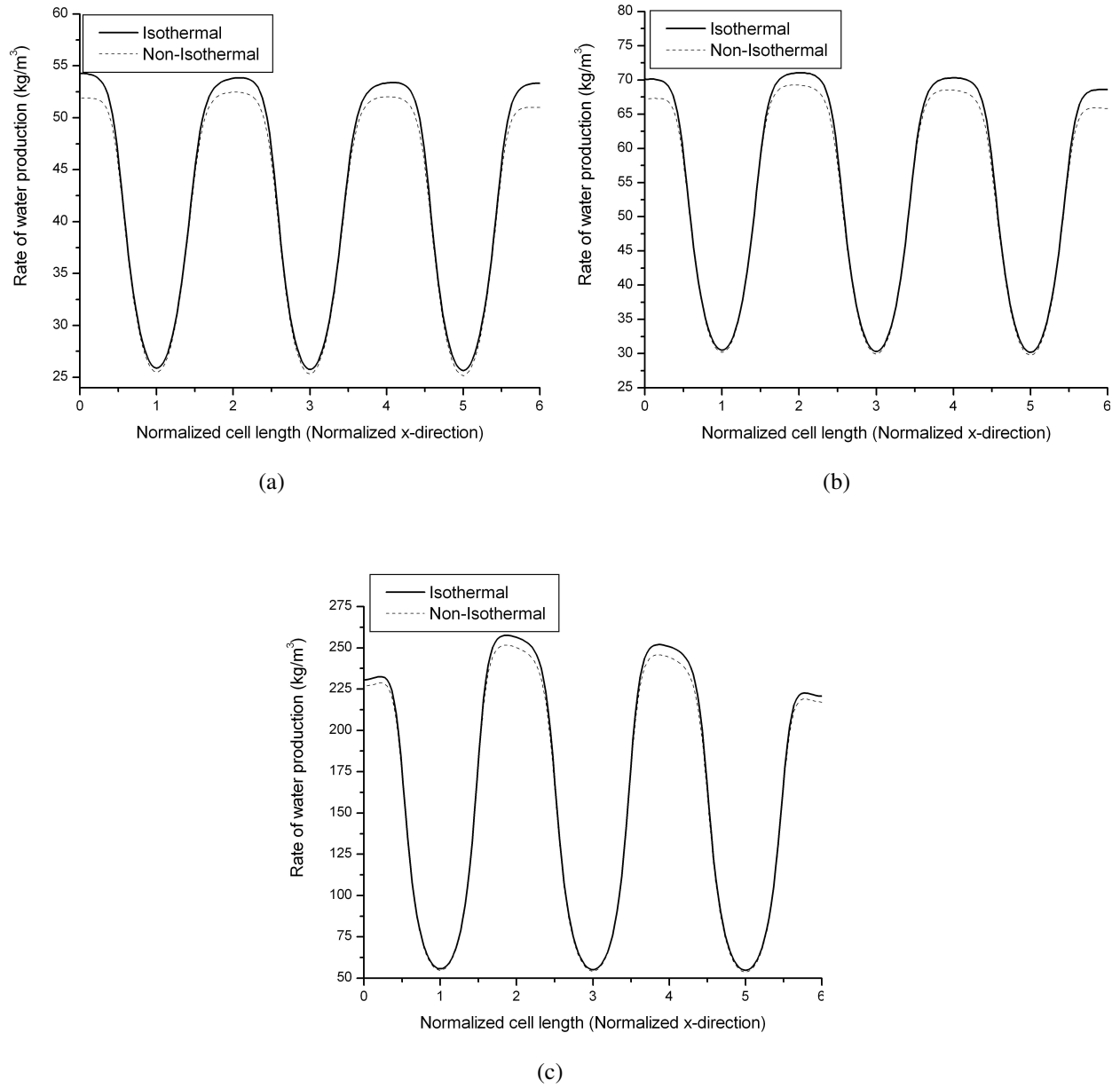


Figure 6.6: Rate of water production in (kg/m^3) for the single phase isothermal and non-isothermal cases along the normalized x-direction for different normalized y values (a) 3; (b) 3.5; (c) 4

CHAPTER 6. NON-ISOTHERMAL MODEL RESULTS

Further, it should be noted that from Figure 6.7, it is clear that the trend of the total current density in both models (isothermal and non-isothermal) is very similar. The change in temperature is not significant enough in order to alter the path taken by species and therefore, the overall trend of the electrochemical reaction.

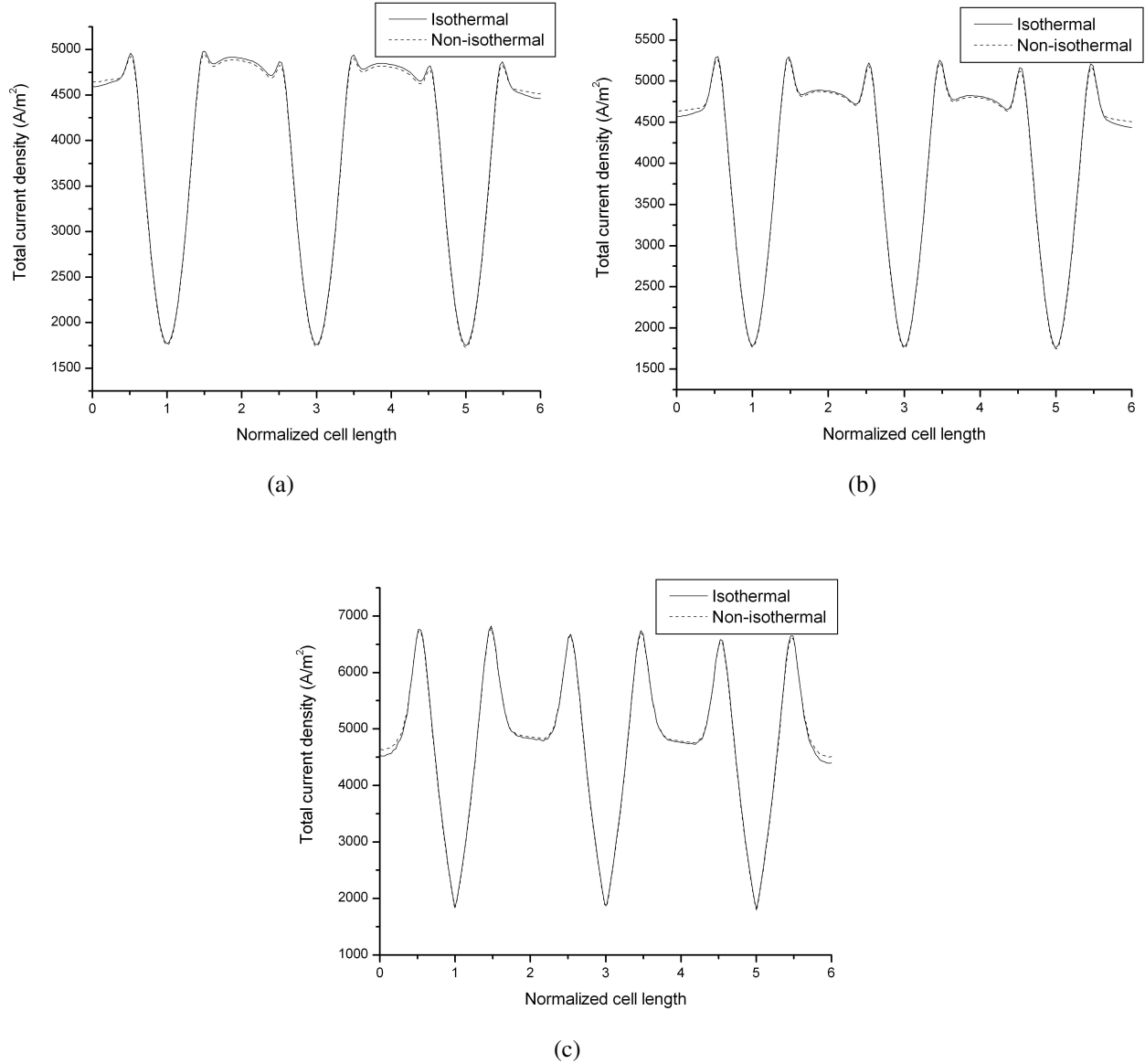


Figure 6.7: Total current density (A/m^2) for the single phase isothermal and non-isothermal cases along the normalized x-direction for different normalized y values (a) 3; (b) 3.5; (c) 4

Finally, it should be added that even with the consideration of the energy equation for the single phase model, the relative humidity in the backing and catalyst layers is still higher than 100% in some areas. Therefore, there exists the need to investigate the multi-phase, non-isothermal model, which will be discussed in the next section.

6.2 Multi-Phase Model Results

In this section, the results of the multi-phase, non-isothermal model are presented. The capillary pressure is modeled using the Leverette function, the operating conditions of the cell are 80°C and 5 atm, the cell voltage is 0.7 V, the oxidant is fully humidified air and the permeability of the porous media is $5.5 \times 10^{-11} \text{ m}^2$.

The temperature profile in the bipolar plate, gas diffusion layer and catalyst layer is given by Figure 6.8. In comparison to the single phase model temperature profile, it can be seen that the temperature variation is very small. Water production is in the liquid form only and the inlet relative humidity is 100%; thus, liquid water evaporates. The evaporation of liquid water results in the absorption of heat as mentioned earlier in the formulation section, section 3.5.6.

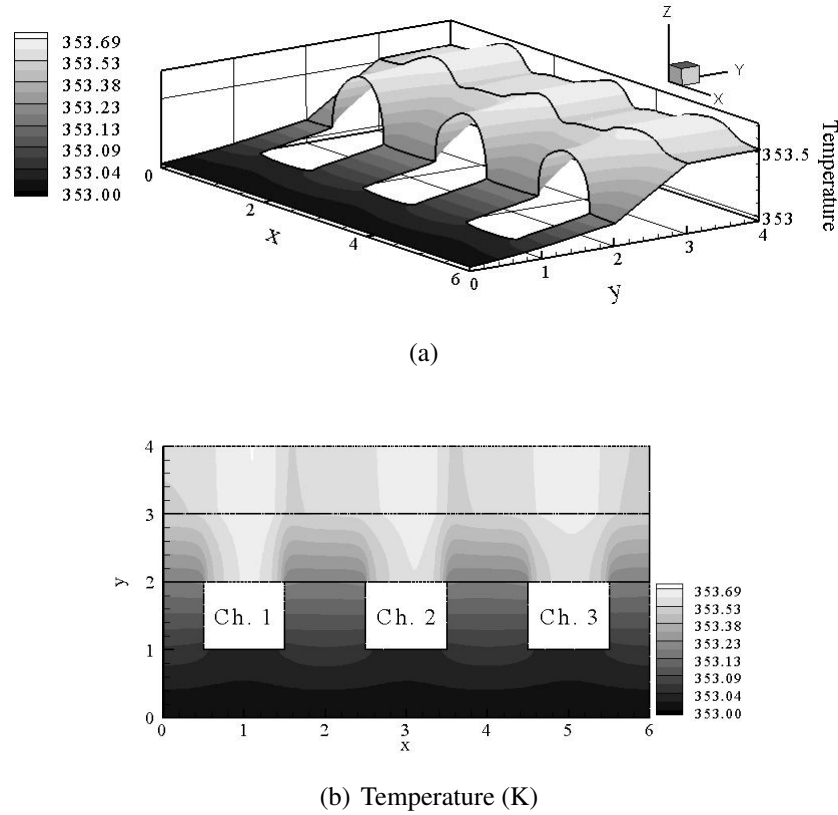


Figure 6.8: (a) 3-D surface plot of the temperature in the bipolar plate and backing and catalyst layers. Note $y = 4$ is the catalyst layer/membrane interface; (b) Contour plot of temperature (K) in the bipolar plate and gas diffusion and catalyst layers for the multi-phase model. The Leverette function is used to describe the capillary pressure relation against the liquid water saturation. x and y coordinates have been normalized for better presentation of results. (see Figure 6.1)

Figure 6.9 is a representation of the temperature profile along the normalized x -direction for different normalized y values. The permeability value used to generate this figure is $5.5 \times 10^{-11} m^2$. This figure can be used to show the two-dimensional variation of temperature in the gas diffusion and catalyst layers. It is apparent that the temperature increases very rapidly in the gas diffusion layer and its profile is very much two-dimensional. In the catalyst layer, the temperature profile is more one-dimensional in the x -direction. This trend can be attributed to the production of liquid water in the catalyst layer. Since the production of liquid water increases along the thickness of the catalyst layer, the amount of water evaporated increases; thus, more heat is absorbed.

Next the saturation of liquid water in the cathode should be investigated and Figure 6.10 shows

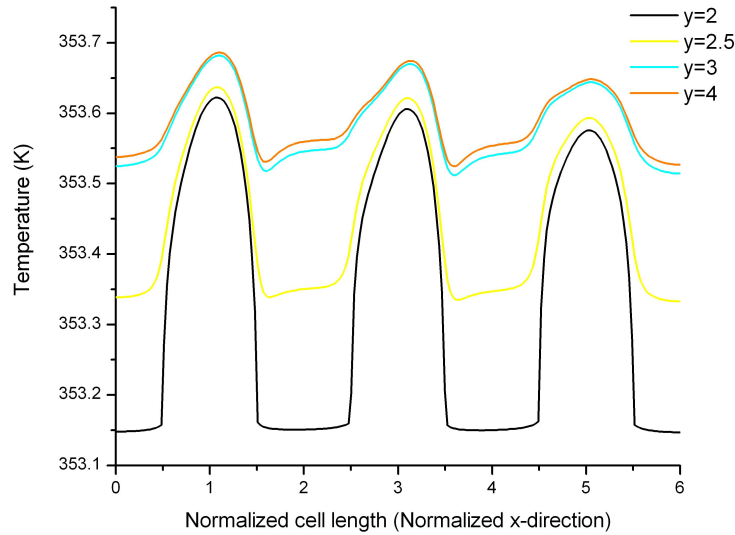
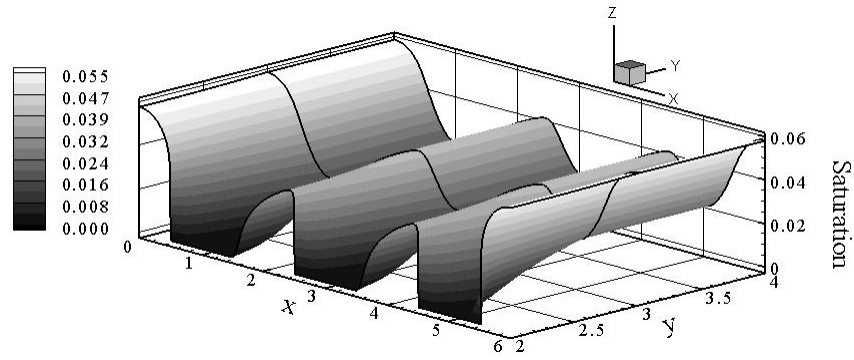


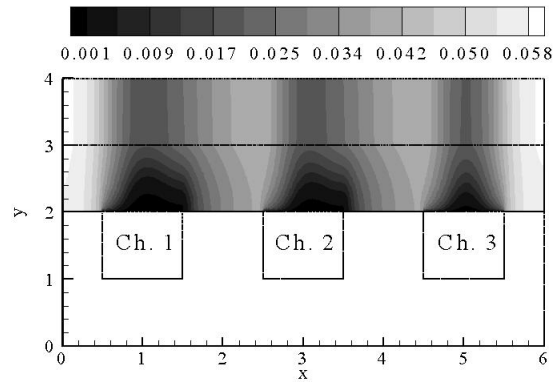
Figure 6.9: Temperature variation along the x-direction for different y values for a permeability value of $5.5 \times 10^{-11} \text{ m}^2$

the surface plot of the liquid water saturation in the backing and catalyst layers for the two-phase, non-isothermal model. The amount of liquid water increases towards the catalyst layer/membrane interface due to the electrochemical reaction. The cross flow phenomenon is also obvious.

Since the variation in temperature is being accounted for, the saturation profile should be investigated against that of the multi-phase, isothermal model. It is essential to find out how the liquid water is affected due to temperature. As expected, the saturation will decrease due to the heat generation as shown in Figure 6.11. Due to the heat generation, the saturation decreases by up to 2%. The figure shows that the saturation follows a similar profile in both cases. The cross flow phenomenon due to the pressure drop and the high permeability value is very apparent in both cases. In addition, the saturation level increases along the direction of the flow (y-direction).



(a)



(b) Saturation

Figure 6.10: (a) 3-D surface plot of the liquid water saturation in the backing and catalyst layers. Note $y = 4$ is the catalyst layer/membrane interface; (b) Contour plot of liquid water saturation in the gas diffusion and catalyst layers for the multi-phase model. The Leverette function is used to describe the capillary pressure relation against the liquid water saturation. x and y coordinates have been normalized for better presentation of results. (see Figure 6.1)

CHAPTER 6. NON-ISOTHERMAL MODEL RESULTS

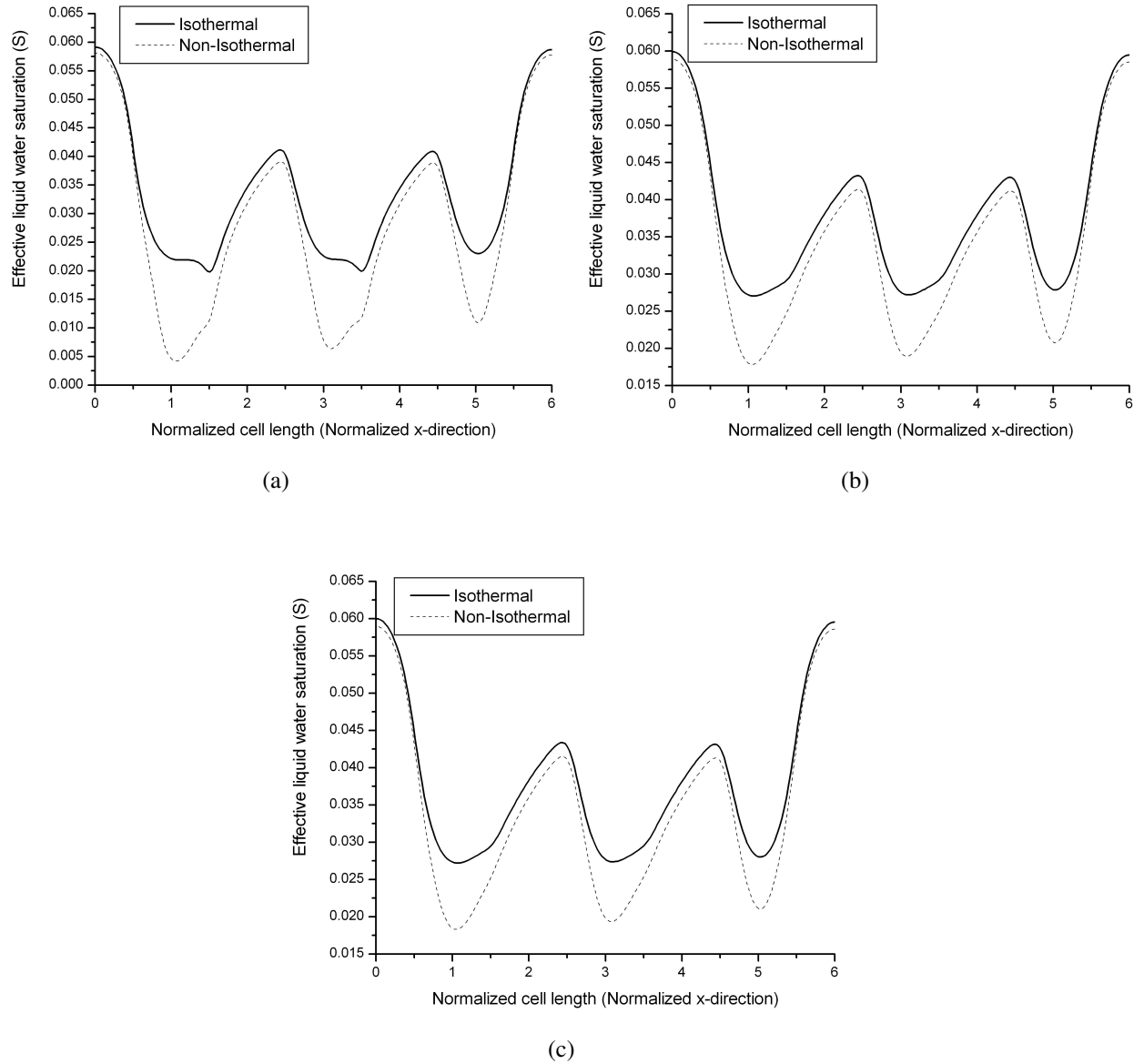


Figure 6.11: Comparison of the saturation levels of the isothermal and non-isothermal models along the normalized x-direction for different normalized y values with a permeability value of $5.5 \times 10^{-11} \text{ (m}^2\text{)}$ (a) 2.5; (b) 3; (c) 4

6.3 Sensitivity Analysis for Multi-Phase Model

In this section a sensitivity analysis will be carried out to study the following cases,

1. Inlet relative humidity of 100% vs. that of 50% - To show the effect of the inlet relative humidity on the temperature distribution
2. Cases with permeability values of $5.5 \times 10^{-13} \text{ (m}^2\text{)}$ and $5.5 \times 10^{-10} \text{ (m}^2\text{)}$ - To show the effect of cross flow on the distribution of temperature
3. Shoulder/channel width ratio of 1:2 and 2:1 - To show the effect of the shoulder/channel width ratio on the distribution of temperature

The capillary pressure dependency on liquid water saturation is modeled using the Leverette function and the cell voltage is 0.7 V

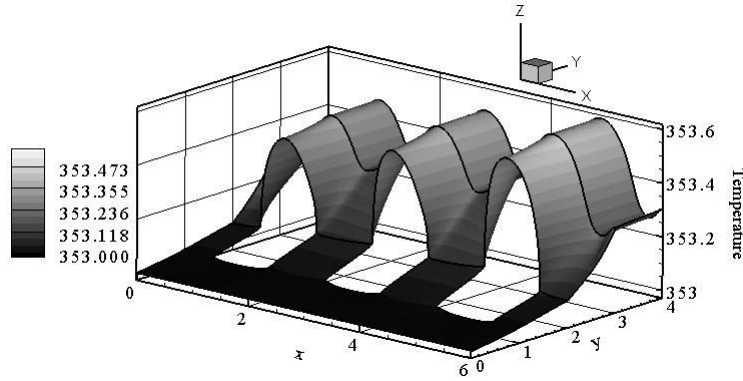
6.3.1 Effect of Inlet Relative Humidity

The multi-phase model has been solved under the assumption that the production of water is in liquid form only. Thus, the inlet relative humidity should have a significant effect on the temperature distribution. The evaporation of the liquid water will result in the loss of heat and therefore affecting the temperature. In this section, the effect of reducing the inlet relative humidity from 100% to 50% on the temperature profile will be investigated. The permeability of the porous media is $5.5 \times 10^{-11} \text{ (m}^2\text{)}$, the cell voltage is 0.7 V and the pressure drop is 349 Pa and 329 Pa for an inlet relative humidity of 100% and 50%, respectively. Figure 6.12 illustrates the two-dimensional variation of the temperature in the bipolar plate and backing and catalyst layers when the inlet relative humidity is 50%. It is seen that the temperature increases along the thickness of the layers. It is higher at the areas under the channel than those under the land. The profile of the temperature is very close to that when the inlet relative humidity is 100%. Therefore, Figure 6.13 is constructed to illustrate the two-dimensional variation of temperature for the two values of inlet relative humidity. The observed trends can be summarized as follows,

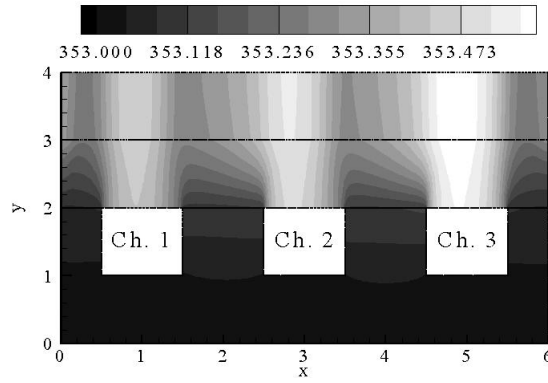
CHAPTER 6. NON-ISOTHERMAL MODEL RESULTS

- First, the temperature profile is similar for both values of inlet relative humidity. The temperature increases in the thickness of the cell (from the channel towards the membrane)
- The transfer of energy through convection is apparent in both cases.
- Finally, the temperature associated with the 100% inlet relative humidity is higher than that with an inlet relative humidity of 50%. With an inlet relative humidity of 50%, more liquid water evaporates in order to reach the equilibrium point between the two phases of water. Hence, more energy is released due to this evaporation.

CHAPTER 6. NON-ISOTHERMAL MODEL RESULTS



(a)



(b) Temperature (K)

Figure 6.12: (a) 3-D surface plot of the temperature in the bipolar plate and the backing and catalyst layers with an inlet relative humidity of 50%. Note $y = 4$ is the catalyst layer/membrane interface; (b) Contour plot of the temperature in the bipolar plate and the gas diffusion and catalyst layers for the multi-phase model with an inlet relative humidity of 50%. The Leverette function is used to describe the capillary pressure relation against the liquid water saturation. x and y coordinates have been normalized for better presentation of results. (see Figure 6.1)

CHAPTER 6. NON-ISOTHERMAL MODEL RESULTS

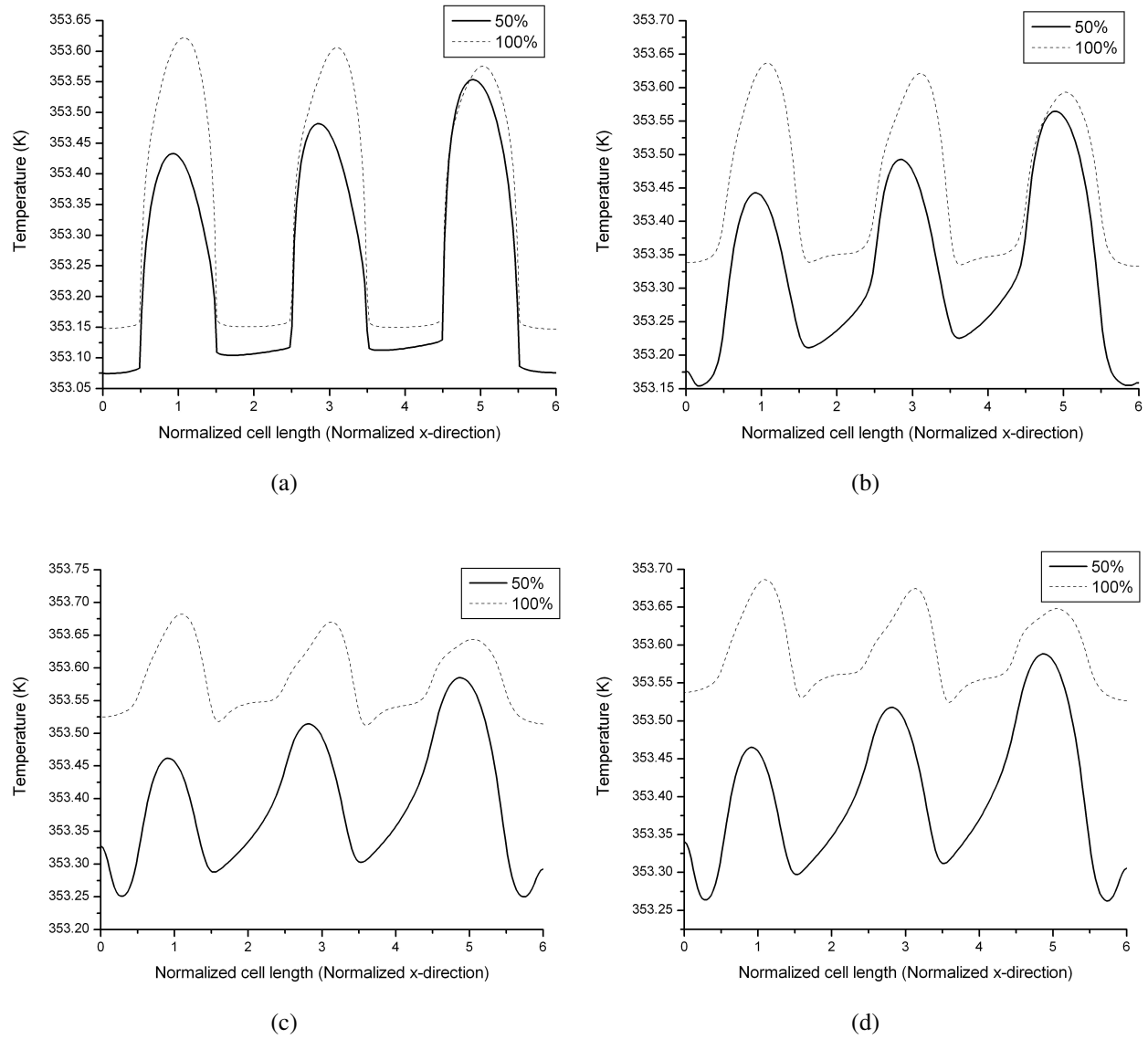


Figure 6.13: Effect of inlet relative humidity on the temperature variation along the normalized x-direction for different normalized y values (a) 2; (b) 2.5; (c) 3; (d) 4

CHAPTER 6. NON-ISOTHERMAL MODEL RESULTS

The rate of water evaporation for the multi-phase, isothermal and non-isothermal cases with an inlet relative humidity of 50% along the normalized x-direction for different normalized y values is shown in Figure 6.14. The evaporation rate corresponding to the isothermal model is slightly higher than that corresponding to the non-isothermal model. The increase in temperature in the non-isothermal model results in an overall decrease in the reaction rate as shown earlier; thus, a decrease in the amount of liquid water available for evaporation. In addition, revisiting equation 3.63, it can be seen that the rate of evaporation is dependent on the saturation pressure. An increase in temperature results in an increase in saturation pressure and a decrease in the evaporation rate.

CHAPTER 6. NON-ISOTHERMAL MODEL RESULTS

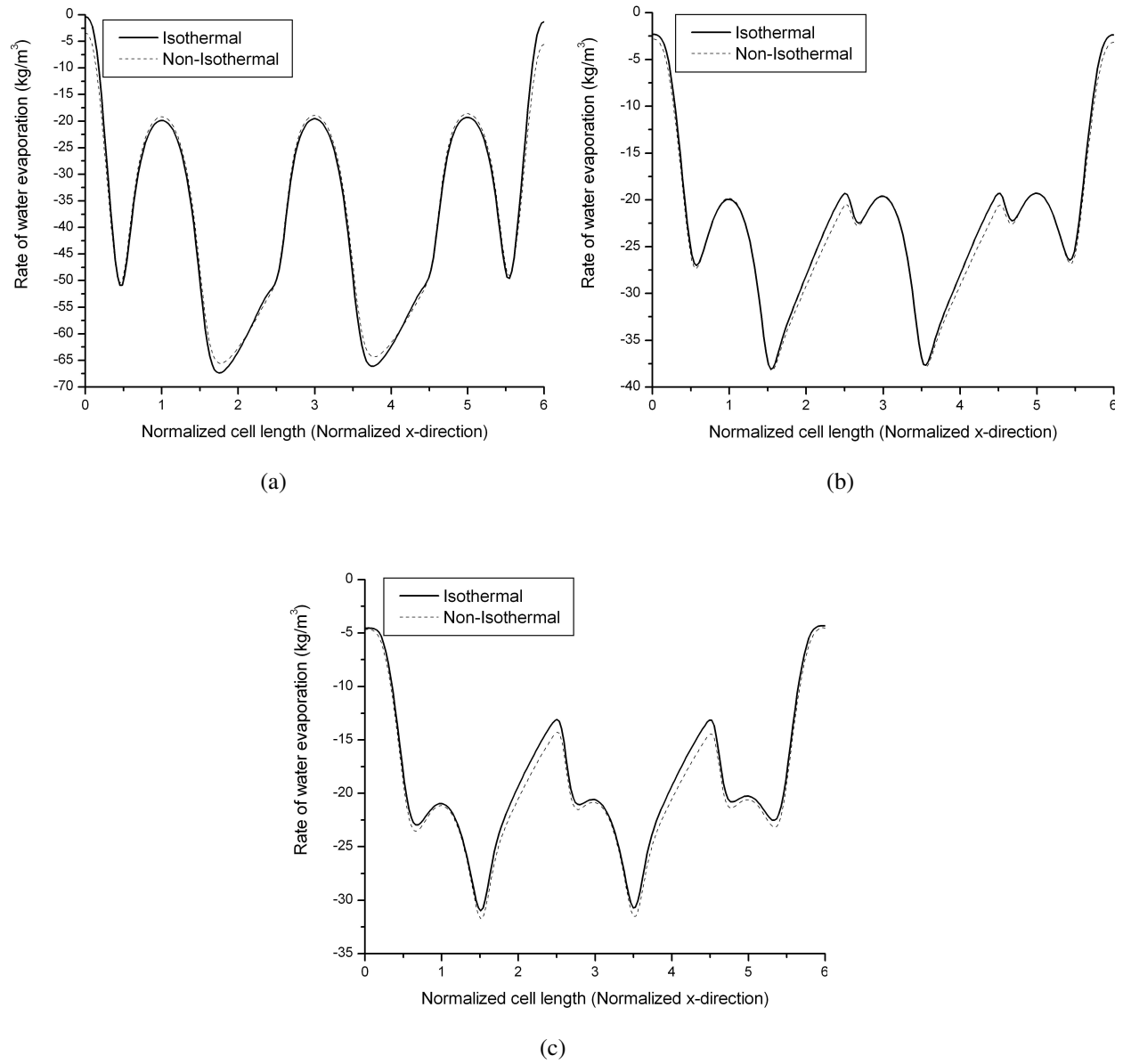
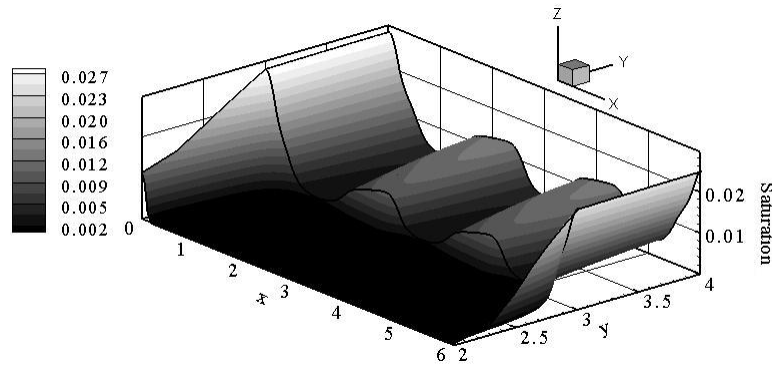


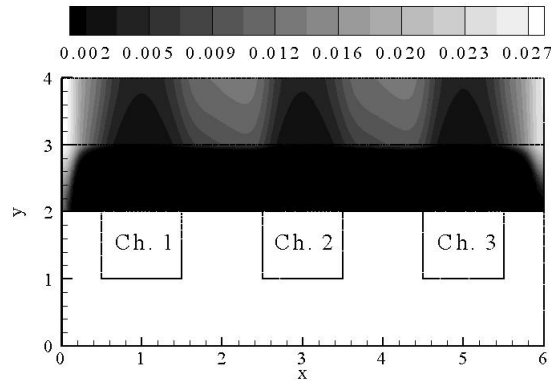
Figure 6.14: Rate of water evaporation for the isothermal and non-isothermal cases with an inlet relative humidity of 50% along the normalized x-direction for different normalized y values (a) 3; (b) 3.5; (c) 4

CHAPTER 6. NON-ISOTHERMAL MODEL RESULTS

Finally, the liquid water saturation in the backing and catalyst layers for an inlet relative humidity of 50% is given in Figure 6.15. It is seen that at the areas under the land, the liquid water saturation is higher in the catalyst layer. This explains the higher evaporation term under these areas and in turn the lower temperature value under these areas. With the evaporation of liquid water more heat is absorbed.



(a)



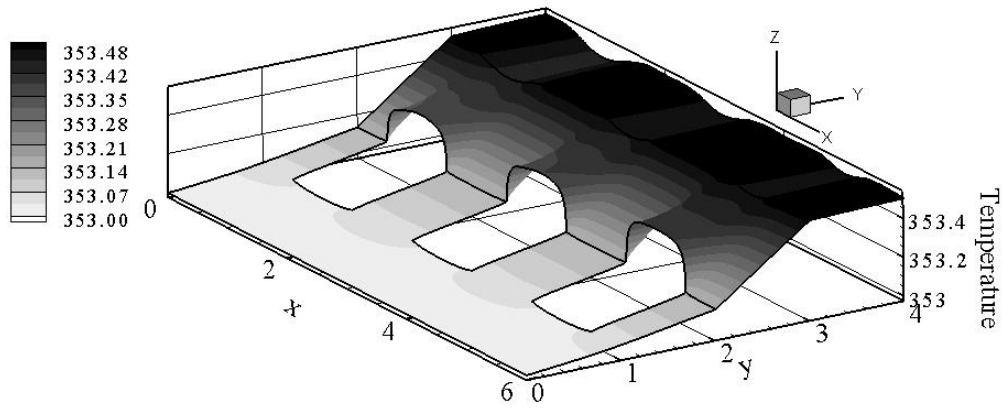
(b) Saturation

Figure 6.15: (a) 3-D surface plot of the liquid water saturation in the backing and catalyst layers with an inlet relative humidity of 50%. Note $y = 4$ is the catalyst layer/membrane interface; (b) Contour plot of liquid water saturation in the gas diffusion and catalyst layers for the multi-phase model with an inlet relative humidity of 50%. The Leverette function is used to describe the capillary pressure relation against the liquid water saturation. x and y coordinates have been normalized for better presentation of results. (see Figure 6.1)

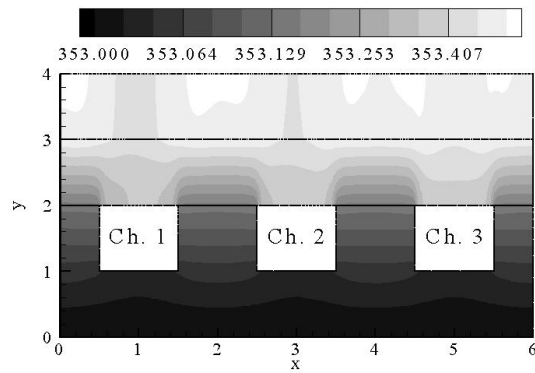
6.3.2 Effect of Permeability

From the discussion of the multi-phase, isothermal model it was concluded that the permeability of the porous media plays a significant role in determining the performance of the cell as well as the amount of liquid water. Therefore, it is necessary to investigate the effects of permeability on the temperature profile. In addition, it is necessary to investigate how the temperature change effects the cross flow phenomenon. Since pressure drop along the channel flow field is taken into account, the transfer of energy through convection in the gas diffusion and catalyst layers is considered.

Figures 6.16 and 6.17 show the distribution of the temperature in the bipolar plate and gas diffusion and catalyst layers for a permeability value of $5.5 \times 10^{-13} \text{ (m}^2\text{)}$ and $5.5 \times 10^{-10} \text{ m}^2$, respectively. It is seen that with a high permeability value, the temperature is increased. This can be explained by the increased total current density. In addition, the transfer through convection is very clear with a high permeability value due to the velocity gradient.



(a)



(b) Temperature (K)

Figure 6.16: (a) 3-D surface plot of the temperature in the bipolar plate and backing and catalyst layers for $\kappa = 5.5 \times 10^{-13} (m^2)$. Note $y = 4$ is the catalyst layer/membrane interface; (b) Contour plot of temperature (K) in the bipolar plate and gas diffusion and catalyst layers for the multi-phase model for $\kappa = 5.5 \times 10^{-13} (m^2)$ and the Leverette function used to describe $P_c(S)$. x and y coordinates have been normalized for better presentation of results. (see Figure 6.1)

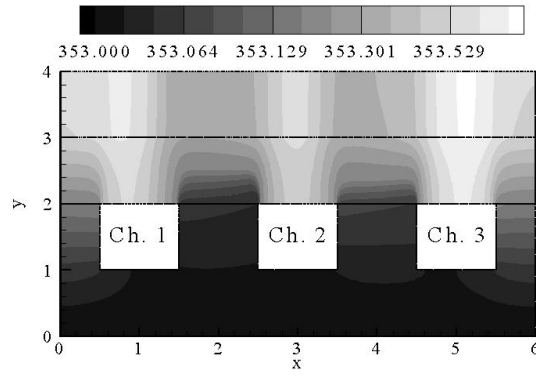
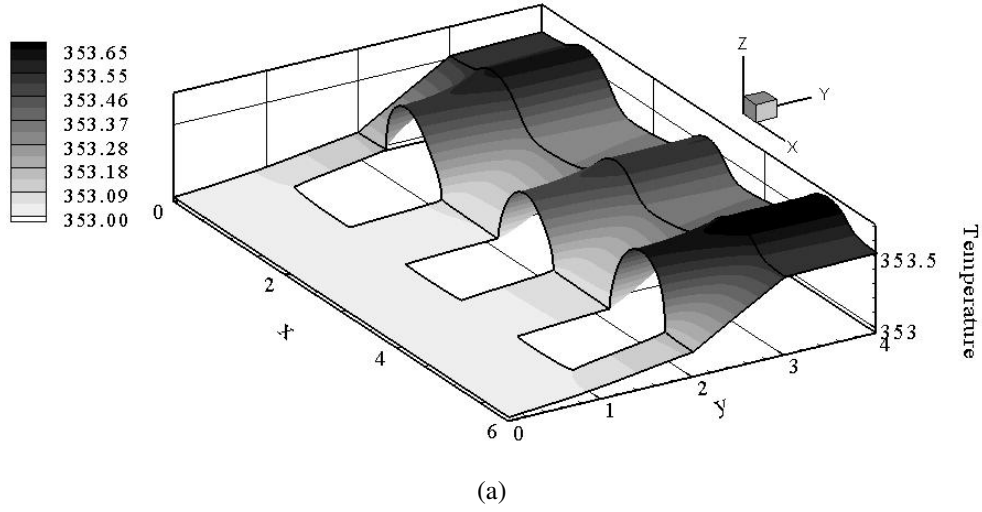


Figure 6.17: (a) 3-D surface plot of the temperature in the bipolar plate and backing and catalyst layers for $\kappa = 5.5 \times 10^{-10} (m^2)$. Note $y = 4$ is the catalyst layer/membrane interface; (b) Contour plot of temperature (K) in the bipolar plate and gas diffusion and catalyst layers for the multi-phase model for $\kappa = 5.5 \times 10^{-10} (m^2)$ and the Leverette function used to describe $P_c(S)$. x and y coordinates have been normalized for better presentation of results. (see Figure 6.1)

CHAPTER 6. NON-ISOTHERMAL MODEL RESULTS

Temperature variation along the cell length at different positions along the thickness has been plotted for three permeability values in Figure 6.18. The black line, red line and dark cyan line represent the temperature variation for permeability values of $5.5 \times 10^{-13} (m^2)$, $5.5 \times 10^{-11} (m^2)$ and $5.5 \times 10^{-10} (m^2)$, respectively. For all values of permeability, the temperature profile in the gas diffusion layer is more of a two-dimensional nature, while it becomes more one dimensional in the catalyst layer. In the catalyst layer the change of temperature occurs with the change of cell length. Further, one of the most apparent similarities in temperature profile among all values of permeability is the increased heat generation under the channel areas. The temperature is higher under the channel areas than under the land areas. This is attributed to the fact that at the bipolar plate boundary, the temperature is assumed to be uniform. The overall heat generation with low permeability values is lower than that with high permeability values. This is attributed to the slower rate of oxygen consumption with low permeability values. Finally, the effect of convection on the temperature profile is apparent for high permeability values. The heat is carried away from the areas under the land between the channels. This phenomenon is clearly observed with a permeability of $5.5 \times 10^{-10} (m^2)$. There exists a variation of temperature along the cell length which is exaggerated in the catalyst layer. This exaggeration in temperature variation is attributed to liquid water evaporation. As discussed earlier, a high permeability value results in an aggressive removal of water in both, liquid and vapor form. Thus, liquid water evaporates releasing heat.

CHAPTER 6. NON-ISOTHERMAL MODEL RESULTS

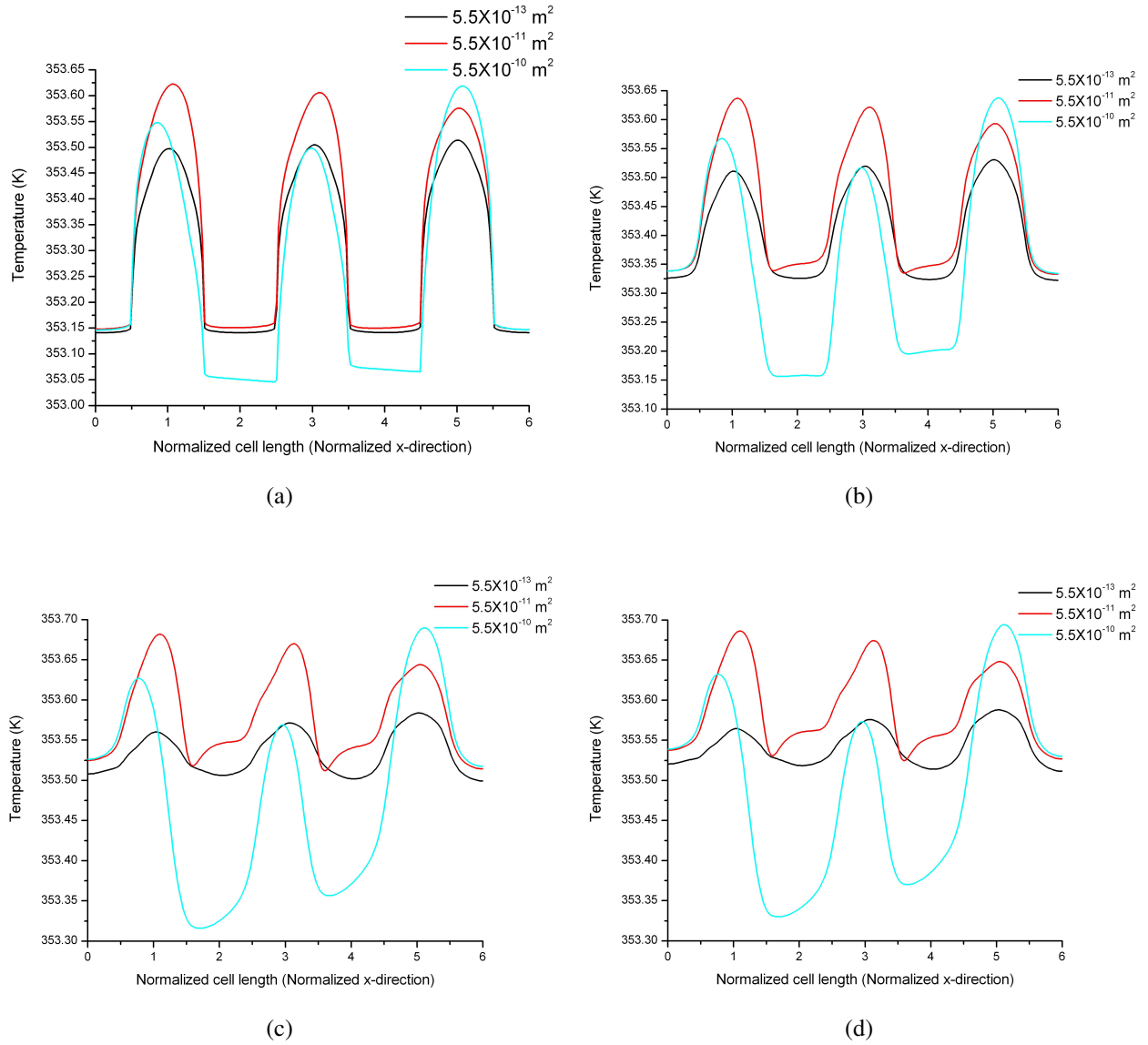
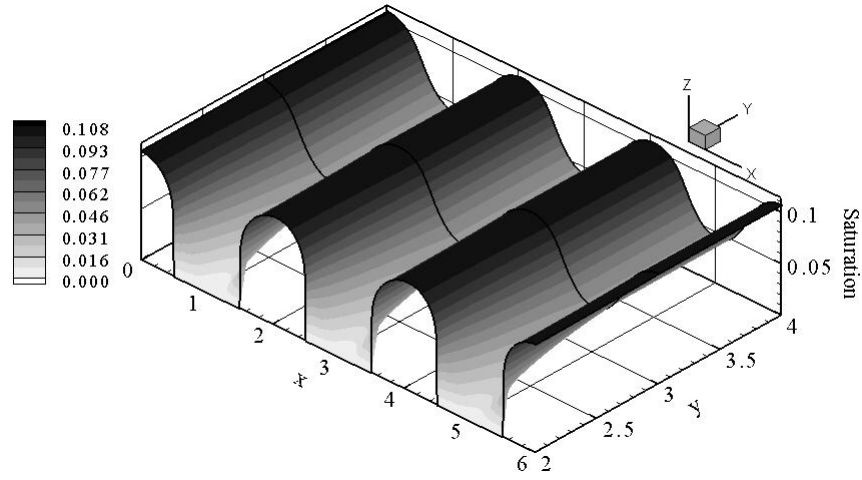


Figure 6.18: Effect of permeability on the temperature variation along the normalized x-direction for different normalized y values (a) 2; (b) 2.5; (c) 3; (d) 4

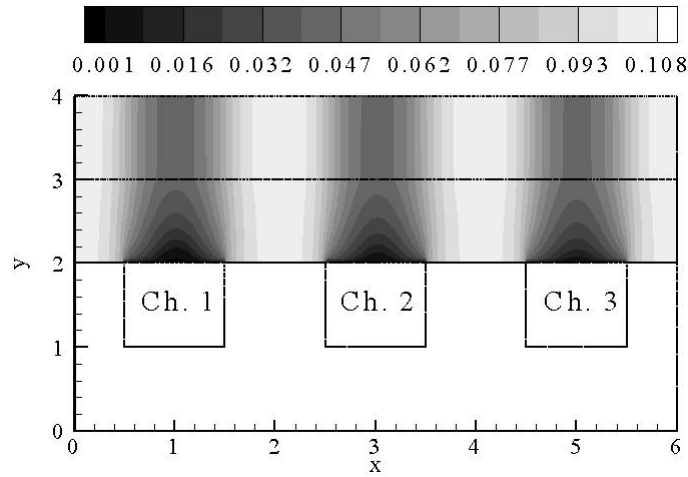
CHAPTER 6. NON-ISOTHERMAL MODEL RESULTS

The saturation profile of liquid water in the gas diffusion and catalyst layers is shown in Figures 6.19 and 6.20 for permeability values of $5.5 \times 10^{-13} \text{ (m}^2\text{)}$ and $5.5 \times 10^{-10} \text{ (m}^2\text{)}$, respectively. The cross flow phenomenon is clearly observed with a high permeability value. In fact, with a permeability value of $5.5 \times 10^{-10} \text{ (m}^2\text{)}$, the liquid water saturation in the gas diffusion layer is almost zero. This indicates that the cross flow phenomenon is significant in the gas diffusion layer and assists in the liquid water removal. Liquid water accumulates between channels when the permeability of the layers is low. The only means of water removal from the cell is through diffusion. This means that only the liquid water, which is immediately above the channel will be removed, while the liquid water existing under the land areas will have to accumulate. With the existence of the cross flow phenomenon, the velocity gradient created by the pressure drop along with a high permeability value results in the assistance of liquid water removal. Liquid water is being pushed by the gas into adjacent channels; thus, it is transported out of the cell.

The effect of the temperature change on the cross flow phenomenon should also be examined. In Figure 6.21, the x-direction velocity taken at the cross-section of $y = 3.5$ for the multi-phase, isothermal and non-isothermal models for permeability values $5.5 \times 10^{-13} \text{ (m}^2\text{)}$, $5.5 \times 10^{-11} \text{ (m}^2\text{)}$ and $5.5 \times 10^{-10} \text{ (m}^2\text{)}$ is plotted along the normalized x-direction. It is seen here that the addition of heat has little effect on the magnitude of the cross flow. It also has no effect on the trend of the cross flow. This can be explained by the fact that the temperature change is very small.

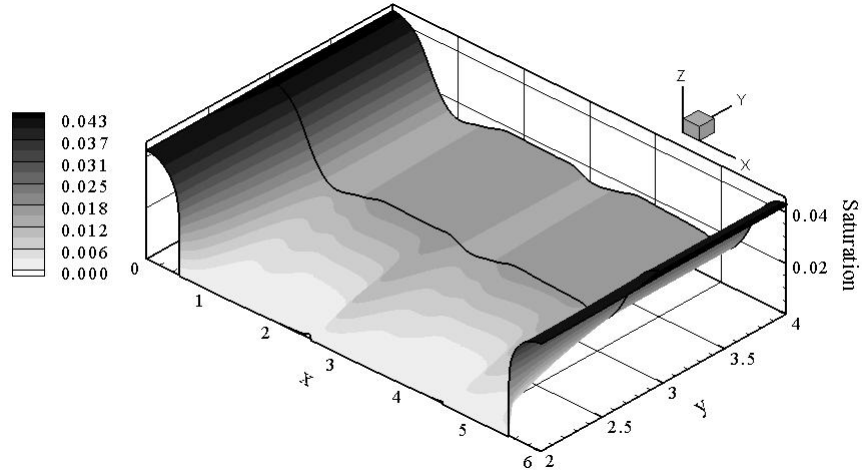


(a)

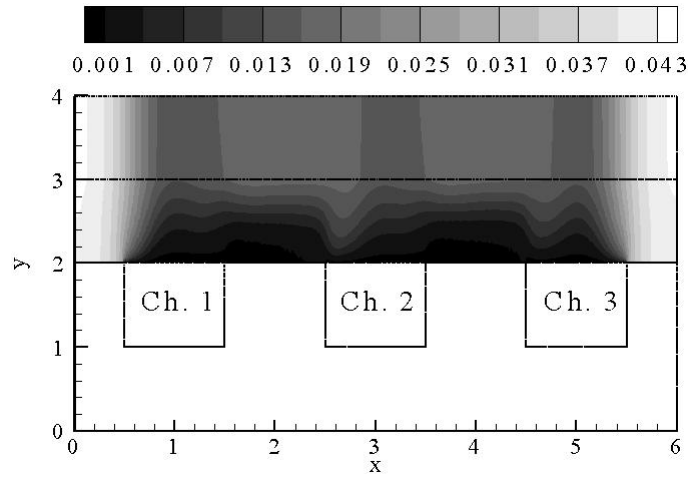


(b) Saturation

Figure 6.19: (a) 3-D surface plot of the liquid water saturation in the backing and catalyst layers for $\kappa = 5.5 \times 10^{-13} \text{ (m}^2\text{)}$. Note $y = 4$ is the catalyst layer/membrane interface; (b) Contour plot of liquid water saturation in the bipolar plate and gas diffusion and catalyst layers for the multi-phase model for $\kappa = 5.5 \times 10^{-13} \text{ (m}^2\text{)}$. The Leverette function used to describe $P_c(S)$. x and y coordinates have been normalized for better presentation of results. (see Figure 6.1)



(a)



(b) Saturatoin

Figure 6.20: (a) 3-D surface plot of the liquid water saturation in the backing and catalyst layers for $\kappa = 5.5 \times 10^{-10} (m^2)$. Note $y = 4$ is the catalyst layer/membrane interface; (b) Contour plot of liquid water saturation in the bipolar plate and gas diffusion and catalyst layers for the multi-phase model for $\kappa = 5.5 \times 10^{-10} (m^2)$. The Leverette function used to describe $P_c(S)$. x and y coordinates have been normalized for better presentation of results. (see Figure 6.1)

CHAPTER 6. NON-ISOTHERMAL MODEL RESULTS

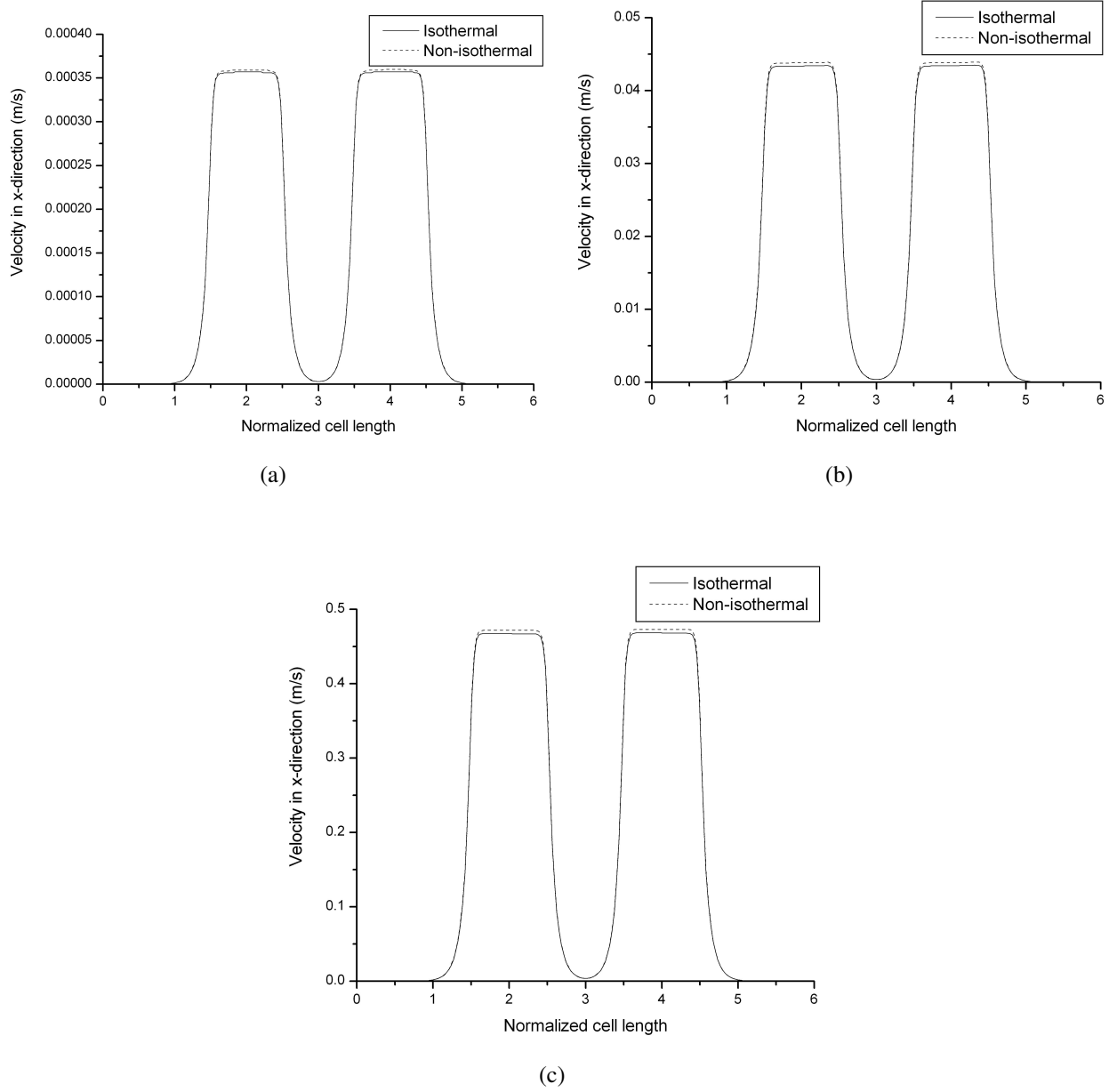


Figure 6.21: Comparison of the cross flow amount between the isothermal and non-isothermal multi-phase cases at a normalized y value of 3.5 for different permeability values of (a) $5.5 \times 10^{-13} \text{ (m}^2\text{)}$; (b) $5.5 \times 10^{-11} \text{ (m}^2\text{)}$; (c) $5.5 \times 10^{-10} \text{ (m}^2\text{)}$

At the end of this section, it should be mentioned that the current density associated with a permeability value of $5.5 \times 10^{-13} (m^2)$, $5.5 \times 10^{-11} (m^2)$ and $5.5 \times 10^{-10} (m^2)$ is $3770 (A/m^2)$, $3886 (A/m^2)$, and $3929 (A/m^2)$, respectively. The results of the multi-phase, isothermal model showed that a high permeability results in the highest current density, which is still the case.

6.3.3 Effect of Shoulder(Land)/Channel Width Ratio

For this section recall that the width ratio is calculated as follows,

$$\frac{\text{Shoulder}}{\text{Channel}} = \frac{W_s}{W_d} \quad (6.1)$$

where, W_s is the width of the shoulder and W_d is the channel width. Figure 6.22 gives a pictorial illustration of the two parameters; W_s and W_d .

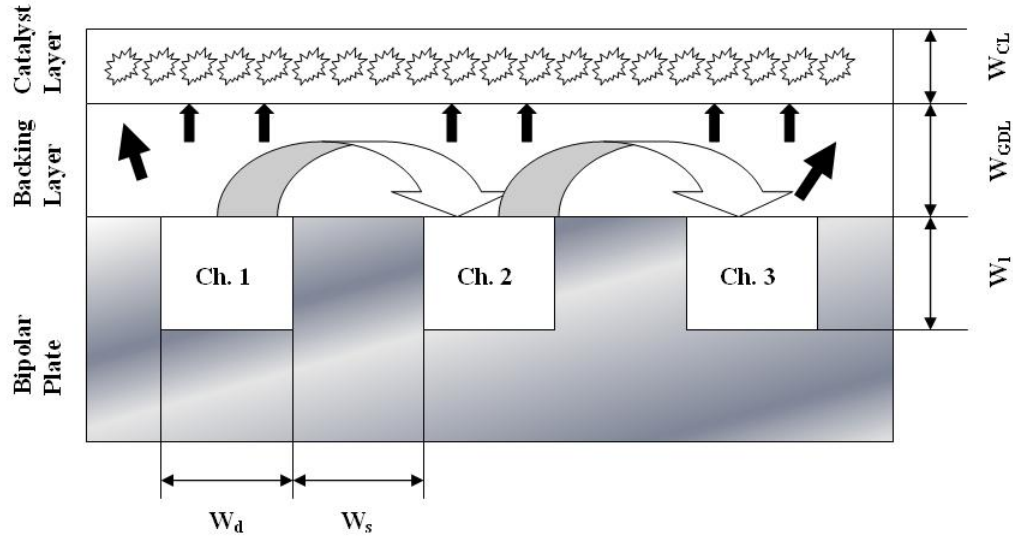


Figure 6.22: Illustration of shoulder to channel width ratio

The temperature distribution for two values of shoulder/channel width ratio is discussed in this section. It is expected that the heat generation would differ significantly due to the change in the width ratio. Heat generation is highly non-uniform along the various domains in the the fuel cell. The temperature distribution for width values of 1:2 and 2:1 is shown in Figures 6.23 and 6.24, respectively. It is clear that the temperature distribution varies with the width. For better

CHAPTER 6. NON-ISOTHERMAL MODEL RESULTS

understanding of the dependency of the temperature on the width ratio, the temperature along the x-direction at different y values is plotted for shoulder/channel ratios of 1:2 and 2:1 and shown in Figure 6.25. A decrease in the width ratio results in a slight increase in the temperature due to the increase in the resultant current density.

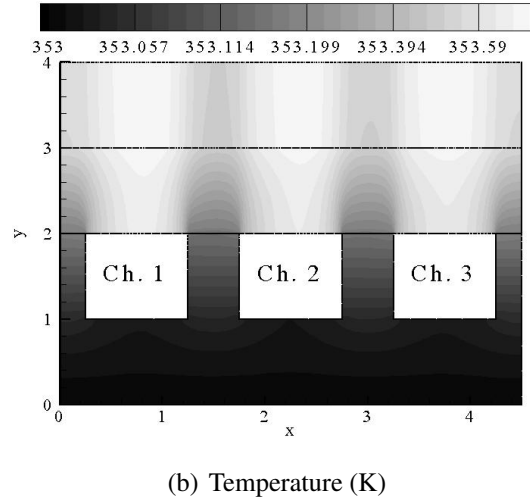
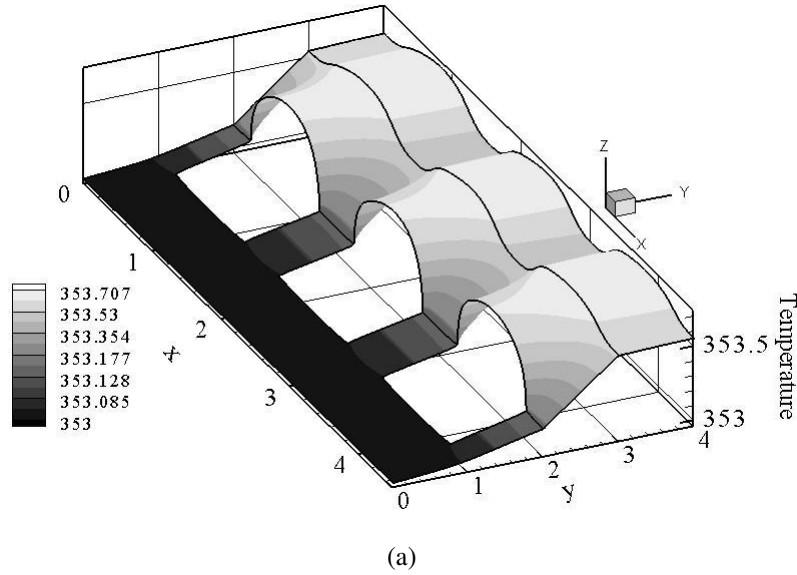


Figure 6.23: (a) 3-D surface plot of temperature (K) in the bipolar plate and the gas diffusion and catalyst layers for an S/C width ratio of 1 : 2; (b) Profile of temperature (K) in the bipolar plate and the backing and catalyst layers with an S/C width ratio of 1 : 2. x and y coordinates have been normalized for better presentation of results. (see Figure 6.1)

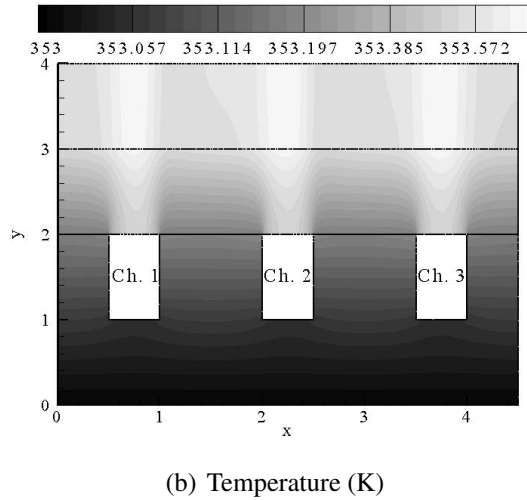
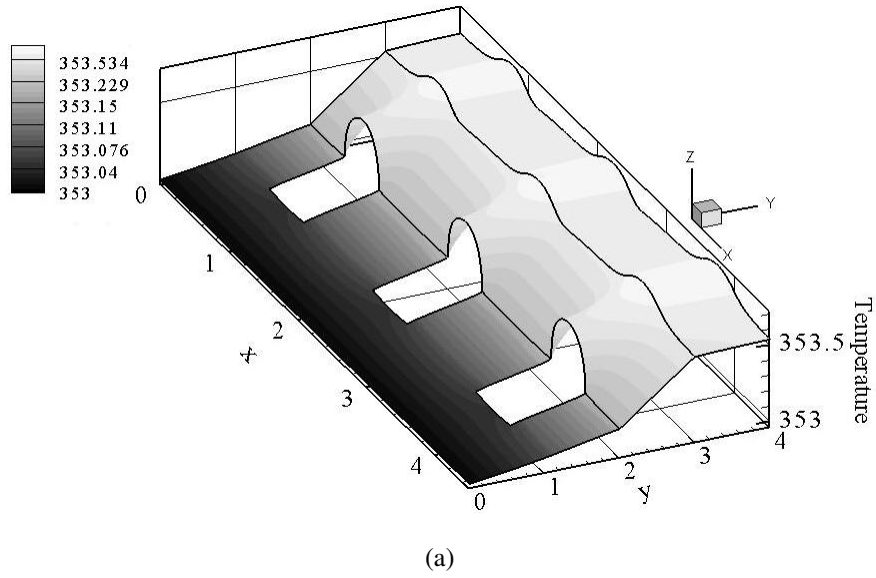


Figure 6.24: (a) 3-D surface plot of temperature (K) in the bipolar plate and the gas diffusion and catalyst layers for an S/C width ratio of 2 : 1; (b) Profile of temperature (K) in the bipolar plate and the backing and catalyst layers with an S/C width ratio of 2 : 1. x and y coordinates have been normalized for better presentation of results. (see Figure 6.1)

CHAPTER 6. NON-ISOTHERMAL MODEL RESULTS

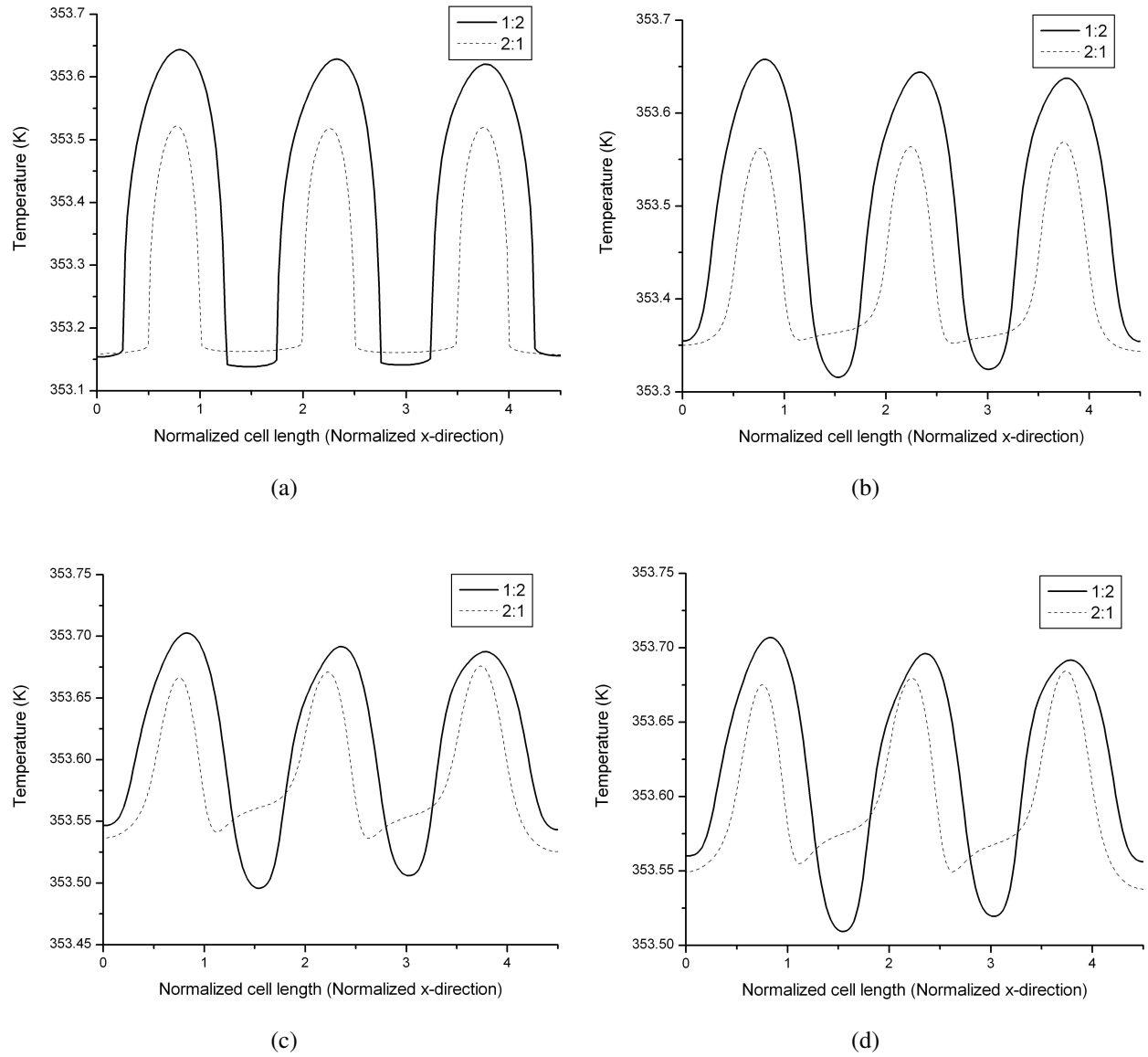
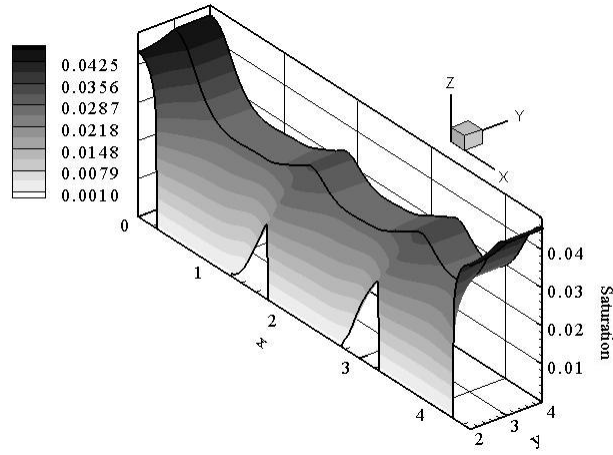


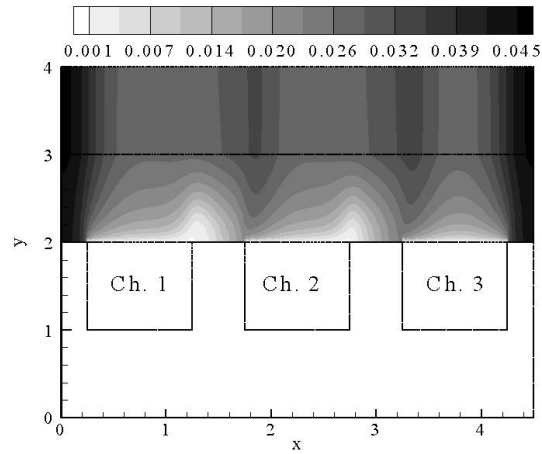
Figure 6.25: Effect of shoulder/channel ratio on the temperature variation along the normalized x-direction for different normalized y values (a) 2; (b) 2.5; (c) 3; (d) 4

CHAPTER 6. NON-ISOTHERMAL MODEL RESULTS

The liquid water saturation profile in the backing and catalyst layers for a width ratio of 1:2 and 2:1 is shown in Figures 6.26 and 6.27, respectively. The leakage of liquid water between adjacent channels is clearly seen with a shoulder to channel width ratio of 1:2. The short shoulder width decreases the total distance needed to travel. In addition, the larger channel width increases the pressure gradient and in turn increases the velocity gradient, which directly affects the amount of cross flow. Consequently, the amount of liquid water remaining in the cell is decreased with the decrease of the shoulder to channel width ratio. This decrease is despite the fact that the total current density is higher with a lower shoulder to channel width ratio. The total current density is 4146 (A/m^2) and 3751 (A/m^2) for a shoulder to channel width ratio of 1:2 and 2:1, respectively. Compared to the isothermal model results there is a very slight decrease in performance due to heat generation. Recall, the current density for the isothermal model is 4170 (A/m^2) and 3764 (A/m^2) for a shoulder to channel width ratio of 1:2 and 2:1, respectively.

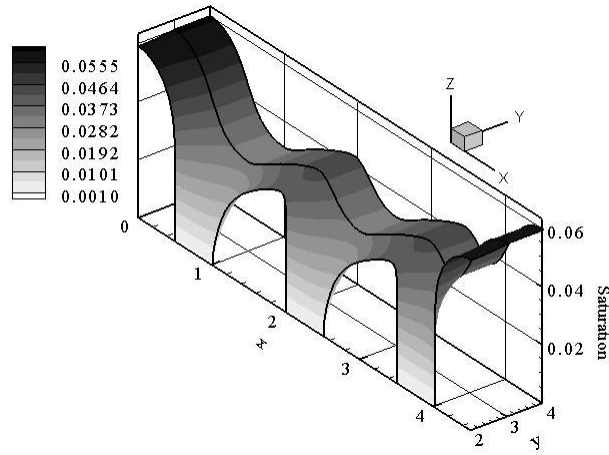


(a)

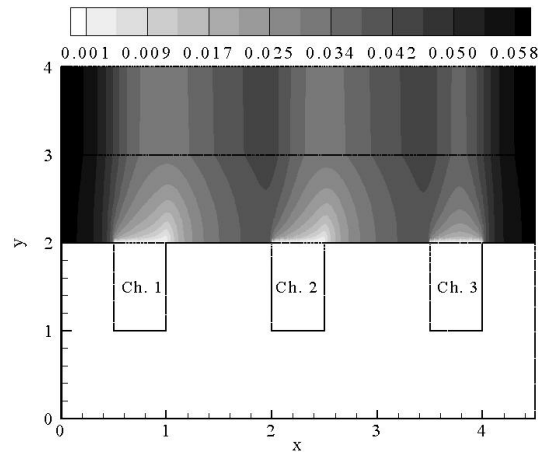


(b) Saturation

Figure 6.26: (a) 3-D surface plot of liquid water saturation in the gas diffusion and catalyst layers for an S/C width ratio of 1 : 2; (b) Profile of liquid water saturation in the backing and catalyst layers with an S/C width ratio of 1 : 2. x and y coordinates have been normalized for better presentation of results. (see Figure 6.1)



(a)



(b) Saturation

Figure 6.27: (a) 3-D surface plot of liquid water saturation in the gas diffusion and catalyst layers for an S/C width ratio of 2 : 1; (b) Profile of liquid water saturation in the backing and catalyst layers with an S/C width ratio of 2 : 1 x and y coordinates have been normalized for better presentation of results. (see Figure 6.1)

Chapter 7

Concluding Remarks

Two-dimensional isothermal and non-isothermal models for the cathode of a polymer electrolyte membrane fuel cell have been developed. The models are applied to investigate species transport, electro-chemical reaction and heat transport in three domains of the cathode, bipolar plate and backing and catalyst layers. In this thesis, the catalyst layer is modeled as a finite domain rather than just a boundary. A serpentine channel flow field is used to investigate the cross flow of species between neighboring channels. Conservation equations are applied to the solid, gaseous and liquid phases to generate comprehensive results. The commercial software, COMSOL Multiphysics, was used to solve the governing equations numerically. A detailed analysis on the species transport and electrochemical reaction was put forward for an isothermal, single phase case and an isothermal, multi-phase case. The isothermal, multi-phase case was then used to discuss in detail the cross flow phenomenon and its effects on liquid water removal from the cell, the effects of inlet relative humidity on the presence of liquid water in the cell and its performance and the effects of the shoulder/channel width ratio on the performance of the cathode. In the multi-phase, isothermal model, the dependency of the capillary pressure (driving force of liquid water) on saturation was represented using two different expressions. The two relations are explored and their differences discussed. The non-isothermal cases were used to explore the heat generation in the cathode of the cell. The energy equation was first applied to the single phase model in order to investigate its effects on the water vapor presence and to indicate that even with the addition of heat, the

CHAPTER 7. CONCLUDING REMARKS

consideration of liquid water still needs to be addressed. The energy equation was then applied to the multi-phase model to investigate the effects of the permeability, inlet relative humidity and shoulder/channel width ratio on the heat generation in the cathode.

The results of the single phase, isothermal model revealed that due to the pressure drop along the channel flow field, leakage of species between two adjacent channels occur. This phenomenon is observed through the examination of the oxygen mass fraction. The distribution of oxygen concentration is shown to be two-dimensional. In the x-direction, the concentration of oxygen is higher under the channel areas than under the land areas, while, in the y-direction the oxygen concentration decreases from the gas diffusion layer/channel interface to the catalyst layer/membrane interface. Oxygen is readily supplied to the areas under the channel, while it needs to travel a longer distance to reach the areas under the land. The decrease of oxygen concentration along the catalyst layer thickness is explained by the electro-chemical reaction that occurs in the layer. The rate of reaction in the catalyst layer increases along the thickness of the catalyst layer implying that oxygen is being consumed along the layer. In addition, it is shown that the rate of oxygen consumption is higher under the land areas. This is explained by the transfer of electrons. The solid potential is shown to be higher under the land areas since electrons have to travel around the channel. The losses due to proton transfer are found to be much smaller than those due to electron transfer. The observations made, led to the conclusions that enhancement of the catalyst layer should be made around the catalyst layer/membrane interface since the electrochemical reaction occurs more readily around that boundary. In addition, the focus should be put on enhancing electron transfer in the cell. The investigation of the relative humidity of the vapor water in the gas diffusion and catalyst layers revealed that this quantity is above 1 in certain areas and therefore, the need for a multi-phase model arisen. The overall behavior of the species transport and the electrochemical reaction for the isothermal, multi-phase model is shown to be very similar to that of the isothermal, single phase model. The presence of liquid water, however, led to a decrease in the performance of the cathode since liquid water blocks some of the available sites for reaction. With the consideration of pressure drop along the channel, the removal of liquid water from the cell is shown to be a combination of the capillary diffusion and the diffusion of water vapor.

CHAPTER 7. CONCLUDING REMARKS

A sensitivity analysis was carried out to study the effects of inlet relative humidity, cross flow and shoulder/channel width ratio. An inlet relative humidity of 90% and 80% led to the highest performance in the cathode. The relative humidity in the gas diffusion and catalyst layers corresponding to an inlet relative humidity of 90% and 80% was shown to be very close to 100% in the catalyst layer and in turn resulted in a high electrolyte conductivity. It was shown that the electrolyte conductivity plays a significant role in determining the overall performance up to a point. Once the electrolyte conductivity reaches 7.7 S/m, the liquid water saturation in the layers becomes the determining step in the performance of the cathode. The analysis of the inlet relative humidity effects showed that the catalyst layer plays a very important role in controlling the water concentration in the cell both in vapor and liquid forms. The evaporation of liquid water seems to mostly occur in the catalyst layer. This is expected since the production of water occurs in the catalyst layer; hence, depending on the thermodynamic properties of the cell at the time of water production, water will either evaporate or condense before leaving the catalyst layer.

The investigation of pressure drop and the permeability can be classified into the category of cross flow phenomenon investigation. A velocity gradient is created due to the pressure drop and its enhanced with the an increase in the permeability value. With no pressure drop along the channel flow field, it was shown that liquid water will accumulate in the areas under the land and results in a 2% reduction of performance. The permeability of a material measures the ability of this material to transmit fluids and directly affects the capillary diffusion coefficient. Three permeability values are investigated $5.5 \times 10^{-13} \text{ m}^2$, $5.5 \times 10^{-11} \text{ m}^2$, and $5.5 \times 10^{-10} \text{ m}^2$. The cross leakage between channels is reduced with the use of a low permeability value of $5.5 \times 10^{-13} \text{ m}^2$ and therefore the performance of the cathode is reduced. The removal of liquid water from the gas diffusion layer is lowered and the cross leakage between channels is diminished. Diffusion is the only means of liquid water removal. A high permeability value of $5.5 \times 10^{-10} \text{ m}^2$ results in an increased cross leakage between channels; thus, enhanced water removal between neighboring channels.

Five different values of the shoulder to channel width ratio were explored; 1:2, 2:1, 1:1, 1:3, 3:1. An optimal width ratio was found to be around 1:2 and 1:3. Increasing the width of the channel results in an increased flow of oxidant. Further decrease in the width ratio might result

CHAPTER 7. CONCLUDING REMARKS

in a decrease in performance since the shoulder area is needed for the electron transport. With a wider channel, more oxygen is being supplied. Finally, the cross flow phenomenon between adjacent channels was found to decrease with an increase in the shoulder to channel width ratio.

The sensitivity analysis was done using both the Leverette function and the Brooks and Corey relation. The results revealed that the Leverette function leads to better performance and reduced liquid water saturation than the Brooks and Corey relation. However, the overall trend of results is similar for both relations.

The isothermal models were extended to investigate the heat transport for both the single phase and multi-phase cases. The single phase, non-isothermal model showed that the temperature variation in the bipolar plate is very small due to the high thermal conductivity of the plate. The pressure drop along the channel flow field contributes to the heat transfer via convection in the gas diffusion and catalyst layers. The average temperature over the catalyst layer is higher than that over the gas diffusion layer due to the heat addition through the electrochemical reaction. The saturation pressure was shown to vary according to the temperature and its profile resembles that of the temperature. The comparison of the non-isothermal and isothermal cases revealed that heat generation results in reduced performance. Further, even though, compared to the isothermal case, the relative humidity in the gas diffusion and catalyst layers is decreased by about 5%, it is still higher than 100%. Thus, the energy equation needed to be applied to the multi-phase model.

The non-isothermal, multi-phase model was created in order to investigate the temperature profile with the presence of liquid water. Compared to the non-isothermal, single phase case, the overall temperature in the gas diffusion and catalyst layers is decreased. This occurs for two reasons, the decrease in current density in the multi-phase model and the loss of heat due to the evaporation of liquid water. The analysis was then extended to study the effect of the permeability value on the temperature. Three permeability values were investigated $5.5 \times 10^{-13} \text{ m}^2$, $5.5 \times 10^{-11} \text{ m}^2$ and $5.5 \times 10^{-10} \text{ m}^2$. With a very high permeability value of $5.5 \times 10^{-10} \text{ m}^2$, the heat is carried away from the areas under the land and therefore, the temperature is decreased. For all permeability values, the variation of temperature is two-dimensional in the gas diffusion layer. While, in the catalyst layer, the temperature profile seems to be more one-dimensional. Compared to the

CHAPTER 7. CONCLUDING REMARKS

isothermal, multi-phase model, the saturation levels were shown to decrease by 2% due to heat addition. However, the overall performance of the cathode decreased for all permeability values with the addition of heat. Further, the analysis was extended to investigate the decrease of the inlet relative humidity and its effects on the temperature profile. An inlet relative humidity of 50% and 100% was used in order to draw the appropriate conclusions. The temperature profile is similar for both values of inlet relative humidity. The temperature increases in the thickness of the cell (from the channel towards the membrane). The transfer of energy through convection is apparent in both cases. Finally, the temperature associated with the 100% inlet relative humidity is higher than that with an inlet relative humidity of 50%. With an inlet relative humidity of 50%, more liquid water evaporates in order to reach the equilibrium point between the two phases of water. Hence, more energy is released due to this evaporation. Finally, decreasing the shoulder/channel width ratio leads to an increase in the temperature of the cell since the overall current density is increased with a small shoulder to channel width.

7.1 Summary

The overall trend of the electrochemical reaction as well as the species and heat transport is summarized below.

1. Due to the geometry of the channel flow field chosen, oxygen is readily supplied to the areas under the channel; thus, its concentration is lower under the land areas.
2. The dependency of the rate of reaction on the overpotential is more significant than its dependency on the oxygen concentration. The rate of reaction is higher under the land areas.
3. Losses due to electron transport are more significant than those due to the proton transport. The electrons travel an overall longer distance.
4. Care should be taken when assuming that water exists in vapor form only in the gas diffusion and catalyst layers since the byproduct of the electrochemical reaction in the cathode catalyst layer is water.

CHAPTER 7. CONCLUDING REMARKS

5. The overall behavior of the species transport and the electrochemical reaction for the isothermal, multi-phase model is similar to that of the isothermal, single phase model.
6. For the isothermal, multi-phase model the presence of liquid water led to a decrease in the performance of the cathode since liquid water blocks some of the available sites for reaction.
7. With the cross flow phenomenon, the removal of liquid water from the cell is a combination of the capillary diffusion and the diffusion of water vapor.
8. High permeability values results in an increase in the cross flow phenomenon and enhanced liquid water removal.
9. The presence of a pressure gradient along the channel flow field results in a velocity gradient and therefore the leakage between channels.
10. The electrolyte conductivity plays a significant role in determining the overall performance up to a point. Once the electrolyte conductivity reaches 7.7 S/m, the liquid water saturation in the layers becomes the determining step in the performance of the cathode.
11. The catalyst layer plays a very important role in controlling the water concentration in the cell both in vapor and liquid forms. The evaporation of liquid water seems to mostly occur in the catalyst layer.
12. An optimal shoulder to channel width ratio was found to be around 1:2 and 1:3.
13. The cross flow phenomenon between adjacent channels was found to decrease with an increase in the shoulder to channel width ratio.
14. The results revealed that the Leverette function leads to better performance and reduced liquid water saturation than the Brooks and Corey relation. However, the overall trend of results is similar for both relations.
15. The temperature variation in the bipolar plate is very small due to the high thermal conductivity of the plate.

CHAPTER 7. CONCLUDING REMARKS

16. The pressure drop along the channel flow field contributes to the heat transfer via convection in the gas diffusion and catalyst layers.
17. The average temperature over the catalyst layer is higher than that over the gas diffusion layer due to the heat addition through the electrochemical reaction.
18. Heat generation results in reduced performance.
19. With the consideration of liquid water in the gas diffusion and catalyst layers, the overall temperature in the layers is decreased due to liquid water evaporation.

7.2 Recommendations

This thesis presented a comprehensive model for the cathode of a polymer electrolyte fuel cell. The results of this thesis revealed that there are many other issues that should be addressed in order to increase the capabilities of this model. This section will put forward some recommendations as to what should be investigated.

1. The assumption of a uniform flow in the channel flow field was used in the production of the results. In turn, at the inlet of channels, many parameters such as the pressure, oxygen mass fraction, liquid water saturation were specified. However, for comprehensive analysis of the cathode, the flow in the channel should be modeled and therefore, the values at the channel inlets should be solved for. It is important to investigate the behavior of the flow in the flow channels, since it directly affects the flow in the gas diffusion and catalyst layers.
2. From the results presented, it was seen that due to the geometry of the channels, there is a build up of current around the edges of the channels. Therefore, it is recommended that the channel geometry be investigated and its effects on the flow be shown.
3. A sensitivity analysis should be put forward for the condensation and evaporation terms. Theoretically, these terms should approach infinity in order to approach the equilibrium point.

CHAPTER 7. CONCLUDING REMARKS

4. The production of water should also be investigated. The addition of heat as latent energy is very much related to the production of water and the form of its production. In this thesis, for the multi-phase model, the production of water was assumed to be in liquid form only. Therefore, the analysis should be extended to investigate its production in vapor form only and its production as a mixture of vapor and liquid forms.

References

- [1] S. Oberthur, H. Ott, The kyoto protocol: International climate policy for the 21st century, Germany: Springer-Verlag Berlin Heidelberg, (1999).
- [2] A. Robinson, S. Baliunas, W. Soon, Z. Ronbinson, Environmental effects of increased atmospheric carbon dioxide, found via <http://www.oism.org/pproject/s33p36.htm>, (1998).
- [3] W. Gray, Viewpoint: Get off warming bandwagon, BBC News World Edition, (2000).
- [4] D. Kessel, Global warming - facts, assesment, countermeasures, German Petroleum Institue, Journal of Petroleum Science and Engineering, 26, (2000).
- [5] Statistics Canada, Canadas GHG emissions by sector, end-use and sub-sector and Canadas secondary energy use by sector, end-use and sub-sector, 2002, found at the Following URL, <http://oee.nrcan.gc.ca/neud/dpa/>.
- [6] Energy Information Administration, Department of Energy, USA, Emissions of greenhouse gases in the United States, 2003, found at the following URL, <http://www.eia.doe.gov/oiaf/1605/ggrpt/carbon.html>.
- [7] N. Zamel and X. Li, Life cycle analysis of vehicles powered by a fuel cell and by internal combustion engine vehicles in Canada, Journal of Power Sources, 155 (2006).
- [8] N. Zamel and X. Li, Life cycle comparison of fuel cell vehicles and internal combustion engine vehicles for Canada and the United States, Journal of Power Sources, 162 (2006).
- [9] T. Ralph, G. Hards, and J. Keating. Low cost electrodes for proton exchange membrane fuel cells performance in single cells and Ballard stacks, Journal of the Electrochemical Society, 144(11):3845-3857, (1997).
- [10] N. Zamel and X. Li, Transient analysis of carbon monoxide poisoning and oxygen bleeding in a PEM fuel cell anode catalyst layer, International Journal of Hydrogen Energy, Accepted April 2007.
- [11] J.J. Baschuk and X. Li, Carbon monoxide poisoning of proton exchange membrane fuel cells, International Journal of Energy Research, 25 (2001).

REFERENCES

- [12] J.J. Baschuk and X. Li, Modeling CO poisoning and O_2 bleeding in a PEM fuel cell Anode, *International Journal of Energy Research*, 27 (2003).
- [13] J.J. Baschuk, PhD Thesis, Comprehensive consistent and systematic approach to the mathematical modeling of PEM fuel cells, University of Waterloo, Department of Mechanical Engineering, (2007).
- [14] F. Mighri, M. A. Huneault, M. F. Champagne, Electrically conductive thermoplastic blends for injection and compression molding of bipolar plates in the fuel cell application, *Polymer Engineering and Science*, (2004).
- [15] E. Middleman, W. Kout, B. Vogelaar, Bipolar plates for PEM fuel cells, *Journal of Power Sources*, (2003).
- [16] A. Heinzl, F. Mahlendorf, O. Niemzig, C, Injection moulded low cost bipolar plates for PEM fuel cells, *Journal of Power Sources*, (2004).
- [17] D.R. Hodgson, B. May, P.L. Adcock, New lightweight bipolar plate system for polymer electrolyte fuel cells, *Journal of Power Sources*, (2001).
- [18] N. Cunningham, D. Guay, J.P. Dodelet, Y. Meng, A.R. Hlil, New Materials and Procedures to Protect Metallic PEM Fuel Cell Bipolar Plates, *Journal of the Electrochemical Society*, (2003).
- [19] H. Wang, M.A. Sweikart, J.A. Turner, Stainless steel as bipolar plate material for polymer electrolyte membrane fuel cells, *Journal of Power Sources*, (2003).
- [20] E.A. Cho, U.-S. Jeon, H.Y. Ha, S.-A. Hong, I.-H. Oh, Characteristics of composite bipolar plates for PEMFC, *Journal of Power Sources*, (2003).
- [21] H.C. Kuan, C.C.M. Ma, K.H. Chen, S.M. Chen, Preparation, electrical, mechanical, and thermal properties of composite bipolar plate for a fuel cell, *Journal of Power Sources*, (2004).
- [22] S.-J. Lee, C.-H. Huang, Y.-P. Chen, C.-T. Hsu, PVD coated bipolar plates for PEM fuel cells, *Journal of Fuel Cell Science and Technology*, (2005).
- [23] H. Wang, G. Teeter, J. Turner, Investigation of a duplex stainless steel as polymer electrolyte membrane fuel cell bipolar plate material, *Journal of the Electrochemical Society*, (2005).
- [24] A. Hermann, T. Chaudhuri, P. Spagnol, Bipolar plates for PEM fuel cells: A review, *International Journal of Hydrogen Energy*, (2005).
- [25] X. Li, *Principles of Fuel Cells*, Taylor and Francis, New York (2005).
- [26] D.M. Bernardi and M.W. Verbrugge, Mathematical model of a gas diffusion electrode bonded to a polymer electrolyte, *Journal of the Electrochemical Society*, (1991) 37.

REFERENCES

- [27] D.M. Bernardi and M.W. Verbrugge, A mathematical model of the solid-polymer-electrolyte fuel cell, *Journal of the Electrochemical Society*, (1992) 139.
- [28] T.E. Springer, T.A. Zawodinski, S. Gottesfeld, Polymer electrolyte fuel cell model, *Journal of Electrochemical Society* 138, (1991).
- [29] T.E. Springer, M.S. Wilson, S. Gottesfeld, Modeling and experimental diagnostics in polymer electrolyte fuel cells, *Journal of Electrochemical Society* 140, (1993).
- [30] E.A. Ticianelli, C.R. Derouin, A. Redondo, S. Srinivasan, Methods to advance technology of proton exchange membrane fuel cells, *Journal of the Electrochemical Society*, (1988a) 135.
- [31] C. Marr and X. Li, Composition and Performance Modeling of Catalyst Layer in a Proton Exchange Membrane Fuel Cell, *Journal of Power Sources*, 77 (1997), 17.
- [32] F. Jaouen, G. Lindbergh and G. Sundholm, Investigation of Mass Transport Limitation in the Solid Polymer Fuel Cell Cathode, *Journal of the Electrochemical Society*, 149 (2002), A437.
- [33] R. Bradean, K. Promislow and B. Wetton, Transport Phenomena in the Porous Cathode of a PEMFC, *Numerical Heat Transfer*, 42 (2002), 121.
- [34] Q. Wang, M. Eikerling, D. Song, Z. Liu, T. Navessin, Z. Xie and S. Holdcroft, Functionally graded cathode catalyst layers for PEMFCs, *Journal of Electrochemical Society*, 151 (2004), A950.
- [35] Q. Wang, D. Song, T. Navessin, S. Holdcroft and Z. Liu, A method for optimizing distributions of nafion and Pt in cathode catalyst layers in a PEM fuel cell, *Electrochimica Acta*, 50 (2004).
- [36] D. Song, Q. Wang, Z. Liu, M. Eikerling, Z. Xie, T. Navessin and S. Holdcroft, A mathematical model and optimization of the cathode catalyst layer structure in PEM fuel cells, *Electrochimica Acta*, 50 (2005).
- [37] W. He, J. S. Yi, and T.V. Nguyen, Two-phase flow model of the cathode of PEM fuel cells using interdigitated flow fields, *AIChE Journal*, October, 46 (2000).
- [38] D. Natarajan, T.V. Nguyen, A Two-dimensional, Two-phase, multicomponent, transient model for the cathode of a proton exchange membrane fuel cell, *Journal of Electrochemical Society*, 148 (2001).
- [39] C.Y. Wang, P. Cheng, A multiphase mixture model for multiphase, multicomponent transport in capillary porous media: I. Model development, *International Journal of Heat and Mass Transfer*, 39 (1996).
- [40] P. Cheng, C.Y. Wang, A multiphase mixture model for multiphase, multicomponent transport in capillary porous media: II. Numerical simulation of the transport of organic compounds in the subsurface *International Journal of Heat and Mass Transfer*, 39 (1996).

REFERENCES

- [41] Z.H. Wang, C.Y. Wang, K.S. Chen, Two phase flow and transport in the air cathode of proton exchange membrane fuel cells, *Journal of Power Sources*, 94 (2001).
- [42] M.C. Leverette, Capillary behavior in porous solids, *Tran. AIME* 142, (1941).
- [43] H. Meng, C.Y. Wang, Model of two-phase flow and flooding dynamics in polymer electrolyte fuel cells, *Journal of the Electrochemical Society* (2005), 152.
- [44] U. Pasaogullari, C.Y. Wang, K.S. Chen, Two-phase transport in polymer electrolyte fuel cells with bilayer cathode gas diffusion media, *Journal of the Electrochemical Society* (2005), 152.
- [45] S. M. Senn, D. Poulikakos, Multiphase transport phenomena in the diffusion zone of a PEM fuel cell, *Journal of Heat Transfer* (2005), Vol. 127.
- [46] M. Eikerling, Water management in cathode catalyst layers of PEM fuel cells: A Structure-Based Model, *Journal of the Electrochemical Society*(2006), Vol. 153.
- [47] L. You, H. Liu, A two-phase flow and transport model for the cathode of PEM fuel cells, *International Journal of Heat and Mass Transfer*, 45 (2002).
- [48] M. Hu, X. Zhu, M. Wang, A. Gu, L. Yu, Three dimensional, two phase flow mathematical model for PEM fuel cell: Part I. Model Development, *Energy Conversion and Management*, 45 (2004).
- [49] M. Hu, X. Zhu, M. Wang, A. Gu, L. Yu, Three dimensional, two phase flow mathematical model for PEM fuel cell: Part II. Analysis and Discussion of the Internal Transport Mechanisms, *Energy Conversion and Management*, 45 (2004).
- [50] N.P. Siegel, M.W. Ellis, D.J. Nelson, M.R. von Spakovsky, A two-dimensional computational model of a PEMFC with liquid water transport, *Journal of Power Sources*, 128 (2004).
- [51] J.J. Baschuk and X. Li, A general formulation for a mathematical PEM fuel cell model, *Journal of Power Sources*, 142 (2004).
- [52] E. Birgersson, M. Noponen, M. Vynnycky, Analysis of a two-phase non-isothermal model for a PEFC, *Journal of the Electrochemical Society*, 152 (2005).
- [53] L. Matamoros and D. Brüggemann, Simulation of the water and heat management in proton exchange membrane fuel cells, *Journal of Power Sources*, 161 (2006).
- [54] Y. Wang and C.Y. Wang, Nonisothermal two-phase model for polymer electrolyte fuel cells, *Journal of the Electrochemical Society*, 153 (2006), A1193-A1200.
- [55] J.J. Hwang and P.Y. Chen, Heat/mass transfer in porous electrodes of fuel cells, *International Journal of Hydrogen Energy* (2006), 49.

REFERENCES

- [56] J.J. Hwang, C.H. Chao, C.L. Chang, W.Y. Ho, D.Y. Wang, Modeling of two-phase temperatures in a two-layer porous cathode of polymer electrolyte fuel cells, *International Journal of Hydrogen Energy* (2006), doi: 10.1016/j.ijhydene.2006.06.068.
- [57] C.H. Chao and J.J. Hwang, Predictions of phase temperatures in a porous cathode of polymer electrolyte fuel cells using a two-equation model, *Journal of Power Sources* 160 (2006).
- [58] J.J. Hwang, A complete two-phase model of a porous cathode of a PEM fuel cell, *Journal of Power Sources* (2007), 164.
- [59] J. Park, X. Li, An experimental and numerical investigation on the cross flow through gas diffusion layer in a PEM fuel cell with a serpentine flow channel, *Journal of Power Sources* (2006).
- [60] J.P. Feser, A.K. Prasad, S.G. Advani, On the relative influence of convection in serpentine flow fields of PEM fuel cells, *Journal of Power Sources*, 161 (2006).
- [61] T. Kanazaki, X. Li, J.J. Baschuk, Cross-leakage flow between adjacent flow channels in PEM fuel cells, *Journal of Power Sources*, 162 (2006).
- [62] X. Li, I. Sabir, J. Park, A flow channel design procedure for PEM fuel cells with effective water removal, *Journal of Power Sources* (2006), doi:10.1016/j.jpowsour.2006.10.015.
- [63] R.K. Shah and A.L. London, *Laminar flow forced convection in ducts*, New York: Academic Press, (1978).
- [64] I.E. Idelchik, *Handbook of Hydraulic Resistance* (3rd Edition), CRC Press: Boca Raton (1994).
- [65] C. Wang, *Multiphase flow and heat transfer in porous media*, *Advances in Heat Transfer*, 196 (1997).
- [66] K. Vafai and C. Tien, Boundary and inertia effects on flow and heat transfer in porous media, *Journal of Heat and Mass Transfer*, 24 (1981).
- [67] A. Adamson, *Physical Chemistry of Surfaces* (5th Edition). Wiley, New York, (1990).
- [68] H.M. Yu, C. Ziegler, M. Oszcipok, M. Zobel, C. Hebling, Hydrophilicity and hydrophobicity study of catalyst layers in proton exchange membrane fuel cells, *Electrochimica Acta*, 51 (2005).
- [69] J. Ihonen, M. Mikkola, G. Lindbergh, Flooding of gas diffusion backing in PEFCs: physical and electrochemical characterization, *Journal of Electrochemical Society*, 151 (2004).
- [70] M.V. Williams, E. Begg, L. Bonville, H.R. Kunz, J.M. Fenton, Characterization of gas Diffusion layers for PEMFC, *Journal of Electrochemical Society*, 151 (2004).

REFERENCES

- [71] U. Pasaogullari, C.Y. Wang, Liquid water transport in gas diffusion layer of polymer electrolyte fuel cells, *Journal of Electrochemical Society*, 151 (2004).
- [72] C. Lim, C.Y. Wang, Effects of hydrophobic polymer content in GDL on power performance of a PEM fuel cell, *Electrochimica Acta*, 49 (2004).
- [73] P. Ustohal, F. Stauffer, T. Dracos, Measurement and modeling of hydraulic characteristics of unsaturated porous media with mixed wettability, *Journal of Contaminant Hydrology*, 33 (1998).
- [74] A.Z. Weber, R.M. Darling, J. Newman, Modeling two phase behavior in PEFC's, *Journal of the Electrochemical Society*, 151 (2004).
- [75] A. Demond and P. Roberts., Effect of interfacial forces on two-phase capillary pressure saturation relationships, *Water Resources Research*, 27 (1991).
- [76] A.T. Corey, *Mechanics of Heterogenous Fluids in Porous Media* Water Resources Publications, Fort Collins, (1977).
- [77] J. Chen, J. Hopmans, and M. Grismer, Parameter estimation of two-fluid capillary pressure saturation and permeability functions, *Advances in Water Resources*, 22 (1999).
- [78] M. Kaviani, *Principles of Heat Transfer in Porous Media* (2nd Edition), Springer, New York, (1995).
- [79] *Handbook of Chemistry and Physics*, 87th edition, CRC Press (2006).
- [80] W.Q. Tao, C.H. Min, X.L. Liu, Y.L. He, B.H. Yin, W. Jiang, Parameter sensitivity examination and discussion of PEM fuel cell simulation model validation Part I Current status of modeling research and model development, *Journal of Power Sources*, 160, (2006).
- [81] C.H. Min, Y.L. He, X.L. Liu, B.H. Yin, W. Jiang, W.Q. Tao, Parameter sensitivity examination and discussion fuel cell simulation model validation Part II Results of sensitivity analysis validation of the model, *Journal of Power Sources*, 160, (2006).
- [82] T.A. Zawodzinski, J. Davey, J. Valerio, S. Gottesfeld, *Electrochim. Acta*, 40 (1995).
- [83] F. N. Büchi, G.C. Scherer, *Journal of the Electrochemical Society* 148, (2001).
- [84] A. Parthasarathy, S. Srinivasan and J. Appleby, Temperature dependence of the electrode kinetics of oxygen reduction at the platinum/naion interface-a microelectrode investigation, *Journal of Electrochemical Society*, 139 (1992).
- [85] S. Motupally, J.A. Becker, J.W. Weidner, *Journal of the Electrochemical Society* 147, (2000).
- [86] C. Song, Y. Tang, J.L. Zhang, J. Zhang, H. Wang, J. Shen, S. McDermid, J. Li, P. Kozak, PEM fuel cell reaction kinetics in the temperature range of 23-120, *Electrochimica Acta*, 52 (2007).

REFERENCES

- [87] F.P. Incropera, D.P. Dewitt, Fundamentals of heat and mass transfer, John Wiley & Sons, 5th Edition, 2002.
- [88] E.I. du Pont de Nemours and Company, <http://www.dupont.com>.
- [89] M. Vynnycky, On the modelling of two-phase flow in the cathode gas diffusion layer of a polymer electrolyte fuel cell, Applied Mathematics and Computation (2007), doi:10.1016/j.amc.2006.12.040.
- [90] C. Ziegler, M. Tranitz, J.O. Schumacher, A model for planar self-breathing proton exchange membrane fuel cells in FEMLAB, Proceedings to COMSOL Multiphysics Conference, (2005).
- [91] H. Wu, Masters Thesis, Computational analysis on proton exchange membrane fuel cell technology, University of Ryerson, Department of Mechanical Engineering, (2005).